Ministry of Education and Science of Ukraine
Sumy State University

JOURNAL OF ENGINEERING SCIENCES

Scientific Journal

Volume 9, Issue 1 (2022)

ISSN 2312-2498 (print)
ISSN 2414-9381 (online)

Founded in 2014

Journal of Engineering Sciences is an open-access peer-reviewed scientific journal. It covers urgent issues of up-to-date high-tech production in developing new engineering trends and future technologies. The general topics of the journal include manufacturing, mechanical, and chemical engineering. The publication language is English. The editorial board is represented by scientists from different international research institutions covering the journal's topics and evaluating all the submitted articles. The system of double-blinded review provides a high-quality presentation of articles. The editorial policy, including submission, review, acceptance, and publication of articles, is entirely transparent.

The journal was founded in 2014. It is published by Sumy State University of Ministry of Education and Science of Ukraine under the support of the International Association for Technological Development and Innovations.

ISSN 2312-2498 (print)
ISSN 2414-9381 (online)

The journal is intended for a wide range of scientists, researchers, practitioners, and others interested in manufacturing, mechanical, and chemical engineering. All the publications in the journal are free of articles processing charges (APCs) and articles submission charges.

Recommended for publication
by the Academic Council of Sumy State University,
(order No. 0547-I of 12.09.2022)

The journal is the scientific professional edition of Ukraine (Category "B") in Engineering Sciences ordered by the Ministry of Education and Science of Ukraine, November 7, 2018, No. 1218.

Partners:

– International Association for Technological Development and Innovations, http://iatdi.org;
– Ministry of Education and Science of Ukraine, https://mon.gov.ua;
– Faculty of Mechanical Engineering and Management, Poznan University of Technology (Poland), https://www.put.poznan.pl;
– Faculty of Manufacturing Technologies with a seat in Prešov, Technical University of Košice (Slovakia), http://www.fvt.tuke.sk;
– Faculty of Mechanical Engineering of University of West Bohemia (Czech Republic), http://www.fst.zcu.cz.

Editorial Board: 2, Rymskogo-Korsakova St., 40007, Sumy, Ukraine; Apt. M-211
Contact Phone: +380-993-845-740
E-mail: jes@teset.sumdu.edu.ua
Website: http://jes.sumdu.edu.ua

State registration certificate of the print mass-media No. 20499-10299 PR.

JOURNAL OF ENGINEERING SCIENCES

Volume 9, Issue 1 (2022)

TOPICS

Manufacturing Engineering:

- Machines and Tools;
- Technical Regulations and Metrological Support;
- Materials Science.

Mechanical Engineering:

- Dynamics and Strength of Machines;
- Computational Mechanics.

Chemical Engineering:

- Processes in Machines and Devices;
- Energy Efficient Technologies;
- Environmental Protection.

STATISTICS

- **Publication frequency:** biannually (2 issues per year)
- **Papers per issue:** 15
- **Acceptance rate:** 25 %
- **Timeline:**
  - days from submission of the manuscript to first decision: 30
  - days from acceptance of the article to publication online: 14
- **Editorial Board:**
  - members: 69
  - institutions: 47
  - countries: 26

JOURNAL OF ENGINEERING SCIENCES

Volume 9, Issue 1 (2022)

CONTENTS

MANUFACTURING ENGINEERING

MECHANICAL ENGINEERING

CHEMICAL ENGINEERING

JOURNAL OF ENGINEERING SCIENCES

Volume 9, Issue 1 (2022)

JOURNAL OF ENGINEERING SCIENCES

Volume 9, Issue 1 (2022)

Besedin M., Popowska M., Ivanov V., Trojanowska J. (2022). Digital model and assembling of a lathe. Journal of Engineering Sciences, Vol. 9(1), pp. A1-A8, doi: 10.21272/jes.2022.9(1).a1

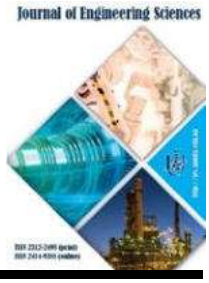

Digital Model and Assembling of a Lathe

Besedin M.[1], Popowska M.[2], Ivanov V.[1*[0000-0003-0595-2660]], Trojanowska J.[2[0000-0001-5598-3807]]

[1] Sumy State University, 2, Rymskogo-Korsakova St., 40007 Sumy, Ukraine;
[2] Poznan University of Technology, 5, M. Skłodowska-Curie Sq., 60-965 Poznan, Poland

Article info:
Submitted: April 18, 2022
Accepted for publication: June 2, 2022
Available online: June 6, 2022

***Corresponding email:**
ivanov@tmvi.sumdu.edu.ua

Abstract. The article aims at developing a digital model of a lathe and the related technology for its assembling. The study is based on analyzing the service purpose and technological capabilities of modern modular machine tools, justification and development of the machine tool design according to the specified production conditions, and development of a technological process for assembling the proposed modular machine tool. The geometric modeling techniques and the design documentation were implemented to justify the rational choice of design parameters of the machine tool design and its spatial model. The proposed approach also considers structural elements and the relationships between them. As a result, a conceptual approach was proposed to design technological processes of lathe assembly with a wide range of technological capabilities. It allows implementation of the up-to-date strategy from idea to finished product at industrial enterprises. The practical significance of the obtained results for the machine-building industry is in the proposed practical recommendations for developing the technological process for assembling lathes.

Keywords: industrial growth, manufacturing engineering, modular machine tool, rational design.

1 Introduction

The modern world machine tool industry is determined by various structural layouts [1]. After analyzing the layout of metal-cutting machines [2–4], it can be summarized that machines with the same type of structures can be composed differently, and vice versa. It is also possible to make certain conclusions about the need to identify and analyze layout quality factors at constructing layouts. To achieve this goal, it is necessary to separate the layout factors of machine tools from the factors that affect the structural development of nodes.

Layout refers to a system of arrangement of modules and guides of a machine tool, distinguished by structure, proportions, and properties [5].

A module is a structurally and functionally complete unit, which is an integral part of the overall design of the designed machine tool. The following modules are distinguished in manufacturing engineering: a technological module is a technological structural unit of the layout. In other words, the smallest component of the machine's layout elements is necessary to perform the shaping operation; a design module is a unit of machine unification, which is both functionally and structurally independent unit that can be used individually and in various combinations with other modules.

The work aims to develop a digital model of a lathe and design the assembly technology. To achieve the set goals, the following tasks need to be solved:

– to analyze the service purpose and technological capabilities of modern modular machine tools;

– to justify and develop the design of a modular machine according to the specified production conditions;

– to develop a technological process for assembling a modular machine tool.

The object of the research is the process of design and technological support of machine-building production. The subject of the research is the assembly process of a multiaxis lathe.

2 Literature Review

The market situation in manufacturing engineering is constantly changing, affecting production needs. To compete with other manufacturers, companies must quickly adapt to the demand for custom orders [6].

Modular and reconfigurable machine tools can be a key solution to meet the demands of today's markets for rapidly changing products and product specifications.

That is why this issue is an important problem in machine-building production today. The ability to reconfigure machine tools according to production requirements offers economic benefits. In the case of a modular layout, the equipment is also justified from an environmental point of view. Thus, modular equipment impacts the sustainable development of manufacturing engineering [7, 8].

The constant change in consumer demands is the subject of today's manufacturing environment [9, 10]. The goal of machine-building companies is to make maximum profit by providing customers with products, which means that product quality, production cost, and final price are key factors. Modular systems are possible options for implementing changes in production systems and production in general [11, 12].

Due to the significant technological development of mechanical engineering, designers and technologists face many production issues [13], particularly regarding the dynamic components of structures, power loads, and temperature modes. Conventionally designed processing equipment usually shows a reasonable efficiency level. However, in cases with a wide range of products or a large number of operations to be performed [14], it is much more reasonable to use modular equipment, especially from an economic point of view [15].

Based on the above factors, in this work, a modular approach was chosen as one of the appropriate and effective ways to implement the processes of manufacturing machine parts.

In modern realities, two main principles for building modular metalworking equipment can be noted. Firstly, the entire machine set is based on the "basic" assembly component. The machine tool company is guided by the principle of creating one basis and a wide range of different modules, the choice of which already depends on the individuality of the order. The production of modular equipment according to this principle is engaged in companies LNL Machine Tools, Inc., Unitech Company Group, Josef Fill Company, Mikron, Huron Graffenstaden, and others.

Secondly, the machine consists of various components, among which it is difficult to identify one main. The key point of this approach is the ability to assemble a wide range of finished units into a machine without much difficulty. The layout of the machine tool depends on the specifics of the order. The production according to this approach is carried out, for example, by the company Shenzhen Zhouyu Intelligent Technology Co., Ltd.

The use of the modular principle of machine tools construction, based on the 2nd principle, allows:

– to reduce the time of development, design, and manufacture of machine tools for processing the specified range of workpieces according to the specified technical and technological characteristics;

– to reduce the cost of metal-cutting machines through standardization and unification of elements;

– to increase the reliability of the machine tool due to the development of the modules and a possible correspondence of this module design to the task;

– to increase machine accuracy;

– to increase the flexibility of machines by allowing them to be reconfigured more quickly to meet specific production conditions;

– to improve operating conditions and maintainability by reducing the variety of kit elements.

3 Research Methodology

Since the kit can perform various production tasks, the task at hand directly impacts the purpose of the kit. This kit can be implemented both in the educational process and in experimental and single-part production.

The kit includes 112 parts and standard products, allowing for the assembly of 17 different layouts, namely: a gear milling machine; an indexing machine; a vertical drilling machine; a horizontal milling machine; a jig saw and arc console machine; a beading machine; and 3 metal lathe layouts; 3 wood lathe layouts; 3 grinding machine layouts and 2 vertical milling machine layouts. Three different layouts can be assembled at the same time. Table 1 shows the main technical parameters of the kit.

Table 1 – Main technical parameters of the kit

Operating voltage, V	Drive power, W	Turning/milling spindle speed, rpm
12	35	20000/12000

Other features and elements depend on the specific layout.

Regardless of the layout, the kit is focused on single-part production. The kit allows you to implement the following machining methods: turning, grinding, milling, drilling, and hole finishing.

Turning is one of the main types of machining that the set can realize. A large number of technological possibilities can be realized with the help of the turning layout. The main advantages of the lathe layout include the following. With the help of turning equipment, it is possible to process many different surfaces, for example, external and internal cylindrical smooth and stepped surfaces, external and internal conical surfaces, grooves, holes, cuts, and others.

The turning layout provides machining of body-of-rotation type workpieces with a maximum diameter of the workpiece to be machined of 50 mm. Workpieces can be based on the outer cylindrical surface with installation in a three-jaw chuck for short parts such as shaft-collars, flanges, and others, or along the outer cylindrical surface and the center hole with installation in a three-jaw chuck and the right center for long parts such as shafts.

The turning layout considered in the paper can be used for machining such materials as non-ferrous metals (e.g., aluminum and copper.), wood, plywood, foam plastic, plastics, and composite materials (carbon fiber and fiberglass). The technical characteristics of the machine are shown in Table 2.

The technological capabilities of the machine tool are illustrated by an example of machining a complex-profile part (Figure 1), which can be machined in one setup.

Table 2 – Technical characteristics of the machine tool

Characteristics	Value
Distance between centers, mm	135
The largest diameter of the workpiece to be machined, mm	50
Drive power, W	35
Supply voltage, V	12
Rotary module rotation range, deg	360
Spindle speed, rpm	20,000
Dimensions, mm	220×160×200
Weight, kg	6.5

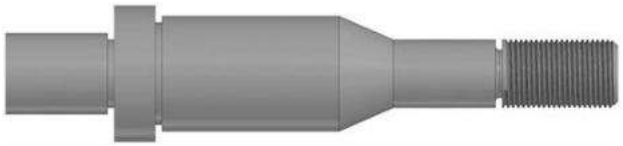

Figure 1 – Body-of-rotation type part for machining on a lathe

The production of this part type in one setup is possible thanks to an additional axis for turning the cutting tool.

The machine layout consists of functional modules, a set of assembly units, and parts that perform a single functional purpose (Figure 2).

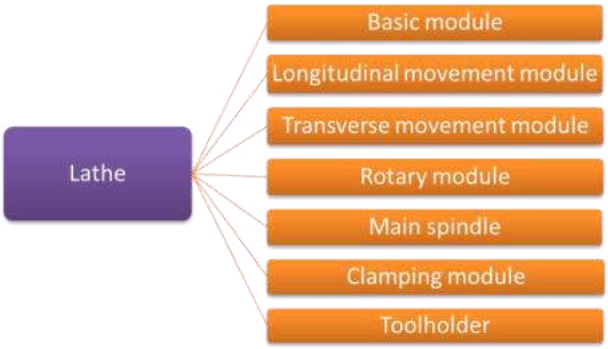

Figure 2 – Structural diagram of the turning layout

The proposed layout (Figures 3–9) consists of a basic module, a longitudinal movement module, a transverse movement module, a rotary module, the main spindle, a clamping module, and a toolholder.

The basic module (Figure 3) consists of the main components of the kit, which are rigid elements of this layout. The base module is used to combine other units and modules. The base module consists of a column and two riser blocks connected with connectors and screws.

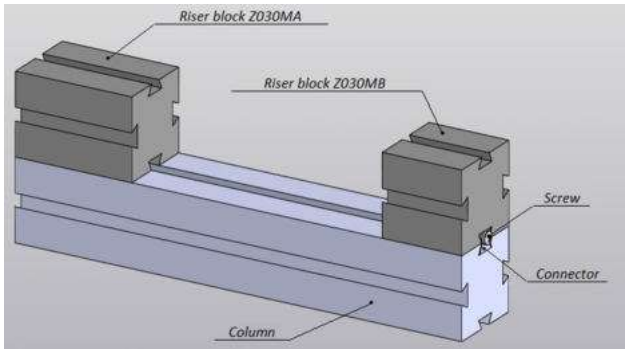

Figure 3 – Basic module

The main task of the longitudinal movement module (Figure 4) is the movement along the *Z* axis of the cutting tool installed in the toolholder, located in the transverse movement module. The longitudinal movement module consists of a longitudinal slideway, a saddle, a lead screw, a strap screwed with two screws, a flywheel fastened with a nut, and a handle.

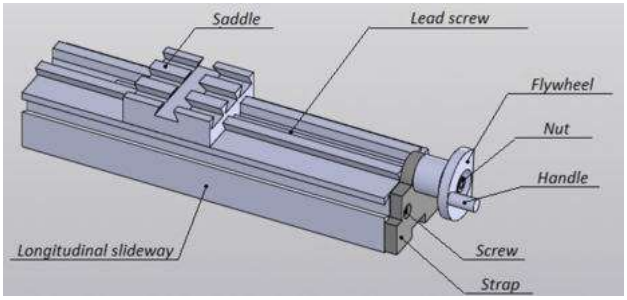

Figure 4 – Longitudinal movement module

The main task of the transverse movement module (Figure 5) is the movement along the *X* axis of the cutting tool installed in the toolholder, located in the rotary module. The transverse movement module consists of a transverse slideway, a lead screw, a strap that is screwed with two screws, a flywheel that is fastened with a nut, and a handle.

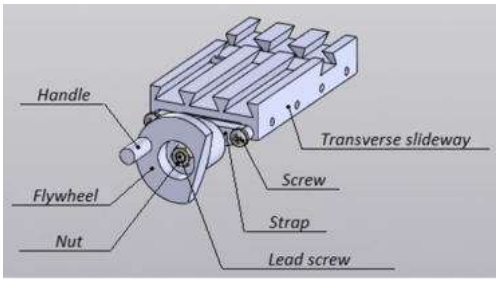

Figure 5 – Transverse movement module out

The main task of the rotary module (Figure 6) is the basing of the toolholder and its rotation. The rotary module consists of a rotary table, a fixing part screwed with two screws, and a transverse movement module.

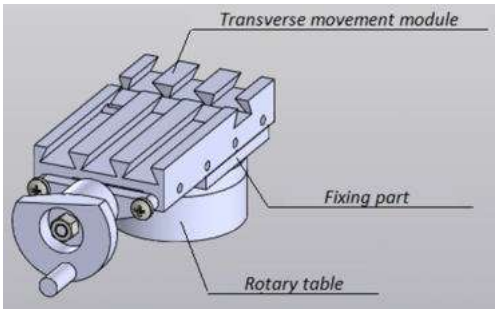

Figure 6 – Rotary module

The main spindle (Figure 7) is an electric motor that transmits rotation to the shaft with a V-belt transmission. A three-jaw chuck is attached to the main spindle, which ensures the workpiece base during machining. The clamping module (Figure 8) clamps workpieces. The clamping module consists of a tailstock, a flywheel, and a handle. The toolholder (Figure 9) is designed to install and fix the cutting tool by pressing with screws. The toolholder is mounted on the rotary module. Figure 10 shows a spatial model of a multiaxis lathe assembly.

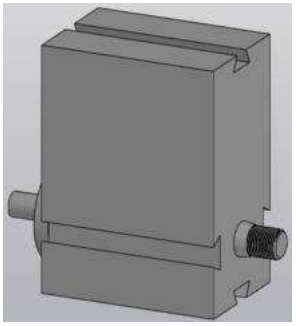

Figure 7 – Main spindle

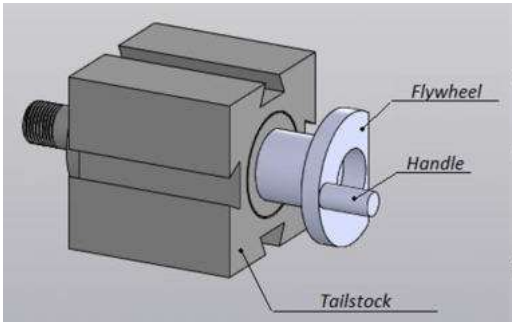

Figure 8 – Clamping module

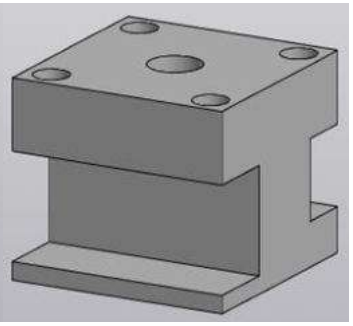

Figure 9 –Toolholder

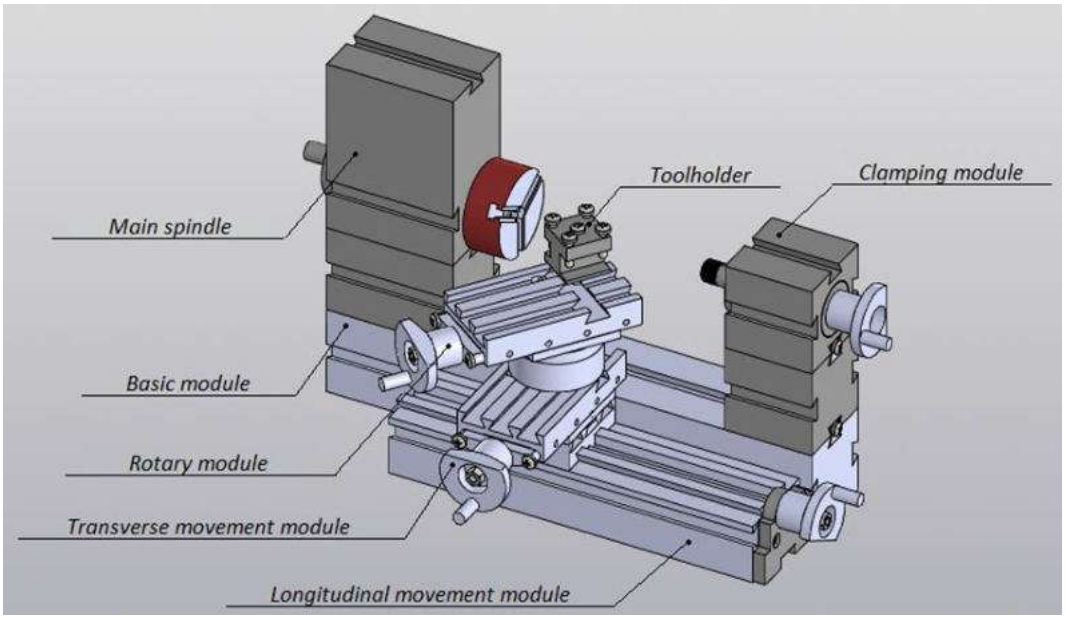

Figure 10 – Assembled lathe

4 Results

A technology for assembling a lathe based on an algorithm, which provides for the preliminary assembly of individual components, has been developed. The developed technological scheme for the base module assembly is shown in Figure 11.

The basic module assembly process starts by connecting two riser blocks (Z030MA and Z030MB) to the column using connectors and screws. Uniform parts can be connected on either side due to their special design. It is also possible to install straps to increase the rigidity of the machine.

The developed technological scheme for the longitudinal movement module assembly is shown in Figure 12.

The assembly process begins by placing the saddle on the longitudinal slideway. After that, the lead screw is screwed on. The strap is screwed on with two screws. The next step is to attach the flywheel with a nut. Handle screwed to the flywheel.

The developed technological scheme for the transverse movement module assembly is shown in Figure 13.

Transverse guides are taken as a basis. The 1st step is positioning the lead screw, after which the strap is screwed with two screws. The next step is to attach the flywheel with a nut. The handle is screwed to the flywheel.

The developed technological scheme for the rotary module assembly is shown in Figure 14.

The assembly process begins by screwing the fixing part to the rotary table with two screws. The next step is to attach the transverse movement module in the assembly to the fixing part.

The developed technological scheme for the clamping module assembly is shown in Figure 15.

The tailstock is taken as the basis of the clamping module, to which the flywheel and handle are attached.

Overall, the developed technological scheme for the lathe assembly as a whole is shown in Figure 16.

Assembling the lathe begins with connecting the main spindle and the clamping module to the basic module using connectors and screws. The next step is to install the transverse movement module on the longitudinal movement module using the fixing part, single-slot nuts, and screws. The rotary module is then mounted on the transverse movement module using single-slot nuts and screws.

The next step is to install these three modules as an assembly unit to the basic module using connectors and screws. The toolholder is then attached to the rotary module with a single-slot nut and screw.

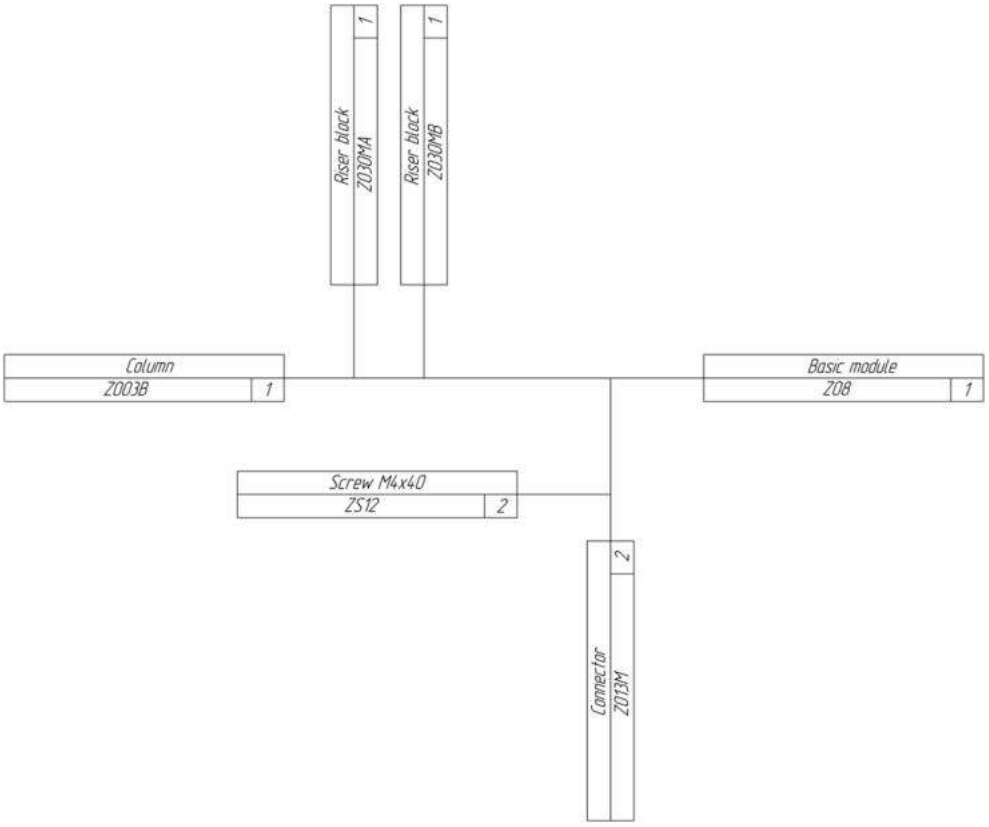

Figure 11 – Basic module assembly scheme

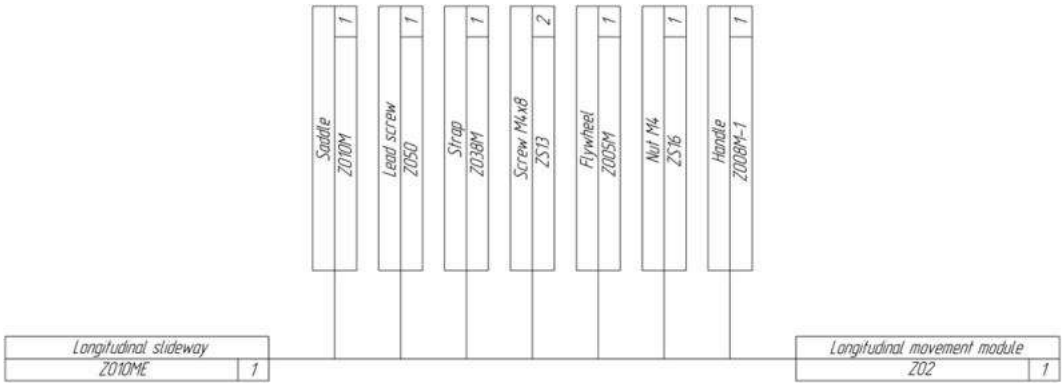

Figure 12 – Longitudinal movement module assembly scheme

Figure 13 – Transverse movement module assembly scheme

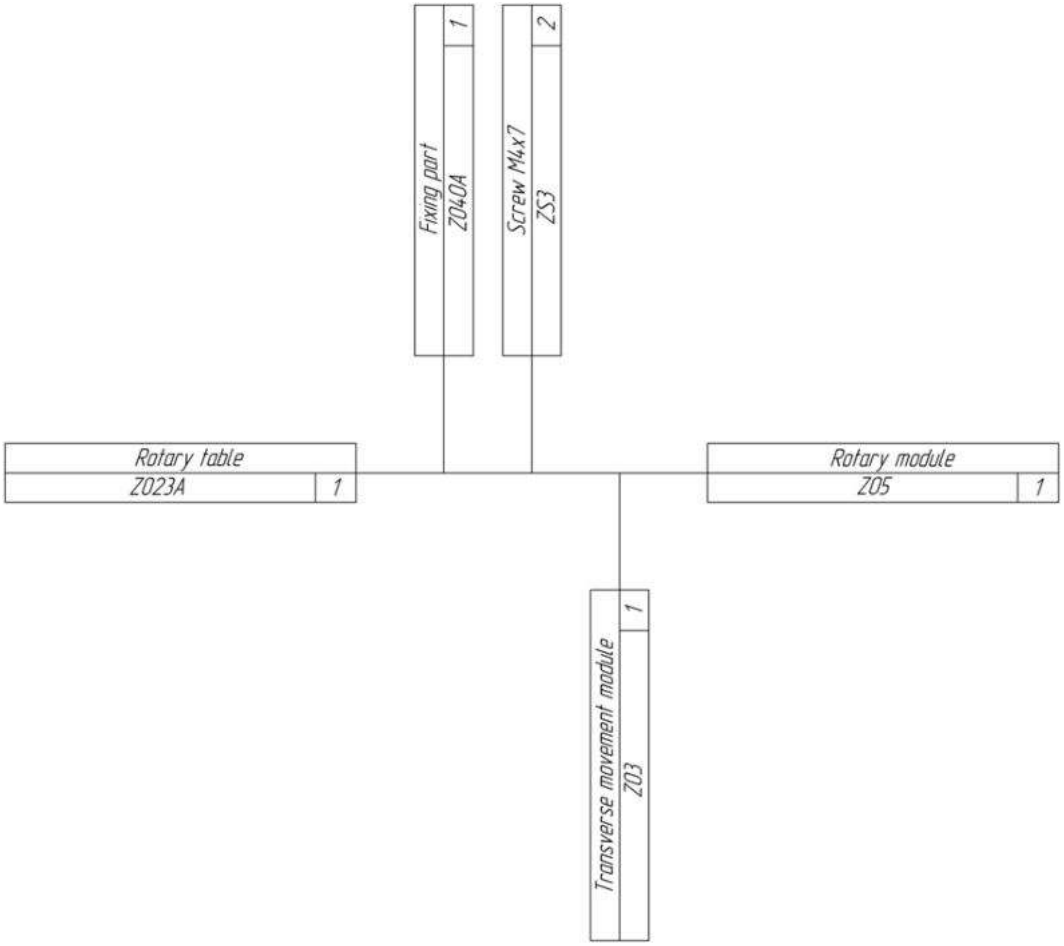

Figure 14 – Rotary module assembly scheme

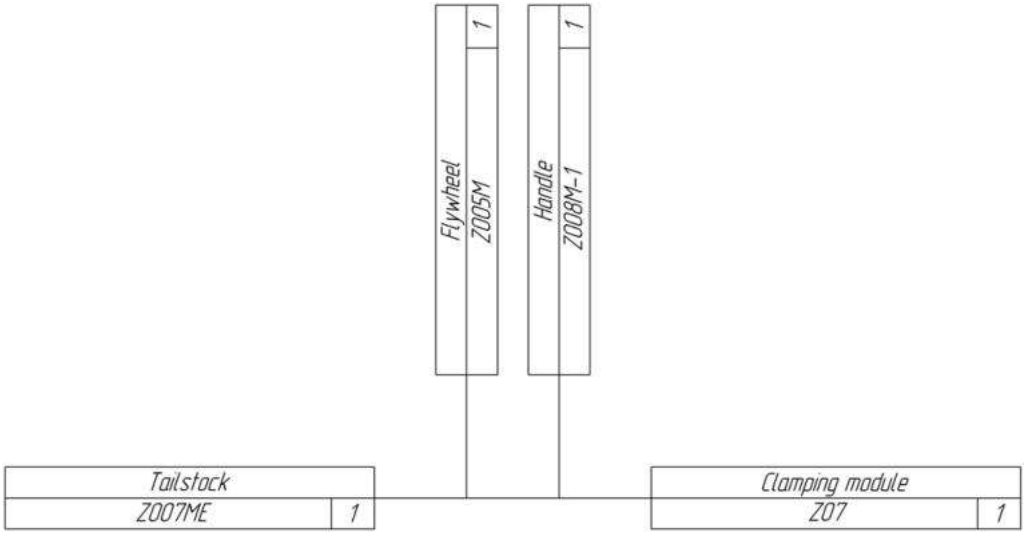

Figure 15 – Clamping module assembly scheme

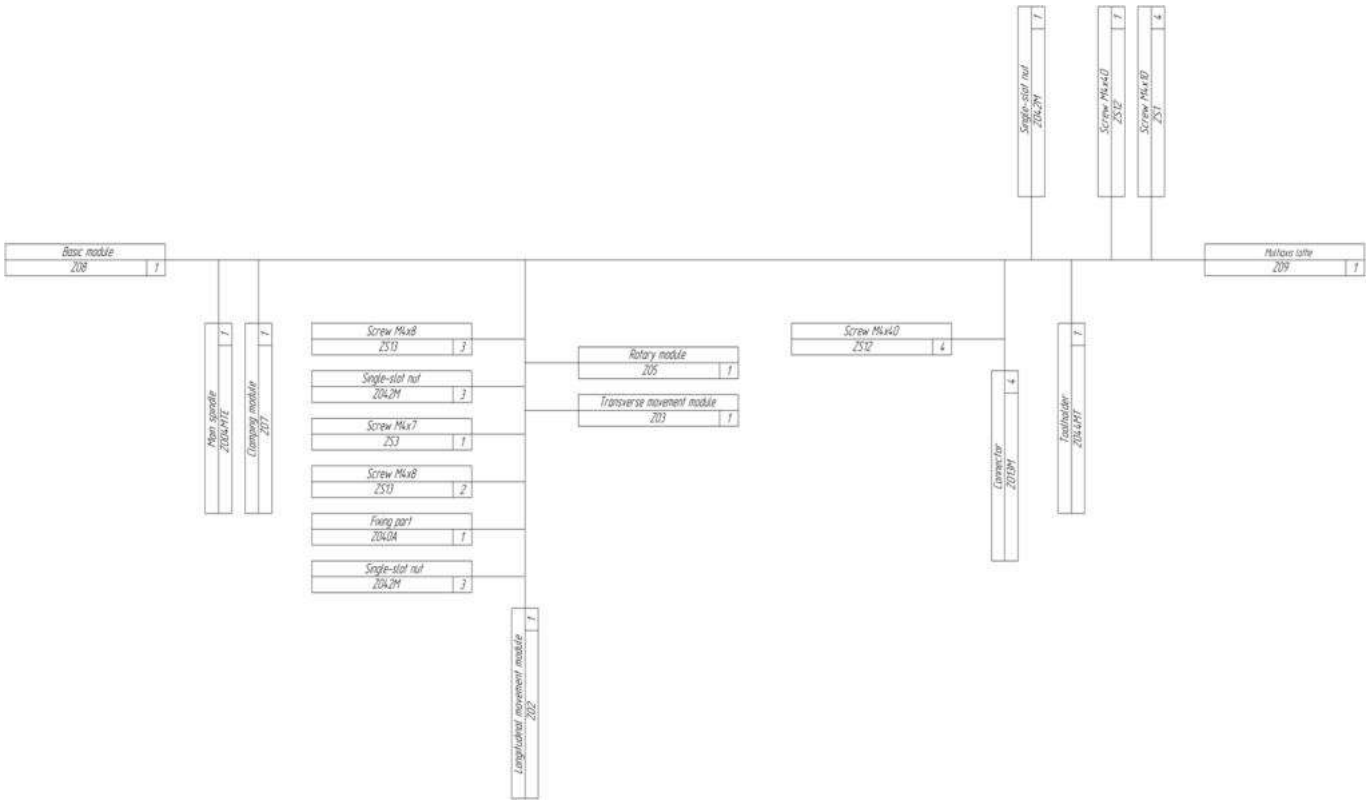

Figure 16 – Lathe assembly scheme

5 Discussion

The work results are based on engineering graphics and geometric modeling, basing theory, modular approach, technological foundations of mechanical engineering, and theoretical methods of standard machine parts manufacturing.

The scientific novelty of the obtained results is as follows. Firstly, the structural diagram and layout design solution for manufacturing a lathe, consisting of seven basic modules, is proposed. Based on this, using geometric modeling methods, a digital model of the machine tool was developed, which considers all the structural elements and the relationship between them, which made it possible to increase production efficiency due to the expansion of the technological capabilities of the machine.

Secondly, a conceptual approach to the design of technological processes of lathe assembly with a wide range of technological capabilities is proposed, which allows the implementation of the strategy "from idea to finished product" and can be implemented in industrial enterprises.

The practical significance of the obtained results for the machine-building industry is to develop practical recommendations for developing the technological process for assembling lathes.

6 Conclusions

The paper analyzes the development trends of the world machine tool industry. Particular attention has been paid to modular machines and their basic technological capabilities. The key trends determining the direction of machine tools development are high-speed machining, multiaxis complex machining by combining different methods, modular design principles, and using combined tools for machining.

Based on the analysis of metalworking equipment designs used for manufacturing parts in multiproduct manufacturing, the expediency of designing a modular lathe has been substantiated. It provides a more comprehensive range of workpieces and production flexibility.

Based on the service purpose of the lathe, the choice of design parameters of the machine tool design has been justified theoretically. The spatial model of the machine tool, which considers all structural elements and relationships between them, has been developed. The related design documentation has been prepared using geometric modeling.

A technological scheme for assembling a lathe and individual functional modules has been developed, which made it possible to develop a technological process for assembling a prototype machine tool and formulate practical recommendations.

7 Acknowledgments

The research was carried out at the Research and Educational Center for Industrial Engineering within the R&D project "Fulfillment of tasks of the perspective plan of development of a scientific direction "Technical sciences" Sumy State University" by the Ministry of Education and Science of Ukraine (State reg. no. 0121U112684). The main results have also been implemented into the educational processes at Sumy State University and Poznan University of Technology.

References

1. Wieandt, A. (1994). Innovation and the creation, development and destruction of markets in the world machine tool industry. *Small Business Economics*, Vol. 6, pp. 421–437.
2. Jedrzejewski, J., Kwasny, W. (2015). Development of machine tool operational properties. *Journal of Machine Engineering*, Vol. 15(1), pp. 5–24.
3. Ganiyusufoglu, Ö. S. (2019). A critical evaluation of current machine tool designs in the digitalized global production networks. In: Monostori, L., Majstorovic, V.D., Hu, S.J., Djurdjanovic, D. (eds) Proceedings of the 4th International Conference on the Industry 4.0 Model for Advanced Manufacturing. AMP 2019. *Lecture Notes in Mechanical Engineering*, pp. 59–67. Springer, Cham, doi: 10.1007/978-3-030-18180-2_5.
4. Möhring, H. C., Müller, M., Krieger, J., Krieger, J., Multhoff, J., Plagge, C., de Wit, J., Misch, S. (2020). Intelligent lightweight structures for hybrid machine tools. *Prod. Eng. Res. Devel.*, Vol. 14, pp. 583–600, doi: 10.1007/s11740-020-00988-3.
5. Peukert, B., Saoji, M., Uhlmann, E. (2015). An evaluation of building sets designed for modular machine tool structures to support sustainable manufacturing. *Procedia CIRP*, Vol. 26, pp. 612–617, doi: 10.1016/j.procir.2014.07.175.
6. Shneor, Y. (2018). Reconfigurable machine tool: CNC machine for milling, grinding and polishing. *Procedia Manufacturing*, Vol. 21, pp. 221–227, doi: 10.1016/j.promfg.2018.02.114.
7. Vafadar, A., Tolouei-Rad, M., Hayward, K. (2019). An integrated model to use drilling modular machine tools. *Int J Adv Manuf Technol*, Vol. 102, pp. 2387–2397, doi: 10.1007/s00170-019-03387-w.
8. Uhlmann, E., Saoji, M., Peukert, B. (2016). Principles for interconnection of modular machine tool frames. *Procedia CIRP*, Vol. 40, pp. 413–418, doi: 10.1016/j.procir.2016.01.081.
9. Bi, Z. (2011). Development and control of a 5-axis reconfigurable machine tool. *Journal of Robotics*, Vol. 2011, 583072, doi: 10.1155/2011/583072.
10. Brunoe, T., Soerensen, D., Nielsen, K. (2021). Modular design method for reconfigurable manufacturing systems. *Procedia CIRP*, Vol. 104, pp. 1275–1279, doi: 10.1016/j.procir.2021.11.214.
11. Bi, Z., Lang, S., Shen, W., Wang, L. (2008). Reconfigurable manufacturing systems: The state of the art. *International Journal of Production Research*, Vol. 46, pp. 967–992, doi: 10.1080/00207540600905646.
12. Bi, Z., Zhang, W. (2001). Modularity technology in manufacturing: Taxonomy and issues. *Int J Adv Manuf Technol*, Vol. 18, pp. 381–390, doi: 10.1007/s001700170062.
13. Bi, Z. M., Lang, S. Y. T., Verner, M., Orban, P. (2008). Development of reconfigurable machines. *Int J Adv Manuf Technol*, Vol. 39, pp. 1227–1251, doi: 10.1007/s00170-007-1288-1.
14. Heilala, J., Voho, P. (2001). Modular reconfigurable flexible final assembly systems. *Assembly Automation*, Vol. 21(1), pp. 20–30, doi: 10.1108/01445150110381646.
15. Andrisano, A. O., Leali, F., Pellicciari, M., Pini, F., Vergnano, A. (2012). Hybrid reconfigurable system design and optimization through virtual prototyping and digital manufacturing tools. *Int J Interact Des Manuf*, Vol. 6, pp. 17–27 (2012), doi: 10.1007/s12008-011-0133-9.

JOURNAL OF ENGINEERING SCIENCES

Volume 9, Issue 1 (2022)

Andrusyshyn V., Luscinski S., Ivanov V., Pavlenko I. (2022). The efficiency of collaborative assembling cells. Journal of Engineering Sciences, Vol. 9(1), pp. A9-A16, doi: 10.21272/jes.2022.9(1).a2

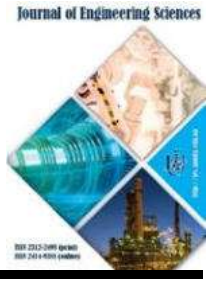

The Efficiency of Collaborative Assembling Cells

Andrusyshyn V.[1*][0000-0001-7223-6520], Luscinski S.[2][0000-0001-7385-6668],
Ivanov V.[1][0000-0003-0595-2660], Pavlenko I.[1][0000-0002-6136-1040]

[1] Sumy State University, 2, Rymskogo-Korsakova St., 40007 Sumy, Ukraine;
[2] Kielce University of Technology, 7, Tysiąclecia Państwa Polskiego Sq., 25-314 Kielce, Poland

Article info:
Submitted: April 15, 2022
Accepted for publication: June 9, 2022
Available online: June 14, 2022

***Corresponding email:**
v.andrusyshyn@tmvi.sumdu.edu.ua

Abstract. To produce competitive products, it is necessary to consider their permanent modernization and adaptation to the emerging needs of a consumer. This feature of up-to-date production inevitably leads to design complexities. As a result, the complexity of a technological assembly process increases, which is a new challenge for enterprises. Simultaneously, in most cases, assembly operations are performed manually due to the complexity or impossibility of automating the assembling process for an extensive range of products. This fact is due to the insufficient flexibility of automation systems. Remarkably, this approach has significant drawbacks, i.e., low productivity and risk of chronic diseases. To solve this problem, the use of collaborative systems was proposed. Such systems have the advantages of both humans and automation tools. As a result, industrial robots can be applied as automation tools. However, when using industrial robots next to workers, the safety requirements are significantly increased since the infliction of industrial injuries is unacceptable. After considering all the above, the article deals with a new scientific and methodological approach to designing security systems of collaborative production cells and their design and effectiveness verification.

Keywords: industrial gripper, manufacturing engineering, assembling efficiency, industrial growth.

1 Introduction

Nowadays, manufacturers of machine-building products face modern production and technological challenges associated with the need to intensify production processes. Under these conditions, one of the effective methods of increasing competitiveness is the automation of production using industrial robots. Since there is a complication in the design of products due to the need for constant improvement of their characteristics and personalization, manual work is still relevant for assembly operations. This fact is due to the complexity of full automation due to the insufficient flexibility and adaptability of the first-generation robots and the inability to perform tasks where human intervention has required a level of intelligence and skills [1].

Also, consideration of the state of assembly automation is due to the popularity of industrial robots in assembly processes. According to the study [2], with all the features of using industrial robots for assembly automation, this task is the third most popular among new installations of industrial robots in the world as of 2020.

Although the robots of the first generation are quite effective in automating monotonous and dangerous work, they cannot fully interact with the production environment and people. Therefore, separate areas are allocated for robot safety, while the workers do not have access to the work area of the industrial robot of the first generation during his work.

However, thanks to advances in the field of robotics, the development of electronics and intelligent sensors, increasing the productivity of computing equipment, and reducing the cost of the solutions mentioned above, more and more tasks can be automated with the help of industrial robots every day while maintaining high quality, productivity, and reliability [3]. These changes made the appearance of second-generation robots (or collaborative robots). They can interact with the environment and directly with humans.

According to the results of the study [4], due to the possibility of combining the flexibility and adaptability of people and the capabilities of collaborative robots (e.g., repeatability and the ability to work continuously for a long time), it became possible to increase the efficiency, economy, flexibility, and productivity of production cells.

Additionally, in work [5], which is devoted to the design of a robotic section for collaborative assembly of pneumatic cylinders, it is additionally indicated that if the accuracy of the collaborative robot is insufficient, a person can compensate for it with the help of tactile sensations.

In addition, according to research, the implementation of collaborative robots significantly reduces the risk of developing occupational diseases. For example, the paper [6] is devoted to the system for evaluating the productivity of a collaborative cell for the assembly of electronic components and the risk of occupational diseases. It was made due to the frequent absence of workers due to absenteeism caused by occupational diseases of the musculoskeletal system. The use of a collaborative robot helped to reduce the number of awkward positions and reduce the burden on the worker. Work [7] is devoted to the design of a collaborative robotic cell for the assembly of a hinge of equal angular velocities. The use of a collaborative robot helped to reduce the load on the operator by approximately 60%. Complete automation of this process is impossible due to the need for high accuracy and flexibility.

This became the reason for the growing popularity of collaborative robots: the number of new installations from 2017 to 2020 doubled – from 11,000 up to 22,000 pcs. [2]. In addition, each famous industrial robot manufacturer has several collaborative robot models in their catalog (e.g., ABB YuMi, Fanuc CR Series, and KUKA LBR IIWA) [8].

Also, collaborative production cells increase production efficiency and are generally economically beneficial.

For example, due to the increasing complexity of the design of cars, the possibility of automating production with the help of collaborative robots was considered, considering the cycle time and the number of people and robots. The parameters of the work of humans and robots separately and together were compared. The results indicate a significant increase in the productivity of the assembly area. One of the reasons the authors cite the ability to allocate human and robotic resources in real time for the work plan execution [9]. Also, collaborative works can support the execution of tasks by a person at low costs [1], thus ensuring the profitability of partial automation of the assembly process.

Optimum planning is necessary to ensure the economic efficiency of the assembly area using collaborative robots. As an example of research in this direction, researchers for the correct assessment of the workstation launched a simulation model, with the help of which they received more data to understand the system, which allows making the right decision about the means that are used on the cell [4].

Increasing the efficiency of human-collaborative robot cooperation is facilitated by the fact that the robot can perform several functions, for example, be a basic assembly device, feed a tool, apply grease, and glue. For example, BMW is trying to introduce collaborative robots that help people with tools during assembly [10].

Moreover, thanks to the development of end-effector elements, these tasks can be combined, as the robot can quickly change the end-effector, for example, with the SCHUNK SWS Series pneumatic replacement system.

Also, collaborative work during assembly can perform various tasks, be a device with many degrees of freedom, feed a tool, apply a coating, and more. At the same time, task data can be combined due to the possibility of quick tool change.

In addition, to increase the efficiency of interaction between a person and a collaborative robot, it is necessary to evaluate the effectiveness of various options for information exchange. According to work [5], there are the following types of human-robot interaction:

– transmission of information through effort: in this type, the interaction occurs through explicit and intentional contact, while the robot must be able to respond adequately to the application of force;

– contactless data transfer, for example, through gestures or voice commands;

– data transmission through the interface, for example, buttons, touch screen.

Also, the introduction of collaborative robots has enabled the implementation of a learning-by-demonstrating system through efforts to simplify precinct commissioning, made possible by advanced sensors and artificial intelligence tools that recognize whether human interaction was intentional or unintentional and smooth out errors for smoother control. This allows you to reduce the time of production preparation due to the absence of the need to create and debug a control program and perform a collision check [11].

Using robots next to people requires ensuring the safety of people from injuries that the robot can inflict on them. Article [12] is devoted to analyzing the state of development of collaborative systems, including employee safety. According to the study, several ISO standards have been introduced to classify the interaction of humans and collaborative robots. For example, the ISO 8373 standard defines terms related to manipulating industrial robots used in industrial settings, including human-robot interaction.

The ISO 10218 standard, in two parts, defines the safety requirements and limitations of an industrial robot when interacting with people.

The ISO 15066 standard complements the previous standard and describes the procedure for limiting the speed values of the robot links, which in turn affects the maintenance of force and moment values at a safe level for humans. Based on these requirements, the following control modes were defined:

– the controlled speed with a safety rating (the robot stops when a person enters an unwanted zone);

– method of manual control (no restrictions on the speed of the elements, but the person himself generates commands for complete control of the robot);

– control of speed and distance (depending on the distance between the person and the robot, the maximum possible speed of the robot elements also changes);

– limitation of power and force to a safe for threshold person.

In addition, a classification of interaction levels directly affects security requirements: coexistence, cooperation, and interaction, in which interaction can be physical and non-contact [13].

Additionally, the following strategies for ensuring human safety have been implemented recently [12, 14]:

– robot stop functions, separately both protective and emergency stop;

– limitation of the speed of the central point of the tool;

– a visual indication of the state of the collaborative robot is necessary;

– limiting the robot's working area to the minimum necessary volume;

– establishing the minimum permissible distance between a person and a robot;

– assessment of the possibility of a collision in real-time, e.g., using machine vision systems [7];

– technological and ergonomic requirements: it is necessary to minimize the number of objects with sharp edges, ensure the absence of vibrations transmitted to a person, and analyze the area for enough free space to prevent the possibility of a person being pinched.

The work aims to improve the efficiency of the assembly processes of the connecting rod-piston group by existing safety standards.

To achieve the set goal, the following tasks have been formulated. Firstly, to investigate the current state of development of collaborative systems and justify the feasibility of implementing a collaborative assembly cell. Secondly, to develop assembly technology and design and technological support of a collaborative assembly cell. Finally, evaluate the effectiveness of the collaborative assembly cell.

The object of research is the design of a robotic cell. The subject of the study: designing a collaborative production area for the assembly operations of the connecting rod and piston group.

2 Research Methodology

2.1 Justification of the need to design a collaborative assembly cell

Research methodology is based on the theoretical foundations of mechanical engineering technology, the foundations of designing gripping devices for industrial robots, standards in designing collaborative robotic areas, and the method of finite element analysis.

Since collaborative work has proven its effectiveness in industry, analysts predict a significant increase in the number of enterprises in the coming years and the next decade [15].

It is proposed to design and implement a collaborative assembly area for assembly operations of the connecting rod-piston group (Figure 1).

The connecting rod-piston group is used in internal combustion engines, for example, in cars, motorcycles, brush cutters, gasoline saws, and other small equipment, as well as in piston compressors. This technique is quite widespread and is available to many consumers around the world.

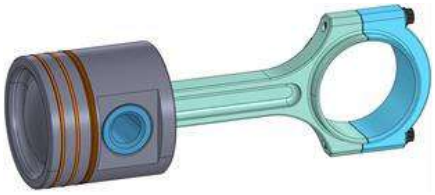

Figure 1 – Connecting rod-piston group

Simultaneously, the complexity of automation lies in the high accuracy of the elements. In addition, the constant change in environmental emission standards forces manufacturers to permanently improve internal combustion engines' efficiency. That is why the assembly section must be flexible and work with various designs of the connecting rod and piston group. In addition, the use of manual labor is associated with the danger that arises since certain structural implementations of this unit involve heating the connecting rod, which can lead to industrial injuries. That is why the most rational option for implementing the assembly process is the implementation of collaborative assembly.

2.2 Planning the structure of the assembly operation

The assembling process for connecting the rod-piston group consists of the following stages:

1) install the rod into the device (this stage ensures accurate positioning of the rod relative to the piston);

2) apply oil to the outer cylindrical surface of the rod;

3) apply oil to the holes in the piston for locating the rod;

4) heat the neck of the connecting rod to the temperature of 280-320 °C (to prepare for pressing);

5) clamp connecting rod in the jaws;

6) connect the connecting rod, the piston, and the rod (it is necessary to pay attention to the correctness of the mutual location of the parts);

7) remove the rod from the device;

8) check the smoothness of the connecting rod's movement relative to the piston (after cooling the parts);

9) put the assembly unit in the container.

With manual assembly, all operations are performed sequentially, which increases the time spent on the operation.

Since the use of collaborative robots makes it possible to perform certain stages in parallel, it is proposed to organize the work of the collaborative section according to the following scheme (Figure 2).

To perform the assembly operation according to this scheme, it is necessary to develop a plan for the collaborative cell (Figure 3).

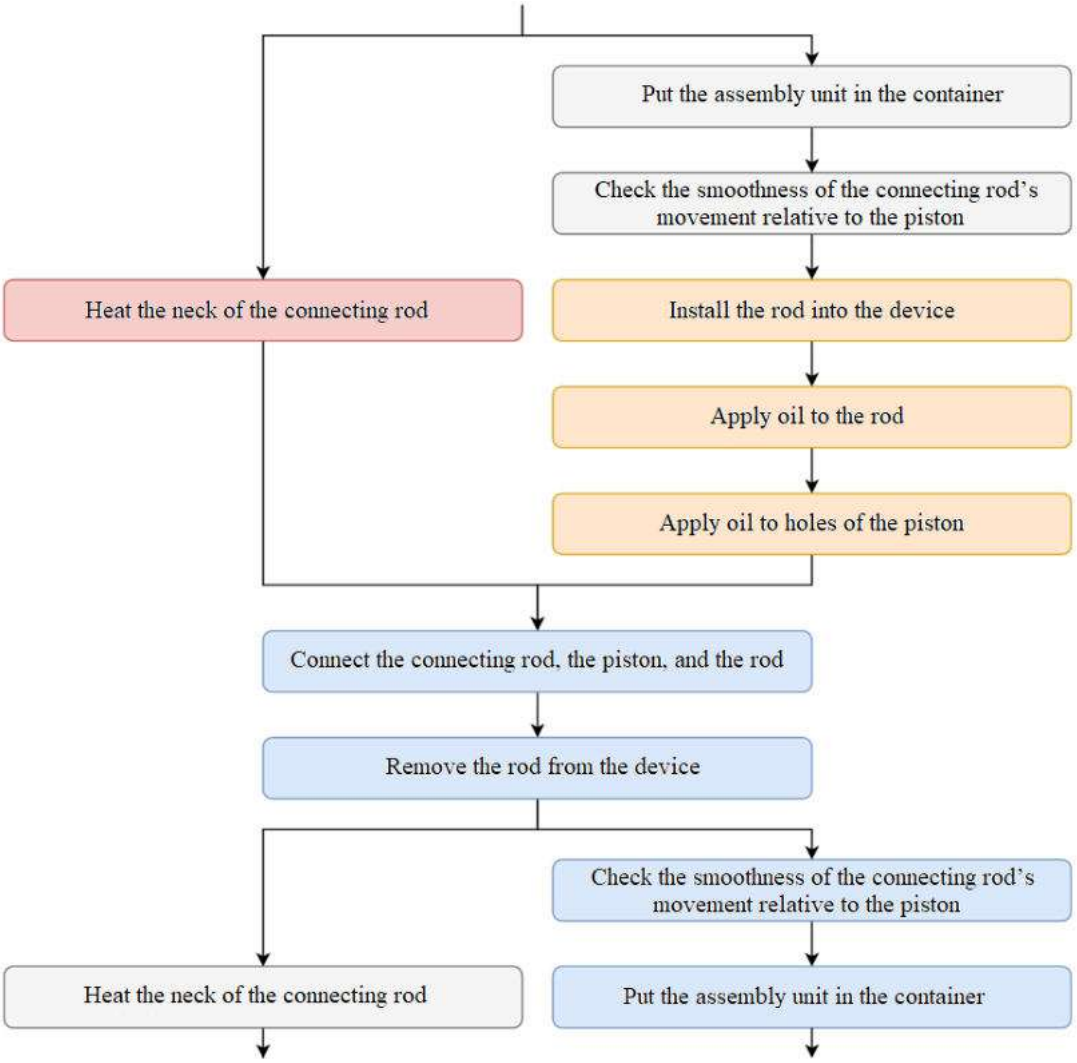

Figure 2 – Assembling chart

The collaborative section works as follows: parts for assembly are fed by a conveyor in random order, after which a delta robot, using machine vision systems, sorts of rods, connecting rods and pistons into sets. Next, the collaborative robot feeds the connecting rod into the installation for its heating, feeds the piston and pin for their further preparation for assembly, and feeds the tested assembly unit to the output conveyor.

Using a robot for heating will allow accurate control of the heating time and ensures the absence of human contact with dangerous equipment. During the heating of the connecting rod, the operator installs the rod in a special device that will ensure the correct location of the rod relative to the piston and applies oil to the outer cylindrical surface of the rod and the piston holes.

After preparing the piston and pin and heating the connecting rod, the collaborative robot hands the connecting rod to the operator for the assembly process.

According to the drawing, the operator connects the rod and piston and waits for the assembly unit to cool down. To ensure safety, the working table is monitored by a machine vision system for the contact of the hot connecting rod with the operator. After that, the operator removes a special device from the rod. Next, the operator checks the smoothness of the stroke of the piston relative to the connecting rod, and the collaborative robot feeds the new connecting rod into the installation for its heating.

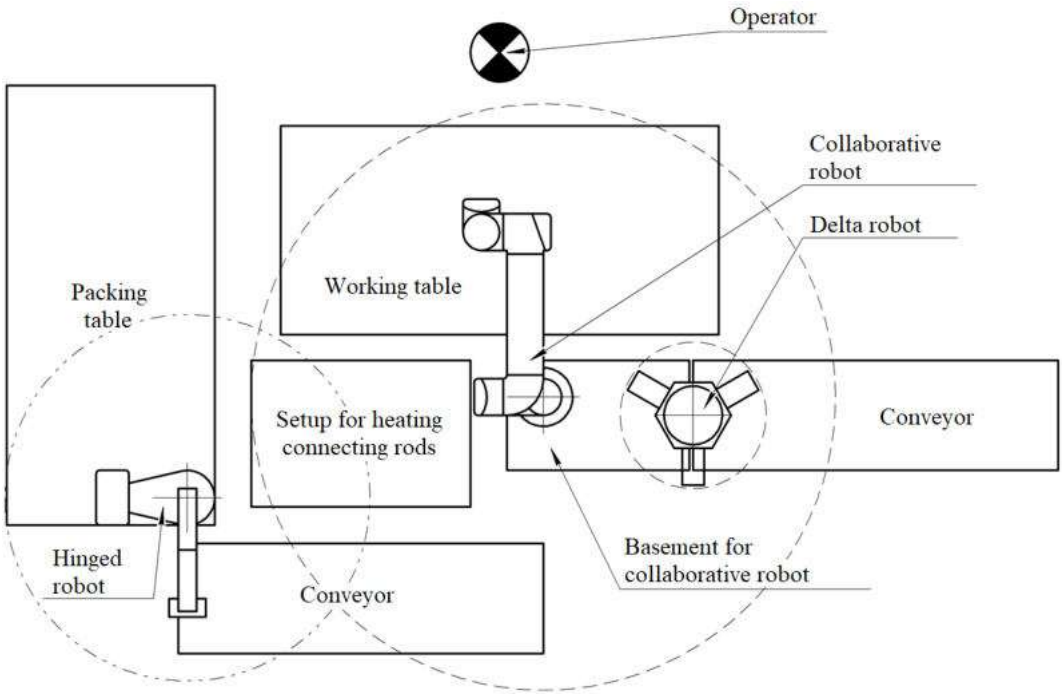

Figure 3 – Assembling cell

2.3 Selection of technical support for the mechanical assembly cell

Using a delta robot based on Delta XS [16] is suggested for sorting parts. Robots with delta kinematics are best suited for sorting because the low moving mass allows for high movement speeds. Open drawings and software for its management will allow it to be modernized in the future according to production needs.

As a gripping device, it is proposed to use adaptive rods of the DHAS series and a parallel pneumatic gripper of the HGPL-B series (Festo) [17].

Using a pneumatic gripper allows for sufficient clamping force, and using adaptive polyurethane rods allows for flexibility (the ability to clamp parts of different standard sizes without readjustment). At the same time, using polyurethane provides temperature resistance, resistance to the action of lubricants, and wear resistance.

To work with the operator, it is suggested to use the Universal Robot UR5 collaborative robot (Figure 4). This solution has a sufficient load capacity for these tasks, a working area, and protection against splashes.

Figure 4 – Collaborative robot "Universal Robot UR5"

A new design of a grasping device for a collaborative robot is proposed. The general view of the capturing device is shown in Figure 5.

The flexibility of the gripping device allows you to clamp parts of various standard sizes reliably. To ensure operator's safety, rubber pads are provided in places with sharp edges. The weight of the gripping device is 3 kg, and the carrying capacity of the robot is 5 kg.

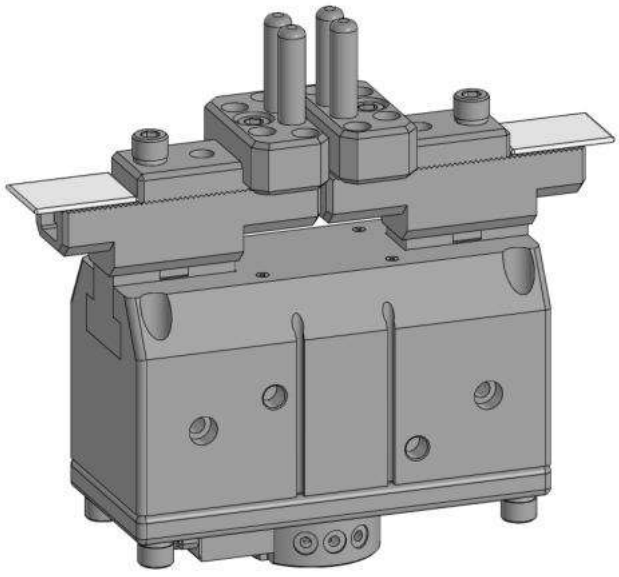

Figure 5 – Fixture design

The proposed design of the gripping device ensures a reduction of time spent on production preparation, increasing the degree of flexibility, which contributes to the expansion of the range of sizes of parts to be installed, and compensation for errors related to the technological process of obtaining blanks.

It is suggested to use the Annin Robotics AR3 robot for packing ready-made assembly units. Its advantages include sufficient carrying capacity for these tasks, simplicity, availability of access to technical documentation for future modernization, and cheapness. As a gripping device, it is proposed to use the adaptive rods of the DHAS series and the parallel pneumatic gripper of the HGPL-B series (Festo).

3 Results

3.1 Strength calculations

To check the gripping device for the strength and reliability of fixing the workpiece, it is necessary to perform calculations of the mechanical system "gripping device – part" using finite element analysis in the ANSYS Workbench software.

Friction coefficients were used in the calculations: steel-steel pair – 0.15; steel-aluminum pair - 0.17.

The value and direction of the applied effort when capturing the part are given in Figure 6.

The calculation results (movement and deformation of elements of the gripping device) are shown in Figure 7.

The analysis results indicate that the gripping device can be used to clamp and move parts in production.

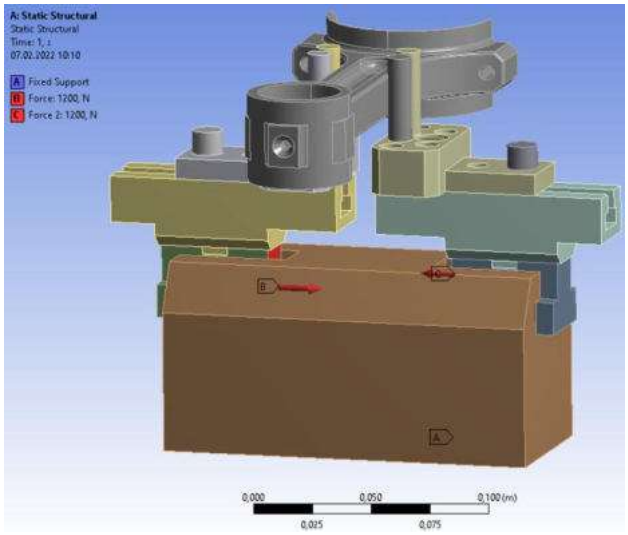

Figure 6 – Clamping forces

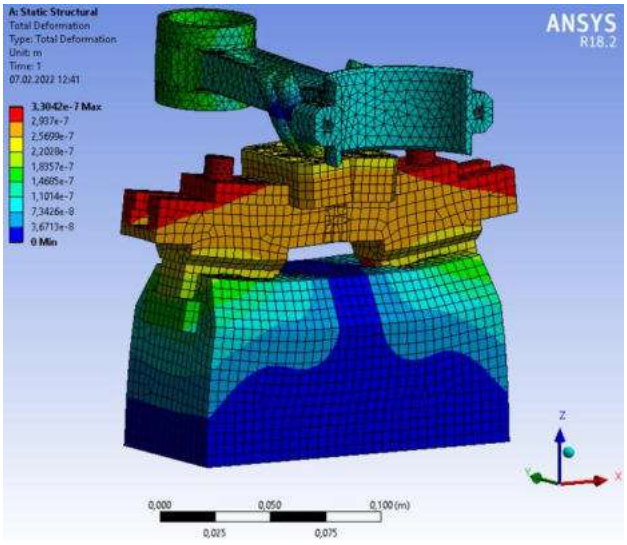

a

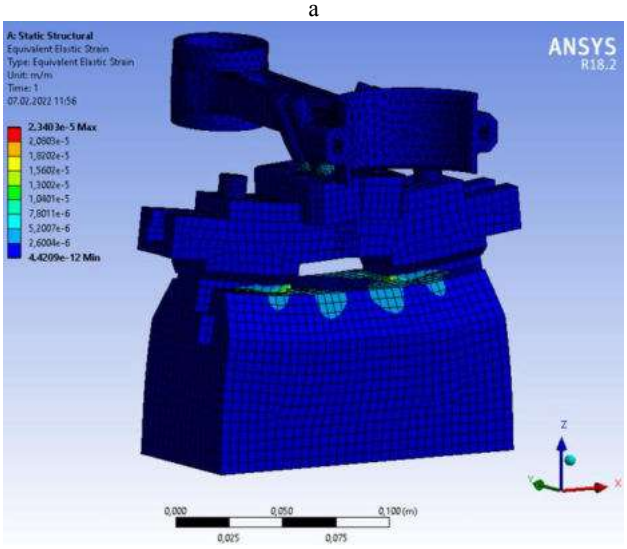

b

Figure 6 – Displacements (a) and elastic strain (b)

3.2 Calculations of labor intensity

To evaluate labor efficiency, it is necessary to calculate the cycle time for fully manual and collaborative assembly.

The assigned time norms for all transitions of the assembly operation for manual and collaborative assembly are indicated in Table 1.

It should be noted that some technological transitions are performed in parallel, and therefore, it reduces the time spent in implementing the scalding process. Calculations confirmed that manual assembly takes 6.16 minutes and collaborative assembly – 4.1 minutes, which is 34% less.

Table 1 – Labor intensity of assembly, min

No.	Content	Assembling type	
		Manual	Collaborative
1	Install the rod into the device	0.60	N/A*
2	Apply oil to the outer cylindrical surface of the rod	0.17	
3	Apply oil to the holes in the piston to locate the rod	0.17	
4	Heat the neck of the connecting rod to the temperature of 280-320 °C	2.60	2.6
5	Clamp connecting rod in the jaws	0.12	–
6	Connect the connecting rod, the piston, and the rod	0.90	0.9
7	Remove the rod from the device	0.60	0.6
8	Check the smoothness of the connecting rod's movement relative to the piston	0.50	N/A
9	Put the assembly unit in the container	0.50	
	Total values:	6.16	4.1

* Simultaneously with heating.

Therefore, the productivity of the assembly operation increases. Additionally, the automation of the assembly process due to the implementation of a collaborative area ensures a reduction in the risk of burns for the fitter-assembler and reduces the load on him during the performance of tasks.

4 Discussion

The scientific novelty of the obtained results is as follows. Firstly, a new approach to designing the technology of assembly of products in the conditions of multi-item production by introducing a collaborative assembly area, which increases production efficiency, is proposed.

Secondly, the expediency of the design was substantiated, and the design and technological support of the collaborative assembly cell was developed, which allows for an increase in the assembly process of the connecting rod-piston group in the conditions of multi-item production.

Finally, a new design of a gripping device for a collaborative robot is proposed, which expands the production area's technological capabilities due to the possibility of installing parts in a specific range of standard sizes, increasing the assembly process efficiency.

The practical significance of the obtained results for the machine-building industry consists of developing design and technical documentation for a collaborative assembly cell, design documentation for a new gripping device, and practical recommendations.

5 Conclusions

Thus, the current development of collaborative systems in mechanical engineering has been studied. The expediency of implementing a collaborative assembly cell to increase the assembly process efficiency in multi-item production conditions has been substantiated.

A new approach to the design of the structure of the assembly operation is proposed on the example of the assembly process of the connecting rod-piston group using robots, which made it possible to reasonably redistribute the technological transitions between the operator and the robots.

Also, a design solution for a collaborative assembly area for assembling a connecting rod-piston group is proposed. It improves the product assembly process in conditions of multi-item production by 34% compared to manual assembly.

Finally, a new design of a gripping device for a collaborative robot is proposed and developed, which reduces the time spent related to production preparation, increases the degree of flexibility, and compensates for errors related to the technological process of receiving blanks.

6 Acknowledgments

The research was carried out at the Research and Educational Center for Industrial Engineering within the R&D project "Fulfillment of tasks of the perspective plan of development of a scientific direction "Technical sciences" Sumy State University" by the Ministry of Education and Science of Ukraine (State reg. no. 0121U112684) under the support of Smart Production Systems Modelling Laboratory (Centre for Science, Research and Innovation CENWIS).

References

1. Weckenborg, C., Spengler, T. S. (2019). Assembly line balancing with collaborative robots under consideration of ergonomics: A cost-oriented approach. *IFAC-PapersOnLine*, Vol. 52(13), pp. 1860-1865.
2. IFR International Federation of Robotics. Available online: https://ifr.org/ifr-press-releases/news/robot-sales-rise-again.
3. Çil, Z.A. et al. (2020). Mathematical model and bee algorithms for mixed-model assembly line balancing problem with physical human-robot collaboration. *Applied Soft Computing*, Vol. 93, 106394.
4. Dalle Mura, M., Dini, G. (2019), Designing assembly lines with humans and collaborative robots: A genetic approach. *CIRP Annals*, Vol. 68(1), pp. 1-4.
5. Tlach, V. et al. (2019). Collaborative assembly task realization using selected type of a human-robot interaction. *Transportation Research Procedia*, Vol. 40, pp. 541-547.
6. Borges, G. D. et al. (2021). Decision-making framework for implementing safer human-robot collaboration workstations: System dynamics modeling. *Safety*, Vol. 7(4), 75.
7. Cherubini, A. et al. (2016). Collaborative manufacturing with physical human–robot interaction. *Robotics and Computer-Integrated Manufacturing*, Vol. 40, pp. 1-13.
8. Collaborative Robots. ABB Robotics. Available online: https://new.abb.com/products/robotics/collaborative-robots.
9. Nourmohammadi, A., Fathi, M., Ng, A. H. C. (2022). Balancing and scheduling assembly lines with human-robot collaboration tasks. *Computers and Operations Research*, Vol. 140, 105674.
10. How Human-Robot Teamwork Will Upend Manufacturing. MIT Technology Review. Available online: https://www.technologyreview.com/2014/09/16/171369/how-human-robot-teamwork-will-upend-manufacturing.
11. Al-Yacoub, A. et al. (2021). Improving human robot collaboration through force/torque based learning for object manipulation. *Robotics and Computer-Integrated Manufacturing*, Vol. 69, 102111.
12. Hjorth, S., Chrysostomou, D. (2022). Human–robot collaboration in industrial environments: A literature review on non-destructive disassembly. *Robotics and Computer-Integrated Manufacturing*, Vol. 73, 102208.
13. Hentout, A. et al. (2019). Human-robot interaction in industrial collaborative robotics: A literature review of the decade 2008-2017. *Advanced Robotics*, Vol. 33(15-16), pp. 764-799.
14. Michalos, G. et al. (2015). Design considerations for safe human-robot collaborative workplaces, Vol. 37, pp. 248-253.
15. The Future of Collaborative Robots. Automate. Available online: https://www.automate.org/a3-content/future-of-collaborative-robots.
16. Delta X - Affordable & Efficient Delta Robot Series. Delta X Robot Store. Available online: https://store.deltaxrobot.com.
17. Gripper. Festo Croatia. Available online: https://www.festo.com/cms/hr_hr/70021.htm.

JOURNAL OF ENGINEERING SCIENCES

Volume 9, Issue 1 (2022)

Javanbakht T. (2022). Investigation on the rheological properties of polydimethylsiloxane. Journal of Engineering Sciences, Vol. 9(1), pp. C1-C7, doi: 10.21272/jes.2022.9(1).c1

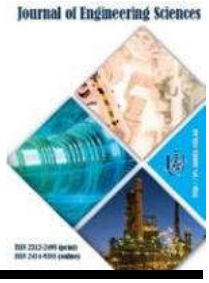

Investigation on the Rheological Properties of Polydimethylsiloxane

Javanbakht T.

Department of Chemistry and Biochemistry, Department of Physics, Concordia University, Richard J. Renaud Science Complex, 714,1 Sherbrooke St. West, H4B 1R6, Montreal, Quebec, Canada

Article info:
Submitted: January 20, 2022
Accepted for publication: March 18, 2022
Available online: March 23, 2022

***Corresponding email:**
taraneh.javanbakht@concordia.ca

Abstract. This paper focuses on studying the rheological properties of polydimethylsiloxane (PDMS). This polymer has been used to fabricate membranes and filters in engineering. The analysis of the rheological properties of this polymer is required for a further investigation of its mechanical behavior. In this study, the rheological behavior of PDMS is reported at different temperatures. This polymer showed steady shear viscosity during a short duration. However, this behavior changed with time and increased more with increasing temperature. The impact of the temperature increase was also observed when the shear viscosity of PDMS increased with shear strain. The increase of torque with shear strain and time was observed at different temperatures. Shear stress increased linearly with the shear rate at 20 °C and 40 °C. As expected, the deformation of the polymer required less shear stress with the increase of temperature. However, the change of shear stress with the shear rate at 60 °C was not linear, and the slope of the curve increased more at high shear rates. The results of this investigation can provide the required information for a better fabrication of membranes and filters with this polymer.

Keywords: rheology, polymer, mechanical properties, materials science, industrial growth.

1 Introduction

Polydimethylsiloxane (PDMS) is a “silicone rubber” polymer. Different steps such as hydrolysis and anionic, cationic, and radiation polymerization are used to synthesize this polymer [1, 2]. PDMS is transparent and resistant to thermal change, oxidation, and UV radiation [3–6]. It is worth noting that silicones do not produce any toxic material apart from a small amount of smoke during their combustion [3, 7]. Moreover, the thermal decomposition temperatures of PDMS are different because of significant differences in siloxane bond strength and segment flexibility in the main polymer chain, which also affect their toughening when used to prepare composites [3, 8]. The good elasticity of the siloxane chain can affect the hydrophobic properties of silicones and their low-temperature resistance. However, it can reduce the stability of these polymers at higher temperatures [9].

Different reaction mechanisms involve thermal depolymerization: random chain cleavage, attack of the PDMS chain end groups, and external reactions [10]. The type of functional groups and their positions on the chain and the molecular weight of PDMS affect the process of thermal depolymerization of the polymer [11]. It was shown that replacing end hydroxyl groups with methyl groups could increase the thermal resistance. Cyclic siloxane oligomers were produced in this process [12]. Besides, vinyl end groups could change the polymer’s thermal degradation mechanism [13].

Silicone-based materials contain different substances, such as crosslinking systems, rheology modifiers, and adhesion promoters. [14–19]. The silicone-based framework can also be used to design nanoporous materials [20]. The surface hydrophilization of PDMS can be produced when plasma oxidation or UV radiation is applied. This can improve cell adhesion, help assemble microdevices, and improve samples’ wetting with physiological fluids [21, 22].

A study showed that the chemical treatment of PDMS can affect the rheological behavior of the nanocomposites prepared with it [23]. Another study revealed that the variations of the properties of the pressure-sensitive adhesives changed with the type and loading of filler concerning their rheological properties [24]. Another parameter that influences the nanocomposite thermal conductivity is the critical filler fraction, affecting the liquid-solid transition and interface conductance [25].

2 Research Methodology

The improvement of the mechanical behavior of PDMS depends on a better understanding of its rheological properties, which can lead to an appropriate investigation of these nanocomposites.

In this study, the rheological properties of PDMS at different temperatures are reported. This investigation allows a better understanding of the mechanical behavior of this polymer. This is the first investigation of this polymer reported with the analysis of rheological parameters at different temperatures to the author's knowledge.

PDMS (#423785) was purchased from Sigma Aldrich. The purchased polymer was in solution, and it was used in the rheological assessments without adding no other chemical.

The rheological properties of PDMS were determined with an Anton Paar MCR-302 rheometer [26–29]. The circular rheological measurements were performed in triplicate at 20 °C, 40 °C, and 60 °C [30].

The data analysis was performed with QtiPlot, a software that calculates mean values and standard deviations [31–34]. The statistical significance of the data was determined for all the graphs.

3 Results and Discussion

Figure 1 shows the viscosity of PDMS vs. the shear rate at different temperatures.

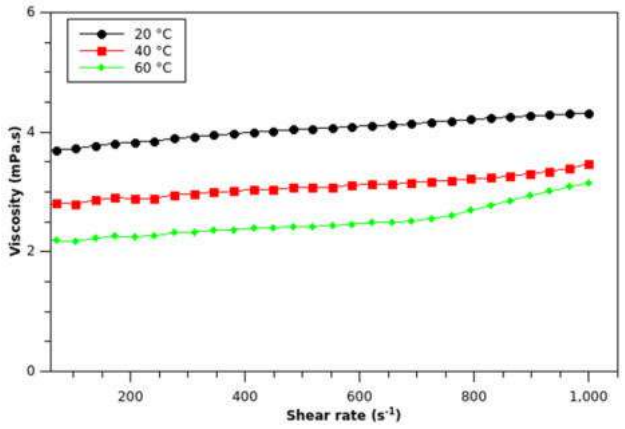

Figure 1 – Viscosity of PDMS vs. shear rate

As shown in Figure 1, the viscosity of PDMS increased with the increase of shear rate with a slight change. It was observed that the increase of viscosity was more at 60 °C at high shear rates, and the increase of viscosity with the shear rate was less at lower temperatures.

Figure 2 shows the change of viscosity of PDMS vs. shear strain at different temperatures.

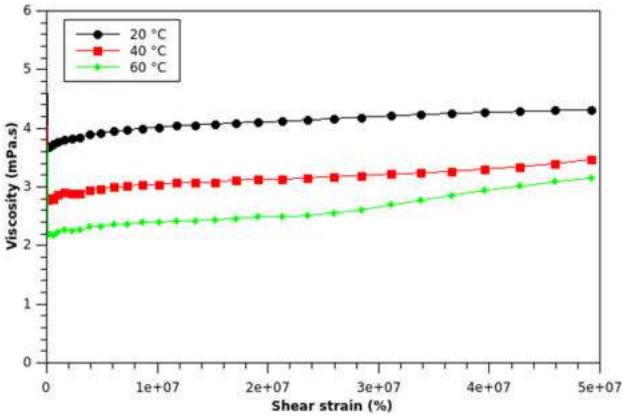

Figure 2 – Viscosity of PDMS vs. shear strain

As seen in this figure, the viscosity of PDMS increased with shear strain at all temperatures. The shear-thickening behavior of this polymer was more at 60 °C than in lower temperatures. The viscosity of the polymer became constant and reached a plateau at lower shear strain values. As the variation of viscosity with shear rate, in this case, also the shear thickening was stronger at 60 °C at high shear strain values. Although the variation of viscosity vs. shear strain of PDMS was almost linear at 20 °C at high shear strain values, it showed a slight increase at 40 °C. These results were attributed to the effect of temperature on the mobility of the polymer chains that led to its deformation.

The viscosity of PDMS vs. time curves at different temperatures is displayed in Figure 3. As shown in this figure, the changes in the viscosity of the polymer with time were similar to its changes with shear rate and shear strain, as shown in Figures 1, 2.

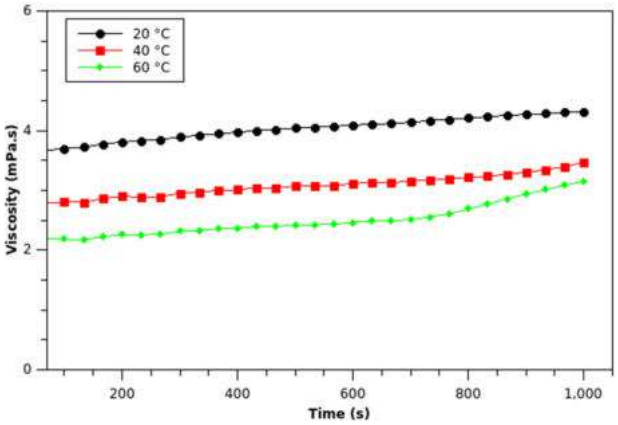

Figure 3 – Viscosity of PDMS vs. time

The viscosity values of PDMS vs. time at different temperatures are presented in Table 1. As observed in this table at 20 °C, the increased value of 0.28 mPa·s in viscosity was observed for PDMS between 600 s and 200 s. This increase was 0.23 mPa·s between 1000 s and 600 s. At 40 °C, this increase was 0.22 mPa·s between 600 s and 200 s and 0.35 mPa·s between 1000 s and 600 s, respectively, whereas it was 0.21 mPa·s in the first period and 0.68 mPa·s in the 2nd period, respectively. Therefore, the consistency between the results of this table and those of Figure 3 was observed.

Table 1 – Viscosity values of PDMS vs. time

Polymer/viscosity, mPa·s	Time (s)		
	200	600	1000
20 °C	3.81 ± 0.03	4.09 ± 0.01	4.32 ± 0.01
40 °C	2.90 ± 0.03	3.12 ± 0.01	3.47 ± 0.01
60 °C	2.26 ± 0.06	2.47 ± 0.01	3.15 ± 0.01

Figure 4 shows the torque vs. shear strain of PDMS at different temperatures. The torque values increased with shear strain at 20 °C, 40 °C, and 60 °C. However, an increase in the curve slope was observed at high shear strains at 60 °C. Moreover, as expected, the application of less amount of torque was required when the temperature increased.

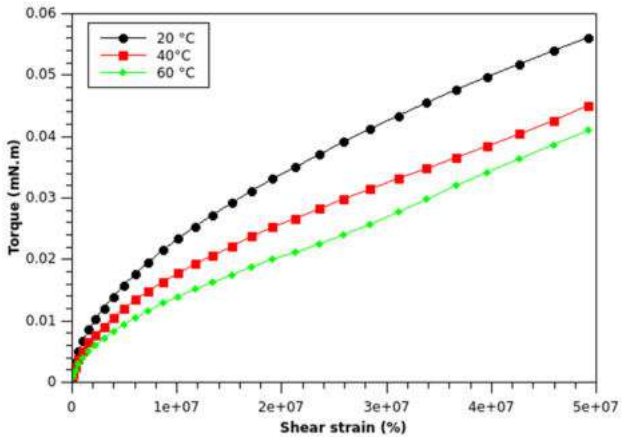

Figure 4 – Torque vs. shear strain of PDMS

The changes in the torque values for PDMS vs. time at different temperatures are displayed in Figure 5.

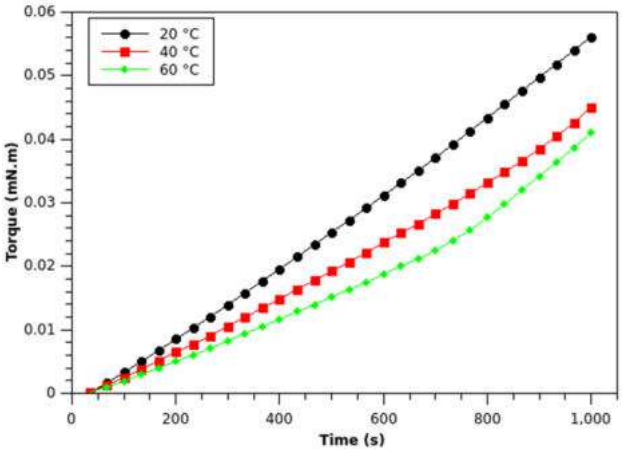

Figure 5 – Torque vs. time for PDMS

As shown in Figure 5, the torque values increased linearly with time at 20 °C and almost linearly at 40 °C, but the slope of the curve increased at 60 °C.

Figure 6 shows the shear stress vs. shear rate curves of PDMS at different temperatures. As observed in this figure, a linear increase and almost a linear increase of shear stress with the increase of shear rate were observed at 20 °C and 40 °C. However, this change was not linear at 60 °C.

Figure 7 shows the shear stress vs. shear strain curves of PDMS at different temperatures. The same shear stress changes were observed in Figure 7 as in the torque in Figure 4.

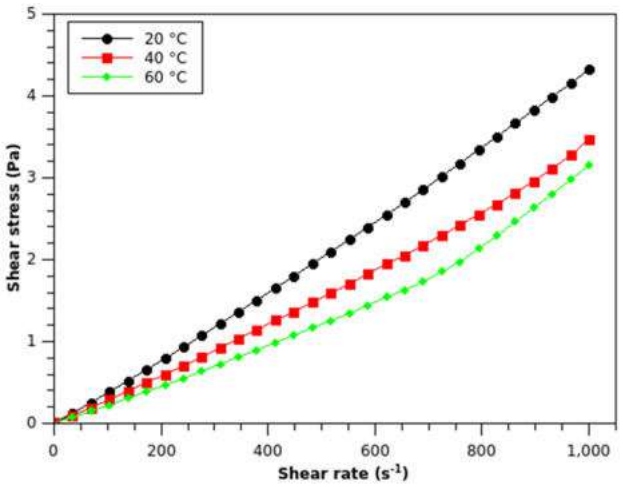

Figure 6 – Shear stress of PDMS vs. shear rate

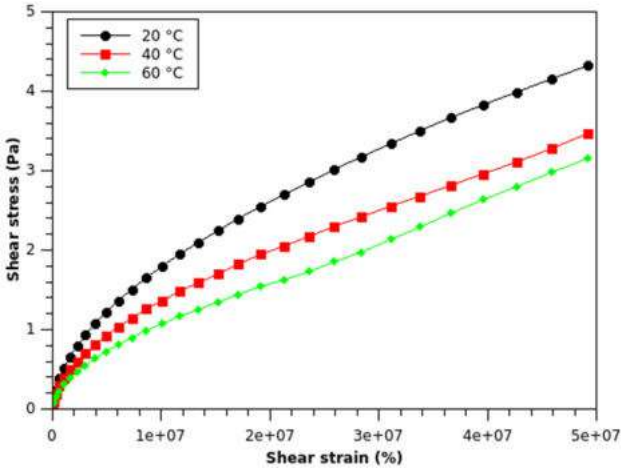

Figure 7 – Shear stress of PDMS vs. shear strain

Table 2 represents the shear stress values of PDMS vs. shear strain at different temperatures. As expected, the shear strain increase of the polymer from $1 \cdot 10^6$ to $2 \cdot 10^7$ would require more increase in the shear stress at 20 °C than 40 °C or 60 °C. However, closer shear stress values were required when the shear strain increased from $2 \cdot 10^7$ to $4 \cdot 10^7$.

Table 2 – Shear stress values of PVA and PEG vs. shear strain

Polymer/ shear stress, Pa	Shear strain, %		
	$1 \cdot 10^6$	$2 \cdot 10^7$	$4 \cdot 10^7$
20 °C	0.52 ± 0.01	2.70 ± 0.01	4.00 ± 0.01
40 °C	0.39 ± 0.02	2.05 ± 0.02	3.11 ± 0.01
60 °C	0.31 ± 0.01	1.63 ± 0.02	2.80 ± 0.01

4 Discussion

The pace of applications of PDMS in the preparation of the membranes and filters is expected to accelerate as this polymer has shown appropriate properties in new rubbers [35–42]. Various materials have been investigated with previous applications in materials science, pure sciences, and engineering [43–51].

These materials could modify the properties of PDMS in the mentioned applications. This could be directed toward the exploration of its novel applications.

Recently the properties of some polymers have been investigated that can be used to prepare blends with PDMS [52–60]. It is worth noting that adding some nanomaterials without or with other polymers to PDMS can prepare diverse nanocomposites with interesting properties [61–68].

Carbon nanotubes, polyamide with metal-organic framework nanoparticles, poly (vinylidene fluoride), and poly (ether ketone) have been used for the preparation of new membranes [69–74].

More investigations on these materials, including PDMS, can improve the quality of new membranes and filters [75–77].

5 Conclusions

This investigation reported the rheological properties of PDMS at different temperatures. The polymer showed viscosity stability at 20 °C and 40 °C vs. shear rate. However, at 60 °C more significant viscosity increase was observed at high shear rates. Moreover, the viscosity of PDMS increased at all temperatures with shear strain, which revealed its shear thickening behavior. The changes in the viscosity of the polymer were like its changes with shear rate and shear strain vs. time. The increase of torque with shear strain and time and shear stress with shear rate and time were observed in this investigation. However, the patterns of the change of these parameters were different at 60 °C in comparison with lower temperatures. This study can better prepare membranes and filters with this polymer regarding its rheological properties.

6 Acknowledgments

The author would like to thank Professor Ingo Salzmann for providing PDMS.

References

1. Velkov, A. (2013). *Polydimethylsiloxane (PDMS)*, Springer-Verlag Berlin Heidelberg, E. Droli, L. Giorno (eds.), Encyclopedia of Membranes, pp. 1–2. https://doi.org/10.1007/978-3-642-40872-4_1400-1.
2. Mark, J.E. (2009). *Polymer Data Handbook*, 2nd edn., Oxford University Press, Oxford.
3. Zielecka, M., Rabajczyk, A., Pastuszka, L., Jurecki, L. (2020). Flame resistant silicone-containing coating materials, *Coatings*, Vol. 10, 479. https://doi.org/10.3390/coatings10050479.
4. Dvornic, P.R. (2000). *Thermal Properties of Polysiloxanes in Silicon-Containing Polymers: The science and technology of their Synthesis and Applications*, Jones, R.G., Ando., W., Chojnowski, J., Eds.; Springer: Dordrecht, The Netherlands, pp. 185–213.
5. Dobkowski, Z., Zielecka, M. (2002). Thermal analysis of the poly(siloxane)-poly(tetrafluoroethylene) coating system, *J. Therm. Anal. Calorim.*, Vol. 68, 147–158. https://doi.org/10.1023/A:1014937004491.
6. Tiwari, A., Nema, A.K., das, C.K., Nema, S.K. (2004). Thermal analysis of polysiloxanes, aromatic polyimide and their blends, *Thermochimica Acta*, Vol. 417(1), 133–142. https://doi.org/10.1016/j.tca.2003.10.003.
7. Hamdani, S., Longuet, C., Perrin, D., Lopez-cuesta, J.M., Ganachaud, F. (2009). Flame retardancy of silicone-based materials, *Polym. Degrad. Stabil.*, Vol. 94, 465–495. https://doi.org/10.1016/j.polymdegradstab.2008.11.019.
8. Kwan, M., Braccini, M., Lane, M.W., Ramanath, G. (2018). Frequency-tunable toughening in a polymer-metal-ceramic stack using an interfacial molecular nanolayer, *Nature Communications*, Vol. 9, 5249. https://doi.org/10.1038/s41467-018-07614-y.
9. Zielecka, M., Bujnowska, E. (2006). Silicone-containing polymer matrices as protective coatings. Properties and applications. *Prog. Org. Coat.*, Vol. 55, 160–167. https://doi.org/10.1016/j.porgcoat.2005.09.012.
10. Dvornic, P.R. (2004). *High Temperature Stability of Polysiloxanes in Silicon Compounds: Silanes and Silicones*, Gelest Catalog, Gelest, Inc.: Morrisville, PA, USA, pp. 419–432.
11. Grassie, N., Macfarlane, I.G. (1978). The thermal degradation of polysiloxanes–I. Poly(dimethylsiloxane). *Eur. Polym. J.*, Vol. 14, 875–884. https://doi.org/10.1016/0014-3057(78)90084-8.
12. Jovanovic, J.D., Govedarica, M.N., Dvornic, P.R., Popovic, I.G. (1998). The thermogravimetric analysis of some polysiloxanes. *Polym. Degrad. Stabil.*, Vol. 61, 87–93. https://doi.org/10.1016/S0141-3910(97)00135-3.
13. Deshpande, G., Rezac, M.E. (2001). The effect of phenyl content on the degradation of poly(dimethyl diphenyl) siloxane copolymers. *Polym. Degrad. Stabil.*, Vol. 74, 363–370. https://doi.org/10.1016/S0141-3910(01)00186-0.
14. Zelisko, P.M., Amelien, K., Frampton, M. (2008). *Enzyme-mediated cross-linking of silicone polymers*, US Patent WO2008154731A1.
15. Rambarran, T., Gonzaga, F., Brook, M.A. (2012). Generic, metal-free crosslinking and modification of silicone elastomers using click ligation, *Macromolecules*, Vol. 45(5), 2276–2285. https://doi.org/10.1021/ma202785x.
16. Springael, S., Wolf, A.T.F. Stammer, A. (2005). Room temperature vulcanizable (RTV) silicone compositions having improved body, UK Patent GB2413332A.
17. Pan, K., Zeng, X., Li, H., Lai, X. (2016). Synthesis of silane oligomers containing vinyl and epoxy group for improving the adhesion of addition-cure silicone encapsulant, *Journal of Adhesion Science and Technology*, Vol. 30(10), pp. 1–12. https://doi.org/10.1080/01694243.2016.1142806.

18. Liu, J., Yao, Y., Chen, S., Li, X., Zhang, Z. (2021). A new nanoparticle-reinforced silicone rubber composite integrating high strength and strong adhesion, *Composites Part A: Applied Science and Manufacturing*, Vol. 151, 106645. https://doi.org/10.1016/j.compositesa.2021.106645.
19. Gordy, T.A., Ung, N.S., Fritz, U., Fritz, O., Wojcik, R. (2008). Compositions and devices comprising silicone and specific polyphosphazenes, US Patent 0095816 A1.
20. Muramoto, N., Matsuno, T., Wada, H., Kuroda, k., Shimojima, A. (2021). Preparation of an ordered nanoporous silicone-based material using silica colloidal crystals as a hard template, *Chem. Lett.*, Vol. 50, pp. 1038–1040. https://doi.org/10.1246/cl.210046.
21. Nahmias, Y., Bhatia, S.N. (2009). *Microdevices in biology and medicine*, Artech House, Norwood.
22. Ratner B.D., Hoffman A.S., Schoen F.J., Lemons J.E. (1996). *Biomaterials science: an introduction to materials in medicine*, Elsevier Science, Amsterdam.
23. Kim, T., Kim. H. (2020). Effect of acid-treated carbon nanotube and amine-terminated polydimethylsiloxane on the rheological properties of polydimethylsiloxane/carbon nanotube composite system, *The Korea-Australia Rheology Journal*, Vol. 22(3), 205–210.
24. Deshpande, T.D., Singh, Y.R.G., Patil, S., Joshi, Y.M., Sharma, A. (2019). Adhesion strength and viscoelastic properties of polydimethylsiloxane (PDMS) based elastomeric nanocomposites with embedded electrospun nanofibers, *Soft Matther*, Vol. 15, 5739–5747. https://doi.org/10.1039/C9SM00533A.
25. Seshadri, I., Borca-Tasciuc, T., Keblinski, P., Ramanath, G. (2013). Interfacial thermal conductance-rheology nexus in metal-contacted nanocomposites, *Applied Physics Letters*, Vol. 103(17), 173113. https://doi.org/10.1063/1.4824702.
26. Javanbakht, T., David, E. (2020). Rheological and physical properties of a nanocomposite of graphene oxide nanoribbons with polyvinyl alcohol. *Journal of Thermoplastic Composite Matererials*, 0892705720912767. https://doi.org/10.1177/0892705720912767.
27. Javanbakht, T., Laurent, S., Stanicki, D., David, E. (2019). Related physicochemical, rheological, and dielectric properties of nanocomposites of superparamagnetic iron oxide nanoparticles with polyethyleneglycol. *Journal of Applied Polymer Science*, Vol. 137(3), pp. 48280–48289. https://doi.org/10.1002/app.48280.
28. Javanbakht, T. (2021). Comparative study of rheological properties of polyvinyl alcohol and polyethylene glycol, *Journal of Engineering Sciences*, Vol. 8(2), pp. F11–F19. https://doi.org/10.21272/jes.2021.8(2).f3.
29. Kumara, P., Prakash, S.C., Lokesh, P., Manral, K. (2015). Viscoelastic properties and rheological characterization of carbomers, *International Journal of Latest Research in Engineering and Technolog*, Vol. 1(6), 17–30.
30. Javanbakht, T., Laurent, S., Stanicki, D., Salzmann, I. (2021). Rheological properties of superparamagnetic iron oxide nanoparticles, *Journal of Engineering Sciences*, Vol. 8(1), pp. C29–C37. https://doi.org/10.21272/jes.2021.8(1).c4.
31. Javanbakht, T., Laurent, S., Stanicki, D., Frenette, M. (2020). Correlation between physicochemical properties of superparamagnetic iron oxide nanoparticles and their reactivity with hydrogen peroxide. *Canadian Journal of Chemistry*, Vol. 98(10), pp. 601–608. https://doi.org/10.1139/cjc-2020-0087.
32. Javanbakht, T., Bérard, A., Tavares, J. R. (2016). Polyethylene glycol and poly (vinyl alcohol) hydrogels treated with photo-initiated chemical vapor deposition. *Canadian Journal of Chemistry*, Vol. 94(9), pp. 744–750. https://doi.org/10.1139/cjc-2016-0229.
33. Varga, N., Turcsányi, A., Hornok, V., Csapó, E. (2019). Vitamin E-loaded PLA- and PLGA-based core-shell nanoparticles: Synthesis, structure optimization and controlled drug release, *pharmaceutics*, Vol. 11(7), 357. https://doi.org/10.3390/pharmaceutics11070357.
34. Tafulo, P.A.R., Queirós, R.E., González-Aguilar, G. (2009). On the "concentration-driven" methylene blue dimerization, *Spectrochimica Acta Part A*, Vol. 73, pp. 295–300. doi:10.1016/j.saa.2009.02.033.
35. Khoroshavina, Y.V. (2016). Properties of polyphenylsilsesquioxane-polydimethylsiloxane block copolymer and its filled vulcanizates, *Materials Chemistry and Physics*, Vol. 2(1), pp. 28–32.
36. Sales, F.C.P., Souza, A., Ariati, R., Noronha, V. (2021). Composite material of PDMS with interchangeable transmittance: Study of optical, mechanical properties and wettability, *Journal of Composites Science*, Vol. 5(4), 110. https://doi.org/10.3390/jcs5040110.
37. Heris, H., Khavari, A., Ehrlicher, A.J. (2016). Tunable viscoelastic polydimethylsiloxane substrates for cell mechanics and mechanobiology applications, *10th World Biomaterials Congress*, Montreal, Canada. doi: 10.3389/conf.FBIOE.2016.01.02958.
38. Han, X., Du, W., Li, Y., Li, Z., Li, L. (2015). Modulating stability and mechanical properties of silica–gelatin hybrid by incorporating epoxy-terminated polydimethylsiloxane oligomer, *Journal of Applied Polymer Science*, Vol. 133(8). https://doi.org/10.1002/app.43059.
39. Warunek, S.P., Sorenson, S.E., Cunat, J.J., Green, L.J. (1989). Physical and mechanical properties of elastomers in orthodontic positioners, *Americal Journal of Orthodontics and Dentofacial Orthopedics*, Vol. 95, 5, pp. 388–400. https://doi.org/10.1016/0889-5406(89)90300-4.
40. Rodriguez, N., Ruelas, S., Forien, J.-B., Dudukovic, N., DeOtte, J., Rodriguez, J., Moran, B., Lewicki, J.P., Duoss, E.B., Oakdale, J.S. (2021). 3D printing of high viscosity reinforced silicone elastomers, *Polymers*, Vol. 13(14), 2239. https://doi.org/10.3390/polym13142239.
41. (2016). Absorbance analysis of *Escherichia coli* (*E. coli*) bacteria suspension in polydimethylsiloxane (PDMS)-glass based microfluidic, Advanced Materials Research, Ed. K. Noorsal, Vol. 1133, pp. 65–69. https://doi.org/10.4028/www.scientific.net/AMR.1133.65.

42. Andrady, A.L., Llorente, M.A., Mark, J.E. (1992). Effects of dangling chains on some dynamic mechanical properties of model poly(dimethylsiloxane) networks, *Polymer Bulletin*, Vol. 28(1), pp. 103–108. https://doi.org/10.1007/BF01045645.
43. Pourian Azar, N.T., Mutlu, P., Khodadust, R., Gunduz, U. (2013). Poly(amidoamine) (PAMAM) Nanoparticles: Synthesis and Biomedical Applications, *J. Biol. & Chem.*, Vol. 41 (3), pp. 289–299.
44. Javanbakht, T., Hadian, H., Wilkinson, K. J. (2020). Comparative study of physicochemical properties and antibiofilm activity of graphene oxide nanoribbons. *Journal of Engineering Sciences*, Vol. 7(1), pp. C1–C8. https://doi.org/10.21272/jes.2020.7(1).c1.
45. Javanbakht, T., Ghane-Motlah, B., Sawan, M. (2020). Comparative study of antibiofilm activity and physicochemical properties of microelectrode arrays. *Microelectronic Engineering*, Vol. 229, 111305. https://doi.org/10.1016/j.mee.2020.111305.
46. Ghane-Motlagh, B., Javanbakht, T., Shoghi, F., Wilkinson, K. J., Martel, R., Sawan, M. (2016). Physicochemical properties of peptide-coated microelectrode arrays and their in vitro effects on neuroblast cells. *Materials Science and Engineering C*, Vol. 68, pp. 642–650. https://doi.org/10.1016/j.msec.2016.06.045.
47. Elmowafy, E.M., Tiboni, M., Soliman, M.E. (2019). Biocompatibility, biodegradation and biomedical applications of poly(lactic acid)/poly(lactic-co-glycolic acid) micro and nanoparticles, *Journal of Pharmaceutical Investigation*, Vol. 49, pp. 347–380. https://doi.org/10.1007/s40005-019-00439-x.
48. Kharwade, R., More, S., Warokar, A., Agrawal, P., Mahajan, N. (2020). Starburst pamam dendrimers: Synthetic approaches, surface modifications, and biomedical applications, *Arabian Journal of Chemistry*, Vol. 13(7), 6009–6039. https://doi.org/10.1016/j.arabjc.2020.05.002.
49. Djavanbakht, T., Carrier, V., André, J. -M., Barchewitz, R., Troussel, P. (2000). Effets d'un chauffage thermique sur les performances de miroirs multicouches Mo/Si, Mo/C et Ni/C pour le rayonnement X mou. *Journal de Physique IV France*, Vol. 10, pp. 281–287. https://doi.org/10.1051/jp4:20001031.
50. Javanbakht, T., Sokolowski, W. (2015). Thiol-ene/acrylate systems for biomedical shape-memory polymers in *Shape Memory Polymers for Biomedical Applications* (Ed. L'H Yahia), pp. 157–166, Sawston, Cambridge, Woodhead Publishing. https://doi.org/10.1016/B978-0-85709-698-2.00008-8.
51. Djavanbakht, T., Jolès, B., Laigle, A. (2000). Intracellular stability of antisense oligonucleotides protected by the d(GCGAAGC). *Biomedical Society Transactions*, Vol. 28, p. A201. https://doi.org/10.1042/bst028a201c.
52. Van Oosten, A.S.G., Vahabi, M., Licup, A.J., Sharma, A., Galie, P.A., MacKintosh, F.C., Janmey, P.A. (2016). Uncoupling shear and uniaxial elastic moduli of semiflexible biopolymer networks: compression-softening and stretch-stiffening, Sci Rep., Vol. 6, 19270. https://doi.org/10.1038/srep19270.
53. Wilkes, G.L. (1981). An overview of the basic rheological behavior of polymer fluids with an emphasis on polymer melts, *Journal of Chemical Education*, Vol. 58(11), pp. 880–892. https://doi.org/10.1021/ed058p880.
54. Liu, F., Wang, B., Xing, Y., Zhang, K., Jiang, W. (2020). Effect of polyvinyl alcohol on the rheological properties of cement mortar, *Molecules*, Vol. 25, 754. http://doir.org/10.3390/molecules25030754.
55. Kim, J.H., Robertson, R.E., Naaman, A.E. (1999). Structure and properties of poly(vinyl alcohol)- modified mortar and concrete. *Cement and Concrete Research*, Vol. 29(3), pp. 407–415. https://doi.org/10.1016/S0008-8846(98)00246-4.
56. Kim, J.H., Robertson, R.E. (1997). Prevention of air void formation in polymer-modified cement mortar by pre-wetting, *Cement and Concrete Research*, Vol. 27, pp. 171–176. https://doi.org/10.1016/S0008-8846(97)00001-X.
57. Allahverdi, A., Kianpur, K., Moghbeli, M.R. (2010). Effect of polyvinyl alcohol on flexural strength and some important physical properties of Portland cement paste. *Iran. J. Mater. Sci. Eng.*, 7, pp. 1–6.
58. Remiš, T. (2017). Rheological properties of poly(vinyl alcohol) (PVA) derived composite membranes for fuel cells, *J. Phys.: Conf. Ser.*, Vol. 790, 012027. https://doi.org/10.1088/1742-6596/790/1/012027.
59. Krasinskyi, V., Suberlyak, O., Antonuk, V., Jachowicz, T. (2017). Rheological properties of compositions based on modified polyvinyl alcohol, *Adv. Sci. Technol. Res. J.*, Vol. 11(3), pp. 304–309. https://doi.org/10.12913/22998624/76584.
60. Bai, H., Sun, Y., Xu, J., Dong, W., Liu, X. (2015). Rheological and structural characterization of HA/PVA-SbQ composites film-forming solutions and resulting films as affected by UV irradiation time, *Carbohydr. Polym*., Vol. 115, pp. 422–31. http://doi.org/10.1016/j.carbpol.2014.08.103.
61. Smith, A.T., LaChance, A.M., Zeng, S., Liu, B., Sun, L. (2019). Synthesis, properties, and applications of graphene oxide/reduced graphene oxide and their nanocomposites, *Nano Materials Science*, Vol. 1(1), pp. 31–47. https://doi.org/10.1016/j.nanoms.2019.02.004.
62. Meree, C.E., Schueneman, G.T., Meredith, J.C., Shofner, M.L. (2016). Rheological behavior of highly loaded cellulose nanocrystal/poly(vinyl alcohol) composite suspensions, *Cellulose*, Vol. 23(5), pp. 3001–3012. https://doi.org/10.1007/s10570-016-1003-1.
63. Salahshoori, I., Nasirian, D., Rashidi, N., Hossain, K., Hatami, A., Hassanzadeganroodsari, M. (2021). The effect of silica nanoparticles on polysulfone–polyethylene glycol (PSF/PEG) composite membrane on gas separation and rheological properties of nanocomposites, *Polymer Bulletin*, Vol. 78, pp. 3227–3258. https://doi.org/10.1007/s00289-020-03255-8.
64. Heo, J., Tanum J., Park, S., Choi, D., Jeong, H., Han, U., Hong, J. (2020). Controlling physicochemical properties of graphene oxide for efficient cellular delivery, *Journal of Industrial and Engineering Chemistry*, Vol. 88, pp. 312–318. https://doi.org/10.1016/j.jiec.2020.04.030.
65. Faccini, M., Borja, G., Boerrigter, M., Martín, D.M. Crespiera, S.M., Vázquez-Campos, S., Aubouy, L., Amantia, D. (2015). Fabrication and applications of electrospun nanofibers, *Journal of Nanomaterials*, Vol, 2015. 247471. https://doi.org/10.1155/2015/247471.

66. Yan, J., Xiao, W., Chen, L., Wu, Z., gao, J., Xue, H. (2021). Superhydrophilic carbon nanofiber membrane with a hierarchically macro/meso porous structure for high performance solar steam generators, *Desalination*, Vol. 516, 115224. https://doi.org/10.1016/j.desal.2021.115224.
67. Huang, Y., Zhang, L., Lu, H., Lai, F., Miao, Y.-E., Liu, T. (2016). A highly flexible and conductive graphene-wrapped carbon nanofiber membrane for high-performance electrocatalytic applications, Inorganic Chemistry Frontiers, Vol. 3(7), 969–976. https://doi.org/10.1039/C6QI00101G.
68. Pellegrino, J., Schulte, L.R., De la Cruz, J., Stoldt, C. (2017). Membrane processes in nanoparticle production, *Journal of Membrane Science*, Vol. 522, pp. 245–256. https://doi.org/10.1016/j.memsci.2016.09.018.
69. Rashed, A.R.,Merenda, A., Kondo, T., Lima, M., Razal, J., Kong, L., Huynh, C., Dumée, L.F. (2021). Carbon nanotube membranes – Strategies and challenges towards scalable manufacturing and practical separation applications, *Separation and Purification Technology*, Vol. 257, 117929. https://doi.org/10.1016/j.seppur.2020.117929.
70. Sianipar, M., Kim, S.H., Khoiruddin, Iskandar, F., Wenten, I.G. (2017). Functionalized carbon nanotube (CNT) membrane: progress and challenges, *RSC Advances*, Vol. 7(81), pp. 51175–51198. https://doi.org/10.1039/C7RA08570B.
71. Rasid, H.-O., Ralph, S.F. (2017). Carbon Nanotube Membranes: Synthesis, Properties, and Future Filtration Applications, *Nanomaterials*, 7(5), 99. https://doi.org/10.3390/nano7050099.
72. Wang, Z., Wang, Z., Lin, S., Jin, H., Gao, S., Zhu, Y. Jin, J. (2018). Nanoparticle-templated nanofiltration membranes for ultrahigh performance desalination, *Nature Communications*, Vol. 9, 2004. https://doi.org/10.1038/s41467-018-04467-3.
73. Sun, C. (2009). *Poly(vinylidene fluoride) membranes: Preparation, modification, characterization and applications*, PhD Thesis, University of Waterloo, Canada.
74. Yee, R.S.L., Zhang, K., Ladewig, B.P. (2013). The effects of sulfonated poly(ether ether ketone) ion exchange preparation conditions on membrane properties, *Membranes*, Vol. 3, pp. 182–195. https://doi.org/10.3390/membranes3030182.
75. Kausar, A. (2020). Polydimethylsiloxane-based nanocomposite: present research scenario and emergent future trends, *Polymer-Plastic Technology and Materials*, Vol. 59, 11, pp. 1148–1166. https://doi.org/10.1080/25740881.2020.1719149.
76. Liu, Y., Wang, C., Jarrell, R.M., Nair, S., Wynne, K.J., Di, D. (2020). Icephobic, Pt-Cured, Polydimethylsiloxane Nanocomposite Coatings, *ACS Appl. Mater. Interfaces*, Vol. 12(9), pp. 11180–11189. https://doi.org/10.1021/acsami.9b20989.
77. Flores, J.M.B., Garcia, M.G.P., Contreras, G.G., Mendoza, A.C., Arellano, V.H.R. (2021). Polydimethylsiloxane nanocomposite macroporous films prepared *via* Pickering high internal phase emulsions as effective dielectrics for enhancing the performance of triboelectric nanogenerators, *ACS Advances*, Vol. 11(1), pp. 416–424. https://doi.org/10.1039/D0RA07934K.

JOURNAL OF ENGINEERING SCIENCES

Volume 9, Issue 1 (2022)

Islam M. R., Wollega E. (2022). Effect of loading frequency and temperature on the fatigue parameters of asphalt concrete. Journal of Engineering Sciences, Vol. 9(1), pp. D1-D5, doi: 10.21272/jes.2022.9(1).d1

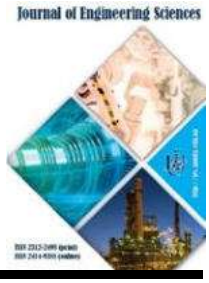

Effect of Loading Frequency and Temperature on the Fatigue Parameters of Asphalt Concrete

Islam M. R., Wollega E.

Colorado State University, 2200, Bonforte Blvd, Pueblo, CO 81001, USA

Article info:
Submitted: March 11, 2022
Accepted for publication: June 9, 2021
Available online: June 13, 2022

***Corresponding email:**
md.islam@csupueblo.edu

Abstract. Investigating the behavior of asphalt concrete at low loading frequency is essential to understand the thermal fatigue damage due to cyclic day-night temperature cycles, where the loading frequency is usually very low. This study determines some properties (e.g., fatigue damage, dissipated energy, and stiffness) of asphalt concrete beam samples at a low frequency of loading using four-point bending test apparatus. Results show that fatigue damage is more significant at a lower frequency of cyclic loading and the number of cycles at failure becomes stable at a frequency equal to or lower than 0.01 Hz. The concept of initial stiffness at the 50th cycle of loading is inappropriate at a low frequency of loading as the stiffness reduction with a number of loadings is so considerable at a frequency of loading. In addition, the dissipated energy per loading cycle decreases with a decrease in loading frequency.

Keywords: asphalt concrete, fatigue life, initial stiffness, frequency, temperature.

1 Introduction

Fatigue cracking is one the most common forms of distress in flexible pavement. It happens due to the repeated tensile strain at the bottom of asphalt concrete (AC) caused by the traffic loading. The integrity of the asphalt concrete material starts losing with the initiation of microcracks upon applying repeated traffic loading. These microcracks coalesce to form macrocracks under further traffic loading, leading to pavement failure. The fatigue behavior of hot-mix asphalt (HMA) has been characterized by four-point bending (4PB) fatigue test in the laboratory by many researchers in the past [1, 2]. In this test, an AC beam is subjected to repeated bending in strain-controlled mode until the stiffness is decreased by 50 % of its initial stiffness, which is the traditional failure criteria. Several factors might affect the test results in the fatigue test. The effect of loading pattern (haversine and sinusoidal) and rest period between loading of the fatigue test have been widely explored in the literature [3–6].

American Association of State Highway Transportation Officials defines fatigue failure as the number of cycles at which material stiffness decreases by 50 % [7, 8]. The initial stiffness of a beam is measured at the 50th cycle of loading to account for the initial setting of the beam. However, one might expect stiffness reduction from the first cycle, especially at higher strain amplitude. Other researchers have used dissipated energy to model fatigue behavior [9–11]. Dissipated energy is defined as energy lost to the system during each loading cycle. Energy loss is due to damping, viscoelastic effects, and damage growth. On the other hand, the Viscoelastic Continuum Damage approach has shown promising results in terms of robustness and efficient utilization of available resources [12, 13]. In addition, the test is typically performed at several temperatures to evaluate the effect of stiffness on the fatigue life since the stiffness of AC is affected mainly by temperature.

The above discussion clarifies that the researchers have widely explored the fatigue damage of AC. The loading pattern, failure criteria, and the effect of temperature are well known. However, the effect of the loading frequency, mainly the low frequency, is still an unknown issue. The behavior of AC at a low frequency of loading is essential to understanding the thermal fatigue behavior. The reason is that the thermal fatigue damage occurs mainly due to the day-night temperature fluctuations whose loading frequency is $1/(24 \cdot 60 \cdot 60) = 1.16 \cdot 10^{-5}$ (Hz). It may mislead or produce wrong results if the behavior of AC at a high frequency (usually 10 Hz) is used to analyze the thermal fatigue damage. Another form of thermal damage, single cycle

low-temperature cracking, also occurs at slow loading (cooling) rate.

The main objective of this study is to investigate the AC's fatigue parameters (flexural modulus, initial stiffness, dissipated energy, and fatigue damage) at a low loading frequency using flexural beam fatigue tests at different temperatures, strain levels, and low frequencies.

2 Research Methodology

Plant-produced asphalt mixture was used to prepare the samples, and the mix was collected from a construction site in cooperation with New Mexico Department of Transportation. This is a widely used dense-graded Superpave (SP) mix, type SP-III, with a maximum aggregate size of 25 mm. The mixture contained 35 % reclaimed asphalt pavement materials. Performance Grade (PG) binder, PG 76-22, was used for an amount of 4.4 % by the weight of the mixture. About 5 % of materials passed through the No. 200 sieve size (0.075 mm).

Figure 1 shows the preparation of the beam sample in the laboratory.

a

b

Figure 1 – Sample's preparation: a – compacted mixture; b – cutting the slab to prepare the beam sample

As a first step, beam slabs of 450×150×75 mm were prepared using a kneading compactor, as shown in Figure 1 a. Before the compaction, the mixture was oven heated for less than an hour. Then, each slab was cut into two beams of 380×63×50 mm using a laboratory saw, as shown in Figure 1 b. The air voids of the samples ranged from 5.1 % to 5.6 %, with an average value of 5.3 %.

Beam fatigue tests were conducted using a sinusoidal waveform with no rest period at different strain levels, temperatures, and frequencies. The support conditions and the geometry of the sample followed the requirements of the AASHTO T 321-07 test protocol [7]. The test program is shown in Figure 2 a, where a sample has been clamped for testing. The middle two clamps are loading frames that apply downward and upward force to attain the predefined strain in the sample. Using the deflection history, the maximum strain and stress in a specimen can be calculated using the following equations, respectively [2]:

$$\varepsilon = 12h\delta/(3L^2 - 4a^2); \quad (1)$$

$$\sigma = PL/(bh^2), \quad (1)$$

where ε – maximum strain; σ – maximum stress, Pa; $P(t)$ – load applied by actuator, N; t – time, s; b – average specimen width, m; h – average specimen height, m; $\delta(t)$ – deflection at the beam center, m; a – distance between inside clamps, m; L – the distance between outside clamps, m.

Sample flexural stiffness is then calculated using σ and ε data recorded from each cycle:

$$E = \sigma_t/\varepsilon_t, \quad (3)$$

where E – flexural stiffness.

Figure 2 b shows a typical test result where the stiffness ratio (SR) (current cycle's stiffness divided by the initial stiffness) decreases with the loading cycle due to microcrack formation. According to the AASHTO T 321-07 test protocol, the stiffness at the 50th cycle of loading was considered the initial stiffness, and the number of cycles at a 50 % reduction in stiffness was considered the failure of the beam AASHTO T 321-07 test protocol [7].

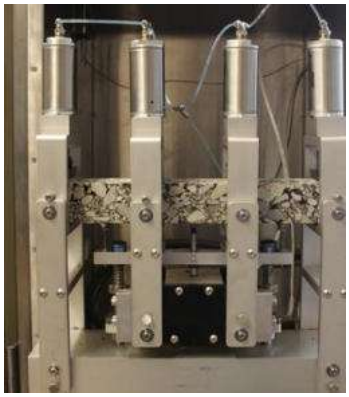

a

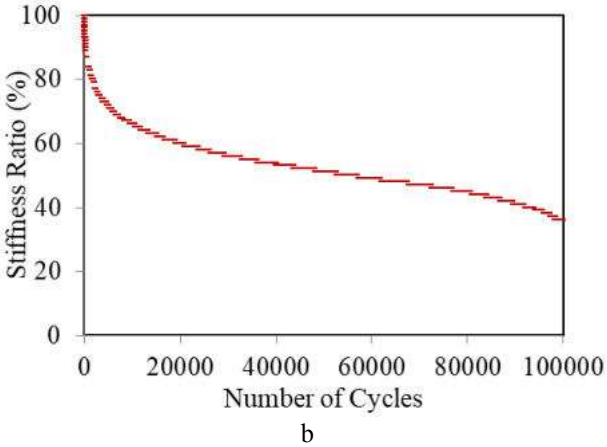

b

Figure 2 – Flexural stiffness test [14]: a – test setup; b – test result

3 Results and Discussion

3.1 Fatigue damage

Fatigue damage occurs due to a repeated loading cycle for developing micro-cracks inside the material, and the material's stiffness decreases with the loading cycle. Figure 3 presents the number of cycles at failure with a frequency of loading at three different strain levels (500 με, 1000 με, and 1500 με).

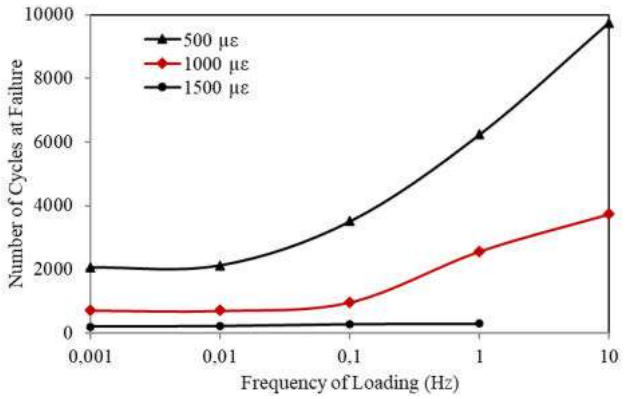

Figure 3 – Allowable load repetitions at different frequencies at 20 °C

The damage is usually more significant if the load sustains a longer time on a material. A similar observation has been made in AC fatigue damage based on the 4PB fatigue test.

Figure 3 shows that the stiffness decreases upon a decrease in loading frequency. For example, the stiffness decreases from 9751 MPa to 2131 MPa for the frequency decrease from 10 Hz to 0.001 Hz at 500 με.

A similar observation has been found for samples tested at 1000 με. Due to the large vertical scale, it is not well depicted for 1500 με.

The test could not be completed at 1500 με and 10 Hz, as it is too difficult to apply this large strain at this very fast rate.

To examine the temperature effect on the fatigue parameters, tests were also conducted at three different temperatures (–10 °C, 20 °C, and 40 °C). The results are presented in Fig. 4. It shows that the temperature has a very good effect on the fatigue damage of AC.

The fatigue damage is less (a more significant number of cycles at failure) at a higher temperature. For example, the numbers of cycles at failure are 17561, 9751, and 3755 at temperatures of 40 °C, 20 °C, and –10 °C, respectively.

In addition, the frequency dependency in the fatigue damage of AC is very low, as occurred at –10 °C in Figure 4. This is because the asphalt material's behavior is elastic at low temperatures.

Another finding from Figures 3, 4 is that the number of cycles at failure becomes stable at a frequency equal to or lower than 0.01 Hz. It is due to the healing behavior of AC. The material gets more time to heal up at a slower loading rate.

The behavior of AC at $1.16 \cdot 10^{-5}$ Hz can be well understood if the test is conducted at 0.01 Hz or, more conservatively, at 0.001 Hz.

More specifically, thermal fatigue damage occurs due to the day-night temperature fluctuations whose loading frequency is $1.16 \cdot 10^{-5}$ Hz.

It is good enough to study the behavior of AC at 0.001 Hz, to understand the fatigue behavior of AC due to day-night temperature fluctuations.

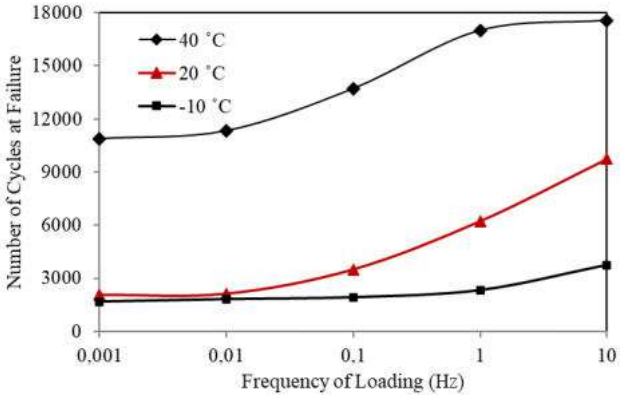

Figure 4 – Allowable load repetitions at different frequencies at 500 με

3.2 Dissipated energy

Dissipated energy (DE) is the area under the stress-strain curve. This part of energy does not recover upon unloading. It accumulates within the material upon applying repeated load. Due to its simplistic nature, dissipated energy approaches are popular among the pavement engineering community to determine the failure point of asphalt samples [15, 16].

Figure 5 shows the DE loop for two tests conducted at frequencies of 0.01 Hz and 10 Hz at 500 με (250 με to –250 με) strain level.

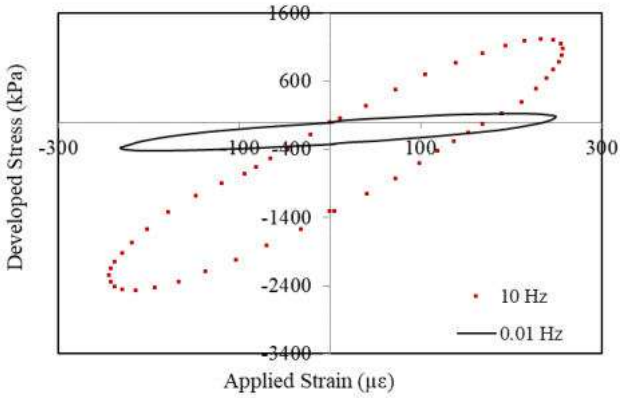

Figure 5 – Hysteresis loop of dissipated energy at 0.01 Hz and 10 Hz

The area of the DE loop of 0.01 Hz is much smaller than the 10 Hz curve. That means the material dissipates less energy at a low frequency of loading. This is because the stiffness of AC decreases with a decrease in stiffness. The DE loop area decreases as the stiffness decreases (under controlled strain test). However, the total DE of any material is independent of the loading mode. Therefore, at a low loading frequency, the material undergoes a more significant number of cycles to reach the DE capacity of AC. More specifically, the number of

cycles at failure is more significant than the traditional criteria of a 50 % reduction in stiffness.

Figure 6 shows the ASU energy ratios (stiffness ratio multiplied by the number of loading cycles) of two samples tested at 10 Hz and 0.01 Hz at 1000 με strain level.

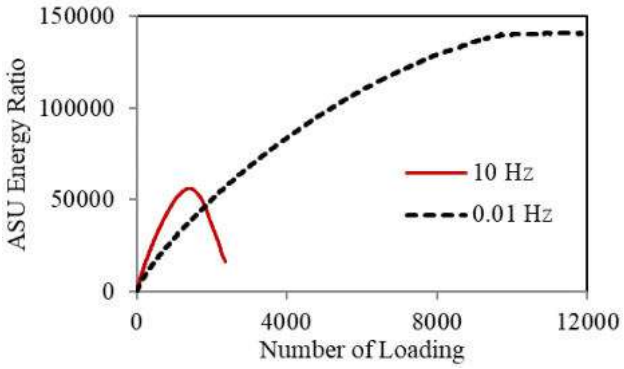

Figure 6 – ASU energy ratio with the number of loading at 1000 με

According to the energy dissipation approach, a material is considered to fail when the ASU energy reaches its peak. The ASU energy ratios of the samples tested at 10 Hz and 0.01 Hz are 56,200 and 140,500 (2.5 times of 56,200), respectively. The corresponding numbers of cycles at failure are 1260 and 9880 for the samples tested at 10 Hz and 0.01 Hz, respectively. This also implies that sample tested at lower loading frequency always has greater fatigue life if the DE approach is adopted, which is the opposite of the traditional criteria of 50 % reduction in stiffness as presented in Figures 3, 4.

Therefore, it can be said that the DE approach cannot predict the failure cycle considering the viscoelastic property of AC.

3.3 Initial stiffness

According to AASHTO T 321-07 (2007), the stiffness at the 50th cycle of loading is considered the initial stiffness. The first 50 cycles are neglected to accommodate the initial setup and stabilization of the test. However, one might expect significant damage in the first 50 cycles of loading, especially at high temperatures and low loading frequency. The effect of a low loading frequency at 20 °C and 500 με is presented in Figure 7.

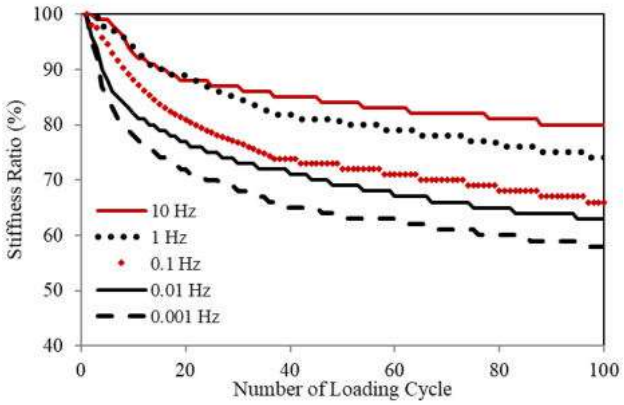

Figure 7 – A decrease in stiffness with a number of loading at 500 με

The decrease in stiffness ratio has been plotted due to loading between 0.0001 Hz and 10 Hz. The vertical dash line cuts the stiffness ratio at the 50th cycle of loading. It can be observed that the stiffnesses decrease to about 84 %, 80 %, 72 %, 69 %, and 63 % for the frequencies of 10 Hz, 1 Hz, 0.1 Hz, 0.01 Hz, and 0.001 Hz, respectively.

The stiffness decrease, especially at 0.1 Hz, 0.01 Hz, and 0.001 Hz, is significant and should not be neglected. In addition, the test stabilizes within 5 cycles of loading at a slow frequency, as shown in Figure 7.

Therefore, it is recommended that the initial stiffness should be considered at the 5th cycle of loading for the testing at 0.1 Hz, 0.01 Hz, and 0.001 Hz of loading.

3.4 Modulus of AC

The flexural modulus of AC is frequency-dependent in addition to the temperature effect. Figure 8 plots the moduli of AC tested at different temperatures at $1.16 \cdot 10^{-5}$ Hz, the frequency of the day-night temperature cycle, using the 4PB test at 200 με.

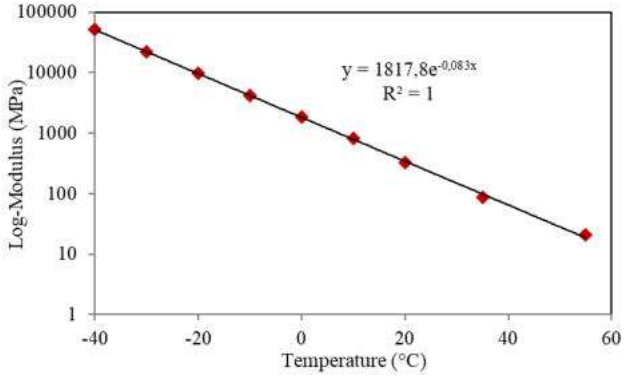

Figure 8 – Modulus of AC at the day-night temperature frequency of $1.16 \cdot 10^{-5}$ Hz

It shows that the stiffness of AC decreases with the expected decrease in frequency. It can also be observed that the modulus is very low compared to the typical values tested at 10 Hz of loading. For example, at 20 °C, the modulus of AC at $1.16 \cdot 10^{-5}$ Hz is 324 MPa, whereas the dynamic modulus of the same material at 10 Hz is 9970 MPa [17].

Therefore, while analyzing thermal fatigue damage, the stiffness should be considered at the frequency of $1.16 \cdot 10^{-5}$ Hz of loading.

4 Conclusions

This study determines AC's fatigue properties such as fatigue damage, dissipated energy, stiffness, and threshold stress-strain at a low loading frequency using 4PB test apparatus. Based on the study's findings, it can be said that fatigue damage increases at a low frequency of cyclic loading using AASHTO failure criteria, and the number of cycles at failure becomes stable at the frequency of equal to or lower than 0.01 Hz. The dissipated energy per cycle of loading decreases with a decrease in loading frequency, and the damage decreases at a low frequency of cyclic loading using the dissipated energy criteria. Considering initial stiffness at the 50th

cycle is not appropriate at a low loading frequency as the stiffness reduction is so considerable at slow loading.

The findings of this study can be used to simulate the behavior of AC better, and research can use the results of this study to develop a new testing program. The above conclusions are because the initial stiffness was considered at the 50th cycle of loading for testing at 10 Hz. For testing at a frequency lower than 10 Hz, the initial stiffness was taken at the 5th cycle of loading. In addition, the current study used a single SP mixture.

References

1. Mamlouk, M., Souliman, M., Zeida, W. (2012). *Optimum Testing Conditions to Measure HMA Fatigue and Healing Using Flexural Bending Test*. Transportation Research Board (TRB) 91st Annual Meeting, Washington, DC., January 22-26, 2012.
2. Tarefder, R., Bateman, D., Swamy, A. (2013). Comparison of fatigue failure criterion in flexural fatigue test. *Int. J. Fatigue*, Vol. 55, pp. 213-219.
3. Castro, M., Sanchez, J. A. (2006). Fatigue and healing of asphalt mixtures: Discriminate analysis 36 of fatigue curves. *J. Transp. Eng.*, Vol. 132(2), pp. 168-174.
4. Al-Khateeb, G., Shenoy, A. (2004). A distinctive fatigue failure criterion. *J. Assoc. Asph. Paving Technol.*, Vol. 73, pp. 585-622.
5. Al-Khateeb, G., Shenoy, A. (2011). A simple quantitative method for identification of failure due to fatigue damage. *Int. J. Damage Mech.*, Vol. 20, pp. 3-21.
6. Pronk, A. C. (2010). *Haversine Fatigue Testing in Controlled Deflection Mode: Is It Possible?* Transportation Research Board (TRB) 89th Annual Meeting 2010, paper no. 10-0485, Washington, D.C., January 10-14, 2012.
7. AASHTO T321-07 (2007). *Determining the Fatigue Life of Compacted Hot-Mix Asphalt Subjected to Repeated Flexural Bending*. Standard Specifications for Transportation Materials and Methods of Sampling and Testing, 27th Edition, American Association of State Highway and Transportation Officials, Washington, DC.
8. Islam, M. R. (2015). *Thermal Fatigue Damage of Asphalt Pavement*. Ph.D. Thesis, University of New Mexico.
9. Rowe, G. M. (1993). Performance of the asphalt mixtures in the trapezoidal fatigue test. *J. Assoc. Asph. Paving Technol.*, Vol. 62, pp. 344-384.
10. Pronk, A. C. (1997). *Comparison of 2 and 4-Point Fatigue Tests and Healing in 4-Point Dynamic Bending Test Based on the Dissipated Energy Concept*. Proc. of the 8th Inter Conference on Asphalt Pavements, Seattle, Washington, USA; August 8-14, 1997, pp. 987-994.
11. Carpenter, S. H., Shen, S. (2005). Application of the dissipated energy concept in fatigue endurance limit testing. *J. Transp. Res. Rec.*, Vol. 1929, pp. 165-173.
12. Daniel, J. S, Kim, Y. R. (2002). Development of a simplified fatigue test and analysis procedure using a viscoelastic continuum damage model. *J. Assoc. Asph. Paving Technol.*, Vol. 71, pp. 619-650.
13. Swamy, A. K. (2011). Evaluating mode of loading effect and laboratory fatigue performance of asphalt concrete using viscoelastic continuum damage mechanics. Ph.D. Thesis, University of New Hampshire.
14. Islam, M. R., Tarefder, R. A. (2015). Quantifying traffic- and temperature-induced fatigue damages of asphalt pavement. *Transp. Infrastruct. Geotech.*, Vol. 2, pp. 18-33, doi: 10.1007/s40515-014-0014-3.
15. Shen, S., Carpenter, S. H. (2005). Application of dissipated energy concept in fatigue endurance limit testing. *J. Transp. Res. Rec.*, Vol. 1929, pp. 165-173.
16. Ghuzlan, K. A., Carpenter, S. H. (2000). Energy-derived, damage-based failure criterion for fatigue testing. *J. Transp. Res. Rec.*, Vol. 1723, pp. 141–149.
17. Islam, M. R., Mannan, U. A., Rahman, A., Tarefder, R. A. (2014). Effects of reclaimed asphalt pavement on hot-mix asphalt. *J. Adv. Civ. Eng. Mater.*, doi: 10.1520/ACEM20130100.

JOURNAL OF ENGINEERING SCIENCES

Volume 9, Issue 1 (2022)

Kulikov O., Ratushnyi O., Moloshnyi O., Ivchenko O., Pavlenko I. (2022). Impact of the closed, semi-opened, and combined contra-rotating stages on volume loss characteristics. Journal of Engineering Sciences, Vol. 9(1), pp. D6-D13, doi: 10.21272/jes.2022.9(1).d2

Impact of the Closed, Semi-Opened, and Combined Contra-Rotating Stages on Volume Loss Characteristics

Kulikov O.[1[0000-0001-7222-8766]], Ratushnyi O.[1*[0000-0002-3525-0953]], Moloshnyi O.[2[0000-0002-2770-963X]], Ivchenko O.[1[0000-0002-4274-7693]], Pavlenko I.[1[0000-0002-6136-1040]]

[1] Sumy State University, 2, Rymskogo-Korsakova St., 40007, Sumy, Ukraine;
[2] Pompax Ltd., Wroclaw, Lower Silesia, Poland

Article info:
Submitted: February 20, 2022
Accepted for publication: June 9, 2021
Available online: June 14, 2022

***Corresponding email:**
o.ratushnij@pgm.sumdu.edu.ua

Abstract. The article is devoted to studying the contra-rotating stages with different impellers and blade discs. Determining the reduction of volumetric losses by modeling the contra-rotating stages in the software package ANSYS CFX. The work aimed to create and study the flow and characteristics: semi-open, closed impellers, and blade discs. As a result of the work, the following contra-rotating stages were determined and compared: the semi-opened impeller with the semi-opened blade disc; the closed impeller with the closed blade disc; the semi-opened impeller with the closed blade disc; the closed impeller with the semi-opened blade disc. As a result of research, fluid flows in contra-rotating stages and their characteristics in the form of pressure and efficiency were obtained. According to the obtained data, the expediency of using contra-rotating stages as a working body of the pump is written.

Keywords: pump, energy efficiency, semi-opened impeller, semi-opened blade disc.

1 Introduction

Today, centrifugal cantilever pumps are widely used in various industries. Such pumps are thoroughly researched and have the best values of pressure and efficiency that can only be achieved. A new branch in pump construction is the cantilever contra-rotating centrifugal pump.

The new pump has a modified flow part and a different principle of operation of energy transfer from the working bodies to the liquid. The pump's impeller rotates clockwise, and the blade disc rotates counterclockwise. This creates a contra-rotating effect between the discs (bd), which transmits much more energy to the fluid than conventional centrifugal pumps [1–9].

Due to speed changes, the pump can create a much higher pressure. This, in turn, leads to increased volumetric losses that occur in the area between the cover disc and the pump housing. A leaking seal can only reduce volumetric losses, not eliminate them. However, exploring the contra-rotating stage with different types of impellers is an option to avoid volumetric losses.

The main advantage of semi-opened and opened impellers is the absence of losses caused by friction of the outer surfaces of the discs and fluid in the pump casing.

There is also no volume loss between the pump casing and the cover disc. However, the use of such impellers reduces efficiency. The channels in the impeller are formed by the blades and a case wall (Figure 1).

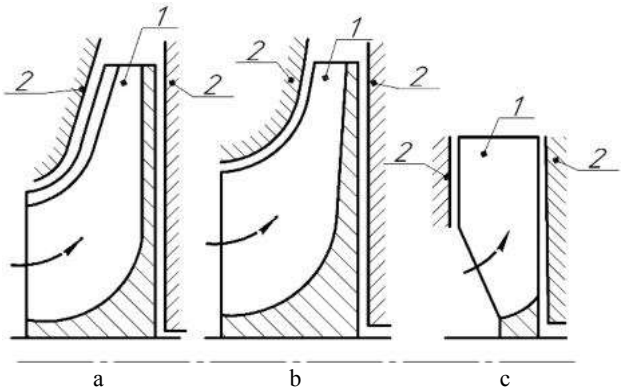

Figure 1 – Schematic representation of the flowing part with impellers of different types: a – closed impeller; b – semi-opened impeller; c – opened impeller; 1 – blade; 2 – housing of the pump

2 Literature Review

Centrifugal pumps mostly use closed impellers. However, nowadays, the impellers are divided into closed according to the design of the discs (Figure 2a), semi-opened (without cover disc, Figure 2b), and opened (without cover disc and part of the main disc (Figure 2c).

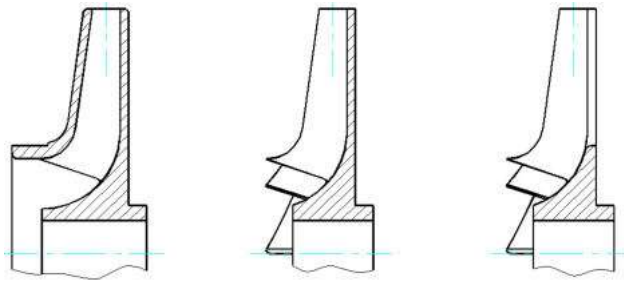

a b c

Figure 2 – Types of impellers depending on the design of the discs: a – opened; b – semi-opened; c – closed

The impeller type choice depends on the pump's purpose and operating parameters. According to the design, the closed impellers (Figure 2a) have front (cover) and rear (main) discs. The semi-opened impellers (Figure 2b) do not have a cover disc, and the blades are attached only to the main disc. The opened (Figure 2c) impellers have attached bushings with blades.

The contra-rotating effect works as follows. For ease of perception, the impeller and blade disc is delivered to a distance "a" (Figure 3).

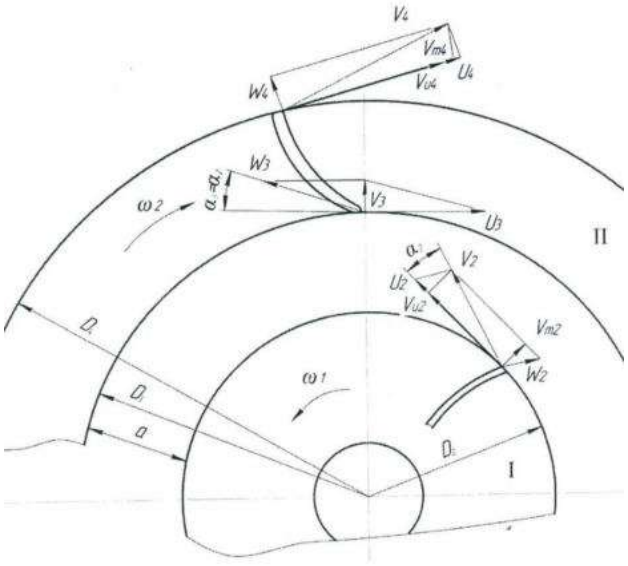

Figure 3 – Flow kinematics in contra-rotating centrifugal systems

Velocity vectors and their components are given for the axisymmetric flow scheme and conditions $\omega_I = -\omega_{II}$ (the gratings rotate in opposite directions with the same angular velocity). In addition, at the entrance to the first grid, selected conditions without circulating leakage. The flow at the entrance to the second grid is coming out of the first. It has a significant moment (twist), created by the first grid ($v_{u2} \cdot r_2$). Simultaneously, its direction is opposite to the second grid's rotation direction.

It should also be noted that the second grid's blades move towards the current coming from the first grid, changing its momentum in a very short time. And this, according to the moment theorem, causes a sharp increase in the force of interaction between the solid surface of the blade and the current that attacks it. This, obviously, leads to a significant increase in the intensity of the energy transfer process. Considering the working process of the contra-rotating blade system and, first of all, the work of the second grid, an assumption arises that the first grid, created at the entrance to the second flow with significant negative circulation, Γ_2 thus provides an intense contra-rotating for the blades of the second rotor (they actively interact). This flow's kinetic energy quickly passes into the state of pressure energy, which resembles the working process in hydraulic machines of the active principle of the action (for example, in jet bucket turbines). As the pressure increases, the volumetric losses will also increase.

In Figure 4, fluid flow and volumetric losses are shown in two contra-rotating stages. The 1st stage (Figure 4a) has cover discs, on the 2nd (Figure 4b) – they are missing.

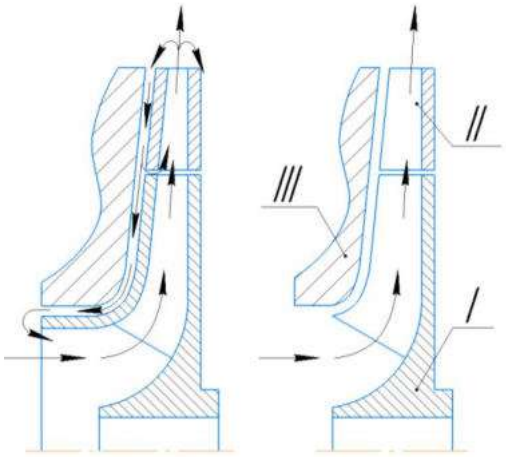

a b

Figure 4 – Volumetric losses in contra-rotating stages: a – the closed type, b – the semi-opened type

Thus, the volume loss can be observed only in Figure 4a.

The study's primary purpose is to increase the energy efficiency of the contra-rotating pump by constructing the impeller with the semi-opened and closed working bodies using the method of numerical research. For this purpose, the following methods were used:

– a study of the flow part of the pump using the known design of the semi-opened and the closed impeller;

– design of impellers for contra-rotating pump with the semi-opened and closed impeller and vane disc of different designs;

– conducting a numerical study of the flow part of the pump using the proposed changes;

– evaluation of the obtained results.

3 Research Methodology

The object of the study is the contra-rotating stage with the base impeller of the pump CNS 180-1900. The following contra-rotating stages were created to reduce volumetric losses. The contra-rotating stages (Figure 5) have impeller I and blade disc II.

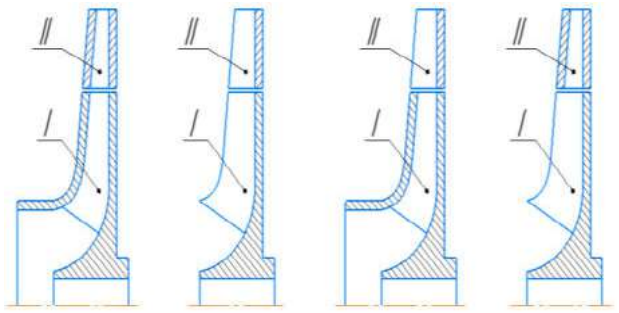

a b c d

Figure 5 – Contra-rotating stages: a – closed impeller and closed blade disc; b – semi-opened impeller with semi-opened blade disc; c – closed impeller and semi-opened blade disc; d – semi-opened impeller and closed blade disc

The following contra-rotating stages have been created for calculations: the closed impeller with the closed blade disc (Figure 5a); the semi-opened impeller with the semi-opened blade disc (Figure 5b); the closed impeller with the semi-opened blade disc (Figure 5c); the semi-opened impeller with the closed blade disc (Figure 5d). Each stage had an impeller with eight blades. A distinctive feature of such stages was the presence of the cover disc and the number of blades in the blade disc, which in turn were equal to 8, 10, and 12 pcs.

In the beginning, the blades of the contra-rotating stages (Figure 6a) with optimal angles of attack of 9° and output of 12° were calculated. With the help of the Solid Works software product (Figure 6b), 3D models of flowing parts of various blades and impellers were created. With the help of ANSYS CFX, the created models were broken on the surface (Figure 6c) and created a calculation grid (Figure 6d).

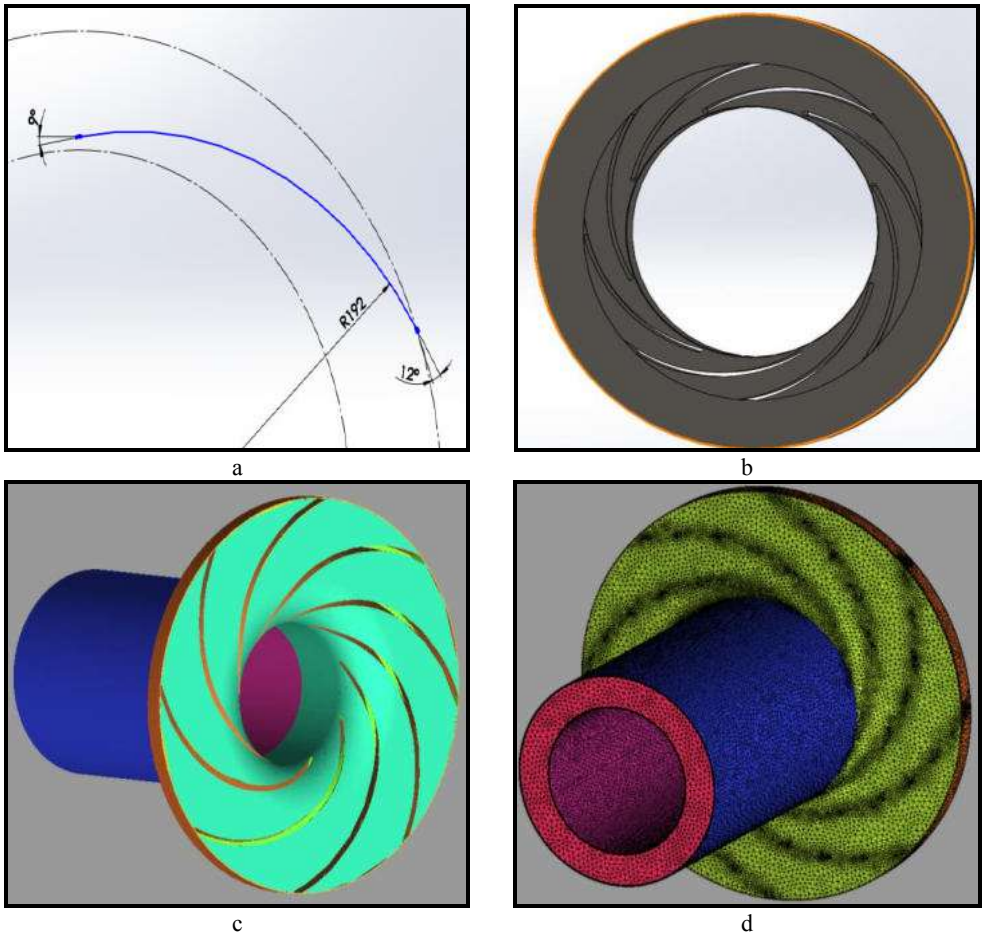

a b c d

Figure 6 – stages of research: a – calculation of blades; b – the creation of 3D models; c – breaking surfaces; d – creating a grid; e – setting boundary conditions; f – numerical calculation

The next step for each model was to set the conditions for input, output, the configuration of the pumped medium, and set specific boundary conditions (Figure 7a). After that, the numerical calculation of the contra-rotating stages was performed (Figure 7b).

The university version of software product ANSYS CFX was used based on the numerical solution method of the fundamental hydromechanics laws [10, 11]: equations of motion of a viscous fluid together with the equation of inseparability.

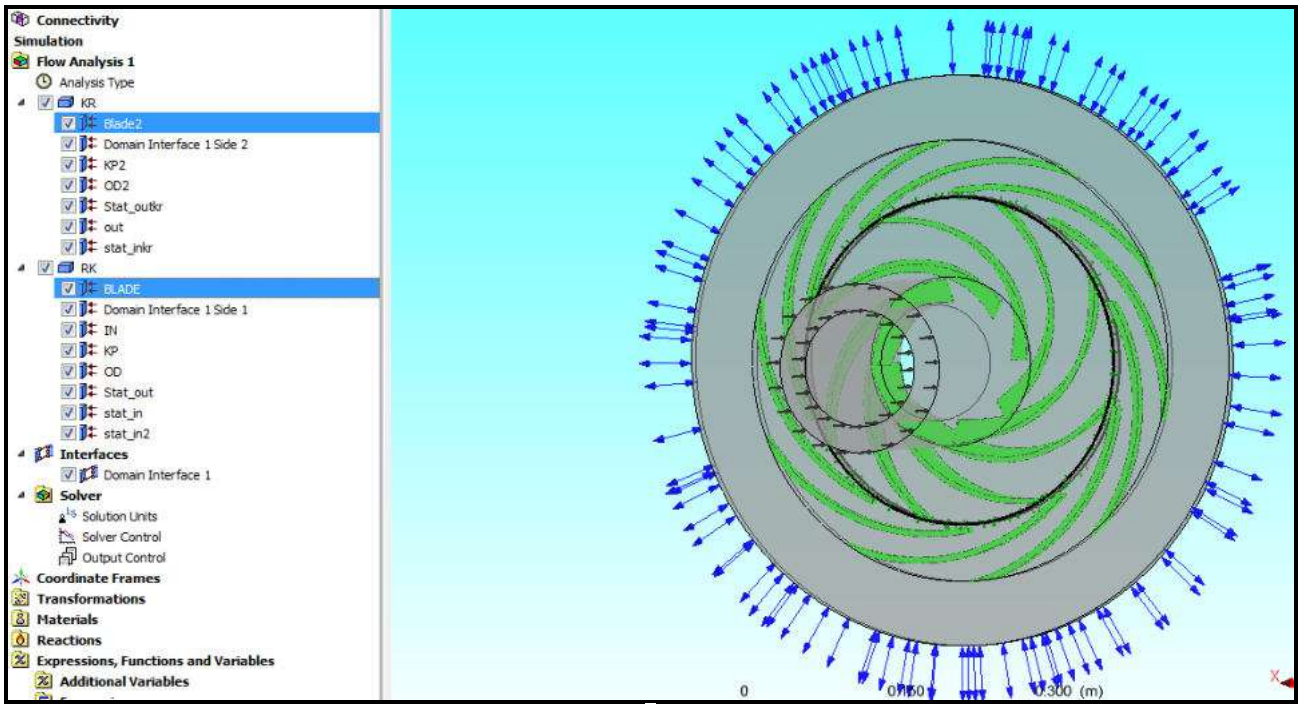

a

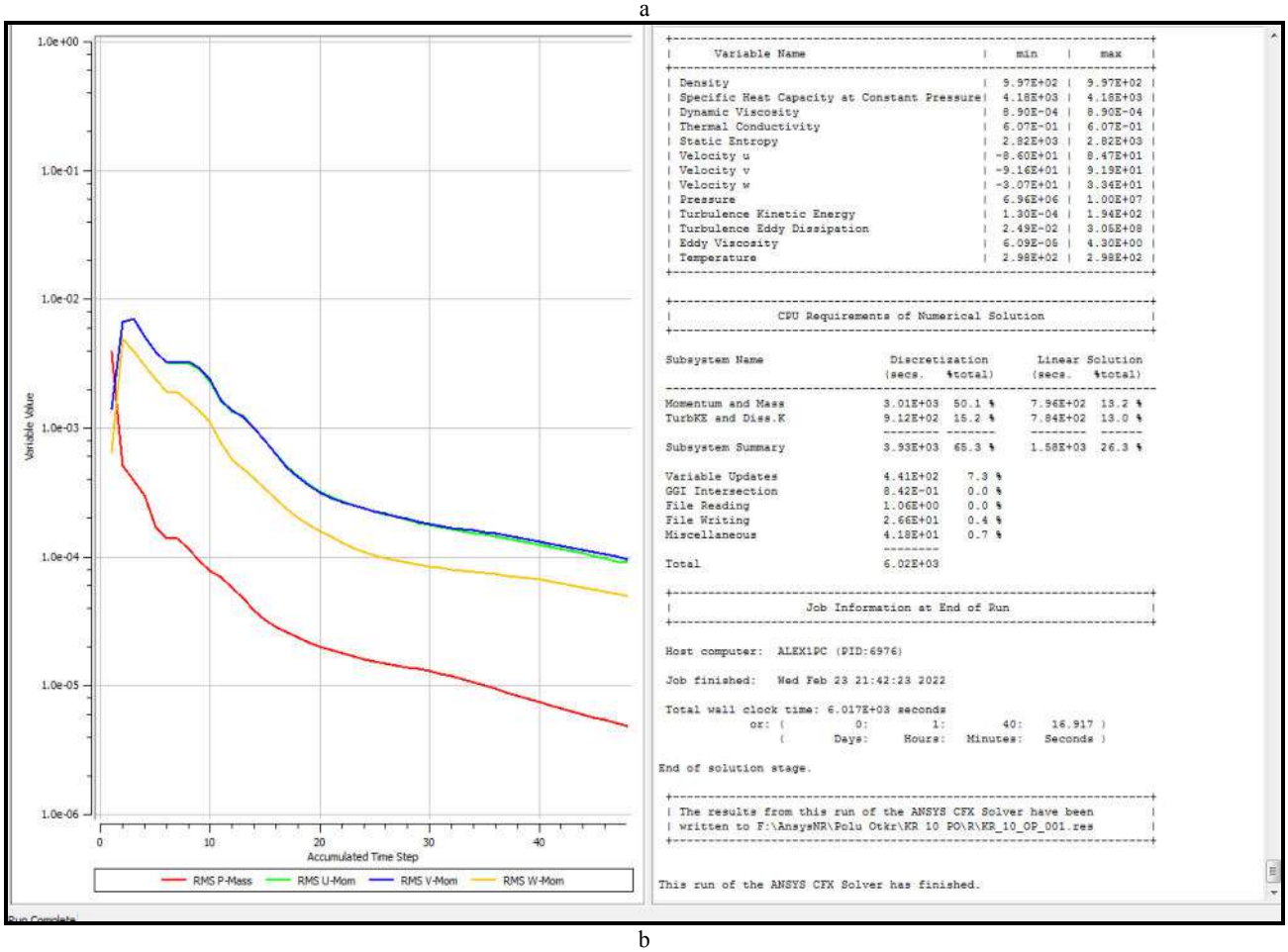

b

Figure 7 – Boundary conditions (a) and numerical calculations (b)

This is a sufficient condition for the validity of the application of the results of numerical research.

It should be noted that ANSYS CFX was repeatedly tested in solving the problems of pump construction, and the discrepancy between numerical and physical modeling results does not exceed 5 %.

Therefore, this software product is suitable for solving the stated research problem. As a result of research the liquid flows in contra-rotating stages, and their characteristics in the form of pressure and efficiency are received.

4 Results

To begin with, the basic impellers without blade discs were calculated (Figure 8). The characteristics of the closed and the semi-opened impeller were obtained to clarify and compare characteristics with contra-rotating stages.

The closed impeller (Figure 8a) has the following parameters: head – 149 m; energy efficiency – 95 %.

The semi-opened impeller (Figure 8b) has the following parameters: head – 113 m; energy efficiency – 76 %.

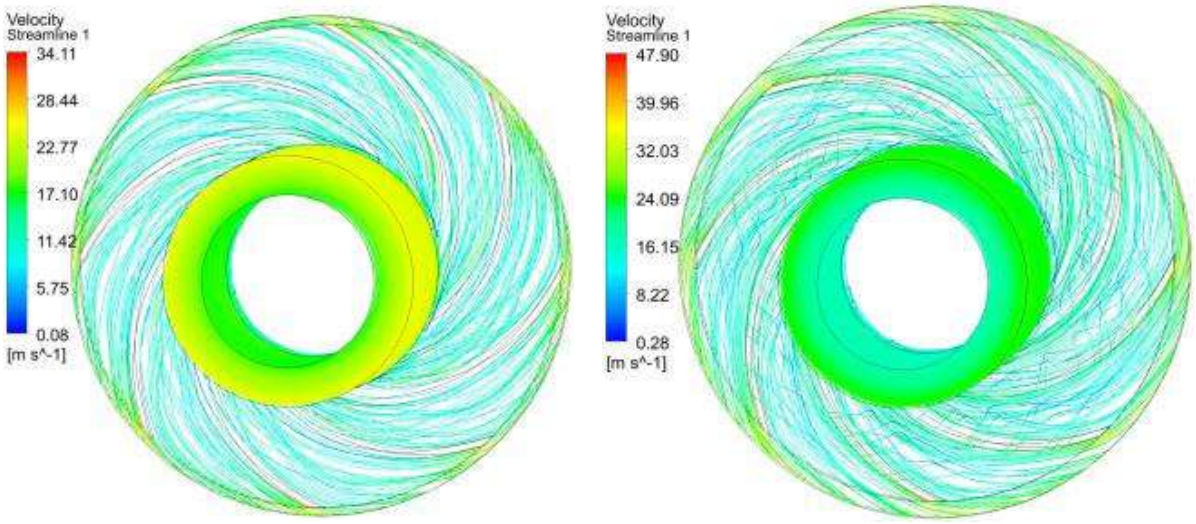

a b

Figure 8 – Closed (a) and semi-open (b) impellers

The fluid flow in the closed wheel is stable, without vortices. The maximum flow rate is 19.3 m/s. As for the semi-opened impeller, we can see fluid flow between the blade channels, leading to vortex formation and reduced efficiency. The maximum flow rate is 26.6 m/s. In addition to the flow of fluid between the housing and the blades, the flow is also stable.

The number of blade discs and impellers was created to study the characteristics of the steps. The closed and the semi-opened contra-rotating stages with the same number of blades were compared with each other.

Withing the 1st comparison, parameters of the closed stage are presented in Figure 9a: the number of blades – 8; head – 382 m, energy efficiency – 56 %. Parameters of the semi-opened stage (Figure 9b): the number of blades $z = 8$; head – 228 m; energy efficiency – 31 %.

After the 2nd comparison, parameters of the closed stage are presented in Figure 10a: the number of blades – 10; head – 357 m; energy efficiency – 55 %. Parameters of the semi-opened stage (Figure 10b): the number of blades – 10; head – 231 m; energy efficiency – 31 %.

Within the 3rd comparison, parameters of the closed stage are presented in Figure 11a: the number of blades – 12; head – 364 m; energy efficiency – 55 %. Parameters of the semi-opened stage (Figure 11b): the number of blades – 12; head – 225 m; energy efficiency – 33 %.

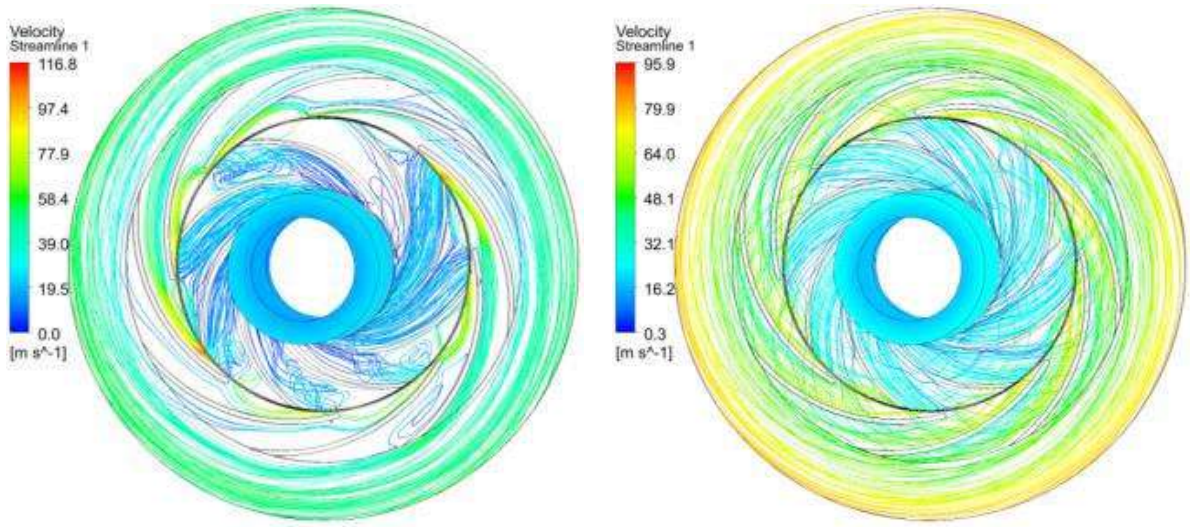

a b

Figure 9 – Closed (a) and semi-open (b) impellers ($z = 8$)

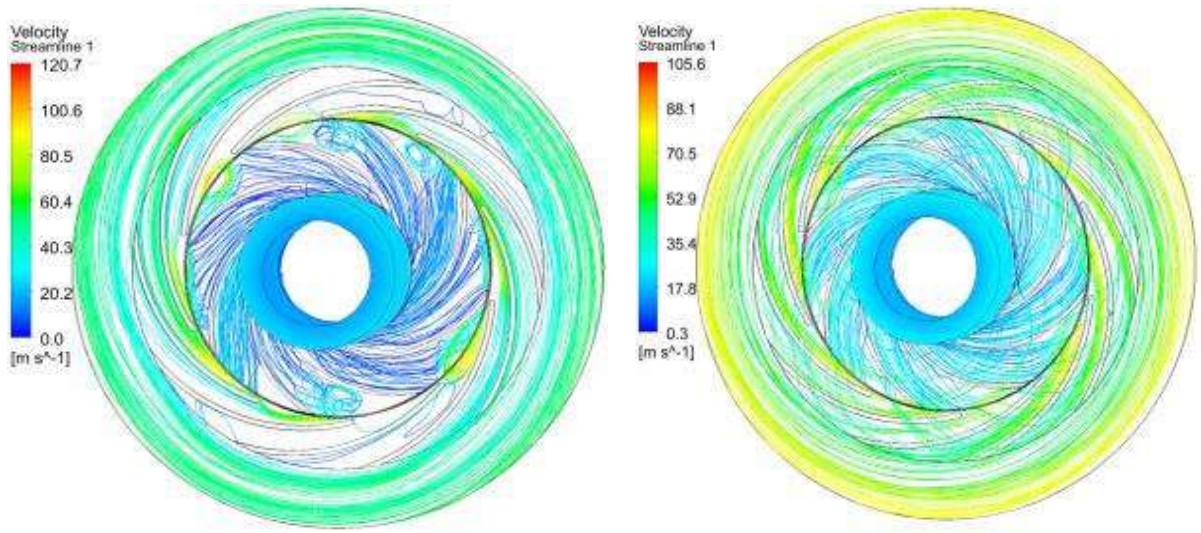

a b

Figure 10 – Closed (a) and semi-open (b) impellers (z = 10)

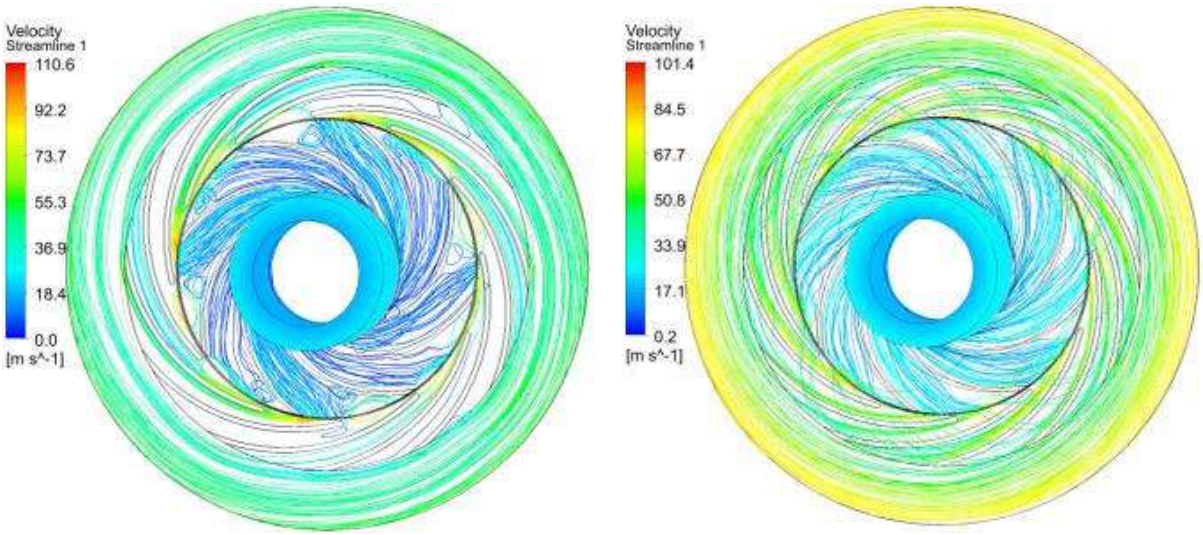

a b

Figure 11 – Closed (a) and semi-open (b) impellers (z = 12)

After the obtained results, a solution was proposed to combine impellers and blade discs of different designs (Figures 12, 13). After considering their pressure and energy efficiency, the interaction of different stage elements becomes essential. For this study, two contra-rotating stages were taken with the number of blades 10 and 12, respectively.

The 1st study with combined elements presents parameters of the closed contra-rotating stage with 10 blades (Figure 12a). The impeller is closed, and the blade disc is semi-opened: head – 286 m., energy efficiency – 36 %. Parameters of the semi-opened contra-rotating stage with 10 blades are presented in Figure 12b). The impeller is semi-opened, and the blade disc is closed: head – 319 m; energy efficiency – 45 %.

The 2nd study with combined elements presents parameters of the closed contra-rotating stage with 12 blades (Figure 13a). The impeller is closed, and the blade disc is semi-opened: head – 256 m; energy efficiency – 37 %.

Parameters of the semi-opened contra-rotating stage with 12 blades (Figure 13b). The impeller is semi-opened, and the blade disc is closed: head – 328 m; energy efficiency – 47 %.

Characteristics of the contra-rotating stage of different designs are summarized in Table 1.

Table 1 – Characteristics of contra-rotating stage of different design

Number of blades	Head, m / Energy efficiency, %			
	Semi-opened blade disc / semi-opened impeller	Closed blade disc / Closed impeller	Semi-opened blade disc / semi-opened impeller	Closed blade disc / Closed impeller
8	228 / 31	382 / 56	N/A	N/A
10	231 / 31	366 / 55	319 / 45	259 / 36
12	225 / 33	364 / 55	328 / 47	256 / 37

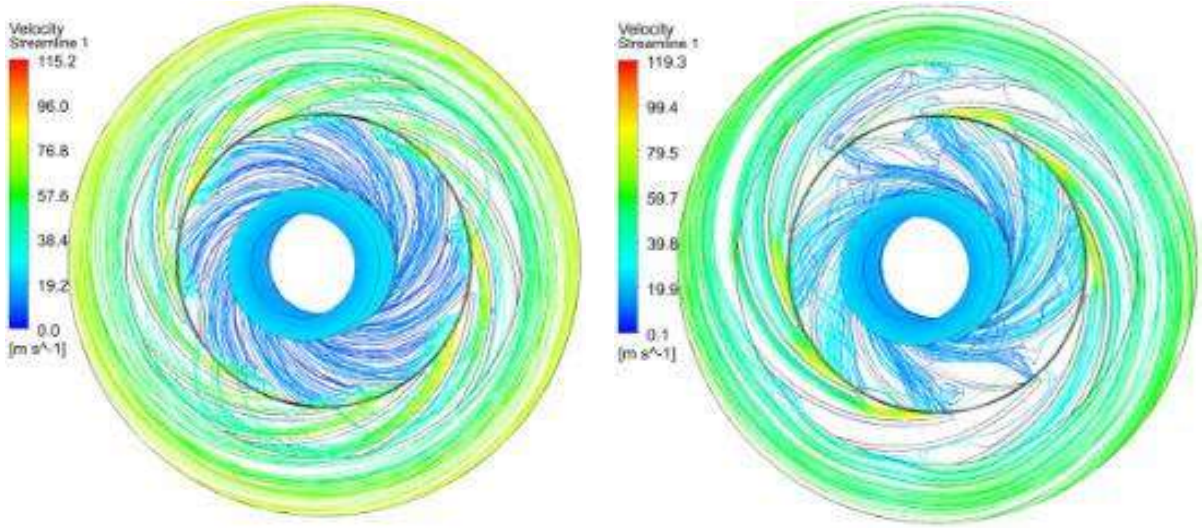

a b

Figure 12 – Impellers with $z = 10$: a – closed impeller and semi-opened blade disc; b – semi-opened impeller and closed blade disc

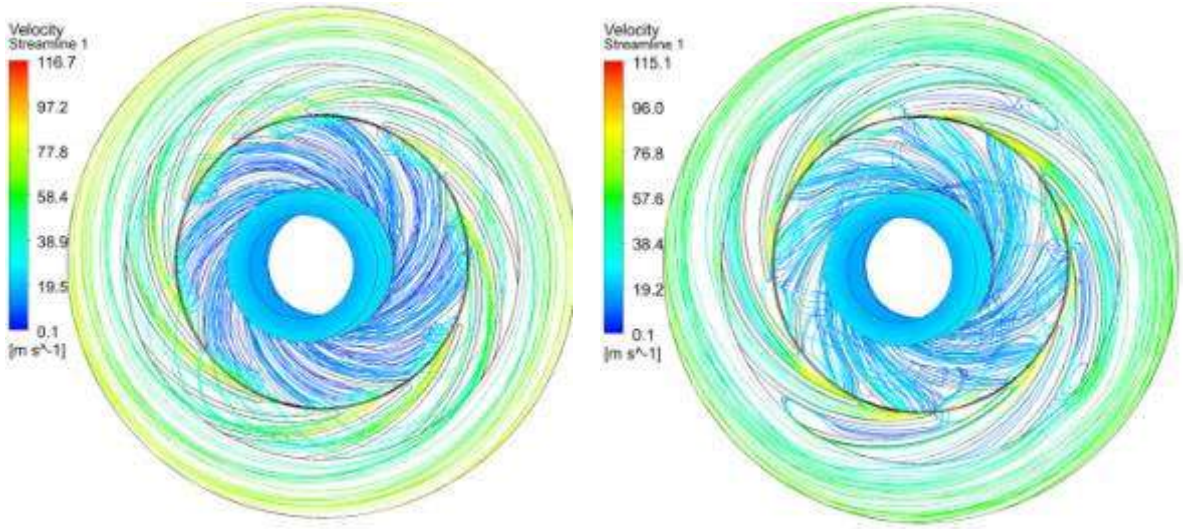

a b

Figure 13 – Impellers with $z = 12$: a – closed impeller and semi-opened blade disc; b – semi-opened impeller and closed blade disc

5 Discussion

As we can see from the results, fluid flow in closed stages has vortex formation (Figures 9a, 10a, and 11a). This all leads to lower efficiency. In semi-opened stages, everything is much better (Figures 9b, 10b, and 11b). The flow of fluid is constant, but there is a flow of fluid from one between the blade channels to another.

Having obtained the characteristics of contra-rotating stages, we can say that they have higher pressure characteristics than the basic impellers, although inferior to them in efficiency. Compared with the semi-opened and closed stage, without considering the number of blades, the semi-opened contra-rotating stage has worse characteristics than the closed. In comparison with separately the closed and the semi-opened contra-rotating stage, we can see that the pressure and efficiency of this blade shape do not change.

Although the most significant pressure in the closed contra-rotating stage is achieved due to the stage, which has eight blades.

For combined impellers with blade disc, in the case of the semi-opened impeller and the closed blade disc system (Figures 12b, 13b), we got much better performance than the closed impeller and the semi-opened blade disc (Figures 12a, 13a).

Comparing a completely closed contra-rotating stage with a stage where the impeller is opened and the blade disc is closed, we can say that the pressure and efficiency have decreased, but thanks to this, we have removed the volumetric losses. Such good pressure characteristics can be explained by the fact that the closed blade disc is at the same time a guide device for the fluid after the semi-opened impeller. The fluid in the disc does not flow between the blade channels, and there is a formation of flow at the outlet.

6 Conclusions

As a result of research, it was found that it is better to use closed steps to get the highest pressure. Fully the semi-opened steps have the worst characteristics. Typically, such impellers are used for liquids with solid impurities, but how this will affect the operation of the contra-rotating stage is unknown. Such contra-rotating stages are best used for pure liquid without impurities. Using the combined contra-rotating stage to prevent massive losses did not live up to expectations. Volumetric losses are much less than losses on efficiency and pressure; therefore, they can be neglected.

Many unexplored factors in this area affect the nature of the flow and the pressure and energy characteristics of the contra-rotating stages. The research in this area is just beginning, and there will be further calculations of the contra-rotating stage.

7 Acknowledgment

The research was carried out at the Research and Educational Center for Industrial Engineering within the R&D project "Fulfillment of tasks of the perspective plan of development of a scientific direction "Technical sciences" Sumy State University" by the Ministry of Education and Science of Ukraine (State reg. no. 0121U112684).

References

1. Kulikov, A. A., Ratushnyi, A. V., Kovaliov, I. A., Mandryka, A. S., Ignatiev, A. S. (2021). Numerical study of the centrifugal contra rotating blade system. *Journal of Physics: Conference Series*, Vol. 1741, 012008, doi: 10.1088/1742-6596/1741/1/012008.
2. Cao, L., Watanabe, S., Momosaki, S., Imanishi, T., Furukawa, A. (2013). Low speed design of rear rotor in contra-rotating axial flow pump. *International Journal of Fluid Machinery and Systems*, Vol. 6(2), pp. 105-112, doi: 10.5293/IJFMS.2013.6.2.105.
3. Cao, L., Watanabe, S., Honda, H., Yoshimura, H., Furukawa, A. (2014). Experimental investigation of blade-to-blade pressure distribution in contra-rotating axial flow pump. *International Journal of Fluid Machinery and Systems*, Vol. 7(4), pp. 130-141, doi: 10.5293/IJFMS.2014.7.4.130.
4. Cao, L. L., Watanabe, S., Imanishi, T., Yoshimura, H., Furukawa, A. (2013). Blade rows interaction in contra-rotating axial flow pump designed with different rotational speed concept. *IOP Conference Series: Materials Science and Engineering*, Vol. 52(2), doi: 10.1088/1757-899X/52/2/022004.
5. Furukawa, A., Takano, T., Shigemitsu, T., Okuma, K., Watanabe, S. (2006). Blade rows interaction of contra-rotating axial flow pump in pressure field on casing wall. *JSME International Journal, Series B: Fluids and Thermal Engineering*, Vol. 49(3), pp. 670-677, doi: 10.1299/jsmeb.49.670.
6. Shigemitsu, T., Furukawa, A., Watanabe, S., Okuma, K., Fukutomi, J. (2008). Internal flow measurement with LDV at design point of contra-rotating axial flow pump. *Transactions of the Japan Society of Mechanical Engineers, Part B*, Vol. 74(5), pp. 1091-1097, doi: 10.1299/kikaib.74.1091.
7. Shigemitsu, T., Watanabe, S., Furukawa, A., Okuma, K. (2005). Air/water two-phase flow performance of contra-rotating axial flow pump and rotational speed control of rear rotor. *Proceedings of 2005 ASME Fluids Engineering Division Summer Meeting, FEDSM2005*, pp. 912-917, doi: 10.1115/FEDSM2005-77002.
8. Zhamalov, A. Z., Obozov, A. D., Issaev, S. A., Kunelbayev, M. M., Baikadamova, L. S. (2013). Simulation model of two-rotor wind turbine with counter-rotation. *World Applied Sciences Journal*, Vol. 22(2), pp. 215-219, doi: 10.5829/idosi.wasj.2013.22.02.19313.
9. Xiuli, W., Bin, L., Yang, L., Yan, Z., Rongsheng, Z., Yun, L., Qiang, F. (2020). Hydraulic optimization of two-way counter-rotating axial flow pump turbine. *Frontiers in Energy Research*, Vol. 8, 577232, doi: 10.3389/fenrg.2020.577232.
10. Barbarelli, S., Castiglione, T., Florio, G., Scornaienchi, N. M., Zupone, G. L. (2016). Design and numerical analysis of a double rotor turbine prototype operating in tidal currents. *Energy Procedia*, Vol. 101, pp. 1199-1206, doi: 10.1016/j.egypro.2016.11.162.
11. Rajeevalochanam, P., Sunkara, S. N. A., Ramana Murthy, S. V., Kumaran, R. S. (2020). Design of a two spool contra-rotating turbine for a turbo-fan engine. *Propulsion and Power Research*, Vol. 9(3), pp. 225-239, doi: 10.1016/j.jppr.2020.08.001.

JOURNAL OF ENGINEERING SCIENCES

Volume 9, Issue 1 (2022)

Mandryka A., Majid A. P., Ratushnyi O., Kulikov O., Sukhostavets D. (2022). Ways for improvement of reverse axial pumps. Journal of Engineering Sciences, Vol. 9(1), pp. D14-D19, doi: 10.21272/jes.2022.9(1).d3

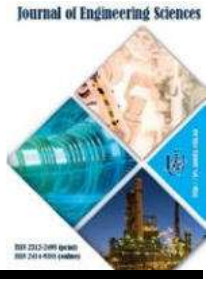

Ways for Improvement of Reverse Axial Pumps

Mandryka A.[1*], Majid A. P.[2], Ratushnyi O.[1[0000-0002-3525-0953]], Kulikov O.[1[0000-0001-7222-8766]], Sukhostavets D.[1]

[1] Department of Applied Hydroaeromechanics, Sumy State University, 2, Rymskogo-Korsakova St., 40007, Sumy, Ukraine;

[2] Katex International Suppliers LLC, 2717, Commercial Center Blvd, Katy, TX 77494, USA

Article info:

Submitted: January 27, 2022

Accepted for publication: June 10, 2021

Available online: June 15, 2022

***Corresponding email:**

a.mandryka@pgm.sumdu.edu.ua

Abstract. The article is devoted to a pilot study of the reverse-bladed pump. The characteristics of the reverse bladed pump are the identical parameters on flow, the head, power, energy efficiency on direct and the return operating modes (at rotation of a rotor of the pump both in one and to the opposite side). The model reversible axial pump with two impeller versions was tested on an experimental bench. The impellers were distinguished by the shape of the profile in the blade sections. The model reversible pump was structurally a reversible axial impeller placed in a cylindrical chamber. Studies were carried out at different angles of rotation of the impeller blades. The power characteristics of tested versions of the pump (impeller) at the design and under loading (unstable operation) modes are given. Low efficiency of the tested versions of the reversible pump compared to the conventional axial pumps is noted, primarily due to the strong influence of the secondary gradients of the pressure factor. The second reason is the profile separation of the flow from the blade surface, to which the tested reverse pump screens are predisposed.

Keywords: reversible pump, fluid flow, pressure head, power, energy efficiency.

1 Introduction

In recent years, the development of some industries has required the creation of a fundamentally new class of the centrifugal (dynamic) pumps, so-called reverse pumps, which have the same parameters in terms of flow, pressure, power, efficiency, cavitation qualities in direct and reverse operation modes of operation, i.e., when the rotor rotates in one or the opposite direction.

The reversible pumps are widely used abroad in the chemical, textile industry, shipbuilding, and hydraulic systems of tidal power plants. In domestic practice, there is no production of such pumps, except for two prototypes, which the Kharkiv Polytechnic Institute developed.

Creating reversible dynamic pumps is a complex technical task (due to a number of their features). At the same time, the domestic practice does not have sufficient information on the calculation and design of such pumps, especially their boost elements.

The issue needs a comprehensive, in-depth examination. All this made this research necessary, its tasks and directions, mainly the creation (development) of boost elements.

For this purpose, two reverse impellers RK-1 and RK-2, with specific speed $n_s = 800$, were designed and tested on an experimental bench.

The task of the tests was to study the working process of the impeller for their improved hydraulic qualities. The working process was analyzed based on the characteristics of the elementary grids located on the cylindrical surfaces of the current and the total (integral) characteristics of the impellers.

The impeller RK-1 is designed by the lifting forces method with the correction for the influence of the grid of infinitely thin plates.

The impeller RK-2 is obtained by design optimization on the computer using the straightforward task of lattice theory [1–4], a radical multi-factor experiment [5], and the calculation of profile losses [6–10].

During the design, both impellers were limited: the outer diameter $D = 0.23$ m, the sleeve is cylindrical, the hub-to-tip ratio of 0.61, the radial component of the input velocity $V_{1u} = 0$, and the constant pressure head H along with radius r.

2 Research Methodology

A particular S-shaped profile symmetrical relative to its geometric center is taken as vane sections for RK-1 [10, 11] (a necessary condition for ensuring the identity of the kinematics of the flow during reversal) (Figure 1).

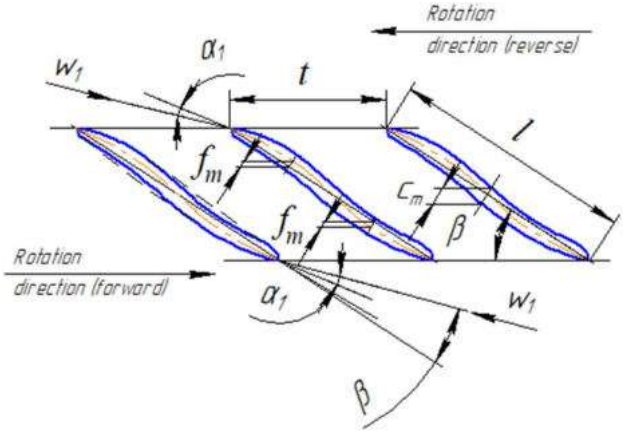

Figure 1 – The reverse pumping grid

For the impeller RK-2, a symmetrical profile [12] has been adopted (Figure 1, dashed line).

The following signatures are used Q – flow rate, m^3/s; H – pressure head, m; n – rotational speed, s^{-1}; r – location radius, m; l – blade length, m; t – blade step, m; β – the angle of the profile installation in the grid, °; α_1 – the angle-of-attack, °; W_1 – relative velocity at the inlet, m/s; f_m – maximum relative curvature of the profile, m; c_m – maximum relative profile thickness, m.

The design parameters of the impellers are presented in Table 1.

The impellers were tested on a hydraulic bench in a cylindrical chamber. The liquid was supplied to and away from the impellers in the axial direction.

The hydraulic characteristics of the tested impellers are presented in Figure 2.

The characteristics were taken at the calculated position of the vane with a rotation angle of $V = 0$. Since the RK-1 did not provide the design parameters for Q and H, it was also tested at $V = 4°$.

The characteristics of the elementary reversible grids are obtained by probing the flow before the impeller and behind them with five-channel ball probes.

Table 1 – The design parameters of the impellers

Impeller	Q, m^3/s	H, m	n, s^{-1}	Section view	r, m	l, m	l/t	β, °	α_1, °	f_m	c_m/l
RK-1	0.17	10	50	Peripheral	0.1150	0.200	1.39	12.8	2.8	0.020	0.040
				Mid	0.0925	0.185	1.59	17.5	5.3	0.030	0.060
				Root	0.0700	0.155	1.76	27.6	11.5	0.040	0.080
RK-2	0.17	10	50	Peripheral	0.1150	0.180	1.00	15.4	4.6	0.015	0.045
				Mid	0.0925	0.160	1.10	19.4	6.0	0.022	0.070
				Root	0.0700	0.140	1.30	26.0	8.6	0.030	0.095

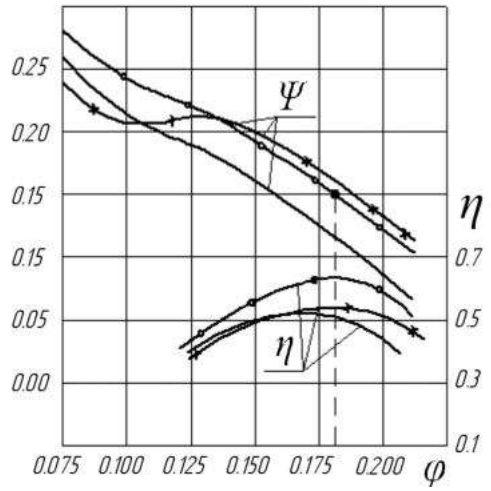

Figure 2 – Hydraulic characteristics of reversible impellers: Ψ – actual head coefficient; η – efficiency; φ – estimated flow (RK-1, $V = 0°$; RK-1, $V = 4°$; RK-2, $V = 0°$)

Probing was carried out in a wide range of flow changes, including such characteristic modes as the calculated mode (mode A), the optimal efficiency mode, and the unstable operation mode (mode B; In the area of pressure-flow characteristic "failure").

Simultaneously, the rotation frequency $n = 50\ s^{-1}$ was kept constant, provided the Reynolds number (flow turbulence) (Reynolds number $Re = (4.6–5.6)\cdot10^4$ was calculated from the total flow rate and diameter of the probe ball). The indicated value of Re was in the range of $(0.04–1.50)\cdot10^5$, i.e., the condition for the constancy of the calibration coefficients of the ball probes was fulfilled [12].

The probes measured the flow in front of the impeller at a distance of $0.65t$ pitch from the blade's leading edge and behind the impeller at a distance of pitch from the trailing edge, where the velocities are almost equalized. The measurements were carried out at eight points along the radius. The extreme measurement points were spaced from the chamber walls and the sleeve by a distance equal to the diameter of the probe ball.

The reliability of the experimental data was verified by comparing the flow rate determined by probe measurements:

$$Q_3 = 2\pi \int_{r_{вт}}^{R} V_z(r) r dr, \quad (1)$$

where V_z – the flow rate component of velocity; R – the outer radius of the impeller, at the inlet and outlet of the impeller with the corresponding flow rates measured by the narrowing device (diaphragm), Q. Typically, the divergence between Q_3 and Q_c was ±3 % before the impeller and ±5 % behind it.

Based on the probing results, the parameters of reverse wheels were determined, particularly the discharge flow coefficient:

$$\varphi = \frac{4Q_3}{\pi D^2(1-d_{вт}^2)u_R}, \quad (2)$$

the head coefficient:

$$\psi = \frac{2gH}{u_R^2}, \quad (3)$$

and energy efficiency parameters of the elementary grids, i.e., the discharge flow coefficient at input "1" and output "2", respectively:

$$\varphi_{1k} = \frac{V_{1z}(r)}{u_R};\ \varphi_{2k} = \frac{V_{2z}(r)}{u_R}, \quad (4)$$

where $V_{1z}(r)$, $V_{2z}(r)$ – the flow rate component of velocity on the radius of the grid r;

The head coefficient:

$$\psi_k = \frac{2gH_k(r)}{u_R^2}; \quad (5)$$

the grid efficiency:

$$\eta_k = \frac{H_k(r)}{H_p(r)}, \quad (6)$$

where $H_k(r)$ – actual increment of the flow specific energy at radius r, m; $H_p(r)$ – the elementary grid head determined by the flow calculation, m.

Since the non-uniformity of the flow was considered increased, the radius of the jet behind the impeller was r_2 along with the radius of the jet in front of the impeller r_1 from the equal flow rates between the jet and the chamber wall. The parameters of the elementary grid were determined in the cylindrical section at the middle radius between r_1 and r_2. The resulting error was not taken into account, as the radii differed insignificantly and could not make inaccuracies in the calculation exceeding the error of the probe measurements themselves.

In the calculation of the grid parameters, we used the adjusted axial velocities, for which the velocities V_{1z} and V_{2z} were multiplied by the coefficients, respectively:

$$\lambda_1 = \frac{Q_c}{2\pi\int_{r_b}^{R} V_{1z}(r)rdr}; \quad (7)$$

$$\lambda_2 = \frac{Q_c}{2\pi\int_{r_b}^{R} V_{2z}(r)rdr}, \quad (8)$$

where r_b – bushing's radius, m.

The noted parameters of the elementary grids were represented by functions of the relative height of the channel $(r - r_b)/(R - r_b)$ angle of attack α_1.

The parameters of individual elementary grids, presented as a function of the relative height of the channel, made it possible to judge the matching of the blade sections in the radial direction, and the parameters represented as a function of the angle of attack α_1, showed changes in the various parameters with varying flow rates.

In particular, to avoid subjective curves in drawing graphs, Figures 3–5 provided a computer selection of the degree of the averaging polynomial.

3 Results and Discussion

Figure 2 shows the total characteristics of the impellers "$\Psi - \varphi$" and "$\eta - \varphi$". As follows from the figure, for RK-1 with the calculated flow coefficient $\varphi = 0.18$, the experimental value of the Head Coefficient $\Psi = 0.12$ is much less than the calculated $\Psi = 0.15$. The divergence is approximately 20 %. This calls into question the correctness of the lifting forces method for calculating the reverse grids of S-shaped profiles if the grid influence is considered according to the Schilzanzl graphs [1]. Using the method in this form does not provide the required impeller head.

The impeller RK-1 achieves the design head values with lower (compared to the calculated) flow rate factors and higher efficiency. In other words, the liquid receives the necessary energy increment at more significant than the calculated angles of attack α_1, and this process is performed with less hydraulic losses.

When the blades turn from $V = 0°$ to $V = 4°$, the impeller pressure increases (as expected). So, in the mode of calculated flow ($\varphi = 0.18$), the actual head coefficient $\Psi = 0.16$ against calculated $\Psi = 0.15$. The efficiency also increased from $\eta = 0.51$ to $\eta = 0.34$. However, the shape of the head-flow characteristic is deteriorating: its "failure" appears in the partial flow zone. (0.085–0.130).

At the impeller RK-2, a reasonably good agreement was observed between the experimental and calculated head coefficients. At the calculated $\varphi = 0.18$, the numerical values of these coefficients differ by no more than 5 %. Based on this, it can be argued that the numerical optimization method [5] using a computer allows you to design reversed impellers for the specified parameters.

Since the impeller RK-2 was designed with efficiency optimization, the impeller's level in the flow coefficient change range was substantially higher than that of the RK-1. In the calculated mode, it was 0.64.

Observed for RK-1 at $V = 4°$ the "fall-in" of the curve "$\Psi - \varphi$" in the range of $\varphi = 0.085–0.130$ indicates a significant change in the picture of a steady, smooth flow around the blades. In more detail, the research reveals the existence of the separated flows at the blade surface in this zone (Figure 5).

It was possible to establish how hydraulic losses in the flow washing elementary reversiblep grids, angle of attack α_1, level of loading of the blade element (measured by the coefficient Ψ_k), and secondary flows, including overflow in the radial clearance at the periphery of the impeller.

From Figure 3, it follows that for the peripheral and middle sections, there are optimal values of the angles of attack α_1. When changing in one direction or another, the value η_k decreases. Besides, the specified angles do not coincide with the calculated angles (Table 1). A relatively more significant mismatch is observed for RK-1.

Here, these angles are much larger than the calculated ones, which agrees with the total characteristic "$\eta - \varphi$" (Figure 2).

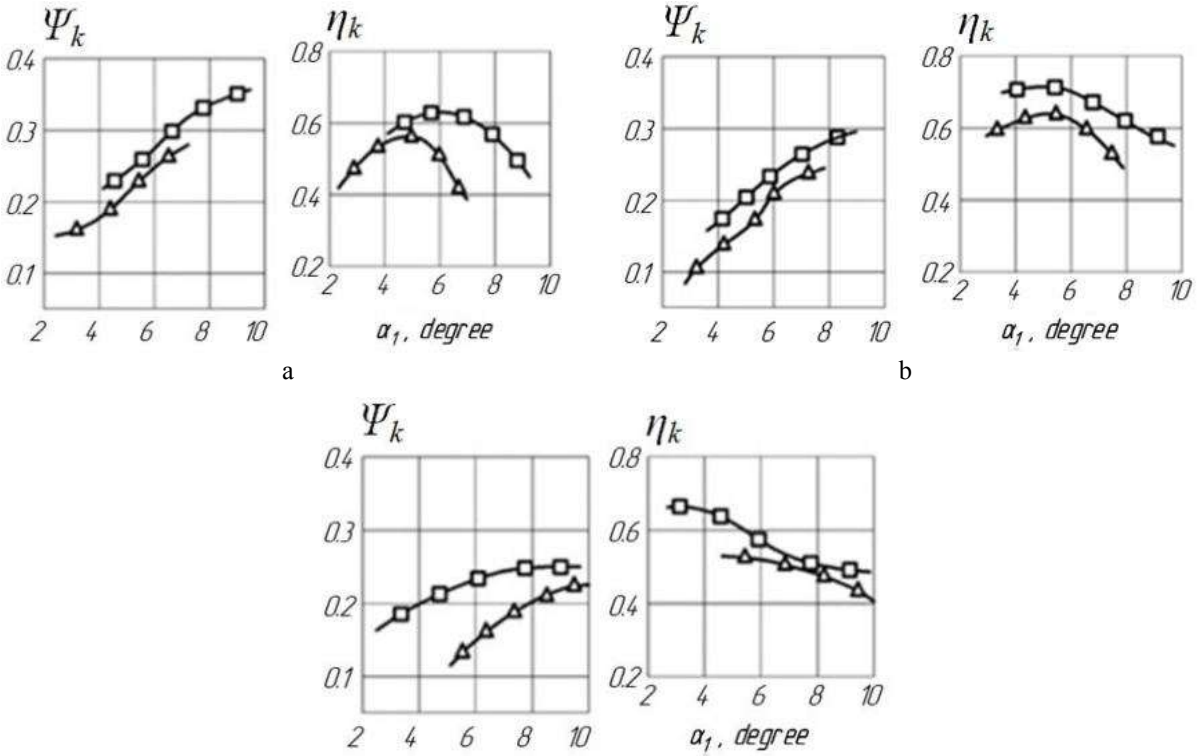

Figure 3 – The characteristics of the elementary grids in non-cavitation operation conditions: a – the peripheral cross-section; b – the middle section; c – the root section (RK-1, $V = 0°$; RK-1, $V = 0°$)

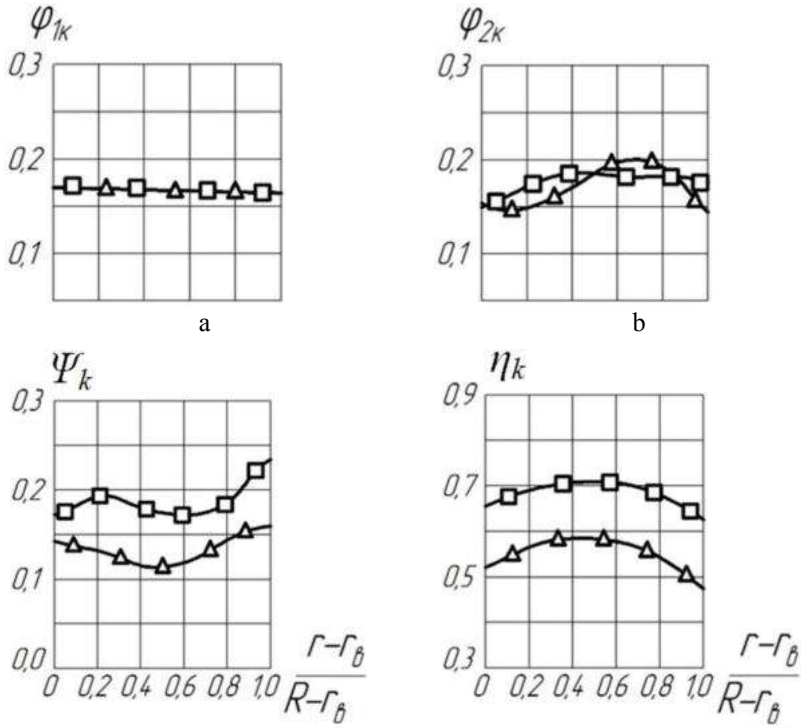

Figure 4 – The radius distribution of the parameters of elementary gratings with a calculated flow rate $V = 0°$ (RK-1, $\varphi = 0°, 180°$; RK-2, $\varphi = 0°, 180°$)

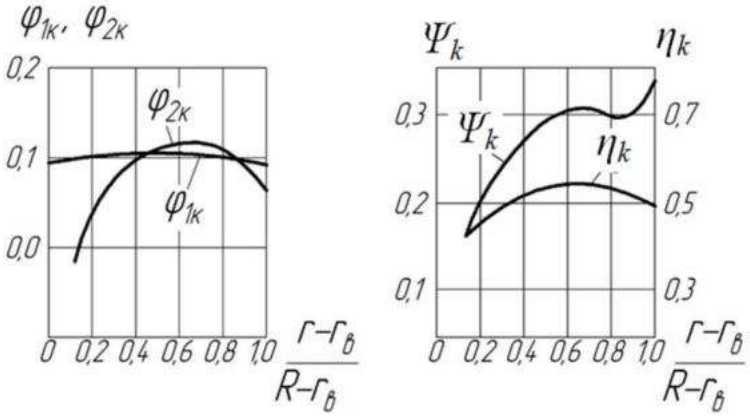

Figure 5 – The radius distribution of the parameters of the elementary grid RK-1 in partial flow rate mode $\varphi = 0.105$ and $V = 4°$

In the direction of the large angles of attack compared with the calculated, the optimal efficiency of the named impeller is shifted.

For RK-2 experimental and design α_1, all sections differ slightly. In the middle section, they are almost the same. This explains a resonably good coincidence of the design and optimal operating modes of the impeller RK-2 (Figure 2).

An analysis of the "$\eta_k - \alpha_1$" curves for RK-2 in the range of the angle-of-attack changes corresponding to the zone of optimal efficiency shows that the η_k on the periphery is by 6–8 %, less than the value of this parameter in the middle blade and by 2.0–2.5 % less than that of the sleeve. Such an increase in energy loss in the end sections of the blade was due to overflows in the radial gap and other secondary flows in this area.

The minimum efficiency η_k noted near the impeller sleeve RK-1 is presumably related to the large thickness of the boundary layer and its possible separation from the blade surface [18].

One of the questions during the research was to determine the permissible load on the blade to take it into account when developing new designs. Based on the obtained experimental data, for the best η_k operation modes of RK-2, it is possible to recommend $\Psi_k = 0.26$–0.29 – for peripheral sections and $\Psi_k = 0.15$–0.17 – for sleeve ones. In this case, the efficiency of the reversing impeller should be expected to be about 0.65–0.66.

Two characteristic modes were selected to represent the radial distribution of parameters across the blade elements: design flow mode (Figure 4) and unstable operation mode (Figure 5). From Figure 5, it can be seen that at the sleeve RK-1, the flow coefficient φ_{2k} is zero or negative. Such a redistribution of the axial velocities indicates the existence of a vortex zone in this region. This is confirmed by visual observations of the flow in stroboscopic lighting (data not shown).

Based on the previous, we have presented a picture of the current around the blade and thus explain the flooding of the head-flow characteristic of the RK-1 impeller at $V = 4°$ in the modes of frequency flows $\varphi = 0.085$–0.130 (Figure 2). Figure 2 shows that with a decrease φ from 0.130 to 0.105 the head Ψ coefficient decreases from 0.212 to 0.205, which may be associated with the formation of the vortices at the sleeve. The presence of such as the flow is further reduced ($\varphi < 0.105$) facilitates the flow conditions of the rest of the blade (since the velocities are redistributed over the height of the channel), which increases from the head.

4 Conclusions

Thus, the economy of the best-tested reverse impeller was 0.63–0.64. The indicated low level of efficiency (compared to the conventional axial wheels is non-reversible) is explained primarily by the strong influence of secondary flows due to the existence of the significant alternating pressure gradients of the head coefficient Ψ_k (Figure 4). An important reason for this was also the possible profile separation of the flow, to which the reversible grids in question are most predisposed.

The presence of alternating gradients of the head coefficients does not recommend any acceptable law of load change along the radius for newly designed reverse pump wheels. This issue needs further study.

To improve the performance of the reversible impellers. It is necessary for a more in-depth study of the effects of secondary flows. Of undoubted interest in this regard are identifying the influence of typical impeller's parameters, length of the blade profile, and the load distribution along the radius on the manifestation of three-dimensional effects.

5 Acknowledgment

The research was carried out at the Research and Educational Center for Industrial Engineering within the R&D project "Fulfillment of tasks of the perspective plan of development of a scientific direction "Technical sciences" Sumy State University" by the Ministry of Education and Science of Ukraine (State reg. no. 0121U112684).

The authors also appreciate the International Association for Technological Development and Innovations for the support during the research.

References

1. Grätzer, G. (1978). *General Lattice Theory*. Basel, Stuttgart: Birkhäuser, doi 10.1007 / 978-3-0348-7633-9.
2. Truijen, D. P. K., De Kooning, J. D. M., Stockman, K. (2021). Drivetrain architectures for a mechanically decoupled contra-rotating reversible pump-turbine. *IEEE/ASME International Conference on Advanced Intelligent Mechatronics*, art. no. 21128193, doi: 10.1109/AIM46487.2021.9517403.
3. Zhu, D., Xiao, R., Liu, W. (2021). Influence of leading-edge cavitation on impeller blade axial force in the pump mode of reversible pump-turbine. *Renewable Energy*, Vol. 163, pp. 939-949, doi:10.1016/j.renene.2020.09.002.
4. Liu, Y., Gong, J., An, K., Wang, L. (2020). Cavitation characteristics and hydrodynamic radial forces of a reversible pump-turbine at pump mode. *Journal of Energy Engineering*, Vol. 146(6), 713, doi: 10.1061/(ASCE)EY.1943-7897.0000713.
5. Johnson, J. L., Leone, F. C. (1977). *Statistics and Experimental Design in Engineering and the Physical Sciences*. John Wiley & Sons, New York.
6. Meng, F., Li, Y., Yuan, S., Wang, W., Zheng, Y., Osman, M. K. (2020). Multiobjective combination optimization of an impeller and diffuser in a reversible axial-flow pump based on a two-layer artificial neural network. *Processes*, Vol. 8(3), 309, doi: 10.3390/pr8030309.
7. Huang, J., Zheng, Y., Kan, K., Xu, Z., Huang, C., Zhou, G., Du, Y. (2022). Hydraulic characteristics of reverse power generation of axial-flow pump. *Journal of Drainage and Irrigation Machinery Engineering*, Vol. 40(3), pp. 230-237, doi: 10.3969/j.issn.1674-8530.20.0207.
8. Zhang, X., Tang, F., Chen, Y., Huang, C., Chen, Y., Wang, L., Shi, L. (2022). Experimental study on the internal pressure pulsation characteristics of a bidirectional axial flow pump operating in forward and reverse directions. *Machines*, Vol. 10(3), 167, doi: 10.3390/machines10030167.
9. Zhou, Y., Zheng, Y., He, Z., Sun, A., Zhang, F., Wang, H. (2019). Pressure fluctuation and fluid-solid coupling in reverse power generation of large axial flow pump. *Journal of Drainage and Irrigation Machinery Engineering*, Vol. 37(6), pp. 480-485, doi: 10.3969/j.issn.1674-8530.18.0034.
10. Ma, P., Wang, J. (2017). An analysis on the flow characteristics of bi-directional axial-flow pump under reverse operation. *Proceedings of the Institution of Mechanical Engineers, Part A: Journal of Power and Energy*, Vol. 231(3), pp. 239-249, doi: 10.1177/0957650917695447.
11. Kang, C., Mao, N., Pan, C., Zhou, Y. (2016). Turbulent flow characteristics in an axial-flow pump at direct and reverse modes. *Journal of Applied Science and Engineering*, Vol. 19(4), pp. 447-458, doi: 10.6180/jase.2016.19.4.08.
12. Husak, O., Panchenko, V. (2022). *Theory of Hydraulic Machines*. Sumy State University, Sumy, Ukraine.

JOURNAL OF ENGINEERING SCIENCES

Volume 9, Issue 1 (2022)

Zahorulko, A., Borsuk, S., Peczkis, G. (2022). Computational analysis of sealing and stability of a deformable floating and fixed rings of an annular seal. Journal of Engineering Sciences, Vol. 9(1), pp. D20-D29, doi: 10.21272/jes.2022.9(1).d4

Computational Analysis of Sealing and Stability of a Deformable Floating and Fixed Rings of an Annular Seal

Zahorulko A.[1*][0000-0002-6198-4643], Borsuk S.[1][0000-0002-1808-0008], Peczkis G.[2][0000-0002-4856-3123]

[1] Sumy State University, 2, Rymskogo-Korsakova St., 40007 Sumy, Ukraine;
[2] Silesian University of Technology, 2A, Akademicka St., 44-100 Gliwice, Poland

Article info:
Submitted: March 21, 2022
Accepted for publication: June 12, 2022
Available online: June 16, 2022

***Corresponding email:**
a.zagorulko@cm.sumdu.edu.ua

Abstract. Solving the hydroelastic problem by using Ansys System Coupling (Mechanical and CFX) for floating and fixed rings of a deformable annular seal made it possible to analyze the influence of the cylindrical shell thickness, the inlet and outlet edge dimensions, inlet pressure, and shaft radial displacement on the hydrostatic pressure distribution and the clearance value on length, leakages, stress-strain state, and radial force. The analysis of static stability at an inlet pressure of 10 MPa for the basic seal design showed that the static radial force in the range of radial movements of the shaft from 0 to 50% of the clearance is centering, even though the inlet part of the seal clearance has a confusor, and the outlet part has diffuser form. However, the dynamic coefficients of the fixed sealing ring have a negative value of direct stiffness but positive values of direct and cross-coupled damping and cross-coupled stiffness. Verifying computational 2D and 3D models with experimental results from the literature showed that the maximum relative error does not exceed 10.7% for the hydrostatic pressure, 18% for the clearance, and 8.6% for the leakage value. Simultaneously, according to the trend, all calculated dependencies are identical to the experimental results.

Keywords: deformable annular seal, clearance, hydroelastic problem, sealing, stability.

1 Introduction

With industry development, the need for pumping and processing large masses of liquid and gaseous products is constantly growing [1]. One of the most critical problems in this area is the problem of creating reliable and hermetic seals. This situation is caused, on the one hand, by high sealing pressures and circumferential speeds, which increase yearly. On the other hand, stringent requirements for sealing and reliability rise along with the growth of parameters.

In modern pumping equipment, non-contact seals of the annular type have become widespread. The peculiarity of these seals is their direct influence on the vibration state of the rotors. Depending on the design of the seals, the hydrodynamic forces arising in them can have both a centering and decentering effect on the rotor. The main disadvantage of such seals is relatively large leakages of the pumped liquid, which reduce the efficiency of the pumps. Therefore, developing and calculating new designs of annular seals that provide small leakages with the guaranteed non-contact operation of the rotor is an urgent and, at the same time, a difficult task, as it is necessary to find a compromise between these conflicting requirements. This provision determines the importance of research aimed at increasing the sealing capacity and vibration reliability of non-contact seals of rotors of high-speed pumps and reducing the complexity of calculations.

For the first time, the deformation problem of an annular seal was considered by Kamal [2]. He developed a simple method of analyzing the flow in an annular seal based on the solution of the Reynolds equation, considering the deformations of the shaft surfaces and the sealing ring as a part of the housing. Subsequently, Pick and Harris solved the hydroelastic problem for the so-called Morrison and Perry seals [3]. They used the finite element method to analyze the deformations of the ring shell and the shaft of the reciprocating joints. The pressure distribution in the seal, the movement of the sealing surfaces, and leakages were determined by the joint solution of the hydrodynamics equations and

elasticity using the successive approximations method. Khvorost, Melnyk, et al. [4] proposed a computational method for calculating the flow in a floating seal considering input losses. Yu.A. Kibets, in his dissertation [5], based on experimental studies, proposed a method for calculating deformable annular seals of turbopump units.

Recently, an increasing number of experimental [6, 7] and theoretical [8, 9] studies are related to analyzing the dynamics and leakages of floating seals of high-speed rotary machines such as aircraft engines, turbopump units, or gas turbines. Studies of static and dynamic lubrication parameters of bearings with floating rings for high-speed turbocompressors deserve special attention [10, 11, 12].

Therefore, this work aims to solve the hydroelastic problem and analyze the static and dynamic stability of the floating and fixed rings of the deformable annular seal of the high-speed turbopump. Verifying the computational model with experimental results from the literature [5].

2 Research Methodology

The hydroelastic problem for floating and fixed rings of a deformable annular seal was solved using Ansys System Coupling [13]. The analysis of ring deformations was performed in the Ansys Transient Structural module, and the calculation of fluid flow through the annular was conducted in the Ansys Fluid Flow (CFX) module.

The basic design of the deformable sealing ring (Fig.1) has the following dimensions and design parameters [5]:

- annular length l = 25 mm;
- shaft diameter d = 120 mm;
- radial clearance h_0 = 0.1 mm;
- cylindrical shell thickness δ = 2 mm;
- inlet edge diameter D_1 = 155 mm;
- inlet edge thickness b_1 = 5 mm;
- outlet edge diameter D_2 = 155 mm;
- outlet edge thickness b_2 = 5 mm;
- d_1 = 122 mm;
- d_2 = 126 mm;
- a = 1 mm;
- undercutting diameter of outlet edge D= 130 mm.

The material of the ring is bronze BrAlFeMg 10-3-2.

Computational studies were carried out for 2D and 3D models of sealing rings. For the 2D model, the static problem of analyzing the stress-strain state in an axisymmetric setting was considered. For the calculation 2D model hexa mesh of the ring and the clearance domain of the deformable floating seal, a sector with an angle of 5 degrees was chosen.

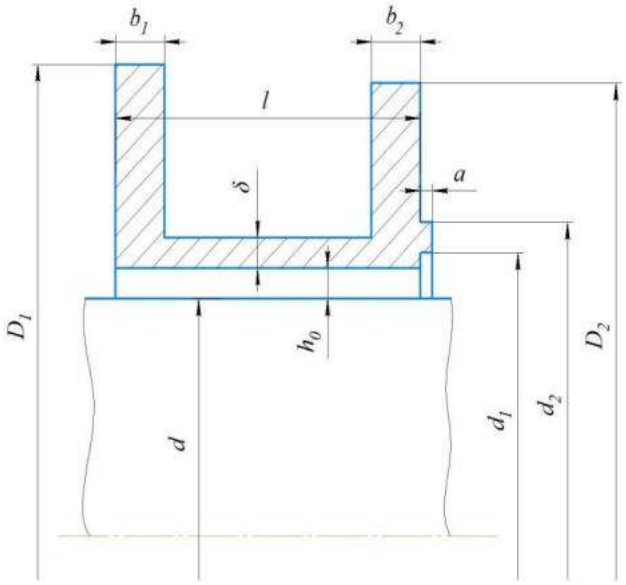

Figure 1 – Diagram of a deformable U-shaped sealing ring

The calculation mesh with boundary conditions is shown in Fig. 2 a,b. The size of the ring mesh is 17170 elements. The dimensionality of the liquid clearance mesh is 10,000 elements. As a boundary condition, the inlet pressure was set on the outer surface of the solid ring. The condition of rotational periodicity symmetry was applied to the side faces of the ring sector. The face surface frictional contact of the ring with the body was modeled with a friction coefficient of f=0.07. An interface for obtaining data on the hydrostatic pressure distribution and transmitting data on the distribution of the deformation was set on the inner surface. For the liquid clearance: on the side faces, the boundary conditions of rotational periodicity, static pressure at the inlet and outlet, on the surface of the shaft and the surface of the inner ring - conditions of the absence of sliding on the walls were set. In addition, on the surface connected to the inner surface of the ring, an interface for transmitting hydrostatic pressure distribution data and obtaining a strain distribution was determined.

A turbulent isothermal flow of water was considered using the k-ε turbulence model. To model the boundary layer, the clearance mesh, which consisted of 10 elements in thickness, thickened near the walls. As a result of the calculations, hydrostatic pressure and clearance distributions along the seal length, the leakages, and the stress-strain state of the annular seal floating ring without considering the shaft rotation were obtained.

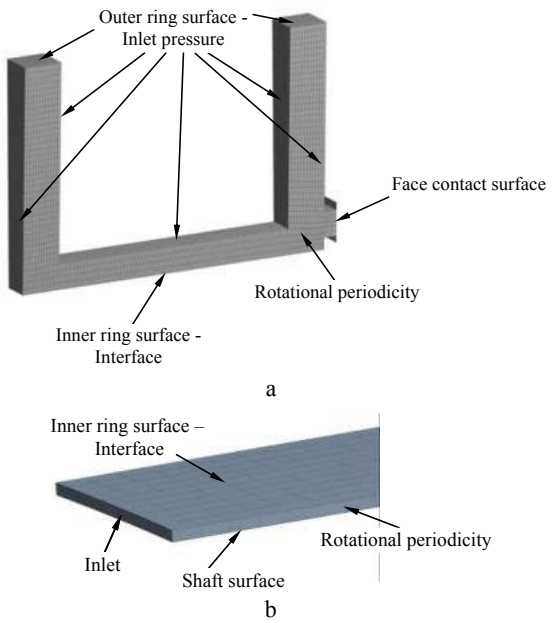

Figure 2 – Calculation mesh of the 2D model of the ring (a) and the clearance (b) of the deformable annular seal

For the 3D model, the complete rotational geometry of the sealing ring and liquid clearance with bonded contact of the face surface was considered. The calculated hexa mesh of the 3D model of the ring and the clearance is shown in Fig. 3a, b. The structured hexa mesh of the ring had 27607 elements, the clearance mesh - 30000. Similar to the 2D model, the inlet pressure was applied to the outer surface of the sealing ring as a boundary condition. A static sealing pressure was set at the inlet of the liquid clearance. Static pressure of 0 Pa was set at the outlet, which is the condition for the outflow of the liquid medium into the atmosphere. The inner cylindrical surfaces from the side of the ring and the clearance were used as interface surfaces. The condition of no sliding was set on the walls of the clearance.

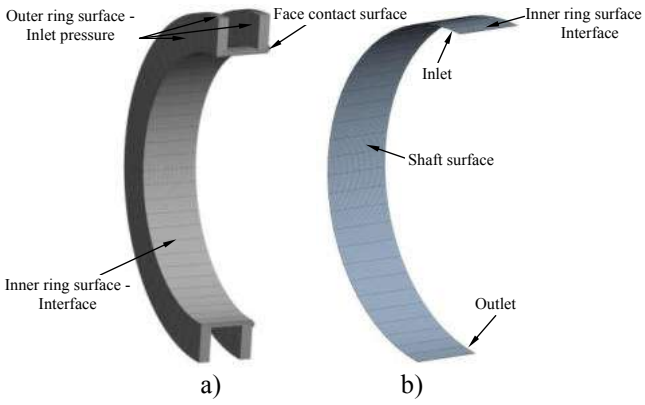

Figure 3 – Calculation mesh of the 3D model of the ring (a) and the clearance (b) of the deformable annular seal

The analysis of the static and dynamic stability of the shaft in the deformable annular seal was performed using the Ansys CFX numerical method of the deformed mesh.

When analyzing the static stability of the floating and fixed rings of the deformable annular seal, a relative radial displacement e=0.2, 0.3, 0.4, 0.5 was applied to the shaft surface depending on which the radial force and the leakages were obtained. The stress-strain state of the fixed ring of the deformable annular seal was analyzed.

When analyzing the dynamic state, with the fixed ring of the deformable annular seal, displacements $z = e_z \cdot \cos(\omega t)$ and $y = e_y \cdot \sin(\omega t)$ were applied to the shaft surface, which specified a direct synchronous whirl along a circular trajectory. At the same time, the rotational speed of the shaft surface was equal to 22,000 rpm. One shaft rotation with 20 timesteps was simulated. The eccentricity $e_z = e_y = 0.01$ mm is equivalent to 10% of the clearance. As a result, the joint hydroelastic problem and shaft whirl along a circular trajectory was solved. Dynamic stiffness and damping coefficients were estimated using the hydrodynamic forces obtained during the calculation [14].

3 Results and Discussion

As a result of the static calculation for the floating and fixed rings of the deformable annular seal, the influence of the cylindrical shell thickness, the inlet and outlet edge dimensions, the inlet pressure, and the radial displacement of the shaft on the hydrostatic pressure and the clearance distributions along the length, leakages, the stress-strain state, and the radial force were analyzed.

The hydrostatic pressure and clearance distributions along the seal length at different cylindrical shell thicknesses (Fig. 4 a,b) show that for the 2D model of the basic design of the seal at δ=2 mm and the inlet-outlet edge thicknesses $b_1=b_2=5$ mm, the calculation results agree well with the results of the experiment. Thus, the maximum relative error does not exceed 10.7% for hydrostatic pressure and does not exceed 18% for clearance. When the thickness of the cylindrical shell is reduced, the minimum clearance decreases by more than two times from h_{min} = 0.0559 mm to h_{min} = 0.0265 mm. Leakages reduce from Q = 1.33 l/s to Q = 0.651 l/s at δ = 2.5 mm and δ = 1.5 mm, respectively (Fig. 5). The profile of the hydrostatic pressure distribution is transformed from uniform close to parabolic to non-uniform with a convex shape of the curve on the confusor part of the clearance and a concave curve on the diffuser part of the clearance. The position of the minimum clearance slightly shifts towards the outlet to the seal.

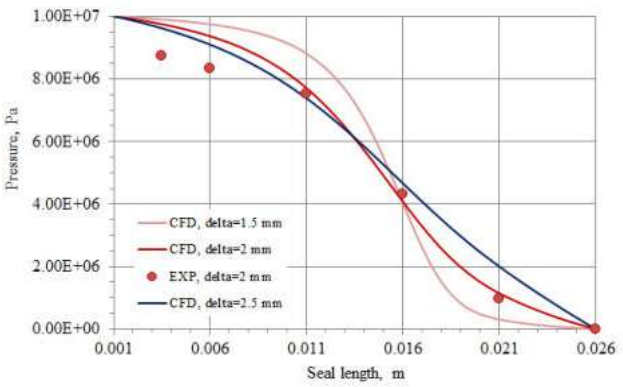

a

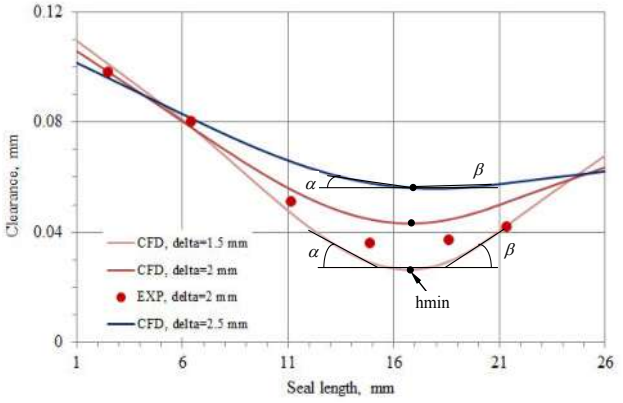

b

Figure 4 – Hydrostatic pressure (a) and clearance (b) distributions along the length of the 2D model of the floating ring at the different cylindrical shell thicknesses

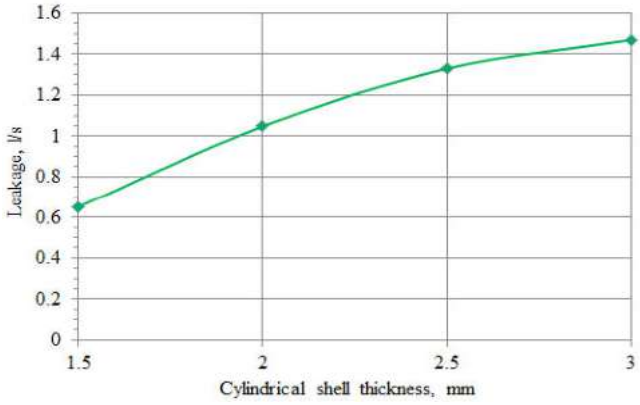

Figure 5 – Dependence of leakage on the cylindrical shell thickness for the 2D model of the floating ring

The radial deformations of the floating sealing ring (Fig. 6 a-d) show that when the thickness of the U-shaped cylindrical shell decreases, the angle of rotation φ increases, first of all, of the outlet edge. The opening angles of the confusor α and diffuser β increase (Fig. 4b).

The hydrostatic pressure and clearance distributions along the length of the floating sealing ring (Fig. 7 a,b) show that as the inlet and outlet edge thicknesses decrease, the pressure distribution profile fills up, and the minimum clearance decreases from h_{min}=0.0416 mm to h_{min}=0.0319 mm. Also, the position of the minimum clearance towards the outlet from the seal changes. With the inlet edge thickness b_1=3 mm and b_1=1 mm, and the outlet edge thickness b_2=1 mm, a confusor shape of the clearance is provided along the entire seal length. Moreover, leakages have a minimum value of Q=0.77 l/s (Fig. 8). Undercutting the outlet edge of the floating seal ring at b_1=b_2=5 mm to a diameter of D=130 mm also leads to the formation of a confusor clearance along the entire length of the seal. Leakages decrease from Q=1.048 l/s to Q=0.875 l/s. The hydrostatic pressure distribution profile has the most filled curve shape.

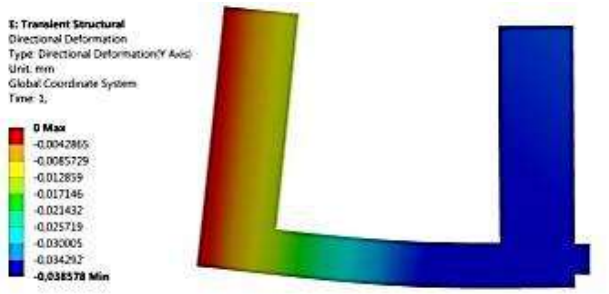

a

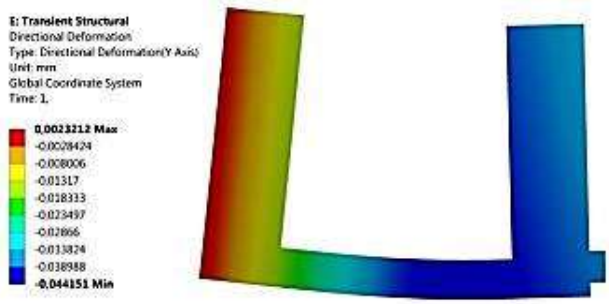

b

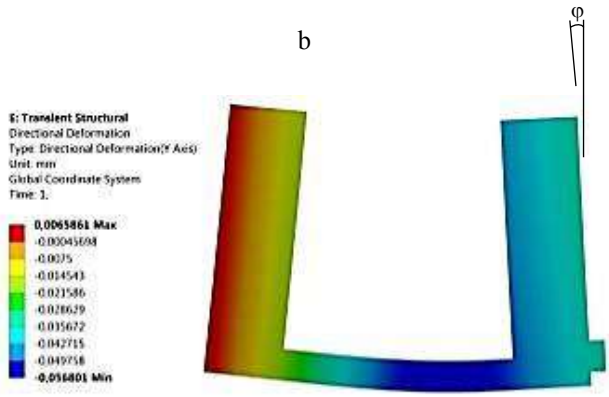

c

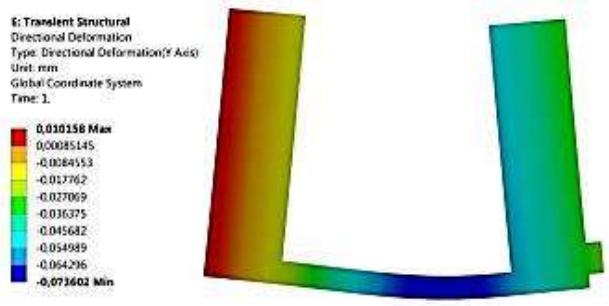

d

Figure 6 – Radial deformations of the 2D model of the deformable floating ring: δ=3 mm (a), δ=2.5 mm (b), δ=2 mm (c), δ=1.5 mm (d)

The radial deformations of the floating sealing ring (Fig. 9 a-f) increase with a decrease in the thickness of the inlet and outlet edges. Moreover, with a reduction in the output edge thickness and its undercutting, the value of the rotation angle of the input edge increases, and the value of the rotation angle of the output edge decreases. Thus, the primary influence on the cone-shaped deflection of the floating sealing ring is the thickness and diametrical size of the output edge.

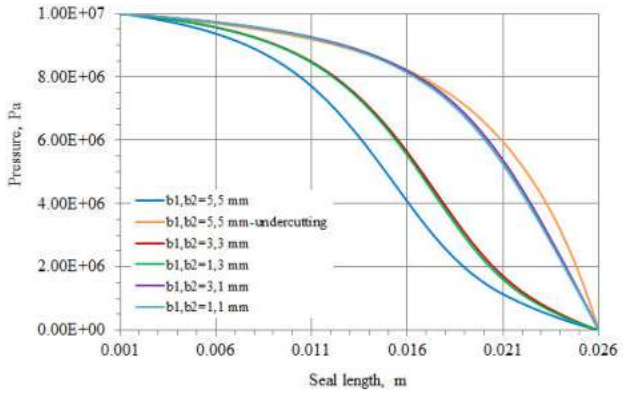

a

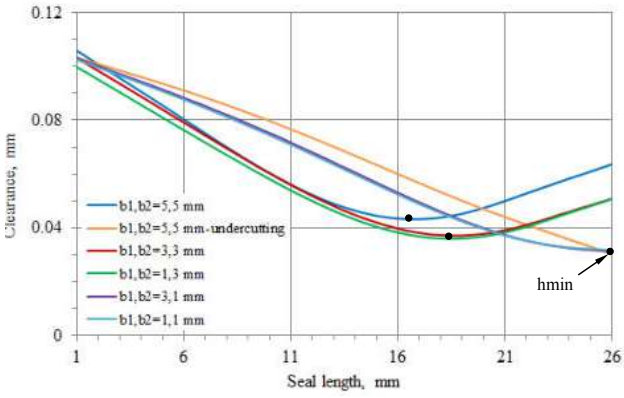

b

Figure 7 – Hydrostatic pressure (a) and clearance (b) distributions along the length of the 2D model of the floating ring with different sizes of the inlet and outlet edges

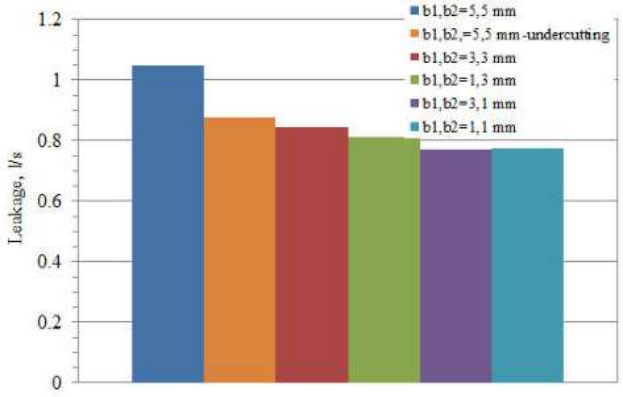

Figure 8 – Leakages in the 2D model of the floating ring with different sizes of the inlet and outlet edges

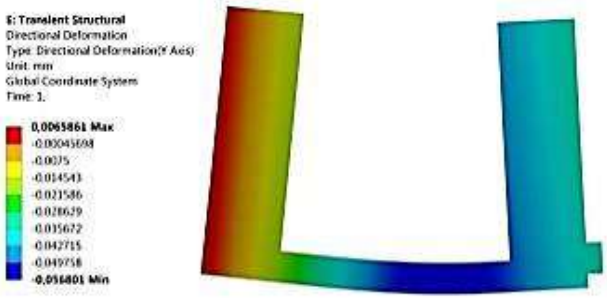

a

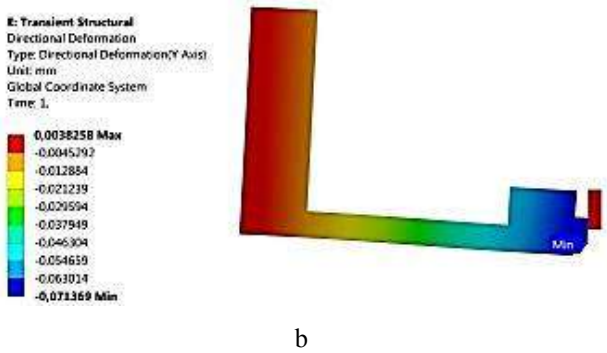

b

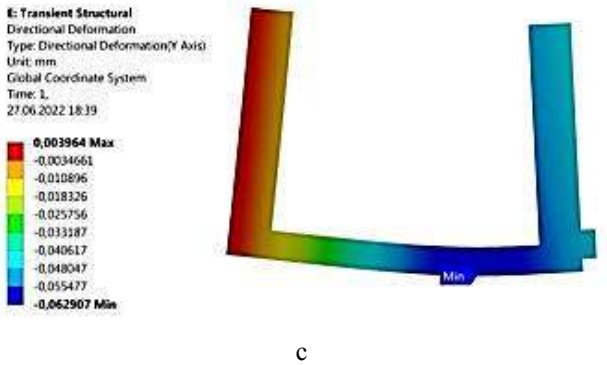

c

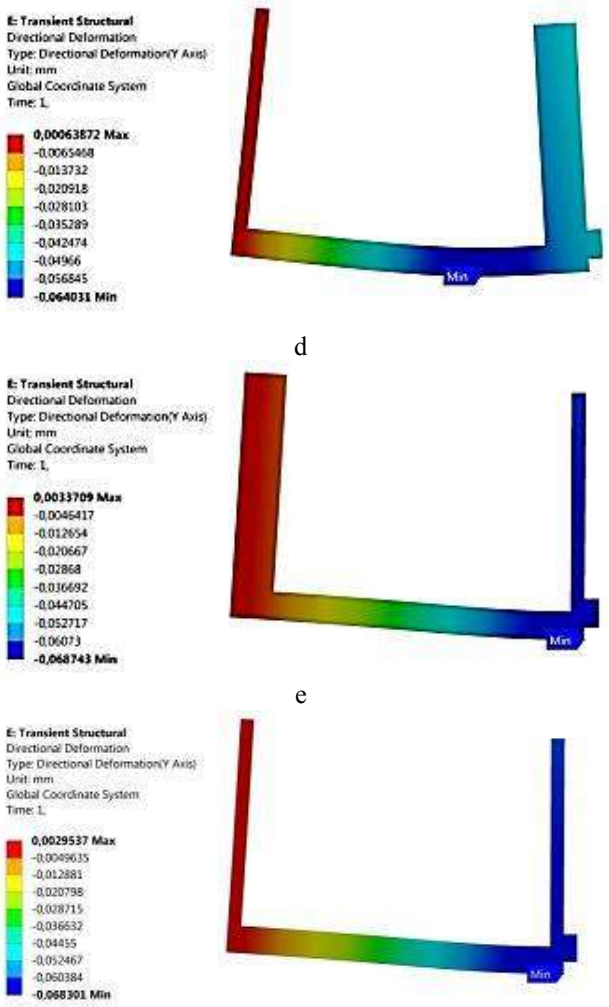

Figure 9 – Radial deformations of the 2D model of the deformable floating ring: $b_1 = b_2 = 5$ mm (a), $b_1 = b_2 = 5$ mm – undercutting (b), $b_1 = b_2 = 3$ mm (c), $b_1 = 1$ mm, $b_2 = 3$ mm (d), $b_1 = 3$ mm, $b_2 = 1$ mm (e), $b_1 = b_2 = 1$ mm (f)

Hydrostatic pressure and clearance distributions along the seal length depending on the sealing pressure for the basic design of the seal with a floating ring (Fig. 10 a, b) show an increase in the pressure profile and a decrease in the value of the minimum clearance with an increase in the inlet pressure. The gap size decreases almost twice from $h_{min} = 0.0872$ mm to $h_{min} = 0.0432$ mm at $P_{in} = 2$ and 10 MPa, respectively.

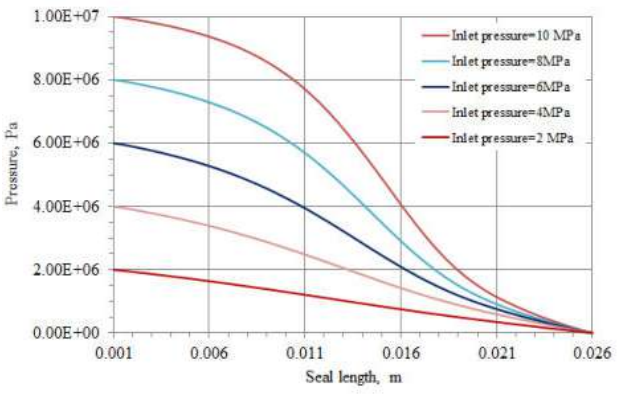

a

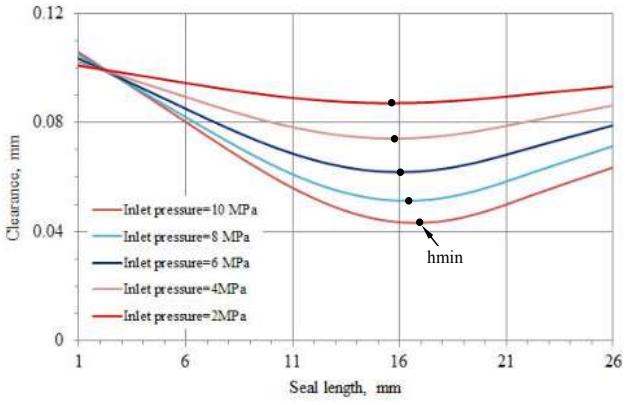

b

Figure 10 – Hydrostatic pressure (a) and clearance (b) distributions along the length of the 2D model of the deformable floating ring at different sealing pressures for the basic seal design ($\delta = 2$ mm, $b_1 = b_2 = 5$ mm)

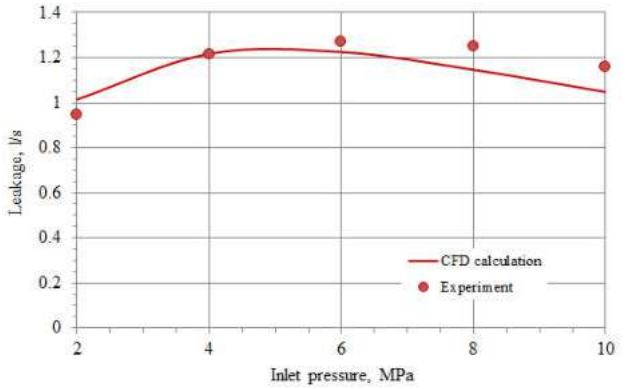

Figure 11 – Leakages depending on the inlet pressure in the 2D model of the deformable floating ring of the basic seal design ($\delta = 2$ mm, $b_1 = b_2 = 5$ mm)

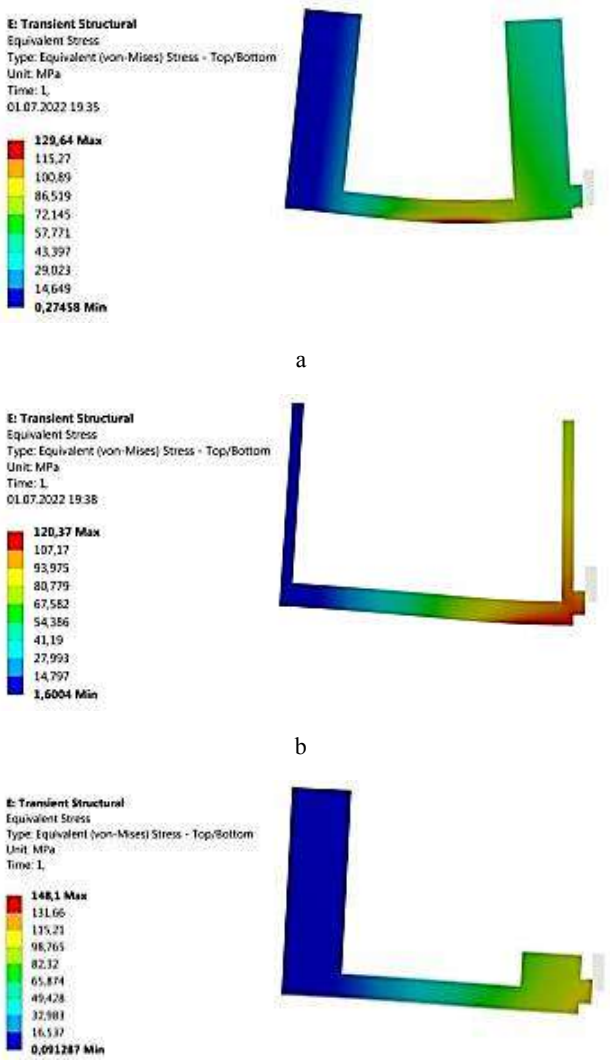

Figure 12 – Equivalent stresses in the basic design $b_1=b_2=5$ mm (a), design with $b_1=b_2=1$ mm (b), and design with undercutting $b_1=b_2=5$ mm (c) 2D model of seal

Also, the minimum clearance position slightly shifts towards the outlet from the seal. This fact explains the quadratic change in the leakages from the sealing pressure (Fig. 11). First, there is an increase in leakage up to a pressure value of approximately 6 MPa, and then the leakage value begins to decrease at pressures of 8 and 10 MPa. The relative error between calculated and experimental data on the leakages does not exceed 8.6%. At the same time, according to the trend, all calculated dependences are identical to the experimental results.

It is clear that the radial deformations of the floating ring of the basic design increase with increasing inlet pressure. A comparison of the equivalent stresses at an inlet pressure of Pin=10 MPa (Fig. 12) for the basic design, a design with minimal thickness of the inlet and outlet edges, and a design with undercutting of the outlet edge showed that the most significant value of stress is in the design with undercutting of the outlet edge.

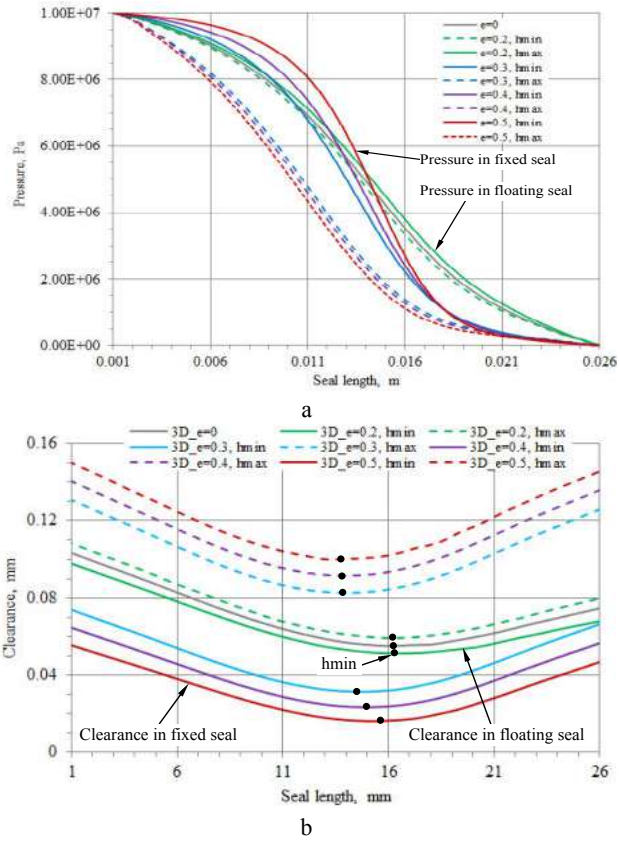

Figure 13 – Hydrostatic pressure (a) and clearance (b) distributions along the length of the 3D model of the deformable floating and fixed rings at different shaft radial displacements

Moreover, the equivalent stresses are significantly lower than the allowable stress for the material of 340 MPa.

Hydrostatic pressure and clearance distributions along the length of floating and fixed deformable seal rings at different shaft radial displacements (Fig. 13 a, b) show that for the 3D model of the floating ring, the difference between pressure and clearance distributions in the places of minimum and maximum clearances is insignificant. This is because, with a relative radial displacement of the shaft e=0.2, the radial hydrostatic force in the seal displaces the ring in the reverse direction by e=0.16. That is, by approximately 80% of the previous radial displacement of the shaft. At the same time, the radial force is equal to 521.2 N, and the frictional force in the contact of the floating ring is equal to 453.3 N (Fig. 14 b). And this means that the radial force is only 13% more than the friction force. At the same time, the amount of leakages Q=1.36 l/s almost does not change, and the amount of radial force increases significantly less than for a fixed ring if compared with the concentric position of the shaft e=0 (Fig. 14 a,b). But on the contrary, for a fixed ring, the difference between the hydrostatic pressure and clearance distributions in the places of minimum and maximum clearances is significant and is associated with a more substantial radial displacement of

the shaft e=0.3, 0.4, 0.5 (Fig. 13 a,b). The minimum clearance varies in size and position along the seal length (Fig. 13 b), which is explained by the difference between the hydrostatic pressure profiles. The increase in leakage and radial force from the radial displacement of the shaft for the design of the seal with a fixed deformable ring occurs according to linear dependencies (Fig. 14 a,b).

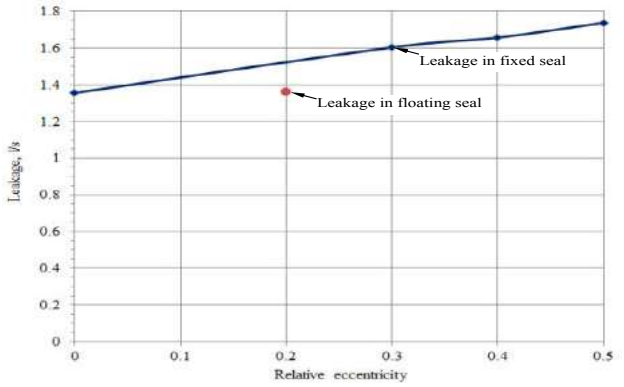

a

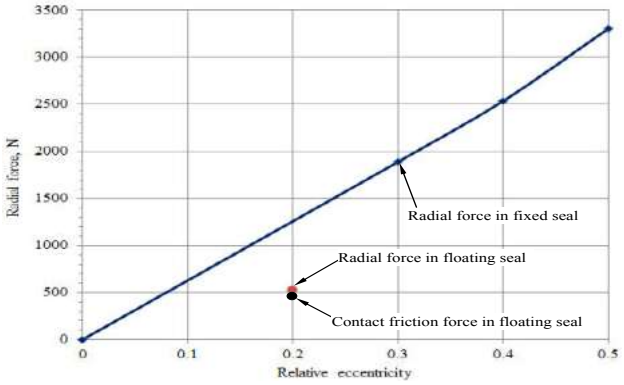

b

Figure 14 – Dependence of leakage (a) and radial force (b) on the shaft radial displacement for a 3D model of deformable floating and fixed annular seal rings

Fixation of the deformable sealing ring is because with an increase in the relative radial displacement of the shaft, there is an increase in the radial force that tries to move the ring in the opposite direction, which leads to significant deformations of the calculation mesh and this makes it impossible to perform further calculations.

Radial displacement and equivalent stresses of the 3D model of the sealing ring are presented in Figures 15 a, b.

A comparison of the radial deformations of the static and fixed dynamic 3D models (Fig. 16 a,b) shows that a more significant amount of deformation and movement of the minimum clearance position towards the seal outlet occurs in the static model. This is because the floating ring in the static model can move the face contact surface, unlike the fixed ring in the dynamic model. However, the dynamic model of the undercutting ring design (Fig. 16 c) has the most considerable deformation, even though the ring is fixed.

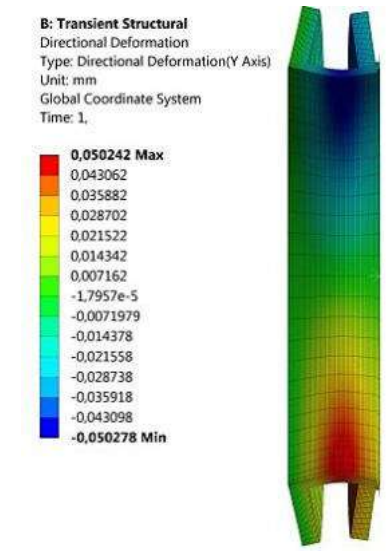

a

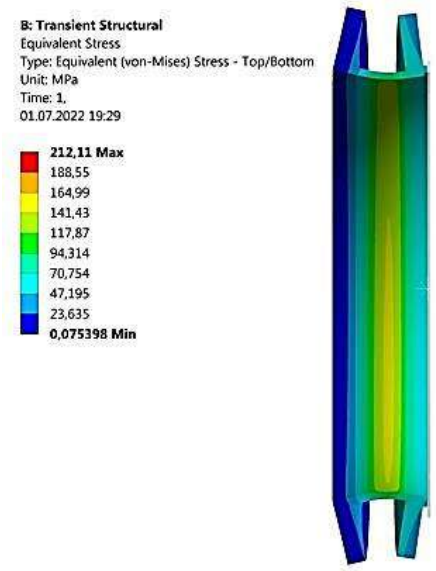

b

Figure 15 – Radial deformations (a) and equivalent stresses (b) of the 3D model of the deformable floating ring at e = 0.2

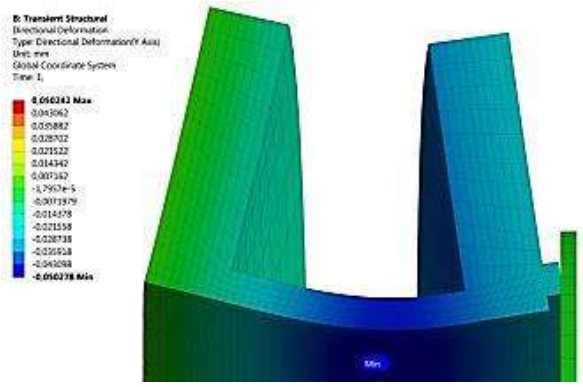

a

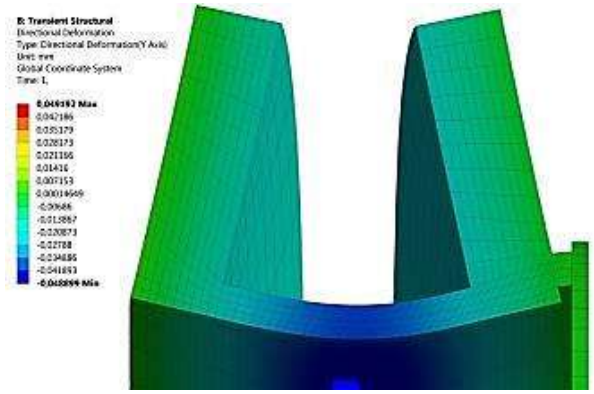

b

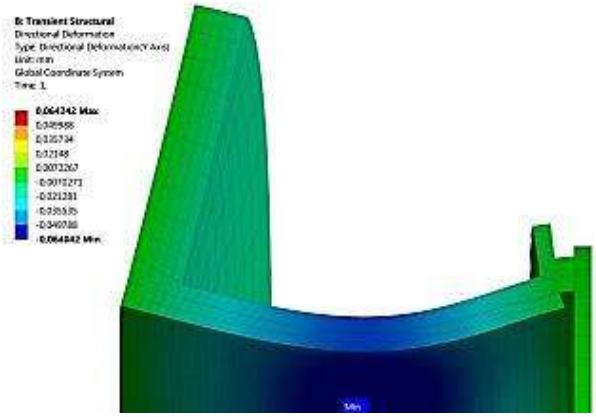

c

Figure 16 – Radial deformations of static (a) and fixed dynamic 3D models of the basic design $b_1 = b_2 = 5$ mm (b) and design with undercutting $b_1 = 3$ mm, $b_2 = 1$ mm (c)

As a result of a dynamic calculation, based on hydrodynamic forces in the clearance of the deformable fixed ring of the annular seal, the coefficients of direct and cross-coupled stiffness and damping were estimated. The minimum clearances and leakages in the basic design and the design with undercutting b_1=3 mm, b_2=1 mm were obtained (Table 1, Fig. 16 b,c).

Table 1 – Dynamic coefficients, leakages, and minimum clearances for two designs of deformable annular seals

Design, mm	k, N/m	C, N·s/m	–K, N/m	c, N·s/m	Q, l/s	h_{min}, mm
b1=b2=5, δ=2	7.94e7	4.75e8	2.36e8	7.22e8	1.3	0.05
b1=3, b2=1 (under-cutting) δ=2	1.00e8	6.00e8	3.00e08	8.00e8	1.0	0.04

Both designs have a negative coefficient of direct stiffness and positive coefficients of direct and cross-coupled damping and cross-coupled stiffness. This indicates the dynamic stability of the shaft in these seals. However, the negative direct stiffness must be considered when calculating the critical shaft speed. In the undercutting design, the absolute values of all dynamic coefficients increase, which is associated with a decrease in the clearance and, accordingly, the amount of leakages. The negative stiffness coefficient is due to an increase in the total velocity of the fluid flow in the place with the minimum clearance (Fig. 17).

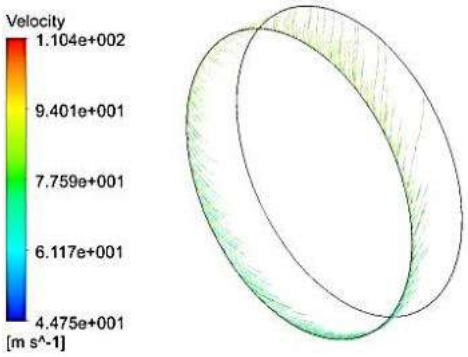

Figure 17 – Streamlines velocity in a 3D dynamic model of a fixed ring of a deformable annular seal

4 Conclusions

Solving the hydroelastic problem by using Ansys System Coupling (Mechanical and CFX) for floating and fixed rings of a deformable annular seal made it possible to analyze the influence of the cylindrical shell thickness, the inlet and outlet edge dimensions, inlet pressure, and shaft radial displacement on the hydrostatic pressure and the clearance distributions along the length, leakages, stress-strain state, and radial force.

Verification of computational 2D and 3D models with experimental results known from the literature showed that the maximum relative error does not exceed 10.7% for the hydrostatic pressure, 18% for the clearance, and 8.6% for the leakages. At the same time, according to the trend, all calculated dependencies are identical to the experimental results. Some slight discrepancy between the calculation and the experiment results is explained by the simulation being performed without considering the pressure losses at the seal inlet.

The calculation studies showed that due to the deformations of the U-shaped ring under the sealing pressure, the clearance and leakages in the deformable seal are significantly reduced. By selecting the cylindrical shell thickness and the inlet and outlet edge thicknesses, it is possible to influence the size and the clearance shape between the shaft and the ring. Reducing the cylindrical shell thickness reduces the minimum clearance size and increases the opening angle of the confusor and diffuser channels, which are formed at the inlet and outlet parts of the seal. Reducing the inlet and outlet edge thickness reduces the minimum clearance value and increases the confusor clearance length. This occurs due to deformations and movement of the face contact surface in the radial direction to the shaft surface. The formation of a confusor clearance along the entire seal length also

ensures a separate reduction in thickness and undercutting of the outlet edge of the deformable seal. In this case, leakages are visibly reduced.

An increase in the sealing pressure for the basic design of the seal naturally leads to a decrease in the minimum clearance value due to the deflection of the cylindrical shell and the radial movement of the face contact surface. The opening angles of the confusor and diffuser increase. Leakages initially increase to a pressure value of 6 MPa and then decrease. The curve has a parabolic shape.

The maximum stresses for all considered designs of the deformable annular seal do not exceed the maximum allowable material stress of 340 MPa.

In the static analysis, at an input pressure of 10 MPa and a radial displacement of the shaft e=0.2, self-centering of the floating sealing ring occurs under the action of a centering radial force. An increase in the shaft radial displacement from e=0.3 to e=0.5 in a seal with a fixed ring leads to a linear increase in the centering radial force and leakages. Static stability is ensured even in the presence of confusor and diffuser clearances regions along the length of the seal.

The analysis of the dynamic stiffness and damping coefficients for the fixed ring of the deformable seal of the basic design with the input and output edges thickness of 5 mm and the design with the input edge thickness of 3 mm and output edge thickness of 1 mm with undercutting shows the presence of a negative value of direct stiffness, which is caused by an increase in the total velocity of the fluid flow in the place of the minimum clearance. At the same time, reducing the thickness of the edges reduces the value of the minimum clearance and leads to an increase in the absolute value of the dynamic coefficients of direct and cross-coupled stiffness and damping. Regardless of the negative direct stiffness, the dynamic stability of the seal is ensured. However, the negative value of direct stiffness must be considered when calculating the critical shaft rotation speed.

5 Acknowledgments

The Sumy State University supported this article. Project: Research on the “Analysis of the Influence of Hydrodynamic Forces Acting in Narrow Clearances of Seals and Bearings on Increasing Energy Efficiency and Reducing the Harmful Emissions and Vibrations of Centrifugal Machines” (0120U102004) of Sumy State University funded by the Ministry of Education and Science of Ukraine.

References

1. Martsynkovskyy V.A. (2005). Hermomechanics, its role in ensuring the efficiency and environmental friendliness of pumping and compressor equipment. *Bulletin of Sumy State University, Series “Technical Sciences”*, Vol. 1(73), pp. 5–10.
2. Kamal, M. M. (1968). A high pressure clearance seal. *ASME. J. of Lubrication Tech.*, Vol. 90(2), pp. 412–416, doi: 10.1115/1.3601575.
3. Pick, R. J., Harris, H. D. (1980). Morrison and parry seals for water pressures up to 345 MPa. *J. Pressure Vessel Technol*., Vol. 102(1), pp. 84–89, doi: 10.1115/1.3263306.
4. Khvorost, V. A., Pryadko, S. V., Mel’nik, V. A. et al. (1987). Method of calculating floating seals. *Vestn. Mashinostr.*, Vol. 6, pp. 23–25.
5. Kibets, Yu.A. (1988). Development of methods for calculating deformable annular seals of turbopump units. CSc. thesis. Kharkiv, Ukraine.
6. Arghir M. (2015). Experimental study of floating ring annular seals using high-speed optical techniques and mark tracking methods. *CFM 2015 - 22ème Congrès Français de Mécanique*. Lyon, France.
7. Li, G., Zhang, Q., Huang, E., Lei, Z., Wu, H., Xu, G. (2019). Leakage performance of floating ring seal in cold/hot state for aero-engine. *Chinese J Aeronaut*, Vol. 32, pp. 2085–2094, doi: 10.1016/j.cja.2019.03.004.
8. Ha, T.-W., Lee, Y.-B., Kim, C.-H. (2002). Leakage and rotordynamic analysis of a high pressure floating ring seal in the turbo pump unit of a liquid rocket engine. *Tribol Int*, Vol. 35, pp. 153–61, doi: 10.1016/S0301-679X(01)00110-4.
9. Duan, W., Chu, F., Kim, C.-H., Lee, Y.-B. (2007). A bulk-flow analysis of static and dynamic characteristics of floating ring seals. *Tribol Int*, Vol. 40, pp. 470–480, doi: 10.1016/j.triboint.2006.04.010.
10. Xie, Z., Zhu, W. (2022). An investigation on the lubrication characteristics of floating ring bearing with consideration of multi-coupling factors. *Mech Syst Signal Process*, Vol. 162, 108086, doi: 10.1016/j.ymssp.2021.108086.
11. Zhang, Y., Wang, W., Wei, D., Wang, G., Xu, J., Liu, K. (2022). Coupling analysis of tribological and dynamical behavior for a thermal turbulent fluid lubricated floating ring bearing-rotor system at ultra-high speeds. *Tribol Int*, Vol. 165, 107325, doi; 10.1016/j.triboint.2021.107325.
12. Novotný, P., Škara, P., Hliník, J. (2018). The effective computational model of the hydrodynamics journal floating ring bearing for simulations of long transient regimes of turbocharger rotor dynamics. *Int J Mech Sci*, Vol. 148, pp. 611–619, doi: 10.1016/j.ijmecsci.2018.09.025.
13. Workbench User’s Guide, Release 18.2, ANSYS Inc., 2017.
14. Zahorulko, A. V., Gerasimiva, K. P., Altyntsev, E. I., Hudkov, S. N. (2009). Computer modeling of the spatial flow in the annular channel of the annular seal-bearing. *Eastern European Journal of Advanced Technologies*, Vol. 6/7(42), pp. 22–26.

JOURNAL OF ENGINEERING SCIENCES

Volume 9, Issue 1 (2022)

5-th Grabchenko's International Conference on Advanced Manufacturing Processes (InterPartner-2023)

Dear Colleagues!

We would like to invite you to submit original and unpublished research papers to the **5-th Grabchenko's International Conference on Advanced Manufacturing Processes (InterPartner-2023)**, organized by Odessa Polytechnic National University, National Technical University «Kharkiv Polytechnic Institute», Sumy State University and International Association for Technological Development and Innovations, which will be held on September 05–08, 2023 in Odessa, Ukraine. The official website is http://interpartner.odessa.ua

InterPartner-2023 focuses on promoting research and developmental activities, intensification of scientific information interchange between researchers, developers, and engineers. The conference is an ideal platform for people to share views and experiences in fields of **Manufacturing Engineering**, **Mechanical Engineering**, **Materials Science**, and **Quality Assurance**.

Authors should submit their papers online using the EasyChair Conference Management System. The submission page for InterPartner-2023 is https://easychair.org/conferences/?conf=interpartner2023

The deadline for paper submission is **February 15, 2023**. After the careful reviewing process, all accepted papers will be published and submitted to the database Scopus, Web of Science, and |other indexing services. Accepted papers must be presented at the conference by one of their authors, who commit to register and attend the conference. The Steering Committee reserves the right to exclude papers that have not been presented from the proceedings.

Looking forward to your submissions!

Best regards,

Prof. Volodymyr Tonkonogyi,
Conference Chair

JOURNAL OF ENGINEERING SCIENCES

Volume 9, Issue 1 (2022)

Nogueira E. (2022). Thermodynamic performance of boehmite alumina nanoparticle shapes in the counterflow double pipe heat exchanger. Journal of Engineering Sciences, Vol. 9(1), pp. F1-F10, doi: 10.21272/jes.2022.9(1).f1

Thermodynamic Performance of Boehmite Alumina Nanoparticle Shapes in the Counterflow Double Pipe Heat Exchanger

Nogueira E.

Department of Mechanic and Energy, State University of Rio de Janeiro,
R. São Francisco Xavier, 524, Maracanã St., 20550-013, Rio de Janeiro, Brazil

Article info:
Submitted: January 21, 2022
Accepted for publication: March 18, 2022
Available online: March 21, 2022

***Corresponding email:**
elcionogueira@hotmail.com

Abstract. This work compares a theoretical model with a consolidated numerical model related to the thermodynamic performance of boehmite alumina nanoparticles in different formats in a counterflow double pipe heat exchanger. The shapes of the non-spherical nanoparticles under analysis are platelets, blades, cylindrical, and bricks. The second law of thermodynamics is applied to determine Nusselt number, pressure drop, thermal efficiency, thermal and viscous irreversibilities, Bejan number, and the out temperature of the hot fluid. The entropy generation rates associated with the temperature field and the viscous flow are graphical determined. The numerical model uses the k-ε turbulence model, which requires empirical factors to simulate turbulent viscosity and rate of generation of turbulent kinetic energy. Compatibility between the models was demonstrated. It was shown that the maximum absolute numerical error between the quantities Nusselt number, heat transfer rate, and pressure drop for established and specific conditions is less than 12.5 %.

Keywords: energy efficiency, thermal efficiency, Reynolds number, Nusselt number, process innovation.

1 Introduction

The optimization of heat exchangers has become a constant due to the increasing energy demand, and several alternative methods have been proposed. Conventional methods use fin systems, tabulators, and others. However, one of the current methods that have seen remarkable growth involves using fluids with a higher thermal conductivity than usual fluids, metallic or non-metallic solid nanoparticles in base fluids. In addition, recent studies indicate that non-spherical nanoparticles of different shapes can contribute to greater thermal performance than spherical nanoparticles.

The present work aims to compare analytical and numerical models that use the second law of thermodynamics to determine the thermal performance of a double tube heat exchanger. The numerical model, developed by Mostafa Monfared et al. [1], presents results for generating thermal and viscous entropy using nanoparticles of different shapes.

2 Literature Review

Mostafa Monfared et al. [1] numerically analyze the effects of the shape of boehmite alumina nanoparticles on the entropy generation characteristics of a double tube heat exchanger. The non-spherical nanoparticles used in the analysis are of the cylindrical, blade, platelet, and brick type and were dispersed in mixtures of water and ethylene glycol (50%). The entropy generation rates, thermal and frictional, were determined numerically, and the results demonstrated that non-spherical nanoparticles generally provide greater thermal performance than spherical nanoparticles. Furthermore, they conclude that non-spherical platelet-shaped nanoparticles perform better and that the thermal entropy generation rate gives the highest contribution to the total entropy generation rate.

Behrouz Raei and Sayyed Mohsen Peyghambarzadeh [2] experimentally investigated the thermal efficiency of γ-Al_2O_3/water nanofluids using a double tube heat exchanger with nanoparticles dispersed in distilled water at 0.05–0.15 % vol. Experiments were carried out under a turbulent flow regime ($1.8 \cdot 10^4 < Re < 4 \cdot 10^4$) and

nanofluid inlet temperatures ranging from 45 °C to 65 °C. The results obtained in the study showed that the addition of nanoparticles to the base fluid increases the heat transfer rate by up to 16 %. Furthermore, they find that the thermal performance factor of this nanofluid reaches 1.1 for a concentration of 0.15 % vol. and a Reynolds number equal to 18,000.

Salah Almurtaji et al. [3] present a work that provides a review of the technology used in heat exchangers and analyzes how nanofluids can improve thermo-hydraulic performance. In addition, they discuss the nanofluid development process and emphasize the role of nanoparticles as fundamental elements to increase the thermal efficiency of heat exchangers in future applications.

Xiao Feng Zhou and L. Gao [4] uses the effective differential medium theory, considering the interfacial thermal resistance between solid particles and the host medium, to determine the effective thermal conductivity in nanofluids of non-spherical solid particles. They report an increase in the effective thermal conductivity of non-spherical nanoparticles. Furthermore, they draw attention to the fact that the increase in interfacial thermal resistance between the media causes degradation in the rise in thermal conductivity. The theoretical and experimental results show the non-linear dependence of the effective thermal conductivity on the volume fractions of non-spherical nanoparticles.

Elena V. Timofeeva et al. [5] experimentally evaluate the efficiency of nanofluids and the relationship between thermal conductivity and viscosity. They investigate and model thermal conductivity and viscosity in a fluid consisting of equal ethylene glycol and water volumes. They note that thermal conductivity is affected due to interfacial interactions proportional to the surface area of the nanoparticles and that this also plays a crucial role in determining viscosity. They demonstrate that nanofluid viscosity can be reduced by adjusting the pH of the nanofluid without affecting thermal conductivity.

Máté Petrik et al. [6] carry out studies to numerically investigate the heat transfer in a double tube heat exchanger. They find that there are constructions of heat exchangers capable of transferring the specified heat transfer rate. Still, only one geometry has a lower cost for the material type, inside and outside diameters, and tube length. They find that the thermodynamic performance of the heat exchanger strongly depends on the geometry. They show that the configuration that allows for the highest version can be determined from the initial conditions when specified flow rates and outlet temperatures.

Hamid Shamsabadi et al. [7] perform a numerical simulation to investigate thermal and viscous irreversibilities for Al_2O_3-nanofluid in a pipeline with porous baffles. The Reynolds number, the nanoparticles volume fraction, the number of baffles, and the Darcy number were used to determine the thermal and viscous entropy generation rates and the Bejan number. They determined that the viscous and thermal entropy generation rates decrease with the increasing number of baffles for $N > 4$ and that the reductions are equal to 14 % and 32 %, respectively. In addition, they find that thermal entropy generation is dominant, except in the space between the lower and upper deflectors where the velocity gradients are high.

Adrian Bejan [8] published during the 1980s a review on the application of the second law of thermodynamics with emphasis on aspects related to the entropy generation rate. He discussed relevant aspects related to thermal irreversibility and viscous irreversibility. The most pertinent part of the review highlights how reducing irreversibilities at the component level affects the entire system.

Ahmad Fakheri [9] presents effectiveness as the ratio between the current heat transfer rate and the ideal heat transfer rate, based on the second law of thermodynamics. It defines efficiency as a function of a single dimensionless parameter called the fin analogy. It shows how efficiency and irreversibility defined based on the second law of thermodynamics provide a new avenue for designing and analyzing heat exchangers. It determines expressions for efficiency to be applied to parallel flow, counterflow, and cross-flow heat exchangers. The approach based on the second law of thermodynamics makes the performance analysis of heat exchangers simpler and more elegant. Nogueira E. [10; 11] uses this new way for studying heat exchangers.

Nogueira E. [10] applies the second law of thermodynamics in a shell and tube heat exchanger. Water-ethylene glycol associated with volume fractions of nanoparticles flows in the tube and water flows in the shell. Nanofluids of Ag and Al_2O_3 enters the reservoir at 90 ºC and water at 27 ºC. The volume fractions of nanoparticles are equal to 0.01, 0.10, and 0.25. It is demonstrated that using the second law and efficiency, effectiveness, and irreversibility concepts, the thermal performance of the heat exchanger is strongly affected by the flow regime.

Nogueira E [11] uses the second law and concepts of efficiency and effectiveness to determine the heat transfer rate in a shell and helical coil tube heat exchanger where the water is heated. The objective of the work is to determine the heat transfer rate that satisfies the imposed conditions for heating the solution of water and ammonium nitrate (ANSOL) without crystallization. The Reynolds number, the Nusselt number, and the global heat transfer coefficient are the intermediate quantities needed to reach the objective.

3 Research Methodology

Ethylene glycol flows in the inner tube with dispersed non-spherical Boehmite Alumina nanoparticle fractions. Hot water flows in the annular region opposite the nanofluid. The hot fluid enters the outer tube at a uniform temperature equal to 35 °C. The nanofluid enters the inner tube at a uniform temperature equal to 25°C. The Reynolds number associated with the hot fluid is fixed and equal to 10,000. The Reynolds number associated with the nanofluid varies from 10,000 to 20,000. The

volume fractions of nanoparticles vary between 0.005 and 0.020, from 0.5 % to 2.0 %. Figure 1 schematically represents the counterflow double pipe heat exchanger. Table 1 presents the thermodynamic property values for water, ethylene glycol, and the spherical nanoparticles of Boehmite Alumina. The length of the tube is equal to 1.5 m, and the diameters of the inner and outer tubes are 8.83 mm and 30.85 mm, respectively.

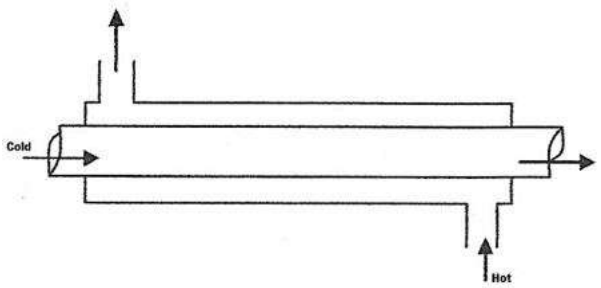

Figure 1 – The design scheme of a counterflow double pipe heat exchanger

Table 1 – Hot (water), cold (ethylene glycol 50 %) fluids and nanoparticles properties

Param.	ρ, $\frac{kg}{m^3}$	k, $\frac{W}{m \cdot K}$	C_p, $\frac{J}{kg \cdot K}$	μ, 10^{-3} $\frac{kg}{m \cdot s}$	v, 10^{-6} m/s^2	α, 10^{-6} m/s^2
Hot	994	0.623	4178	0.72	0.724	0.150
Cold	1067	0.38	3300	3.39	24.045	0.108
Al_2O_3	3950	31.9	873	–	–	9.250
B alum.	3050	30	618	–	–	15.90

Table 2 below was included in the numerical article published by Mostafa Monfared et al. [1] and presented coefficients that characterize non-spherical nanoparticles concerning dynamic and thermal aspects. The coefficient C_k characterizes the thermal conductivity, and the coefficients A_1 and A_2 characterize the dynamic viscosity. These coefficients are used in the present analytical model.

Table 2 – Coefficients that characterize the non-spherical shape of nanoparticles in dynamic viscosity and thermal conductivity [1]

Type	C_k	A_1	A_2
Platelets	2.61	37.1	612.6
Blades	2.74	14,6	123.3
Cylindrical	3.95	13.5	904.4
Bricks	3.37	1.9	471.4

The properties of the nanofluids are given by:

$$\rho_{nano} = \rho_{Particle}\,\phi + (1-\phi)\,\rho_C; \quad (1)$$

$$\mu_{nano} = \frac{\mu_C}{(1-\phi)^{2.5}}; \quad (2)$$

$$\mu_{nano} = \mu_C\,(1 + A_1\,\phi + A_2\phi^2)\;for\;non - spherical\;shape; \quad (3)$$

$$Cp_{nano} = \frac{Cp_{Particle}\,\rho_{Particle}\,\phi + (1-\phi)\,Cp_C\,\rho_C}{\rho_{nano}}; \quad (4)$$

$$k_{nano} = \left[\frac{[k_{Particle}+2\,k_C+2\,(k_{Particle}-k_C)\,(1-0.1)^3\,\phi]}{[k_{Particle}+2\,k_C+2\,(k_{Particle}-k_C)\,(1-0.1)^2\,\phi)]}\right] K_C; \quad (5)$$

$$k_{nano} = k_C\,(1 + C_k\,\phi)\;for\;non - spherical\;shape; \quad (6)$$

$$\nu_{nano} = \frac{\mu_{nano}}{\rho_{nano}}; \quad (7)$$

$$\alpha_{nano} = \frac{k_{nano}}{\rho_{nano}\,Cp_{nano}}; \quad (8)$$

$$Pr_{nano} = \frac{\mu_{nano}}{\alpha_{nano}}, \quad (9)$$

where ϕ – the nanoparticle volume fraction;

$$Nu_{nano} = \frac{\left(\frac{f}{8}\right)(\mathrm{Re}_{nano} - 1000)\,\mathrm{Pr}_{nano}}{1 + 12.7\left(\frac{f}{8}\right)^{\frac{1}{2}}\left(Pr^{\frac{2}{3}} - 1\right)}; \quad (10)$$

where Nu_{nano} – the Nusselt number for the nanofluid. Equation (10) is provided by Gnielinski [12]:

$$f = (0.79\,lnRe_{nano} - 1.64)^{-2}; \quad (11)$$

$$h_{nano} = \frac{Nu_{nano}\,K_{nano}}{D_C}, \quad (12)$$

where h_{nano} – the convective heat transfer coefficient, and D_C is the inner diameter;

$$Nu_h = 0.023\,{Re_h}^{0.8}\,{Pr_h}^{0.4}; \quad (13)$$

$$h_h = \frac{Nu_h \cdot k_h}{Dh_h}; \quad (14)$$

$$Dh_h = D_h - D_c, \quad (15)$$

where Nu_h, h_h, and Dh_h – the Nusselt number, convective heat transfer coefficient, and hydraulic diameter for the hot fluid; D_h – the out diameter;

$$As_C = \pi\,D_C\,L_{DPHE}; \quad (16)$$

$$As_h = \pi\,Dh_h\,L_{DPHE}, \quad (17)$$

where As_C and As_h – the superficial areas of heat exchange; L_{DPHE} – the length of the double pipe heat exchanger;

$$Nu_{Med} = \frac{Nu_{nano} + Nu_h}{2}; \quad (18)$$

$$h_{Med} = Nu_{Med}\left(\frac{K_{nano}}{D_C}\right) \quad (19)$$

$$A_{Med} = \frac{As_h + As_C}{2}; \quad (20)$$

$$Uo = \frac{1}{\frac{1}{h_{Med}}}, \quad (21)$$

where Uo – the global convective heat transfer coefficient;

$$Ac_C = \frac{\pi\, {D_C}^2}{4}; \quad (22)$$

$$Ac_h = \frac{\pi\, {Dh_h}^2}{4}; \quad (23)$$

where Ac_C and Ac_h – the cross-sectional areas of the inner and outer tubes, respectively;

$$\dot{m}_h = \frac{Re_h\, \mu_h\, Ac_h}{Dh_h}; \quad (24)$$

$$\dot{m}_C = \frac{Re_{nano}\, \mu_{nano}\, Ac_C}{D_C}; \quad (25)$$

where $\dot{m}_h$ and $\dot{m}_C$ – the mass flow rate of hot and cold fluid, respectively;

$$C_h = \dot{m}_h\, Cp_h; \quad (26)$$

$$C_{nano} = \dot{m}_C\, Cp_{nano}; \quad (27)$$

where C_h and C_{nano} – heat capacity of hot and nanofluid, respectively;

$$C^* = \frac{C_{min}}{C_{max}}; \quad (28)$$

$$NTU = \frac{Uo\, A_{Med}}{C_{min}}; \quad (29)$$

where NTU is the number of the transfer unit;

$$Fa = \left(\frac{NTU}{2}\right)(1 - C^*), \quad (30)$$

where Fa – the nondimensional fin analogy number for the counterflow heat exchanger;

$$\eta_T = \frac{tanh(Fa)}{Fa}; \quad (31)$$

$$\varepsilon_T = \frac{1}{\frac{1}{\eta_T\, \mathrm{NTU}} + \frac{1 + \mathrm{C}^*}{2}}; \quad (32)$$

where η_T – the thermal efficiency; ε_T – the effectiveness;

$$\dot{Q} = (Th_i - Tc_i)\, C_{min}\, \varepsilon_T; \quad (33)$$

$$\dot{Q}_{max} = (Th_i - Tc_i)\, C_{min}; \quad (34)$$

where $\dot{Q}$ – the heat transfer rate;

$$Th_o = Th_i - \frac{\dot{Q}}{\dot{m}_h\, Cp_h}; \quad (35)$$

$$Tc_o = Tc_i + \frac{\dot{Q}}{\dot{m}_c\, Cp_{nano}}; \quad (36)$$

$$\sigma_T = \left(\frac{C_h}{C_{min}}\right) ln\left(\frac{Th_o}{Th_i}\right) + \left(\frac{C_{nano}}{C_{min}}\right) ln\left(\frac{Tc_o}{Tc_i}\right); \quad (37)$$

where σ_T – the thermal irreversibility;

$$\dot{S}_{Tgen} = \sigma_T\, C_{min}; \quad (38)$$

where $\dot{S}_{Tgen}$ – the thermal entropy generation rate;

$$V_C = \frac{\dot{m}_C}{\rho_{nano}\, Ac_C}; \quad (39)$$

$$V_h = \frac{\dot{m}_h}{\rho_{nano}\, Ac_h}; \quad (40)$$

$$f_C = \frac{0.316}{{Re_{nano}}^{0.25}}; \quad (41)$$

$$f_h = \frac{0.316}{{Re_h}^{0.25}}; \quad (42)$$

where f_C and f_h – the friction factors for cold and hot fluids, respectively;

$$\Delta P_C = \frac{f_C\, \left(\frac{L_{DPHE}}{D_C}\right) \rho_{nano}\, {V_C}^2}{2}; \quad (43)$$

$$\Delta P_h = \frac{f_h\, \left(\frac{L_{DPHE}}{Dh_h}\right) \rho_h\, {V_h}^2}{2}; \quad (44)$$

where ΔP_h and ΔP_C – the pressure drops for hot and cold fluids, respectively;

$$Pc_2 = Ph_2 = Patm; \quad (45)$$

where $Pc_2\ and\ Ph_2$ – the outlet pressures (according to the hypothesis).

Then:

$$Pc_1 = Pc_2 + \Delta P_C; \quad (46)$$

$$Ph_1 = Ph_2 + \Delta P_h; \quad (47)$$

$$Pc_{21} = \frac{Pc_2}{Pc_1}; \quad (48)$$

$$Ph_{21} = \frac{Ph_2}{Ph_1}; \quad (49)$$

$$R = \frac{Th_i - Th_o}{Tc_o - Tc_i}; \quad (50)$$

$$\sigma_f = \left(\frac{C_h}{C_{min}}\right) ln(Ph_{21}) + \left(\frac{C_{nano}}{C_{min}}\right) R\, ln(Pc_{21}); \quad (51)$$

$$\dot{S}_{fgen} = \sigma_f \, C_{min}; \tag{52}$$

where σ_f and $\dot{S}_{fgen}$ – the viscous irreversibility and the viscous entropy generation rate;

Finally, we have:

$$Be = \frac{\dot{S}_{Tgen}}{\dot{S}_{Tgen} + \dot{S}_{fgen}}, \tag{53}$$

where Be – the Bejan thermodynamic number.

4 Results and Discussion

Figure 2 shows values for the Nusselt number as a function of the Reynolds number of the nanofluid for a volume fraction rate equal to 2.0 %.

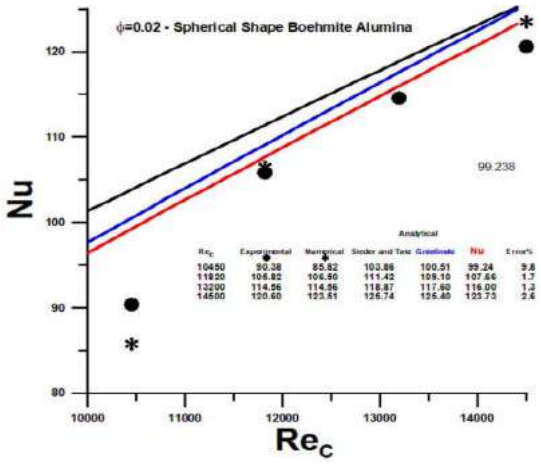

Figure 2 – Nusselt number vs. Reynolds number for Spherical Boehmite Alumina

The equations used to determine the Nusselt number for the nanofluid were independently determined by Sieder, Tate, and Gnielisnki. The highlight in red shows results for the Nusselt number used in work, resulting from the average of the Nusselt numbers in both media. When compared with experimental results presented in [1], the absolute error is less than 10 % within the range of Reynolds number values under analysis. For high Reynolds numbers, the values show better precision.

Figures 3, 4 show values for Nusselt number as a function of Reynolds number for 0.5 % and 2.0 % of nanoparticles fraction. The performance of non-spherical platelet nanoparticles and the low performance for the spherical particle Boehmite Alumina stands out. The results of Boehmite Alumina are inferior to Ethylene Glycol.

Nusselt number as a function of the volume fraction for the Reynolds number of the nanofluid equal to 10,000 is shown in Figure 5. The Nusselt number increases with the addition of the volume fraction for all non-spherical nanoparticles. Conversely, the spherical particles decrease the Nusselt number, emphasizing Boehmite Alumina, which presents values lower than Ethylene Glycol.

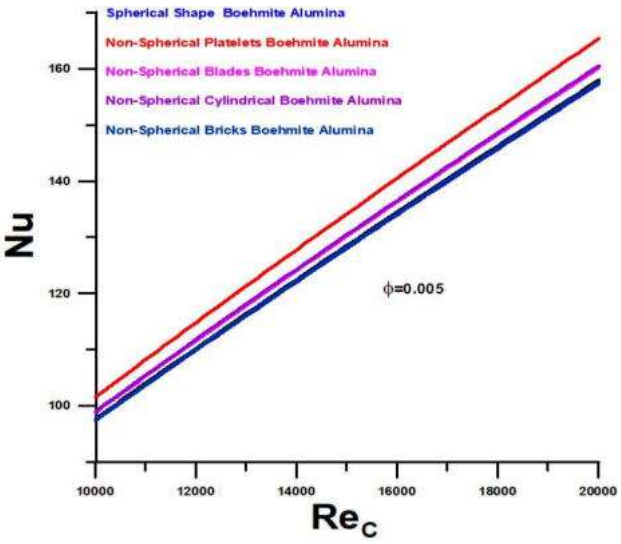

Figura 3 – Nusselt number vs. Reynolds number for the volume fraction of 0.5 % vol.

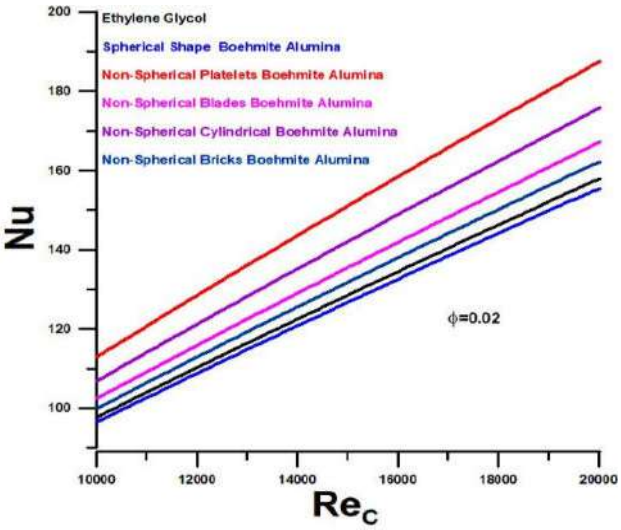

Figura 4 – Nusselt number vs. Reynolds number for the volume fraction of 2.0 % vol.

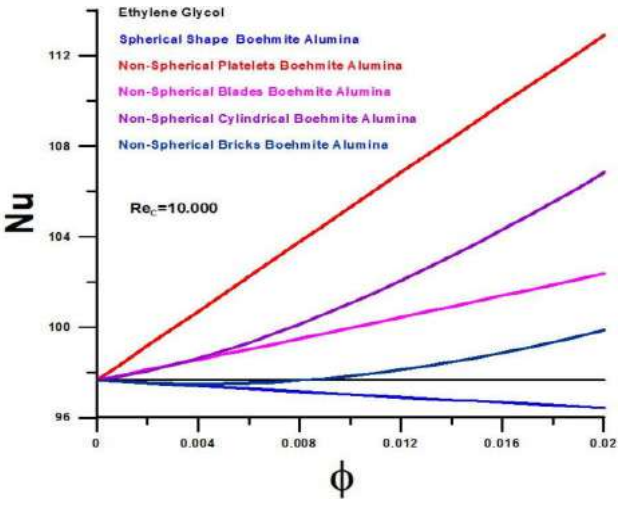

Figure 5 – Nusselt number vs. volume fraction for Re_c = 10,000

The highest value obtained for the Nusselt Number is associated with platelet nanoparticles, followed by cylindrical, blades and bricks. The numbers obtained for the Nusselt number with $Re_c = 20{,}000$ are higher than those obtained for $Re_c = 10{,}000$, as shown in Figure 6. The observed trend remains the same concerning the nanoparticles under analysis.

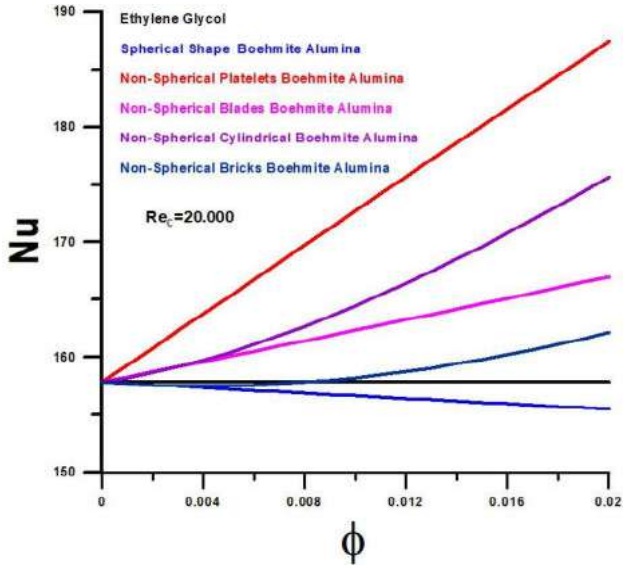

Figure 6 – Nusselt number vs. volume fraction for $Re_c = 20{,}000$

As a function of the volume fraction, values for heat transfer rate are shown in Figure 7.

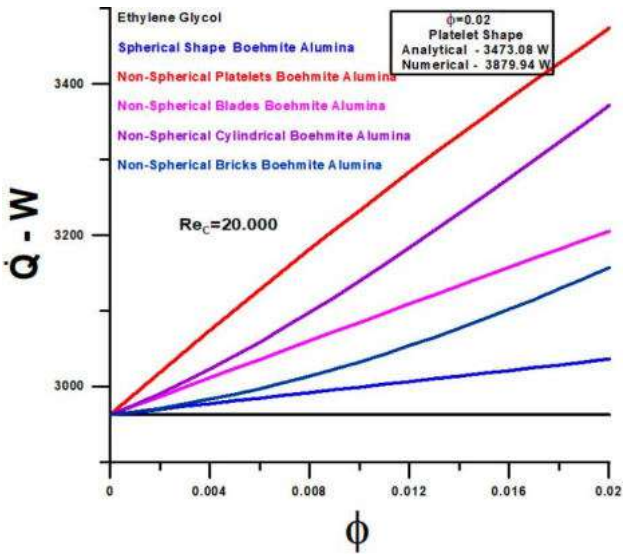

Figure 7 – Heat transfer rate vs. volume fraction for $Re_c = 20{,}000$

The thermal performance presented for non-spherical nanoparticles is equivalent to that already observed. However, it is worth noting that the spherical nanoparticle of Boehmite Alumina has a higher heat transfer rate than Ethylene Glycol for the entire volume fraction range under analysis.

In the highlight, a comparison between the analytical and numerical models is presented, with values taken from the reference [1], with an absolute percentage error equal to 10.5 %.

Pressure drop as a function of volume fraction, with $Re_c = 20{,}000$, is shown in Figure 8.

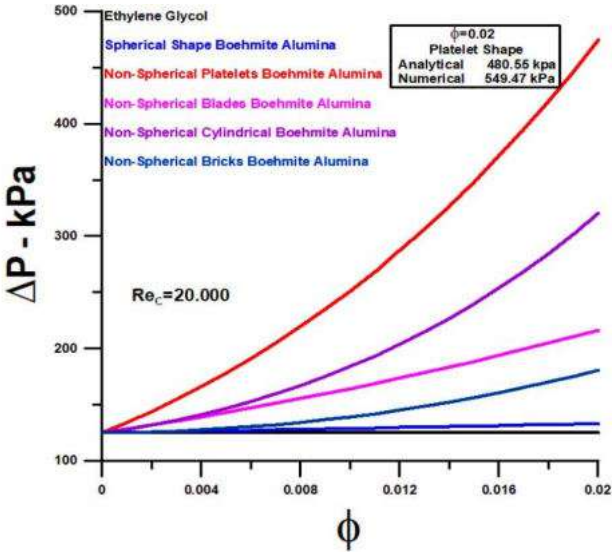

Figure 8 – Pressure drop vs. volume fraction with $Re_c = 20{,}000$

Pressure drop increases with volume fraction for all nanoparticles. The highest value obtained for the pressure drop is associated with platelet nanoparticles, followed by cylindrical, blades, bricks, and spherical nanoparticles, equivalent to the Nusselt number. In the highlight, a comparison between the analytical and numerical models is presented, with values taken from the reference [1], with an absolute percentage error equal to 12.5%.

Figure 9 presents results for thermal efficiency as a function of nanoparticles volume fraction for the highest Reynolds number under analysis, i.e., $Re_c = 20{,}000$.

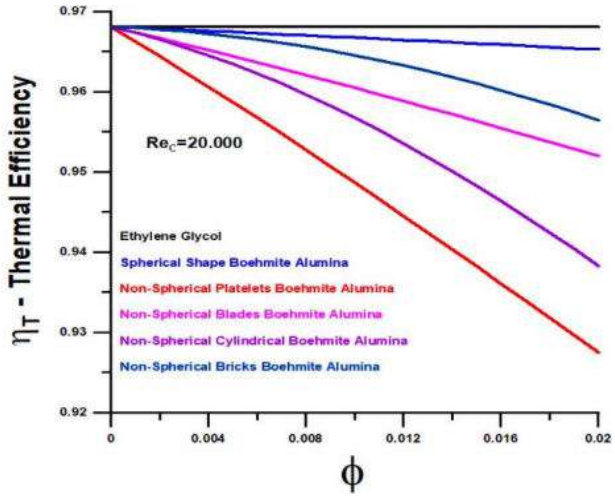

Figure 9 – Thermal efficiency vs. volume fraction for $Re_c = 20{,}000$

Thermal efficiency decreases with increasing volume fraction for all nanoparticles, with a lower value for the nanoparticle that has greater value for the heat transfer rate for non-spherical platelet nanoparticles. However, the thermal efficiency is high in all situations, with a value close to 1 for ethylene glycol. As a partial conclusion, it can be anticipated that there are conditions to increase the Reynolds number or the volume fraction for all nanoparticles.

Thermal irreversibility appears in Figure 10 and shows the opposite trend to thermal efficiency, increasing where efficiency decreases.

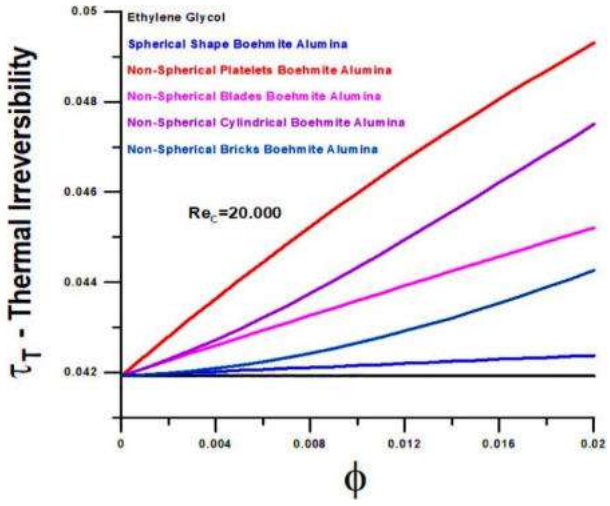

Figure 10 – Thermal irreversibility vs. volume fraction with Re_c = 20,000

However, the irreversibility is significantly low, demonstrating, once again, that there is an enormous possibility of increasing the Reynolds number, or the volume fraction of nanoparticles, to achieve greater thermal performance for the heat exchanger in question.

Figure 11 presents results for viscous irreversibility as a function of volume fraction for the highest Reynolds number under analysis, i.e., Re_c = 20,000.

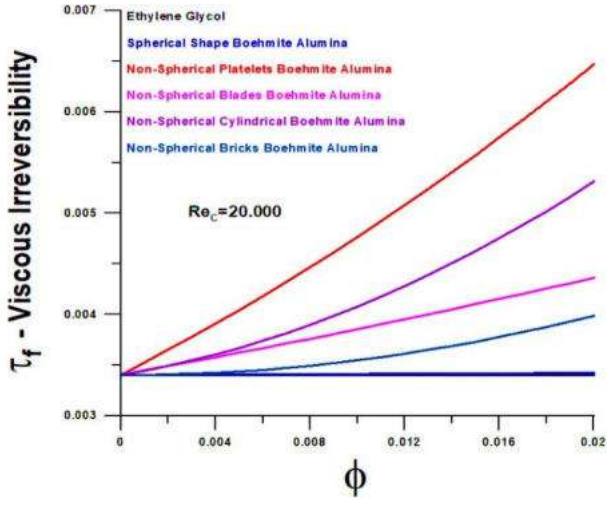

Figure 11 – Viscous irreversibility vs. volume fraction for Re_c = 20,000

Viscous irreversibility increases with the volume fraction for all nanoparticles and presents shallow values in all situations under investigation, with an order of magnitude lower than thermal irreversibility.

Figures 12, 13 show thermal entropy generation rate values as a function of Reynolds number, Re_c = 20,000, and volume fractions of 0.5 % and 2.0 %.

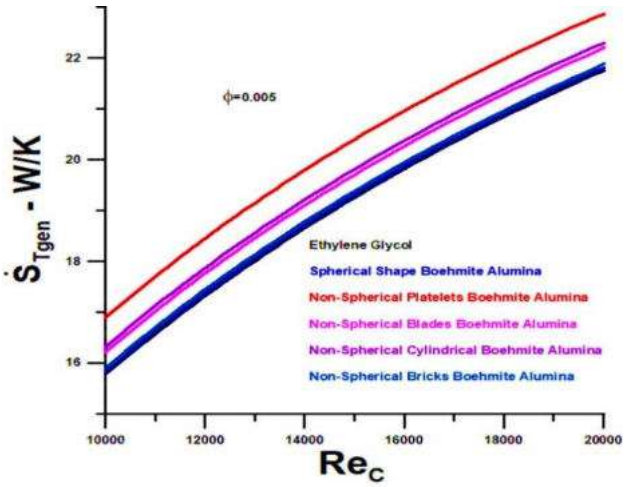

Figure 12 – Thermal entropy generation rate vs. Reynolds number and volume fraction of 0.5 %

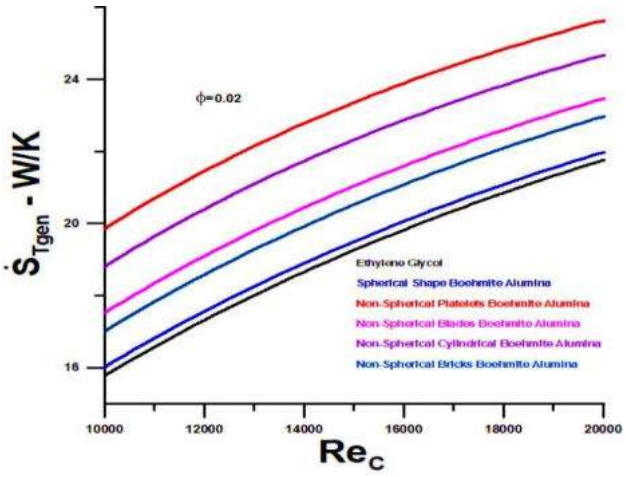

Figure 13 – Thermal entropy generation rate vs. Reynolds number and volume fraction of 2.0 %

Again, the high performance of non-spherical platelet nanoparticles and the low performance for the spherical particle Boehmite Alumina stands out.

Thermal entropy generation rate as a function of volume fraction, for Re_c = 20,000, is shown in Figure 14. The results presented are like those already offered through thermal irreversibility, varying in absolute terms as a function of the minimum thermal capacity under analysis.

The viscous entropy generation rate is shown in Figure 15 and shows values approximately ten times smaller than the thermal entropy rate. The entropy generation rates show higher results for the non-spherical

platelet nanoparticle, followed by the cylindrical, blade, bricks, and spherical Boehmite alumina.

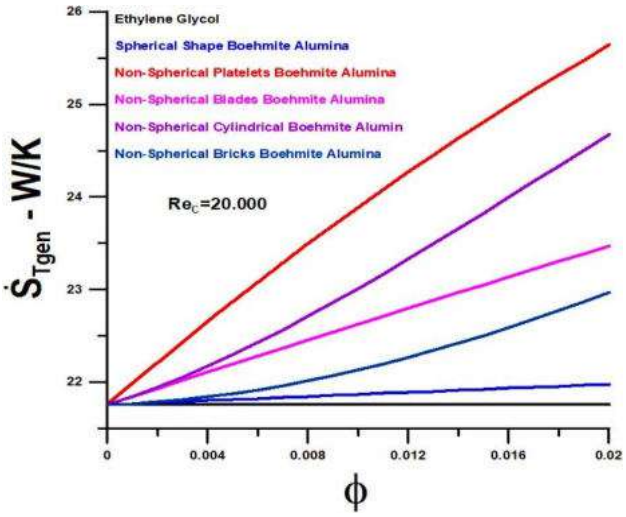

Figure 14 – Thermal entropy generation rate vs. volume fraction for Re_c = 20,000

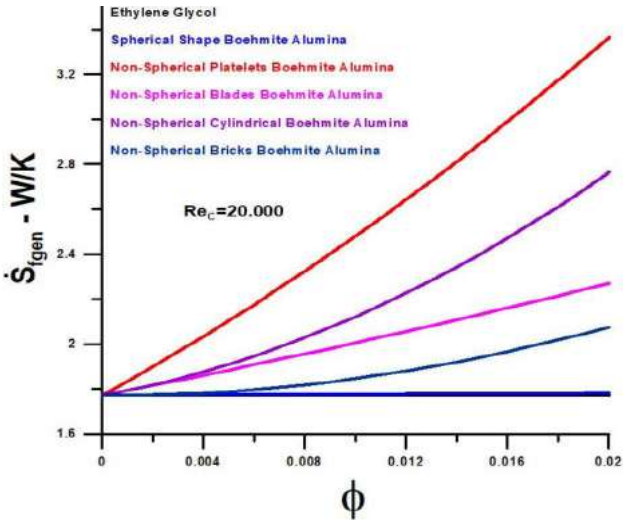

Figure 15 – Viscous entropy generation rate vs. volume fraction for Re_c = 20,000

Figure 16 shows the relationship between thermal entropy generation rates and the total entropy generation rate, represented by the thermodynamic Bejan number. The results show that the rate of thermal entropy generation is prevalent, with very high values, close to 1, with a tendency to fall for non-spherical nanoparticles as the volume fraction increases – a highlight for non-spherical platelet particles. A similar result is demonstrated for thermal efficiency, as already discussed, where non-spherical platelet particle has minor efficiency compared with the others.

Figures 17, 18 show exit temperatures for the hot fluid as a function of the Reynolds number. The outlet temperature decreases with increasing Reynolds number. The non-spherical platelet nanoparticle has lower exit temperatures compared to other nanoparticles. When the nanoparticle volume fraction is greater than 2.0 %, the exit temperature is lower than the volume fraction of 5.0 %.

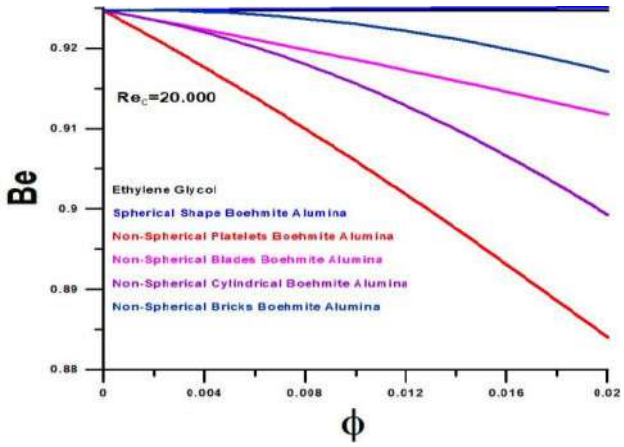

Figure 16 – Bejan vs. volume fraction for Re_c = 20,000

Figure 19 shows the exit temperature as a function of the volume fraction for Reynolds equal to 20,000. The exit temperature decreases with the addition of the Reynolds number.

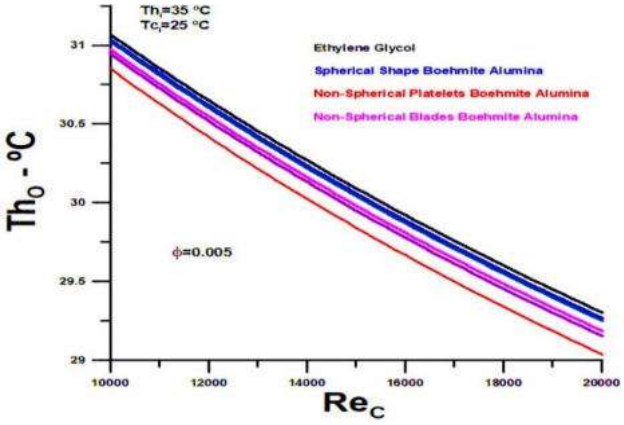

Figure 17 – Hot outlet temperature vs. Reynolds number for the volume fraction of 0.5 %

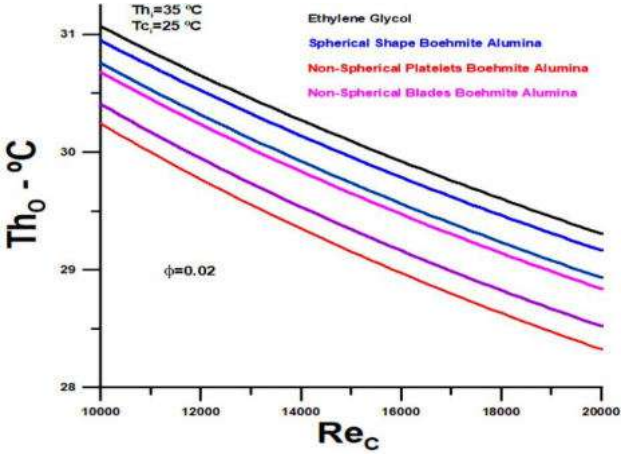

Figure 18 – Hot outlet temperature vs. Reynolds number for the volume fraction of 2.0 %

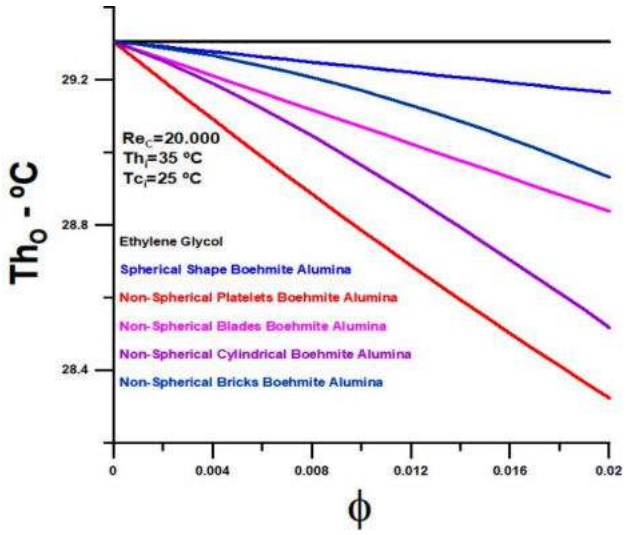

Figure 19 – Hot outlet temperature vs. volume fraction for Re_c = 20,000

The results presented in Figures 17–19 demonstrate, once again, that the heat exchanger has the potential to increase thermal performance, with an increase in Reynolds numbers in both fluids and, or an increase in the percentage of nanoparticles.

Therefore, it is added, for analysis, an expansion for the Reynolds number and the volume fraction, as shown in Figures 20, 21. In these cases, the platelet nanoparticle is considered for analysis since it has better thermal performance.

The heat transfer rate for the non-spherical platelet nanoparticle, with Reynolds number magnification to 40,000 and volume fraction to 8.0 %, asymptotically approximates the maximum exchange possible with the current heat exchanger configuration.

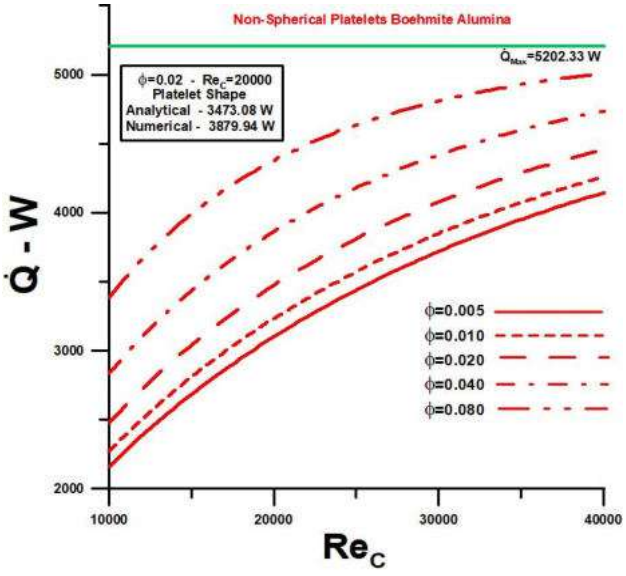

Figure 20 – Heat transfer rate actual and maximum vs. Reynolds number with volume fractions

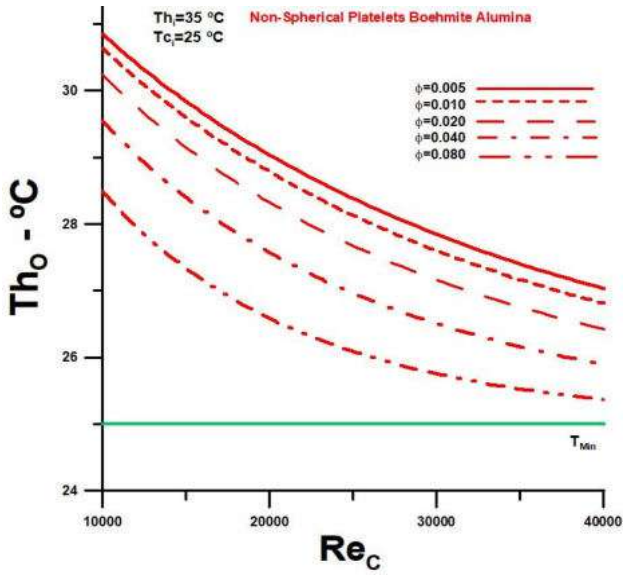

Figure 21 – Outlet hot temperature actual and minimum vs. Reynolds number with volume fractions

The exit temperature for the non-spherical platelet nanoparticle, with Reynolds number magnification to 40,000 and volume fraction to 8.0 %, asymptotically approximate the minimum possible temperature for the current heat exchanger configuration.

The latest results presented in Figures 20, 21 consolidate the conclusions previously presented in this work, and demonstrate that non-spherical nanoparticles, especially platelet nanoparticles, have great potential to improve the thermal performance of heat exchangers in general.

5 Conclusions

Non-spherical nanoparticles dispersed in a mixture of water and ethylene glycol (50 %) were used in an analytical study counterflow double pipe heat exchanger, applying the second law of thermodynamics.

The effect of nanoparticle shapes on the thermodynamic performance of the heat exchanger was analyzed. The analyzed nanoparticles were spherical Boehmite Alumina nanoparticles and non-spherical Boehmite Alumina nanoparticles of platelets, cylindrical, blades, and bricks.

The results of the analytical study were compared with numerical and experimental results presented in the literature regarding the Nusselt number, heat transfer rate, and pressure drop and given maximum absolute error equal to 12.5 %.

The main conclusions of the work are as follows. Firstly, non-spherical nanoparticles have better thermal performance than ethylene glycol (50 %) and spherical nanoparticles.

Secondly, the highlight regarding thermal performance is for non-spherical platelet nanoparticles.

Thirdly, thermal efficiency drops with the volume fraction of nanoparticles. Also, thermal irreversibility increases with the volume fraction of nanoparticles.

Additionally, the relationship between the thermal entropy generation rate and the total entropy generation rate, represented by the Bejan number, is relatively high.

Finally, the analyzed heat exchanger presents better thermal performance with an increase in the Reynolds number in both fluids and an increase in the volume fraction of the nanoparticles concerning what was studied numerically.

References

1. Monfared, M., Shahsavar, A., Bahrebar, M. R. (2019). Second law analysis of turbulent convection flow of boehmite alumina nanofluid inside a double-pipe heat exchanger considering various shapes for nanoparticle. *Journal of Thermal Analysis and Calorimetry*, Vol. 135, pp. 1521-1532, doi: 10.1007/s10973-018-7708.
2. Raei, B., Peyghambarzadeh, S. M. (2019). Measurement of local convective heat transfer coefficient of alumina-water nanofluids in a double tube heat exchanger. *Journal of Chemical and Petroleum Engineering*, Vol. 53(1), pp. 25-36, doi: 10.22059/jchpe.2019.265521.1247.
3. Almurtaji, S., Ali, N., Teixeira, J. A., Addali, A. (2020). On the role of nanofluids in thermal-hydraulic performance of heat exchangers – A review. *Nanomaterials*, Vol. 10, 734, doi: 10.3390/nano10040734.
4. Zhou, X. F., Gao, L. (2006). Effective thermal conductivity in nanofluids of non-spherical particles with interfacial thermal resistance: Differential effective medium theory. *Journal of Applied Physics*, Vol. 100, 024913, doi: 10.1063/1.2216874.
5. Timofeeva, E. V., Routbort, J. L., Singh, D. (2009). Particle shape effects on thermophysical properties of alumina nanofluids. *Journal of Applied Physics*, Vol. 106, 014304, doi: 10.1063/1.3155999.
6. Petrik, M., Szepesi, G., Jármai, K. (2018). Optimal design of double-pipe heat exchangers. *Advances in Structural and Multidisciplinary Optimization*, pp. 755-764, doi: 10.1007/978-3-319-67988-4_57.
7. Shamsabadi, H., Rashidi, S., Esfah, J. A. (2018). Entropy generation analysis for nanofluid flow inside a duct equipped with porous baffles. *Journal of Thermal Analysis and Calorimetry*, Vol. 135, pp. 1009-1019, doi: 10.1007/s10973-018-7350-4.
8. Bejan, A. (1987). The thermodynamic design of heat and mass transfer processes and devices. *Heat and Fluid Flow*, Vol. 8(4), pp. 258-276.
9. Fakheri, A. (2007). Heat exchanger efficiency. *Transactions of the ASME*, Vol. 129, pp. 1268-1276, doi: 10.1016/j.applthermaleng.2017.05.076.
10. Nogueira, E. (2020). Thermal performance in heat exchangers by the irreversibility, effectiveness, and efficiency concepts using nanofluids. *Journal of Engineering Sciences*, Vol. 7, pp. F1-F7, doi: 10.21272/jes.2020.7(2).f1.
11. Nogueira, E. (2021). Efficiency and effectiveness thermal analysis of the shell and helical coil tube heat exchanger used in an aqueous solution of ammonium nitrate solubility (ANSOL) with 20% H_2O and 80% AN. *Journal of Materials Science and Chemical Engineering*, Vol. 9, pp. 24-45, doi: 10.4236/msce.2021.96003.
12. Gnielinski, V. (1976). New equations for heat and mass transfer in turbulent pipe and channel flow. *International Chemical Engineering*, Vol. 16(2), pp. 359-68.

JOURNAL OF ENGINEERING SCIENCES

Volume 9, Issue 1 (2022)

Salahudeen N., Alhassan A. (2022). Adsorption of crystal violet on rice husk activated carbon. Journal of Engineering Sciences, Vol. 9(1), pp. F11-F15, doi: 10.21272/jes.2022.9(1).f2

Adsorption of Crystal Violet on Rice Husk Activated Carbon

Salahudeen N.*, Alhassan A.

Department of Chemical and Petroleum Engineering, Bayero University, Gwarzo Rd, PMB 3011, Kano, Nigeria

Article info:
Submitted: December 17, 2021
Accepted for publication: March 18, 2022
Available online: March 22, 2022

***Corresponding email:**
nsalahudeen.cpe@buk.edu.ng

Abstract. The need to develop effective technology for the treatment of liquid effluent of dye-intensive industries such as textile, rubber, paint, and printing is synonymous with the need to save the life-threatening risks posed by these carcinogenic and mutagenic pollutants on human and aquatic lives. Isotherms of adsorption of crystal violet (CV) on activated carbon (AC) synthesized from rice husk are presented herewith to elucidate the mechanism of the adsorption process of crystal violet dye contaminated water on rice husk activated carbon. AC was synthesized from rice husk via a phosphoric acid activating agent at low temperatures. Langmuir, Freundlich, Temkin and Dubinin–Radushkevich (D-R) isotherm studies were employed. The mean square values for Langmuir, Freundlich, Temkin and D-R models were 0.98, 0.91, 0.94, and 0.63, respectively. Analysis of the isotherms of the adsorption of crystal violet sorbate on the synthesized rice husk sorbent suggested that the adsorption process proceeded via a homogeneous monolayer mechanism. Langmuir isotherm gave the best fit of the adsorption process. Langmuir isotherm constant was –1.40 l/mg, and the equilibrium adsorption capacity was 13.53 mg/g.

Keywords: process innovation, adsorption isotherm, rice husk, activated carbon, crystal violet, energy efficiency.

1 Introduction

Water, an essential lifeline to the survival of humanity and all organisms, is continually being polluted by the day-to-day polluting activities of man, majorly industrial activities. Industrial activities such as textile, rubber, printing, pulp, paper, paint, and cosmetics production employ large volumes of dyes that are eventually released as effluents into the water bodies that provide drinking water for human communities. To avoid or at best reduce the high health risk associated with consumption of the carcinogenic and mutagenic industrial dyes such as crystal violet, effective technology for the treatment of the liquid effluent from dye intensive industries must be given the attention deserves. Dyes are classified as either natural or synthetic. Crystal violet (CV) is one of the dyes used in the textile industry, and it is synthetic. As a synthetic cationic dye, CV is a toxic dye [1, 2].

Treatment of the textile industry's liquid effluent becomes very indispensable to remove dyes and ensure safe effluent discharge to water bodies. Different conventional treatments methods such as precipitation, photo-catalytic decolorization, coagulation, flocculation, membrane separation, adsorption, electrochemical and biological degradation have been examined with varying levels of success by researchers [3]. Of all these methods, the adsorption process has gained more interest in recent times due to its benefits of high efficacy and economic benefits over other methods [4]. Adsorption is a process that occurs when molecules of a gas or liquid solute (sorbate) accumulate on the surface of a solid (sorbent). The adsorption is achieved by the physical or chemical interaction of the sorbate molecules with the active sites presented onto the surface of the sorbent [5–7].

Activated carbon is porous, a carbonaceous material having significant surface area activities for the adsorption of sorbate molecules. Internal pore structure and active sites dominated surfaces of oxygenated functional groups [8–10]. Activated carbon is applied in most industrial water treatment processes such as water treatment plants and municipal waterworks stations. It is also applied to treat industrial liquid and gas effluents as a strategy for pollution control from the source. Activated carbon is also used in other industrial applications where its adsorption potential is exploited for decolorization and deodorization applications such as decolorization of and deodorization of vegetable oil. Activated carbon is synthesized by controlled thermal and acidification of carbonaceous materials such as wood chips, fly ash, and corn cobs rice husk [11–14]. A good choice of raw material for the

synthesis of activated carbon comes with the dual benefit of providing effective adsorption and converting waste to wealth. This work aimed to study the adsorption isotherm of adsorption of dye (CV) contaminated water over a low temperature synthesized activated carbon using rice husk as the raw material.

2 Research Methodology

Sample of rice husk was collected from Gidan Shinkafa Rice Milling Industry, Dakata Area, Kano State. Phosphoric acid and crystal violet powder were purchased, and distilled water was prepared from a water distiller. Equipment used include weighing balance (Model; PE-160), shaker (KJ-201 BS OSCILLATOR), UV-Vis spectrophotometer (Model; Zuzi-4201/20), milling machine, and laboratory oven. Apparatus used include measuring cylinder, conical flask, crucibles, beakers, and spatula.

Dried raw millet stover collected from the farm was washed to remove debris and other impurities. The washed millet stover was sun-dried for two days, after which it was crushed and milled using a milling machine.

Synthesis of activated carbon was carried out at low temperatures using phosphoric acid as the activating agent. 1:2 weight of powdered rice husk and phosphoric acid was measured into a crucible and mixed, which means 5.0 g powdered rice husk plus 10.0 g phosphoric acid. The homogenized mixture was heated at 120 °C for 1 h. After the synthesis, washing to a pH of 7.0 with distilled water was carried out. The washed adsorbent was dried in an oven at 110 °C for 1 h.

Adsorption study of aqueous CV solution (sorbate) on varying samples of synthesized AC (sorbent) was carried out using 50 ml of CV sorbate at a constant initial concentration of 15 mg/l. The adsorption process was achieved by a laboratory shaker's continuous mechanical shaking action. The percentage absorbance (%A) and the equilibrium adsorption capacity of the adsorbent q_e, mg/g, were determined by the following equations:

$$\%A = \frac{C_o - C_e}{C_o} \cdot 100; \quad (1)$$

$$q_e = \frac{C_o - C_e}{m} v, \quad (2)$$

where C_O – the initial concentration of the sorbate; C_e – equilibrium concentration of the sorbate; m – the weight of adsorbent, g; v – the volume of the sorbate.

Isotherm study of the adsorption of CV sorbate on the synthesized sorbent was carried out using Langmuir, Freundlich, Temkin, and Dubini–Radushkevich (D-R) models. Linearized isotherm models were employed. Graphical analysis of the various adsorption parameters of the models obtained from experimental data was carried out to establish the various model parameters.

The Langmuir isotherm mechanism is based on the monolayer adsorption model, and it depicts homogeneity in the adsorbent surface [15]. The Langmuir isotherm model is as given:

$$q_e = \frac{q_\infty b C_e}{1 + b C_e}, \quad (3)$$

where q_∞ – the monolayer theoretical capacity of the adsorbent or the maximum achievable adsorption density (mg of adsorbate per 1 g of adsorbent); b – the Langmuir equilibrium constant, l/mg.

The linearized Langmuir isotherm model is as presented:

$$\frac{C_e}{q_e} = \frac{C_e}{q_\infty} + \frac{1}{q_\infty b}. \quad (4)$$

The Freundlich isotherm mechanism is based on a multilayer adsorption model, and it depicts heterogeneity in the adsorbent surface [16]. The Freundlich isotherm mechanism is based on a multilayer heterogeneous adsorption model. The isotherm model is as given:

$$q_e = K_f C_e^{\frac{1}{n}}, \quad (5)$$

where K_f – the Freundlich multilayer adsorption constant related to bond strength and the dimensionless heterogeneity factor, l/g; n – the adsorption intensity.

The linearized form of the Freundlich isotherm model is as given [17]:

$$log\ q_e = log\ K_f + \frac{1}{n} log\ C_e. \quad (6)$$

The Temkin isotherm mechanism is based on the interaction between the adsorbent surface and the sorbate molecules/ions. The isotherm is developed to assume that the free energy of sorption is a function of the surface coverage [18, 19].

The Temkin isotherm model is as given:

$$A_t C_e = e^{\frac{q_e b_t}{RT}}, \quad (7)$$

where C_e – concentration of the adsorbate at equilibrium, mg/l, q_e – the amount of adsorbate adsorbed at equilibrium, mg/g; T – the temperature, K; R – the ideal gas constant; RT/b_t – a measurement of heat of adsorption; $1/b_t$ – the adsorption potential of the adsorbent, mol/kJ; A_t – Temkin constant as the equilibrium binding constant, l/min, corresponding to the maximum binding energy.

Linearized Freundlich isotherm model is as presented:

$$q_e = \frac{RT}{b_t} ln A_t + \frac{RT}{b_t} ln C_e. \quad (8)$$

The D-R isotherm model is based on Gaussian energy distribution onto a heterogeneous surface. It attempts to estimate the heterogeneity of the surface energies of the adsorbent in an adsorption process. The D-R isotherm model is as given:

$$\frac{q_e}{q_m} = e^{-\beta \varepsilon^2}, \quad (9)$$

where q_m – the theoretical saturation capacity, mg/g; ε – the Polyani potential; β – the Dubinin-Rudushkevich isotherm constant related to the mean free energy of adsorption per mole of the adsorbate, mol^2/kJ^2.

Unlike the other isotherm models, the D-R model makes provision to analyze the type of sorption taking place in an adsorption process. Value of the mean free

energy E, kJ/mol, of adsorption per molecule of the adsorbate approaching the adsorbent from infinity is used to interpret the type of sorption. E is related to β according to [18]:

$$E = \frac{1}{\sqrt{2\beta}}. \quad (10)$$

For a chemisorption process, the value of E ranges between 8–16 kJ/mol, whereas for a purely physical sorption process $E < 8$ kJ/mol [18].

The linearized Dubinin-Redushkevich isotherm model is as presented:

$$lnq_e = lnq_m - \beta\varepsilon^2, \quad (11)$$

where $\varepsilon = RTln\left(1 + \frac{1}{c_e}\right)$.

3 Results

Figure 1 shows the spectrophotometer absorbance of crystal violet (at the wavelength of 565 nm) at varying concentrations of the aqueous crystal violet solution.

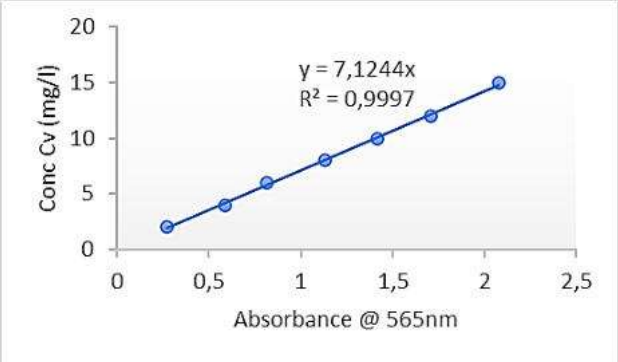

Figure 1 – Spectrophotometer absorbance at a varying concentration of CV

The curve representing the sorbate concentration calibration curve shows a linear relationship between the sorbate concentration and the absorbance. This was used to determine concentrations of sorbate throughout the adsorption study.

Table 1 shows the adsorption equilibrium sorbate concentration at varying contact times.

Table 1 – Equilibrium concentration and adsorption capacity at varying contact time

Time, min	C_e, mg/l	q_e, ml/l
30	6.4	14.3
60	4.8	17.1
90	3.3	19.6
120	2.8	20.3
150	2.2	21.3
180	2.1	21.5
210	1.9	21.9
240	1.5	22.5
270	1.3	22.9
300	1.2	23.0

After starting with the initial sorbate concentration of 15 mg/l, the equilibrium sorbate concentration dropped by 57 % after 30 min to attain 6.4 mg/l. The equilibrium adsorption concentration and adsorption capacity after 30 min were 6.4 mg/l and 14.3 ml/l, respectively.

The equilibrium sorbate concentration value dropped continuously from 6.4 mg/l at 30 min until a relatively constant value of 1.2 mg/l was attained at 300 min. Conversely, the equilibrium adsorption capacity increased continuously from 14.3 ml/l at 30 min until a relatively constant value of 23 mg/l was attained at 300 min. Hence, the adsorption process tends to equilibrium in 300 min.

Figure 2 shows the Langmuir isotherm chart of the adsorption process.

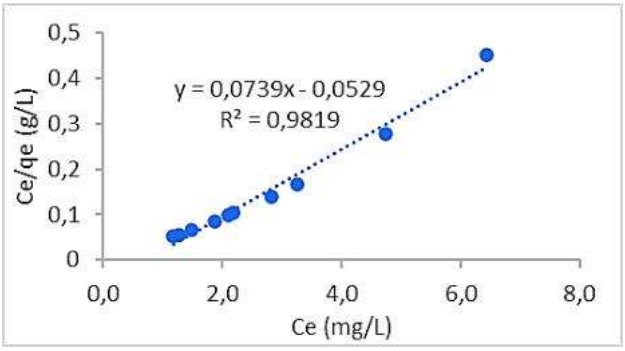

Figure 2 – Langmuir isotherm graph for the adsorption process

A high R^2 of 0.98 showed that the Langmuir model perfectly fit the adsorption mechanism. The graph's slope was 0.074 g/mg. The maximum adsorption capacity of the process was 13.53 mg/g. Langmuir constant b was determined as –1.40 l/mg.

Figure 3 shows the Freundlich isotherm graph for the adsorption of the process.

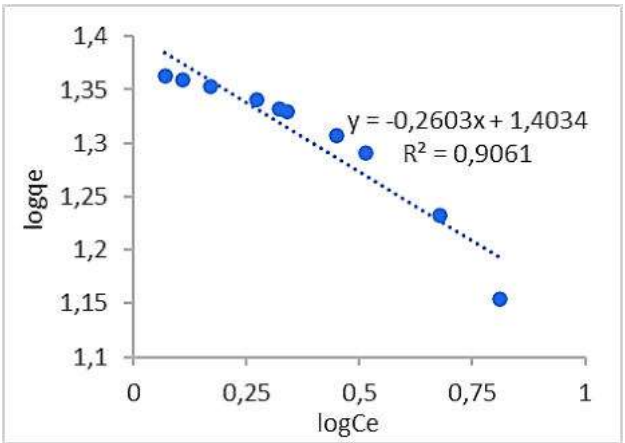

Figure 3 – Freundlich isotherm graph of the adsorption process

The Freundlich model was a fairly representing fit of the adsorption mechanism with a high R^2 of 0.91. The slope and intercept were –0.260 and 1.403, respectively. The Freundlich multilayer adsorption constant K_f was 25.3 l/g, and the dimensionless heterogeneity factor n was –3.84.

Figure 4 presents the Temkin isotherm graph for the adsorption process.

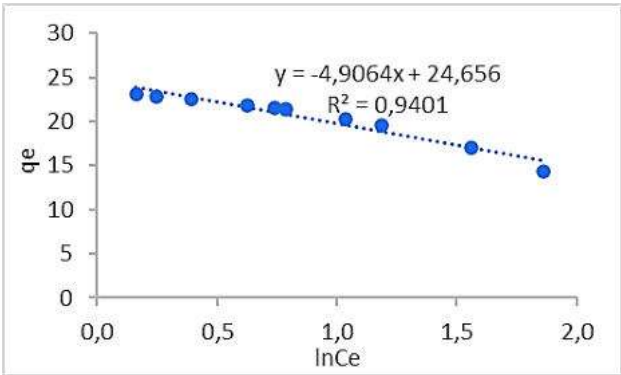

Figure 4 – Temkin isotherm graph of the adsorption process

Freundlich model was also a good fit for the adsorption mechanism having an R^2 of 0.94. The slope and intercept were –4.906 and 24.656, respectively. The adsorption process was conducted at 298 K, using a constant gas value of 8.314 J/(mol·K), the adsorption potential of the adsorbent $1/b_t$ was –0.002 mol/kJ, and the maximum binding energy A_t was 0.007 l/min.

Figure 5 shows the D-R graph for the adsorption process.

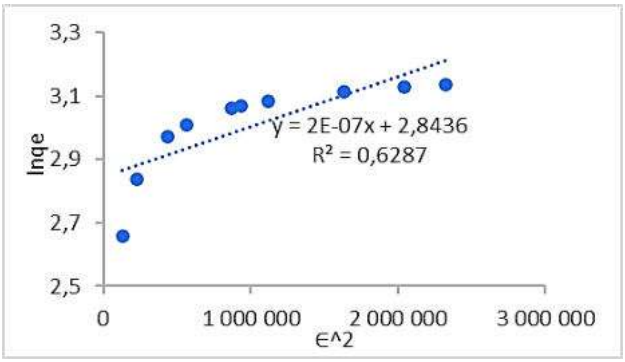

Figure 5 – D-R isotherm graph of the adsorption process

The D-R model did not fit the adsorption mechanism with a poor coefficient of determination, R^2 of 0.63. The slope and intercept were $2.0 \cdot 10^{-7}$ and 4.844, respectively. The theoretical saturation capacity q_m was 17.18 mg/g, and the mean free energy factor of adsorption per mole of the adsorbate β was $-7.0 \cdot 10^{-7}$ mol^2/kJ^2.

Table 2 summarizes the various adsorption parameters determined for the adsorption of CV on the synthesized rice husk AC.

Table 2 – Summary of the various isotherm parameters

Langmuir		Freundlich		Temkin		D-R	
R^2	0.98	R^2	0.91	R^2	0.94	R^2	0.63
q_e, mg/g	13.53	K_f, l/g	25.3	$1/b_t$, mol/kJ	–0.002	q_m, mg/g	17.18
b, l/mg	–1.40	n	–3.84	A_t, l/min	0.007	β, mol^2/kJ^2	$-7.0 \cdot 10^{-7}$

Therefore, the Langmuir isotherm model was the best fit for the adsorption mechanism based on its highest R^2 value of 0.98. Therefore, the adsorption process was homogeneous monolayer adsorption [7, 10]. The equilibrium adsorption capacity was 13.53 mg/g, and the Langmuir constant was negative with a value of –1.40 l/mg.

This implied that the sorbate molecules had a negative binding affinity to the site of the sorbent [15]. Although the Freundlich isotherm gave a high R^2 value of 0.91, the isotherm model was unsuitable for the adsorption mechanism as the Freundlich constant n representing the multilayer adsorption intensity was negative. Hence, the adsorption of CV sorbate molecules on the synthesized AC was not multilayer adsorption. The D-R isotherm representing non-homogenous multilayer adsorption [18] gave the poorest fit of the adsorption mechanism as the R^2 of D-R was the least, having the value of 0.63.

4 Conclusions

Isotherm study of aqueous crystal violet adsorption on activated carbon synthesized from rice husk was carried out using Freundlich, Temkin, Langmuir, and D-R isotherm models.

The R^2 values of the Langmuir, Freundlich, Temkin, and D-R models were 0.98, 0.91, 0.94, and 0.63, respectively. The Langmuir isotherm constant b was –1.40 l/mg. Freundlich isotherm constant n was –3.84. Temkin isotherm constant was 0.007 l/min, and D-R isotherm constant was $-7.0 \cdot 10^{-7}$ mol^2/kJ^2.

Analysis of the isotherms of the adsorption of crystal violet sorbate on the synthesized rice husk sorbent suggested that the adsorption process was homogeneous monolayer adsorption having Langmuir isotherm as the best fit of the adsorption mechanism. This result is consistent with the literature. Most adsorption studies of crystal violet and methyl blue dyes have been reported to fit well with the Langmuir isotherm model [10, 20, 21].

The equilibrium adsorption capacity was determined as 13.53 mg/g. A negative Langmuir constant obtained suggested that the sorbate molecules had a negative binding affinity to the site of the sorbent. The Temkin isotherm gave the second-best fit for the adsorption mechanism with an R^2 value of 0.94. The D-R model was the poorest fit of the adsorption mechanism of this study.

References

1. Hao, O. J., Kim, H., Chiang, P. C. (2000). Decolorization of waste water. *Critical Reviews in Environmental Science and Technology*, Vol. 30(4), pp. 449-505.
2. Bertolini, T. C. R., Izidoro, J. C., Magdalena, C. P., Fungaro, D. A. (2013). Adsorption of crystal violet dye from aqueous solution to zeolites from coal fly and bottom ashes. *Orbital: The Electronic Journal of Chemistry*, Vol. 5(3), pp. 179-191.
3. Ma, H. T., Ly, H. C., Pham, N. B., Nguyen, D. C., Vo, K. T. D., Tuan, P. D. (2017). Effect of the carbonization and activation process on the adsorption capacity of rice husk activated carbon. *Vietnam Journal of Science and Technology*, Vol. 55(4), pp. 494-494.
4. Parshetti, G. K., Parshetti, S. G., Telke, A. A., Kalyani, D. C., Doong, R. A., Govindwar, S. P. (2011). Biodegradation of crystal violet by Agro bacterium radiobacter. *Journal of Environmental Sciences*, Vol. 23(8), pp. 1384-1393.
5. Ojedokun, A. T., Bello, O. S. (2016). Sequestering heavy metals from wastewater using cow dung. *Water Resources and Industry*, Vol. 13, pp. 7-13.
6. Sarma, G. K., Gupta, S. S., Bhattacharyya, K. G. (2019). Nanomaterials as versatile adsorbents for heavy metal ions in water: A review. *Environ. Sci. Pollut. Control Ser.*, Vol. 26, pp. 6245-6278.
7. Somsesta, N., Sricharoenchaikul, V., Aht-Ong, D. (2020). Adsorption removal of methylene blue onto activated carbon/cellulose biocomposite films: equilibrium and kinetic studies. *Mater. Chem. Phys.*, Vol. 240, 122221.
8. Danish, M., Ahmad, M., T. (2018). A review on utilization of wood biomass as a sustainable precursor for activated carbon production and application. *Renew. Sustain. Energy Rev.*, Vol. 87, pp. 1-21.
9. Gonzalez-Garcia, P. (2018). Activated carbon from lignocellulosics precursors: A review of the synthesis methods, characterization techniques and applications. *Renew. Sustain. Energy Rev.*, Vol. 82; pp. 1393-1414.
10. Zakaria, R., Jamalluddin, N. A., Bakar, Z. M. A. (2021). Effect of impregnation ratio and activation temperature on the yield and adsorption performance of mangrove based activated carbon for methylene blue removal. *Results in Materials*, Vol. 10, 100183.
11. Canales-Flores, R. A., Prieto-García, F. (2020). Taguchi optimization for production of activated carbon from phosphoric acid impregnated agricultural waste by microwave heating for the removal of methylene blue. *Diam. Relat. Mater.*, Vol. 109, 108027.
12. Mandal, A., Bar, N., Das, S. K. (2020). Phenol removal from wastewater using low-cost natural bioadsorbent neem (Azadirachta Indica) leaves: Adsorption study and MLR modeling. *Sustainable Chemistry and Pharmacy*, Vol. 17, 100308.
13. Mansour, R. A., El Shahawy, A. Attia, A., Beheary, M. S. (2020). Brilliant green dye biosorption using activated carbon derived from guava tree wood. *Int. J. Chem. Eng.*, Vol. 20, 8053828.
14. Tang, S. H., Zaini, M. A. A. (2020). Development of activated carbon pellets using a facile low-cost binder for effective malachite green dye removal. *J. Clean. Prod.*, Vol. 253, 119970.
15. Islam, M. A., Chowdhury, M. A., Mozumder, M. S. I., Uddin, M. T. (2021). Langmuir adsorption kinetics in liquid media: Interface reaction model. *ACS Omega*, Vol. 6, pp. 14481-14492.
16. Sadegh, H., Ali, G.A.M., Gupta, V. K., Makhlouf, A. S. H., Shahryari-Ghoshekandi, R., Nadagouda, M. N., Sillanpaa, M., Megiel, E. (2017). The role of nanomaterials as effective adsorbents and their applications in wastewater treatment. *J. Nanostructure Chem.*, Vol. 7, pp. 1-14.
17. Salahudeen, N., Ahmed, A. S., Al-Muhtaseb, A. H., Dauda, M., Waziri, S. M., Jibril B. Y. and Al-Sabahi, J. (2015). Synthesis, characterization and adsorption study of nano-sized activated alumina synthesized from kaolin using novel method. *Powder Technology*, Vol. 280, pp. 266-272.
18. Das, B., Mondal, N. K., Bhaumik, R., Roy, P. (2014). Insight into adsorption equilibrium, kinetics and thermodynamics of lead onto alluvial soil. *Int. J. Environ. Sci. Technol.*, Vol. 11, pp. 1101-1114.
19. Said, K. A. M., Ismail, N. Z., Jama'in, R. L., Alipah, N. A. M., Sutan, N. M., Gadung, G. G., Baini, R., Zauzi, N. S. A. (2018). Application of Freundlich and Temkin Isotherm to Study the Removal of Pb(II) Via Adsorption on Activated Carbon Equipped Polysulfone Membrane. *International Journal of Engineering & Technology*, Vol. 7(3.18), pp. 91-93.
20. Senthilkumaar, S., Kalaamani, P., Subburaam, C. V. (2006). Liquid phase adsorption of Crystal violet onto activated carbons derived from male flowers of coconut tree. *Journal of Hazardous Materials*, Vol. B136, pp. 800-808.
21. Aydogmus, R., Depci, T., Sarikaya, M., Kul, A. R., Onal, Y. (2016). Adsorption of Crystal violet on activated carbon prepared from coal flotation concentrate. *IOP Conf. Series: Earth and Environmental Science*, Vol. 44, 052022.

JOURNAL OF ENGINEERING SCIENCES

Volume 9, Issue 1 (2022)

Yurchenko O., Sklabinskyi V., Ochowiak M., Ostroha R., Gusak O. (2022). Rational choice of a basket for the rotational vibropriller. Journal of Engineering Sciences, Vol. 9(1), pp. F16-F20, doi: 10.21272/jes.2022.9(1).f3

Rational Choice of a Basket for the Rotational Vibropriller

Yurchenko O.[1[0000-0002-3047-6654]], Sklabinskyi V.[1[0000-0001-9388-5861]], Ochowiak M.[2[0000-0003-1543-9967]], Ostroha R.[1*[0000-0003-0045-3416]], Gusak O.[1[0000-0003-4372-5776]]

[1] Faculty of Technical Systems and Energy Efficient Technologies, Sumy State University, 2, Rymskogo-Korsakova St., 40007, Sumy, Ukraine;
[2] Faculty of Chemical Technology of Poznan University of Technology, Poznan University of Technology, 4, Berdychowo St., 60-965 Poznan, Poland

Article info:
Submitted: March 11, 2021
Accepted for publication: June 3, 2022
Available online: June 7, 2022

***Corresponding email:**
r.ostroga@pohnp.sumdu.edu.ua

Abstract. The use of processing units for the production of mineral fertilizers in the industry in today's market requires improved product quality and increased productivity. As a result, there is a need to change the design of existing units or some structural elements. Rotary vibroprillers, having a relatively simple design, can be of different designs that directly affect the productivity indicators mentioned above. The study considers the influence of the shape of the basket bottom on the quality of the rotational vibroprillers. After using the governing equation of prills motion in the airflow, a program was developed for automatic control of the rotational speed of the priller based on changes in melt loads. It is established that the size of the spray swath can be changed by varying the rotational speed of the priller. There is a tendency to affect the vibropriller performance by controlling the rotational speed and shape of the basket bottom without performance degradation.

Keywords: process innovation, jet flow, droplet formation, oscillations, energy efficiency.

1 Introduction

For calculating the prilling process of mineral fertilizers in prilling towers, it is essential to choose both the number of prillers to be installed in this tower and the shape of the bottom of the prilling basket of these prillers [1].

All these requirements drive by the need for uniform distribution of droplets and subsequently (as the crystallization of the melt occurs) prills in the cross-section of the prilling tower.

Basically, several types of prillers are used to disperse mineral fertilizer melts. These are static vibrating prillers and rotational prillers [2], which have won the favor of mineral fertilizers producers due to the prills' fine dispersion composition. Slightly less, but centrifugal mechanical prillers are also used with vibration on the melt flow.

Static prillers are currently less used in new prilling towers because they have a low flow rate (capacity t/hour) for mineral fertilizer melt, and it is impossible to change the distribution of prills in the cross-section of the prilling tower by varying the flow rate (capacity) of fertilizer melt which is typical for the production process.

Figure 1 shows an example of a basket design used to distribute the fertilizer melt into streams (jets) and inlets to the basket of a static priller.

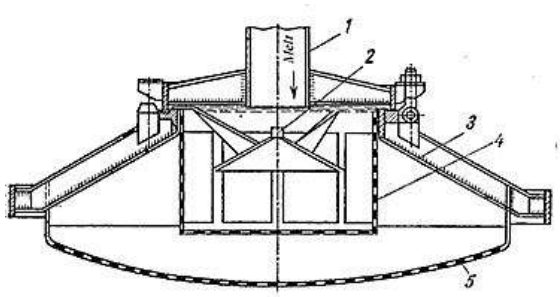

Figure 1 – Static priller: 1 – supply nozzle; 2 – guide cone; 3 – priller casing; 4 – filter screen

Such disadvantages resulting from the melt leakage of the static prillers occurred under the action of hydrostatic pressure, and all the jets of the melt flow nearly at the same speed. This ensures the same conditions for shattering them into droplets only with a constant flow rate of mineral fertilizers [3].

2 Literature Review

In order to make the process of prill formation of high quality, one can use different methods. Thus, in [4], physical modeling of the prill formation process was carried out with the study of the condition of suspension bed formation, which determines the nature of the interaction of the dispersed suspension and the dispersed solid phase. The temperature of prill formation of organic suspensions was experimentally verified, and the operating parameters of the process were determined, and the kinetics of prill growth depending on the dehydration temperature of organic suspensions were studied.

The development of the optimal shape of the working parts of the technological installation can also significantly change the quality of the resulting product. In [5], a mathematical model for estimation of the unsteady concentration of fine particles in the gas flow by time and by the height of the working space of the unit was derived from the description of the physical model of the air separation process for detection the rotating suspended bed and to ensure the loading and unloading of the pneumatic classifier. It was found that the diamond-shaped pneumatic classifier is effective in the separation of prill material, reaching up to 95 % of the target fraction.

The device with inclined perforated boards [6] can provide an active aerodynamic mode. As a result, it is possible to achieve a reduction in the capture of the coarse grade.

The separation or movement of particles and the separation of coarse or fine particles of the fluid flow are critical for ensuring product quality in most industrial processes that involve filtration [7]. The existence of different oscillation modes of droplets depending on the frequencies of the superimposed oscillation is explained in [8] using the proposed model. The study proves this model, and its realization allows us to define analytical dependence for the strain-rate component of droplets.

When designing any machinery, there should be the minimum required set of technical components that provide specific functions [9], and the use of different methods of the hydrodynamic resistance of the operating fluid in rotary machines can increase processing efficiency to obtain finely-dispersed homogeneous mixtures with specific characteristics [10]. Thus, the study [11] confirmed the need for more flexible connections, such as V-belts, in prilling equipment.

As a result of experimentally obtained measurements of the drop of the pressure and velocity of the fluid, it was found that the fluid layer rotates in the vortex chamber and inhibits the vortex flow of the gas phase [12]. It was established [13] that in an air flow with a significant shear effect, the rupture of droplets has certain signs due to stretching and lifting caused by interaction between the deformed droplet and the shear layer.

3 Research Methodology

The above disadvantages were eliminated due to the implementation of rotational vibroprillers, the design of which is shown in Figure 2.

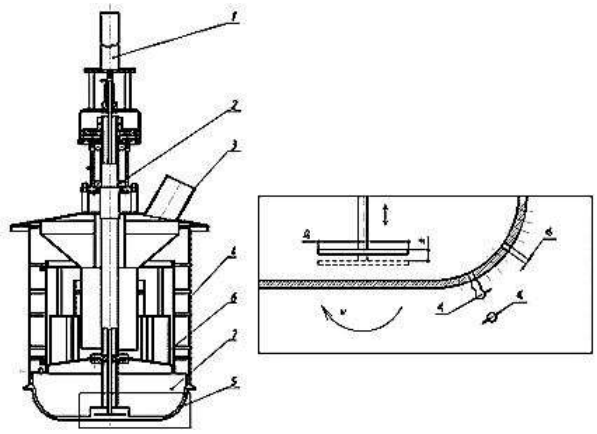

Figure 2 – Rotational vibropriller: 1 – oscillator; 2 – bearing; 3 – inlet nozzle for melt; 4 – cylindrical casing; 5 – perforated bottom (basket); 6 – distributor; 7 – vanes

Rotational vibroprillers (RVP) are characterized by leakage of fertilizer melt under the action of centrifugal force. This force occurs due to the rotation of the perforated basket of the priller [14]. Because of this, it becomes possible to distribute melt droplets on the section of a tower at various distances from its axis, thereby changing the diameter of a dispersion swath of melt.

The Chemical Engineering Department of Sumy State University developed and implemented the RVP with baskets of various shapes for dispersing the mineral fertilizer melt.

Figure 3 shows two designs of RVP with spherical and toroidal-shaped basket bottoms.

Based on the results of the commercial introduction of RVP and based on the results of an industry study of the mineral fertilizer producers that used static prillers before replacing them with RVP, a comparative analysis of product quality was conducted. These comparative characteristics are shown in Table 1.

As is evident from Table 1, it is quite reasonable to conclude that RVP has a much better grain-size composition of the product compared to other vibroprillers. For example, the grain size of less than 1 mm, which is the basis of dust emissions into the atmosphere, is less than 1 %.

The shape of the bottom of the RVP basket is essential based on several requirements. First, it provides the distance from the axes of the holes from which the jets of melt flow. This is necessary to eliminate the crossing of the melt jets and to create conditions for additional grinding of the droplets or, conversely, the merging of the droplets into larger ones which significantly impairs the size of prills.

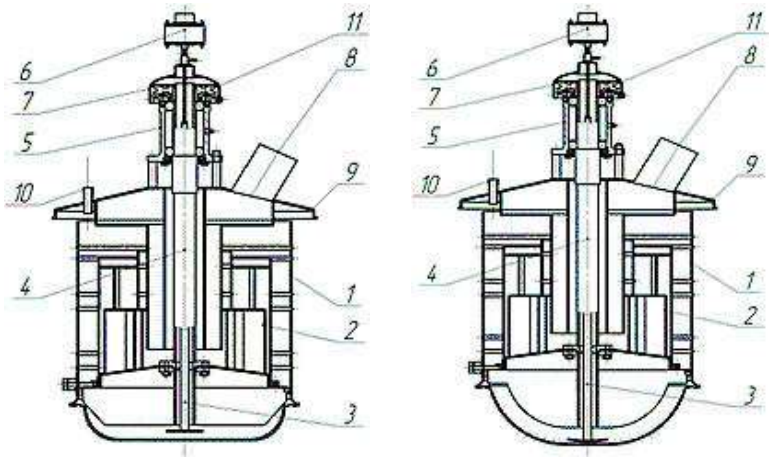

Figure 3 – RVP design: a – toroidal shaped basket bottom; b – spherical shaped basket bottom; 1 – basket with perforated bottom; 2 – distributer; 3 – a rod with spraying element, 4 – shaft; 5 – bearing; 6 – oscillator; 7 – metal cap; 8 – nozzle for melt supply before start-up of the vibropriller; 9 – upper casing half; 10 – nozzle for steam supply before shut-down of the vibropriller; 11 – pulley

Table 1 – Operating data of industrial prillers of different types (production of ammonium nitrate)

Disperser characteristic (spray element)	Diameter of leakage hole, mm	Rotational speed, rpm	Flow rate, t/h	Grain–size composition, %			
				0–1 mm	1–4 mm	2–4 mm	2–3 mm
Priller with spray nozzle	–	–	12	2.2–6.1	80–96	59–63	40–49
Static and acoustic priller	0.85	–	7–18	0.8–1.5	98–99	85–95	80–90
Centrifugal conical priller	–	–	25–70	0.8–2.5	97–99	83–92	75–90
Centrifugal vibrating priller	1.10	35–55	20–100	0.5–1.0	> 99	90–97	> 90

Secondly, the different shape of the bottom allows you to arrange the hole axes for melt jets to flow at different angles to the horizontal plane of the tower. And this also affects the horizontal distance of the prills falling from the axis of the prilling tower.

Taken together, the above factors with an additional factor, such as the rotational speed of the priller basket and, in general, affect the diameter of the melt spray swatch. This is especially important if the tower is rectangular in shape and small in width. In this case, the large diameter of the spray swatch can cause droplets to hit the tower walls, sticking melt on these walls. As a result, it can even lead to the termination of the prilling tower.

4 Results

To develop a theoretical method of calculation and recommendations for selecting the shape of the basket and its rotational speed, the equation of motion of prills in air flow was used:

$$\begin{cases} \frac{d^2x(\tau)}{d\tau^2} = -\frac{3\xi_x\ \rho_{air}\left[\frac{d}{d\tau}x(\tau)+W_x\right]^2}{4\ d_p\rho_p}; \\ \frac{d^2y(\tau)}{d\tau^2} = g - \frac{3\xi_y\ \rho_{air}\left[\frac{d}{d\tau}y(\tau)+W_y\right]^2}{4\ d_p\rho_p}, \end{cases} \quad (1)$$

where ξ – drag coefficient for prills; x, y – horizontal and vertical axes, respectively; ρ_p, ρ_{air} – density of prills and air, respectively, kg/m^3; d_p – average diameter of prills, m; g – acceleration of gravity, m/s^2.

The corresponding calculation scheme is shown in Figure 4.

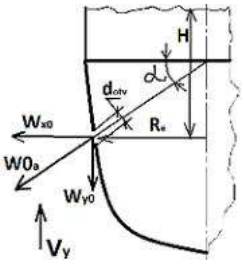

Figure 4 – The scheme of flowing the melt out the basket: H – height, m; R_a – radius on which the leakage occurs, m; α – flow angle of the jet, rad; W_{x0}, W_{y0} – initial values of the horizontal and vertical components of the droplet velocity, respectively, m/s; V_y – air velocity, m/s

Figure 5 shows an example of the calculation result of the radius of the melt spray swath, which corresponds to the horizontal component of the droplet path coming from the largest radius of the basket for ammonium nitrate in the prilling tower of 80 m in height. Signs "x" and "y" (in meters) correspond to the horizontal and vertical distance that the prill passes before it falls at the bottom of the tower.

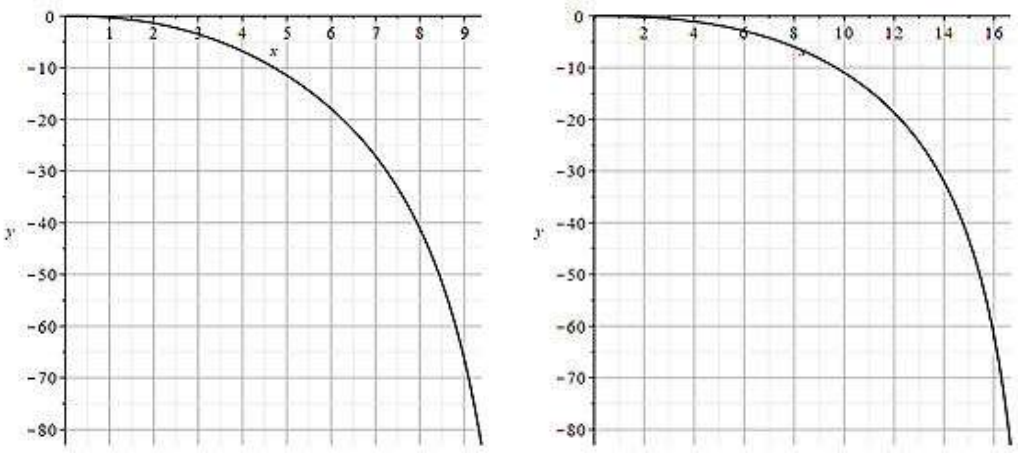

a b

Figure 5 – Changing the radius of the spray swath for RVP's rotational speed of 180 rpm (a) and 250 rpm (b)

This figure corresponds to the radius of the spray swath.

Considering that an increase in the rotational speed by 70 rpm leads to a significant (almost twofold) increase in the spray swath radius, it is possible to influence the dimensions of the spray swatch by changing the rotational speed of the priller.

5 Conclusions

Based on theoretical and experimental studies in industrial conditions, the program of automatic control of the rotational speed of RVP depending on the change of melt loads in an industrial prilling tower was developed and implemented in the production prototype.

Thus, as a result of an experimental study on model and production prototypes and theoretical calculations, the advantages of RVP over other designs of vibroprillers were substantiated.

A method for determining the diameter of the spray swath of mineral fertilizers to develop recommendations for changing the rotational speed of the prillers in industrial conditions and the shape of the basket provided the desired initial inlet direction of jets and prills into the air stream was developed.

6 Acknowledgments

The research results were achieved within the research project "Creation of new granular materials for nuclear fuel and catalysts in the active hydrodynamic environment" (State reg. No. 0120U102036) ordered by the Ministry of Education and Science of Ukraine.

References

1. Kasym, R. T., Skydanenko, M. S., Sklabinskii, V. I. (2012). *Methods for Obtaining Droplets of a Monodisperse Composition*. Modern Technologies in Industrial Production: Proceedings of the 2nd All-Ukrainian Interuniversity Scientific and Technical Conference, Sumy, April 17-20, 2012, Part 2, pp. 116-117.
2. Taran, A. L., Dolgalev, Ye. V., Taran, Yu. A. (2006). Calculation algorithm for a priller with a nozzle for the production of lime-ammonium nitrate in baths. *Bulletin of MITHT*, Vol. 1(3), pp. 42-46.
3. Kazakova, Ye. A. *Granulation and Cooling of Nitrogen-Containing Fertilizers*. Chemistry, 1980.
4. Ostroha, R., Yukhymenko, M., Lytvynenko, A., Bocko, J., Pavlenko, I. (2019). *Granulation Process of the Organic Suspension: Fluidized Bed Temperature Influence on the Kinetics of the Granule Formation*. In: Ivanov V. et al. (eds) Advances in Design, Simulation and Manufacturing. DSMIE 2018. Lecture Notes in Mechanical Engineering. Springer, Cham, pp. 463-471, doi: 10.1007/978-3-319-93587-4_48.
5. Lytvynenko A., Yukhymenko M., Pavlenko I., Pitel J., Mizakova J., Lytvynenko O., Ostroha R., Bocko J. (2019) Ensuring the reliability of pneumatic classification process for granular material in a rhomb-shaped apparatus. *Applied Sciences (Switzerland)*, Vol. 9(8), 1604, doi: 10.3390/app9081604.
6. Ostroha, R., Yukhymenko, M., Lytvynenko, A., Bocko, J., Pavlenko, I. (2019). Granulation process of the organic suspension: Fluidized bed temperature influence on the kinetics of the granule formation. *Lecture Notes in Mechanical Engineering*, Vol. F2, pp. 463-471.
7. Mann, H., Roloff, C., Hagemeier, T., Thevenin, D., Tomas, J. (2017). Model-based experimental data evaluation of separation efficiency of multistage coarse particle classification in a zigzag apparatus. *Powder Technology*, Vol. 313, pp. 145-160, doi: 10.1016/j.powtec.2017.03.003.

8. Pavlenko, I., Sklabinskyi, V., Pitel, J., Zidek, K., Kuric, I., Ivanov, V., Skydanenko, M., Liaposhchenko, O. (2020). Effect of superimposed vibrations on droplet oscillation modes in prilling process. *Processes*, Vol. 8(5), 566, doi: 10.3390/pr8050566.
9. Straka, L., Panda, A. (2018). Optimal preventive maintenance schedule of slewing rings for demanding production machine. *MM Science Journal*, Vol. 12, pp. 2696-2700, doi : 10.17973/MMSJ.2018_12_201872.
10. Fesenko, A., Basova, Y., Ivanov, V., Ivanova, M., Yevsiukova, F., Gasanov, M. (2019). Increasing of equipment efficiency by intensification of technological processes. *Periodica Polytechnica Mechanical Engineering*, Vol. 63(1), pp. 67-73, doi: 10.3311/PPme.13198.
11. Demianenko, M., Starynskyi, O., Pavlenko, I., Sklabinskyi, V., Trojanowska, J., Skydanenko, M., Liaposhchenko, O., Ivanov, V. (2022). *Impact of Dynamic Characteristics of Gears on the Reliability of Prilling Equipment*. In: Knapcikova L., Peraković D., Perisa M., Balog M. (eds) Sustainable Management of Manufacturing Systems in Industry 4.0. EAI/Springer Innovations in Communication and Computing. Springer, Cham, pp. 197-211, doi: 10.1007/978-3-030-90462-3_13.
12. Chen, S., Ouyang, O., Vandewalle, L.A., Heynderickx, G. J., Van Geem, K. M. (2022). CFD analysis on hydrodynamics and residence time distribution in a gas-liquid vortex unit. *Chemical Engineering Journal*, Vol. 446(2), 136812, doi: 10.1016/j.cej.2022.136812.
13. Xu, Z., Wang, T., Che, Z. (2022). Droplet breakup in airflow with strong shear effect. *Journal of Fluid Mechanics*, Vol. 941, A54, doi:10.1017/jfm.2022.326.
14. Artyukhov, A. Ye., Kononenko, M. P. (2013). Analysis of the results of the industrial implementation of rotary vibroprillers of melt in units for the production of ammonium nitrate. Bulletin of Sumy State University. Series “Technical Sciences Series”, Vol. 1, pp. 35-41.

JOURNAL OF ENGINEERING SCIENCES

Volume 9, Issue 1 (2022)

Sharapov S., Husiev D., Krmela J. (2022). Experimental stand for studying the working process in a liquid-vapor jet device with replaceable diffuser parts. Journal of Engineering Sciences, Vol. 9(1), pp. F21-F26, doi: 10.21272/jes.2022.9(1).f4

Experimental Stand for Studying the Working Process in a Liquid-Vapor Jet Device with Replaceable Diffuser Parts

Sharapov S.[1][0000-0002-8433-8580], Husiev D.[1], Krmela J.[2][0000-0001-9767-9870]

[1] Department of Technical Thermal Physics, Sumy State University, 2, Rymskogo-Korsakova St., 40007, Sumy, Ukraine;
[2] Department of Numerical Methods and Computational Modelling, Alexander Dubček University of Trenčín, 1639/2, Študentská St., 911 01, Trenčín, Slovakia

Article info:
Submitted: April 22, 2021
Accepted for publication: June 4, 2022
Available online: June 8, 2022

***Corresponding email:**
d.husiev@kttf.sumdu.edu.ua

Abstract. The article describes the prospects for experimental research of liquid-vapor jet devices with adaptable geometry of the flow part of the primary flow nozzle. To formulate the research objectives, a critical analysis of state-of-the-art studies was conducted among native and foreign scientists studying two-phase jet devices. As a result, of the literature survey, we saw that the working process of the two-phase jet devices, which include liquid-vapor jet devices, is quite complicated to study. So, the achieved results of theoretical studies require clarification and the conduction of additional experimental studies. The article provides a description and experimental research method on the liquid-vapor jet devices with a replaceable diffuser part of the primary flow nozzle. The program and the method contain the range of changing operational parameters while conducting experimental studies. The functional scheme of the experimental scheme and the devices to control and measure pressure in the critical points of the scheme are proposed.

Keywords: primary flow nozzle, pressure measurement, experimental research, jet flow, process innovation.

1 Introduction

Nowadays, creating energy-efficient and environmentally safe devices in all fields of the industry has become a significant problem. Also, the issue of modernization of the existing technological systems and bringing their ecological safety level to state-of-the-art European and world standards has become urgent [1].

In many existing technological systems, where secondary flow pressure is increased using the energy of working primary flow, vapor-jet ejectors are used [2–4]. They have been studied and used since the end of the 19th century. However, there has not yet been any breakthrough leading to improvement in their effectiveness, and it is unlikely that such a breakthrough will happen soon. This is due to the peculiarities of its working process, concerning limitations of pressure increase level in the vapor-jet ejector and the need to constantly generate a significant amount of working vapor, which leads to an increase in the sizes of steam-vapor devices. These drawbacks provide a multi-level vapor-jet device design with transitional capacitors. The efficiency of such a design rarely exceeds 8% [5–7].

The drawbacks mentioned above of steam-jet devices lead to searching for a new solution, one of which is using two-phase jet devices [8, 9]. One of the promising ways may be using the vapor-liquid jet device, the working principle of which is based on jet thermocompression [10–12].

The vapor-liquid jet device's efficiency depends mainly on the efficiency of the working flow going from the primary flow nozzle. In such a device, the generation of working vapor occurs inside it, namely in the diffuser part of the primary flow nozzle, where the process of relaxed vapor generation from incomplete heating of working liquid takes place.

The whole process efficiency directly affects the efficiency of the general vapor-liquid jet device working process. One of the ways to increase the efficiency of the vapor generation process in the primary flow nozzle is by profiling the walls of its diffuser part [13, 14].

2 Literature Review

Jet devices have been used since the end of the 19th century. However, the absence of a united theory helping to describe their working process slowed down their development and expanded their application scope. The author of the article[15] was the first to try to describe the working process of gas ejectors and formulate an ejection equation for it. Further research was aimed at attempts to use different working environments in jet devices in both primary and secondary flow [16–18]. This fact was conditioned by their use in various fields of industry. Nonetheless, the major problem of jet devices is their low efficiency.

The main breakthrough was using two-phase jet devices, including liquid-vapor jet devices, working using principles of jet thermocompression. It is much more efficient than the existing vapor jet analogs but needs further study. Currently, the most reliable mathematic model describing its working process is the authors' model [19, 20], which was designed for the compression's operating working mode and was improved by the author [21] for the vacuum mode of work. Such mathematic models allow getting relatively high efficiency of working jet outflow from active flow nozzle, up to 97%. However, they do not consider the shape of the diffuser part of the primary flow nozzle, where flow deviation from the walls of the nozzle can occur at different working modes and reverse flow.

Many research works were conducted in recent years that showed the importance and need for profiling the diffuser part of the primary flow nozzle. The authors of the works [22–24] conducted a significant part of the theoretical research, which requires further experimental re-examination.

Having analyzed all the above-mentioned experimental data, the authors set themselves a goal to conduct experimental research on the working primary flow nozzle of the liquid-vapor jet device with replaceable diffuser parts of the parabolic, elliptical, logarithmic shape, and shape.

To achieve the goal set, it is necessary to fulfill the following tasks:

– a creation of an experimental stand for studying a liquid-steam jet device with replaceable diffuser parts of the nozzle.

– experimental studies of the features of the working process of a liquid-steam jet device with replaceable diffuser parts of the nozzle to refine the mathematical model;

– experimental studies of the dependence of a liquid-steam jet's consumption and energy parameters, with replaceable diffuser parts of the expanding part of the nozzle on geometric and operating parameters;

– analysis of factors affecting the achievable performance indicators of a liquid-steam jet device with replaceable diffuser nozzle parts;

– refinement and further improvement of the mathematical model of the working process of a liquid-steam jet device, with replaceable diffuser parts of the expanding part of the nozzle;

– verification of the correctness of the obtained scientific results by comparing calculated and experimental data.

3 Research Methodology

3.1 Experimental case studies

According to the chosen object and the set goals, the program, and methods for the experimental research of liquid-vapor jet devices (LVJD) were developed using the proposed approach (Table 1).

Table 1 – Structure of the experimental case studies

Wall type	Parameters	
	p_{01}, bar	$1 - \varepsilon_{s0}$
straight walls	10–15	0.15–0.50
logarithmic shape	10–15	0.15–0.50
elliptical shape	10–15	0.15–0.50
parabolic shape	10–15	0.15–0.50
optimized shape	10–15	0.15–0.50

This table demonstrates the research stages of the flowing mechanism of boiling, unsaturated, and underheated liquid through the widening channels of the different geometrical shapes of a diffuser part.

During experimental research, a series of tests of the liquid-vapor ejector was carried out on the model, manufactured on a 3D printer with different geometric and operating parameters.

The variation range of the geometric parameters include the geometry (shape, length, area of the vertical shift) of the expanding prime flow nozzle part

Variable range of operational parameters:

– prime flow working fluid pressure at the inlet to the nozzle p_{01} = 10–15 bar;

– prime flow working fluid temperature at the inlet to the nozzle T_{01} = 140–190 °C;

– the value of the relative initial prime flow working fluid underheating at the inlet to the nozzle $(1 - \varepsilon_{s0}) =$ $= 0.15–0.50$.

The experiments also include obtaining characteristics and dependencies of LVJD efficiency indexes and visualizing the flow by conducting tests using a 3D printed model of LVJD.

3.2 Experimental equipment

To measure pressure while conducting experimental research, high-accuracy sensors SITRANS P200, manufactured by Siemens, are used (Figure 1) [25].

SITRANS P200, P210, and P220 are compact sensors with a fixed measurement range for measuring absolute and excessive pressure. In this series, two different types of pressure sensors are used: two sensors with a stainless-steel sensor and one sensor with a ceramic sensor. Thus, measuring excessive, absolute and hydrostatic pressure is very easy. These sensors convert the measured pressure into a proportion signal of 4–20 mA / 0–10 V (Table 2).

Figure 1 – SITRANS P200 sensors [25]

Table 2 – Characteristics of the pressure sensor

Body	Stainless steel
Excessive pressure	1–60 bar
Output signals	4–20 mA / 0–10 V
Material of wetted parts	Stainless steel, plastic fitting, and PVC cable
Min. temperature	–15 °C
Max. temperature	125 °C

For data fixation and display, SIREC D400 is used [26] it is a high-end display recorder in 300 mm x 300 mm format with 12,1" Color- LCD-Display in XGA resolution (Figure 2).

Figure 2 – Display recorder SIREC D400 [26]

The benefits of its use are as follows (Table 3): fast scanning rate of 20 / 100 / 200 / 500 ms; internal data buffer from 1 GB up to 4 GB; high accuracy: 0.1%; transmitter power supply 24Vdc; comprehensive math functions; interfaces – Ethernet, RS 485, USB, slot for CD card; data logging via USB interface or by SD card; fast operation through a touch screen; configuration on the device or through the SIREC D manager or server software; NEMA 3/IP65 type front face protection, NEMA 4X/IP66 available as an option; firmware options individual selectable through a flexible credit system.

Because the measured environment temperature exceeds the working temperature ranges of sensors, we use gas coolers. We use cooling element made by ATEK Sensor Technologies (Figure 3) [27].

Table 3 – Characteristics of display recorder

Analog channels	16–48
Digital channels	up to 48
Format	300 mm x 300 mm
Display	12.1" color TFT
Data storage	SD card / USB memory key
Screens	22 (free designable customized)

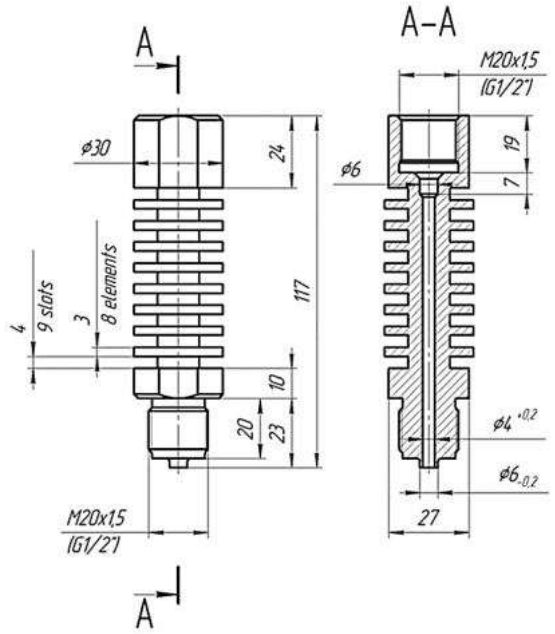

Figure 3 – Cooling element by ATEK Sensor Technologies [27]

Designed to protect pressure gauges and pressure sensors measuring the pressure of steam, hot liquid and other measured media having a high operating temperature from the direct action of the medium. When using an adapter cooler, the temperature of the medium is lowered to the operating temperature of the converter due to heat dissipation.

Technical specification is as follows: case material 304 stainless steel; max. working pressure 580 bar; max. operating temperature 200 °C; length 117 mm; outer diameter 30 mm; Connection of the G 1/2 / M20x1.5 sensor; process connection G 1/2 / M20x1.5.

4 Results and Discussion

4.1 Experimental stand

The experimental setup for the study of a liquid-steam jet device (Figure 4) consists directly of a jet device with replaceable diffuser parts of the primary flow nozzle 1, two heating tanks 2 and 18 for heating the working fluid and auxiliary communications, pipelines, and fittings.

Running water is used as working fluids for the primary and secondary flows of the jet device. When testing a liquid-steam jet device in vacuum mode, the working fluid of the primary flow is taken from tanks 8 and 14, where it is filled from a common network located directly in the test box room and is fed into the heating tank 2 using pumps 9 and 10. Shut-off valves 4 and 12 are used to stop the supply of working fluid to the heating tank after it is filled.

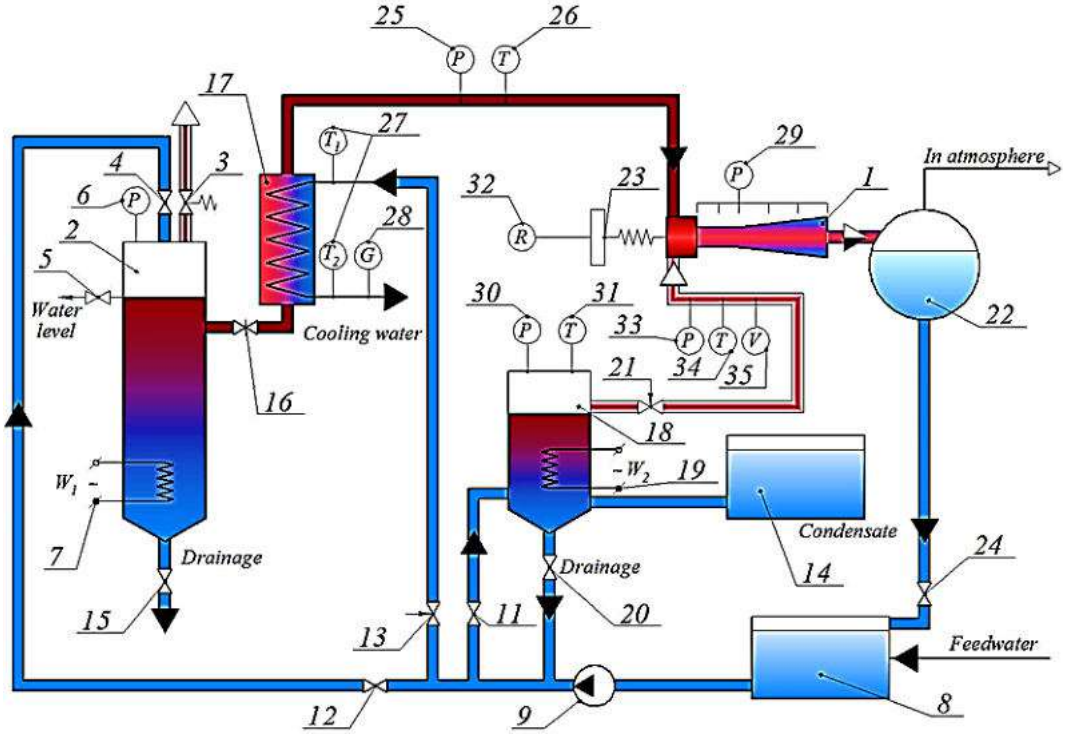

Figure 4 – Experimental stand to study the characteristics of a liquid-steam jet device of a vacuum unit: 1 – liquid-steam jet device, with a replaceable diffuser of the expanding part of the nozzle; 2, 18 – heating vessel; 3 – safety valve; 4, 5, 11, 12, 15, 20, 24 – shut-off valve; 6, 25, 29, 30 – model pressure gauge; 7, 19 – heating element block; 8, 14 – water vessel; 9, 10 – pump; 13, 16, 21 – adjusting valve; 17 – pipe-in-pipe heat exchanger; 22 – separator; 23 – digital scales; 26, 27, 31, 34 – digital multimeter; 28 – mass flow meter; 33 – model vacuum meter; 35 – volume flow meter

Level of the liquid in the heating tank is controlled by valve 5. Then the working fluid is heated by the heating element unit 7 to the required temperature value.

The pressure in the tank is controlled by a pressure gauge showing 6. The safety valve 3 is used for emergency pressure relief in case of exceeding the permissible value. Discharge into the drainage is carried out by means of a valve 15.

After heating and reaching the required pressure value, the working fluid, which is in a state of saturation, is fed through a pipe-in-pipe heat exchanger 17 to the nozzle of the jet device. The liquid flow is regulated by the valve 16. The cooling water for the pipe-in-pipe heat exchanger is taken from tanks 8 and 14, where it comes from the common network. Water circulation through the heat exchanger is carried out using pumps 9 and 10.

The valves of the shut-off valves 11 and 12 are used to open or close the supply of cooling water to the pumps. Regulation of the cooling water supply is carried out by means of an adjustment valve 13. When the working fluid passes through a pipe-in-pipe heat exchanger 17, it is cooled, providing the required amount of underheating. Its pressure does not change at the same time. In the section from the heating tank to the nozzle, the following parameters are monitored: pressure before entering the nozzle of the jet device with a model pressure gauge 25, temperature before entering the nozzle of the jet device with a thermocouple with a digital multimeter 26, the temperature of cooling water at the inlet and outlet of the heat exchanger with two digital multimeters 27, the mass flow of cooling water when it passes through the heat exchanger with a mass flow meter 28.

The secondary flow is steam produced from water, which is taken from the heating tank 18, where it is preheated by a block of heating elements 19 to the required temperature. The pressure in the heating tank 18 is controlled by an exemplary pressure gauge 30.

The temperature in the heating tank 18 is controlled by a thermocouple with a digital multimeter 31. Discharge into the drainage is carried out by means of a valve 20.

The steam is then fed into the ejector. Its flow rate is regulated by the valve 21. In the section from the heating tank 18 to the nozzle of its supply to the ejector, the following parameters are monitored:

– the vacuum value before entering the ejector with an exemplary vacuum gauge 33, the temperature before entering the jet device with a thermocouple with a digital multimeter 34 and the volume flow with a volume flow counter 35. After passing through the ejector, the mixed flow enters the separator 22, where it is divided into vapor and liquid phases. The steam phase is discharged through the pipeline into the environment, and the liquid phase is drained through the pipelines into the tank 14, from which the pump;

– pumps it out to fill the heating tanks 2 and 18 or to cool the working fluid in the heat exchanger 17. The valve of the shut-off valve 24 is used to open or close the discharge of the liquid phase from the separator. When the

flow passes through the ejector, the pressure and vacuum values are measured in five characteristic sections. Pressure measurement is carried out by exemplary pressure gauges and exemplary vacuum gauges 29.

4.2 Digital support system

The Mastech M-838 digital multimeter and the TR-01A thermocouple, which was used to adjust the temperature, may have an average value of systematic error less than 1.5% when measuring the absolute value of pressurization. The ultimate margin of error when measuring temperature with Chromel-Kopel thermocouples in a set with a multimeter of class 0.4, does not exceed 1 °C. The maximum error in measuring mass expenditures according to calibration testing is 3%. For pressure measurement high-accuracy devices are used, whose accuracy classes and margins of error are described in the next section of this article.

As a result of the research, the distribution of pressures and speeds of working fluids in the primary and secondary flow in the flow part of LVJD was obtained. The measurement's margin of error does not exceed 5% with confidence probability 0.95, which is permissible for technical experiments. And similar accuracy in measurements was reached in the works of previous researchers.

The speed in certain points is defined indirectly by measuring pressure, jet pulse and nozzle geometric parameters.

When a metastable superheated liquid flows out of the nozzle, the nature of the formation of the working steam jet and the features of its geometry are revealed at known and constant environmental parameters in the laboratory (pressure and temperature) and a given pressure value in the heating tank for heating the working fluid that is fed to the active nozzle:

– the values of the pressure and temperature of the working liquid at the inlet to the primary nozzle of the jet device, the pressure in the throat of the primary nozzle of the jet device, the reaction force of the jet in the pressure interval in the heating tank for heating the working fluid, which is fed into the primary nozzle of various underheating of the working fluid, will be measured;

– the temperature values at the inlet and outlet of the cooling water passing through the pipe-in-pipe heat exchanger will be measured, as well as the mass flow rate of the cooling water passing through the heat exchanger in the pressure range in the heating tank for heating the working fluid, which is fed into the primary nozzle and various underheating of the working liquid.

5 Conclusions

As a result of the research at the experimental stand, it can be obtained results that allow us to formulate the features of the working process of a liquid-vapor jet device working with replaceable diffuser parts of the nozzle, and to refine the mathematical model based on the results obtained.

As a result of the research, the distribution of pressures and speeds of working fluids in the primary and secondary flow in the flow part of LVJD was obtained. The measurement's margin of error does not exceed 5% with confidence probability 0.95, which is permissible for technical experiments. And similar accuracy in measurements was reached in the works of previous researchers.

References

1. Papadis, E., Tsatsaronis, G. (2020). Challenges in the decarbonization of the energy sector. *Energy*, Vol. 205, doi: 10.1016/j.energy.2020.118025
2. Hemidi, A., Henry, F., Leclaire, S., Seynhaeve, J.M., Bartosiewicz, Y. (2009) CFD analysis of a supersonic air ejector. Part I: Experimental validation of single-phase and two-phase operation. *Applied Thermal Engineering*, Vol. 29(8), pp. 1523–1531, doi: 10.1016/j.applthermaleng.2008.07.003
3. Gagan, J., Śmierciew, K., Butrymowicz, D. (2018). Performance of ejection refrigeration system operating with R-1234ze(E) driven by ultra-low grade heat source. *International Journal of Refrigeration*, Vol. 88, pp. 458-471, doi: 10.1016/j.ijrefrig.2018.02.014
4. Grave, H. (2014). *Steam Jet Vacuum Pumps*. In Vacuum Technology in the Chemical Industry, 1st ed., Wiley-VCH, pp. 81-95, doi: 10.1002/9783527653898
5. Jakończuk, P., Śmierciew, K., Zou, H., Butrymowicz, D., Dudar, A. (2021). Temperature drop of heating fluid as a primary condition for effective utilization of low-grade heat using flash cycles and zeotropic mixtures in refrigeration ejector systems. *Energy Sources, Part A Recover Util Environ Effects*, doi: 10.1080/15567036.2021.1876185
6. Bruche, S., Tsatsaronis, G. (2019). A multi-stage optimization approach for energy supply systems with discrete design decisions. *Proceedings of the ASME 2019 International Mechanical Engineering Congress and Exposition. Volume 6: Energy,* Salt Lake City, USA, doi: 10.1115/IMECE2019-11519
7. Angielczyk, W., Bartosiewicz, Y., Butrymowicz, D. (2020). Development of Delayed Equilibrium Model for CO_2 convergent-divergent nozzle transonic flashing flow. *International Journal of Multiphase Flow*, Vol. 131, doi: 10.1016/j.ijmultiphaseflow.2020.103351
8. Colarossi, M., Trask, N., Schmidt, D. P., Bergander, M. J. (2012). Multidimensional modeling of condensing two-phase ejector flow. International *Journal of Refrigeration*, Vol. 35(2), pp. 290–299, doi: 10.1016/j.ijrefrig.2011.08.013

9. Śmierciew, K., Pawluczuk, A., Gagan, J., Butrymowicz, D. (2019). Thermodynamic analysis of two-phase injector for various working fluids. *Applied Thermal Engineering*, Vol. 157, doi: 10.1016/j.applthermaleng.2019.113713
10. Zou, H., Li, X., Tang, M., Wu, J., Tian, C., Butrymowicz, D., Ma, Y., Wang, J. (2020). Temperature stage matching and experimental investigation of high-temperature cascade heat pump with vapor injection. *Energy*, Vol. 212, doi: 10.1016/j.energy.2020.118734
11. Wang, Y., Morosuk, T., Yang, S., Cao, W. (2020). A graphical method for evaluating the thermodynamic feasibility of absorption vapor compression multi-effect thermal desalination systems. *Desalination,* Vol. 485 doi: 10.1016/j.desal.2020.114448
12. Bonanos, A. M. (2017). Physical modeling of thermo-compressor for desalination applications. *Desalination*, Vol. 412, pp. 13–19, doi: 10.1016/j.desal.2017.03.004
13. Smolka, J., Bulinski, Z., Fic, A., Nowak, A. J., Banasiak, K., Hafner, A. (2013). A computational model of a transcritical R744 ejector based on a homogeneous real fluid approach. *Applied Mathematical Modelling*, Vol. 37(3), pp. 1208–1224, doi: 10.1016/j.apm.2012.03.044
14. Jimenez-Garcia, J. C., Rivera, W. (2019). Parametric analysis on the experimental performance of an ammonia/water absorption cooling system built with plate heat exchangers. *Applied Thermal Engineering*, Vol. 148, pp. 87–95, doi: 10.1016/j.applthermaleng.2018.11.040
15. Gagan, J., Smierciew, K., Lukaszuk, M., Butrymowicz, D. (2018). Investigations of thermal performance of ejection refrigeration system driven by low grade heat. *Applied Thermal Engineering*, Vol. 130, pp. 1121–1138, doi: 10.1016/j.applthermaleng.2017.11.093
16. Luo, J., Morosuk, T., Tsatsaronis, G., Tashtoush, B. (2021). Exergy-based evaluation of a waste heat driven polygeneration system with CO_2 as the working fluid. *International Journal of Exergy*, Vol. 34(1), pp. 50-75, doi: 10.1504/IJEX.2021.112035
17. Tahmasebipour, A., Seddighi, A., Ashjaee, M. (2014). Conceptual design of a super-critical CO_2 brayton cycle based on stack waste heat recovery for shazand power plant in Iran. *Environmental Engineering Science*, Vol. 2(1), pp. 95-101, doi: 10.22059/ees.2014.5012
18. Chen, Y., Zou, H., Dong, J., Xu, H., Tian, C., Butrymowicz, D. (2020). Experimental investigation on refrigeration performance of a CO_2 system with intermediate cooling for automobiles. *Applied Thermal Engineering*, Vol. 174, doi: 10.1016/j.applthermaleng.2020.115267
19. Sharapov, S., Arsenyev, V., Prokopov, M., Kozin, V. (2019). Influence of the passive flow initial parameters on the efficiency of liquid-vapor ejectors. *Advances in Design, Simulation and Manufacturing. DSMIE 2018. Lecture Notes in Mechanical Engineering*, pp. 346–355, doi: 10.1007/978-3-319-93587-4_36
20. Marchenko, V., Osipov, V., Prokopov, M., Sharapov, S. (2009). Principle of stream thermocompression: conception of energetic efficiency and prospect of realization is in small heat energetic. *MOTROL. Motoryzacja i energetylca rolnictwa*, Vol. 11, pp. 70–76.
21. Merzliakov, I., Pavlenko, I., Chekh, O., Sharapov, S., Ivanov, V. (2020). Mathematical modeling of operating process and technological features for designing the vortex type liquid-vapor jet apparatus. *Advances in Design, Simulation and Manufacturing II. DSMIE 2019. Lecture Notes in Mechanical Engineering*, *pp.* 613–622, doi: 10.1007/978-3-030-22365-6_61
22. Sayadi, S., Tsatsaronis, G., Morosuk, T. (2020). Splitting the dynamic exergy destruction within a building energy system into endogenous and exogenous parts using measured data from the building automation system. *International Journal of Energy Research*, Vol. 44(1), pp. 1-16, doi: 10.1002/er.5213
23. Ma, Y., Morosuk, T., Luo, J., Liu, M., Liu, J. (2020). Superstructure design and optimization on supercritical carbon dioxide cycle for application in concentrated solar power plant. *Energy Conversion and Management*, Vol. 206, doi: 10.1016/j.enconman.2019.112290
24. Ma, Y, Morosuk, T, Liu, M, Liu, J. (2020). Investigation of off-design characteristics of an improved recompression supercritical carbon dioxide cycle for concentrated solar power application. *International Journal of Energy Research*, Vol. 45(2), pp. 1818–1835, doi: 10.1002/er.5857
25. *Pressure Transmitters SITRANS P200/P210/P220*. (2021). Product Catalogue, Siemens. Available online: https://assets.new.siemens.com/siemens/assets/api/uuid:4fcb4c2a-285b-4de3-b90d-6f77cc3f35b7/fi01-p200-ua.pdf.
26. *SIREC D200/D300/D400 Display Recorders*. (2016). Product Catalogue, Siemens. Available online: https://cache.industry.siemens.com/dl/files/797/109743797/att_910130/v1/A5E37533305-05en_43-TV-25-43_SIRECD_Manual.pdf
27. *Atek Products Catalogue.* (2017). Product Catalogue, ATEK Electronics Sensor Technologies Inc. Available online: http://www.ateksensor.com/content/img/ATEK_Products_Catalog_2017.pdf.

JOURNAL OF ENGINEERING SCIENCES

Volume 9, Issue 1 (2022)

Anaemeje J. C., Owuama K. C., Okafor O. C., Madu K. E. (2022). Determination of a suitable retrofit of R-134A using refrigerant blends of R290 and R600 aided by an optimization technique. Journal of Engineering Sciences, Vol. 9(1), pp. G1-G7, doi: 10.21272/jes.2022.9(1).g1

Determination of a Suitable Retrofit of R-134A Using Refrigerant Blends of R290 and R600 Aided by an Optimization Technique

Anaemeje J. C., Owuama K. C., Okafor O. C., Madu K. E.

[1] Chukwuemeka Odumegwu Ojukwu University, Uli Campus, Anambra State, Nigeria;
[2] Grundtvig Polytechnic, Oba, Anambra State, Nigeria

Article info:
Submitted: March 11, 2022
Accepted for publication: May 30, 2022
Available online: June 6, 2022

***Corresponding email:**
okaforobiorac@gmail.com

Abstract. The effect of the hydrochlorofluorocarbon (HCFC) and hydrofluorocarbon (HFC) refrigerants on the environment through the attack of its halogen contents-chlorine and fluorine, on the ozone layer and the toxic nature of such refrigerants, has paid the attention of researchers to work towards getting suitable alternatives using hydrocarbons (HC) or its blends with HFC refrigerants. This study was centered on getting a suitable retrofit of R-134A with a good coefficient of performance (COP) and low global warming potential (GWP) using the blends of R-290 and R-600 HCs for use in refrigeration systems. An experimental testing rig was developed by assembling various measuring devices to the operational points of a vapor compression refrigerator. A mixture design was developed using the simplex lattice design (SLD) of design expert software 11.0. The response variables considered were COP and GWP. The experimental design was meticulously followed using 1kg for each refrigerant run, and the temperature and pressure values at the operating points were noted. From the results obtained, blend A had the highest COP of 2.5 and the highest GWP value of 3.93. Blend D had the lowest value of C.O.P. of 1.33, while blend B had the lowest value of GWP of 3.51. Also, the optimal blend was achieved at a mixture factor of 59% R-290a and 41% R-600. The response values obtained at this optimal mixture level were COP-2.05182 and GWP – 3.59. Therefore, the optimal blend obtained would be a better retrofit to R-134a and could be used in refrigeration systems.

Keywords: refrigerants, response surface methodology, performance; global warming potential, vapor compression refrigeration system; energy efficiency.

1 Introduction

A refrigeration system is a thermodynamic-based machine that uses a reversed heat engine cycle principle. The reverse heat engine cycle extracts heat energy from the low-temperature region and discharges it to the high-temperature region. The technology of refrigeration has forever caused a considerable improvement in the human standard of living [1]. The invention of refrigerators and air-conditioners has become a priority for comfortable living.

Refrigeration systems can be of any type: ice refrigeration, air refrigeration system, vapor compression, vapor absorption, adsorption, cascade, mixed, vortex tube, thermoelectric, and steam jet refrigeration systems [2].

Vapor compression refrigeration systems are essential from commercial and domestic utility viewpoints. The refrigeration process depends on the refrigerant type employed, among other factors like the compressor, condenser, and operational characteristics. The concern on the refrigerant type used in refrigeration and air conditioning systems resulted from the negative effects caused by the hydrofluorocarbon (HFC) and hydrochlorofluorocarbon (HCFC) refrigerant types on the ozone layer. These refrigerants are responsible for the depletion of the ozone layer that protects the earth from releasing harmful ultraviolet (UV) radiation and cause the global warming effect. The HFCs refrigerants have lower ozone depletion potential (ODP) but higher global warming potential (GWP) value [1]. This concern has thus drifted the attention of researchers to the use of hydrocarbons and their blends as refrigerants [3-5].

R-134a is an HFC refrigerant that is commonly used in most heating, ventilation, and air conditioning (HVAC) and refrigeration systems owing to its favorable

characteristics, such as low boiling point, low ignition temperature, zero ozone depletion potential (ODP), solubility in water, non-flammability and critical temperature stability. But this refrigerant is characterized by a very high global warming potential (GWP) value of 1300, hence the need to blend it with hydrocarbons (HC) to reduce its value while maintaining good performance characteristics. Several studies have been conducted using various blends of HCs and blends of HFC-R134a with HCs in search of a suitable retrofit of R-134a.

This study is focused on evaluating the global warming potential and coefficient of performance of R-134a and various mixture designs of R-290 and R-600 using a vapor compression refrigeration system.

The mixture designs of R-290 and R-600 were formulated using the simplex lattice design (SLD) tool and optimized using response surface methodology (RSM).

2 Literature Review

The vapor compression refrigeration system (VCRS) operates based on four distinct processes as shown as in Figure 1 [6].

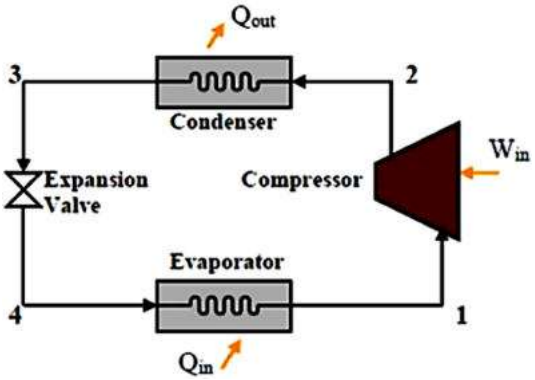

Figure 1 – Process operation of a VCR system [6]

According to [6], the VCR system operation starts with compressing the refrigerant in the compressor device (process 1-2). This process raises the temperature and pressure of the refrigerant so high and then delivers the refrigerant to the condenser (process 2-3) for temperature reduction. The pressure of the refrigerant is reduced in the expansion valve (process 3-4) before the evaporation process that causes the cooling effect (process 4-1). In the quest to get a suitable retrofit of the HCFC and HFC refrigerants, many studies have been carried out in that regard. A study on using R-290 refrigerant as an alternative to R-22 in window air conditioners was carried out by [7].

The results obtained from their study showed that the cooling capacity and energy consumption of R-290 were lower than those of R-22 by 6.6 to 9.7% and 12.4% to 13.5%, respectively. The C.O.P of R-290 was higher than that of R-22 by 2.8% to 7.9%. R-22 and R-290 were analyzed in a 15KW heat pump by [8]. The results showed that R-290 had higher C.O.P. than R-22 by 18%. Also, the C.O.P. of the refrigerant blend of R-290/R-600a and others – R-290, R-1270, R-600, and R-600a, were investigated by [9] in quest of getting an alternative to R-22 used in a heat pump system. The obtained results proved that the cooling and heating capacities of R-290 were smaller and its C.O.P. was slightly higher than that of R-22. The C.O.P. and energy consumption amount of R-134a and that of its various blends of 90/10% for R-134a/R-290 and R-134a/R-600a/R-290 of blend ratio-70/20/10% were studied by [10] in search of a retrofit for R-134a. The study showed that the blend of R-134a/R-290 had the highest C.O.P. The second blend had the least when compared to the base refrigerant, R-134a. He explained that the increase in the C.O.P. of the first blend resulted from the presence of hydrocarbon (HC) in the blend, which caused an increase in the refrigerant's evaporation rate. Also, the blends of R-134a refrigerant consumed less amount of power than the base refrigerant.

3 Research Methodology

3.1 Materials

The materials used in this study are refrigerants, a vapor compression refrigeration (VCR) system, and other devices coupled to the refrigerator system. The experimental test rig used the refrigerator system to study the refrigerants' performance modes at different percentage mass compositions according to the experimental design. These materials are discussed.

Thermometers (digital and infrared types) was used to measure the temperature of the refrigerants at various component unit/points. Four thermometers were employed and installed at the inlet and outlet units of the compressor, exit unit of the condenser and exit point of the system's expansion valve, which was the inlet of the evaporator.

A pressure gauge was used to measure the pressure of the refrigerants at the inlet and exit points of the compressor and at the inlet point of the expansion valve. Therefore, three pressure gauges were used.

A weighing scale was used to measure the compressor's refrigerant mass for each supply charge.

Vapor compression refrigerator (VCR) system with model number IGNIS 570XL was used to experiment.

Refrigerants, R-134a, and different blends of R-290/R-600 were employed in this study. R-134a was used as the base refrigerant while different percentage mass compositions of R-290 and R-600 were experimented on.

The refrigerants were fed into a gas cylinder and then allowed to flow at a mass flow rate of 0.05 kg/s into the compressor.

The gas charging hose was used to transfer the refrigerant charge from the gas cylinder to the compressor.

A vacuum pump machine was used to vacuum the system.

Design expert 11.0 software package is specialized for two goals – Design of Experiments (DOE) and constructing Response Surface Methodology (RSM). Response surface methodology (RSM) is a collection of

mathematical and statistical techniques for empirical model building. By careful design of experiments, the objective is to optimize a response (output variable) that is influenced by several independent variables (input variables). This software tool was used for the experimental design using blends of R290 and R600 as the input variables and coefficient of performance and global warming potential as the response variables to be optimized.

Table 1 shows the functional properties of the refrigerants- the base refrigerant (R-134a) and the HCs blends of R-290 and R-600 used in this study.

Table 1 – Properties of refrigerants [11]

Features	Refrigerant		
	R-134a	R-290	R-600
Chemical formula	CH_2FCH_3	C_3H_8	C_4H_{10}
Appearance	Colourless gas	Colourless gas	Colourless gas
Density, kg/m^3	4.25	2.01	2.51
Molar mass, g/mol	102.03	44.10	58.12
Melting point, °C	–103.3	–187.70	–159.42
Boiling point, °C	–26.3	–42.25	–0.56
ODP	0	0	0
GWP	1300	3.3	4.0

3.2 Experimental setup

The vapor compression refrigeration (VCR) system was used as the testing rig to evaluate the performance of the refrigerants and their blends in quest of finding a good retrofit to R134a with lower global warming potential (GWP) and higher coefficient of performance. Thermometers and pressure gauges were coupled to some units in the refrigerator to evaluate the system's performance while operating on different refrigerant blends. The setup shown in Figure 2 was used for this purpose.

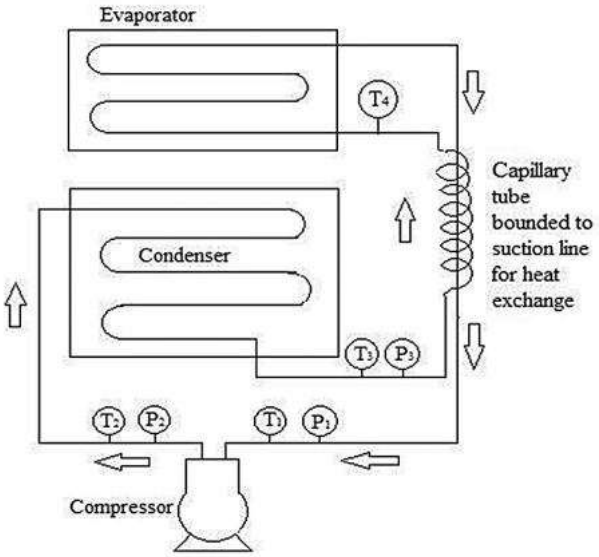

Figure 2 – Schematic diagram of the experimental rig:
T_1 – inlet temperature of the refrigerant at the compressor unit;
T_2 – exit temperature of the refrigerant at the compressor unit;
T_3 – exit temperature of the refrigerant at the condenser unit;
T_4 – inlet temperature of the refrigerant at the evaporator unit;
P_1 – inlet pressure of the refrigerant at the compressor unit;
P_2 – exit pressure of the refrigerant at the compressor unit;
P_3 – exit pressure of the refrigerant at the condenser unit

The method employed in this study stems from the design of the experiment, assembling of the components of the test rig and measurement of the performance parameters of each refrigerant blend, description of the experimental procedures, computation of the global warming potential of each refrigerant blend, computation of the coefficient of performance for each blend, and optimization and analysis of the response variables. These operations are lucidly elucidated.

Design expert software 11.0 was used to perform a mixture design for the two refrigerants- R-290 and R-600. The mixture design, a specialized response surface methodology, employed a simplex lattice design structure in formulating the refrigerant mix using various percentage mass compositions of the refrigerants- R-290 and R-600. The response variables used were: the coefficient of performance and global warming potential. A total of fourteen runs were obtained from the design. The mathematical inequality which governs the mixture design development is given:

$$10 \leq \text{R-290} \leq 70;\ 30 \leq \text{R-600} \leq 90 \qquad (1)$$

The schematic diagram of the test rig (Figure 2) was followed in connecting the various measuring instruments and tools to the vapor compression refrigerator components. Thermometers and pressure gauges were installed at the inlet and outlet units of the compressor, exit unit of the condenser and exit point of the expansion valve of the system which was the inlet of the evaporator. These devices noted the temperatures and pressures at those points.

3.3 Experimental procedure

Two gas cylinders were weighed and noted as M_1 and M_2. Then, the required mass of R-290 for the first run was poured into one of the gas cylinders, and the total mass was noted as M_3. Therefore, $M_3 - M_1$ gave us the actual mass of R-290. The mass of R-600 to be mixed with R-290 according to experimental design was transferred to the second gas cylinder with mass M_2 and the mass was noted as M_4. The difference $M_4 - M_2$ gave the required mass of R-600 for blend formulation. The gas charging hose was used to transfer R-600 gas from the second gas cylinder to the first one and was thoroughly shaken to

form a good mix. The total mass of the mixture was measured and confirmed to be 1 kg. As discussed, all the measuring tools were connected to the compressor, condenser and evaporator. The gas mixture was transferred to the compressor and the refrigerator was powered. The refrigerant blend was allowed to run for twenty minutes after which the temperature and pressure readings of the VCR components were taken and noted. After noting down the readings, the system was powered off and all the gas in the system was evacuated from the compressor unit using the gas charging hose. The vacuum pump machine was connected to the system to remove any remnant gas mixture in the system completely. This was done to avoid any effect on the result of the initial experiment. These procedures were followed repeatedly for all the various mixture designs of R-290 and R-600 refrigerants.

Figure 3 shows the experimental setup.

Figure 3 – Experimental setup

3.4 Computational technique

The model for the estimation of the global warming potential (GWP) of refrigerant blends when those of its refrigerants are known was employed by [12]:

$$(GWP_1 \times M_1) + (GWP_2 \times M_2) = (GWP_b) \quad (2)$$

where $GWP1$ – the global warming potential of refrigerant 1; $GWP2$ – the global warming potential of refrigerant 2, $GWPb$ – the global warming potential of refrigerant blend; M_1 – the percentage mass composition of refrigerant 1 in the blend, %; M_2 – the percentage mass composition of refrigerant 2 in the blend, %.

This model was used to estimate the global warming potential of the various refrigerant blends.

The coefficient of performance of each refrigerant blend was compared with that of the base refrigerant R-134a. As the refrigerant blends have no standard thermodynamic chart as at now, therefore, the values of the operating temperatures and pressures obtained from the experiment were used to evaluate the coefficient of performance of the system using the Carnot cycle efficiency formula employed by [13] and given as follows:

$$\text{C. O. P} = \frac{T_{condenser} - T_{evaporator}}{T_{condenser}}, \quad (3)$$

where $T_{condenser}$, $T_{evaporator}$ – condenser, and evaporator temperature, respectively, °C; C.O.P – coefficient of performance for the system.

The values of the response variables- coefficient of performance and global warming potential were factored into their respective columns in the simplex lattice design structure. The responses were optimized to get a better retrofit of R-134a that would have lower global warming potential and a high coefficient of performance compared to HFC R-134a refrigerants.

4 Results and Discussion

4.1 Performance characteristics

The result of the performance parameters or response variables used to determine the best refrigerant blend that could serve as a good alternative or retrofit of the HFC, R-134a, is presented in Table 2.

Table 2 – Response performance of R-134a and R-290/R-600 blends

Refrigerants	Global warming potential (GWP)	Coefficient of performance (C.O.P.)
R-134a	1300	2.0
Blend A	3.93	2.5
Blend B	3.51	1.7
Blend C	3.79	1.5
Blend D	3.72	1.3
Blend E	3.65	2.0
Blend F	3.86	1.3
Blend G	3.58	2.0

From Table 2, it could be seen vividly that blend A (10% R-290 and 90% R-600) had the highest global warming potential (GWP) value of 3.93. Blend B (70/30% of R-290/ R-600) had the lowest value of 3.51 global warming potential. The high value of global warming potential observed in blend A could be attributed to the high percentage amount of carbon in R-600 which formed 90% of the mass of the mixture. On the other hand, blends B having the lowest GWP value resulted from the lesser amount of R-600 (30%) present in the mix; as such, the percentage of carbon was reduced in the mixture. The GWP of R-134a from table 2 is 1300. Therefore, the blends showed a better value of GWP than the base refrigerant- R-134a. Also, refrigerant blend A (10% / 90% of R-290/R-600) had the highest value of the coefficient of performance – 2.5 than R-134a and other blends. Refrigerant blends- D and F had the lowest C.O.P value of 1.33. These findings could be attributed to the dissipative heat ability of the refrigerants. Refrigerants with more heat dissipative ability will run through the refrigeration cycle more efficiently than the ones with high heat retentive ability or poor thermal conductivity value.

In addition, the result of the performance characteristics of R-134a and the refrigerant blends concerning their respective operational parameters (temperature and pressure) in the refrigerator's components- compressor, condenser, and evaporator is presented in Table 3.

Table 3 – Operating characteristics of the refrigerants at various components of the refrigerator

Refrigerants (blends)	Mass comp., g		Temperature, °C				Pressure, Psi		
	R290	R600	T_1	T_2	T_3	T_4	P_1	P_2	P_3
R-134a			8	110	5	–5	4	135	35
A	100	900	4	81	2	–3	2	61	21
B	700	300	3	86	3	–2	3	64	18
C	300	700	2	90	4	–2	1	61	24
D	400	600	2	86	3	–1	2	53	16
E	500	500	4	84	2	–2	2	51	26
F	200	800	3	87	3	–1	2	60	23
G	600	400	2	83	3	–3	3	60	20

From Table 3, it could be observed that R-134a had the highest inlet temperature into the compressor (T_1), the highest exit temperature from the compressor (T_2), the highest exit temperature from the condenser unit (T_3), the lowest evaporator temperature (T_4), the highest inlet pressure to the compressor unit (P_1), the highest exit pressure from the compressor unit (P_2) and the highest exit pressure from the condenser unit (P_3). The high exit temperature of the refrigerant (R-134a) further confirmed why R-134a is known to consume much power during its cycle operations [14]. A low evaporator temperature attests to a good coefficient of performance, and R-134a had a good coefficient of performance of 2. In comparison to the blends, blend A had the lowest evaporator temperature. This fact explains why it had the highest coefficient of performance compared to the other blends and R-134a.

The behavioral characteristics of the blends could be seen to vary distinctively, and the quest of getting an optimal blend that would comparatively yield better performance objectives and equally serve as a better retrofit for the HFC, R-134a was obtained through optimization technique using simplex lattice design structure which is a specialized response surface methodology tool enshrined in mixture designs.

4.2 Optimization results

From the numerical optimization, the refrigerant blend with the highest desirability value was selected as the best refrigerant that would serve as a better retrofit to R-134a. The desirability plot is shown in Figure 4.

From Figure 4, the highest desirability value of 0.167 was obtained at a mixture blend of 59% R-290 and 41% R-600. The values of the response variables at the gotten optimal mixture blend are shown in Figures 5 and 6.

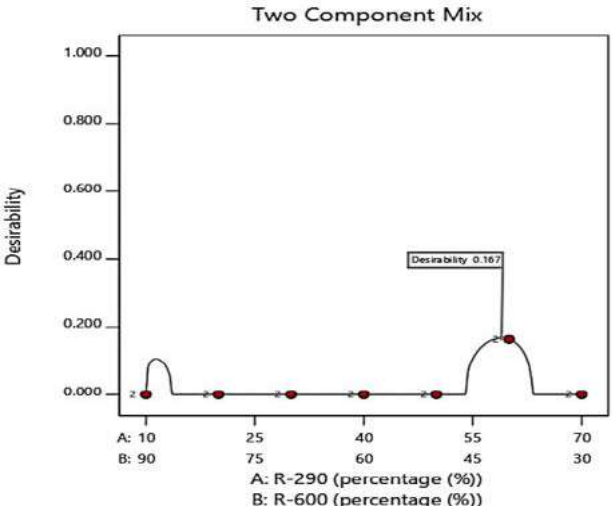

Figure 4 – Desirability of the refrigerant blends

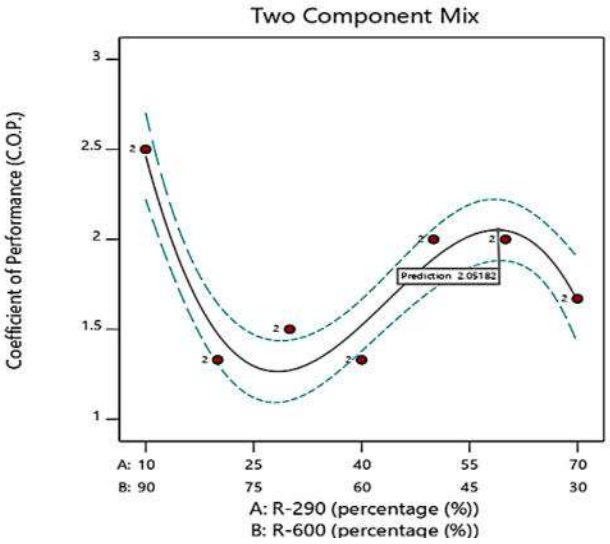

Figure 5 – Coefficient of performance against the mixture compositions

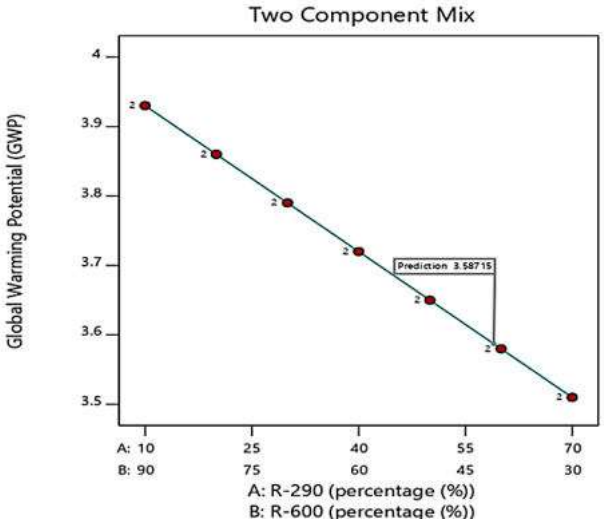

Figure 6 – Global warming potential against refrigerants mixture compositions

From Figure 5, the coefficient of performance obtained at the optimal blend was 2.05. Blend A with mixture compositions of 10% R-290a, and 90% R-600 had the highest coefficient of performance of value 2.50. The difference in performance coefficient between the optimal blend and blend A is 0.45.

A global warming potential value of 3.59 was obtained for the optimal blend, as shown in Figure 6.

The response predicted values' summary statistics are shown in Table 4 for two-sided confidence of 95%.

Table 4 – Summary statistics of the optimization process

Solution 1 of 2 response	Predicted mean	Predicted median	Standard deviation	SE Pred.	95% PI low	95% PI high
Coefficient of performance (C.O.P.)	2.05	2.05	0.16	0.18	1.66	2.44
Global warming potential (GWP)*	3.59	3.59	–	–	3.59	3.59

Blend B (70% R-290 and 30% R-600) had the lowest global warming potential value of 3.51, while blend A had the highest value of 3.91. The optimal blend which balanced the differences in all the refrigerant blends studied differs by 2.2% from blend B.

5 Conclusions

The numerical optimization gave an optimal blend that balanced the differences/discrepancies in the outputted experimental values of the responses for each refrigerant blend. The optimal blend was achieved at a mixture factor level of 59% R-290a and 41% R-600.The response values obtained at this optimal mixture level were coefficient of performance – 2.05 and global warming potential of 3.59. Therefore, the optimal blend obtained would better retrofit R-134a with a global warming potential of 1300 and a performance coefficient of 2.0.

6 Acknowledgment

The authors appreciate the invaluable insights of professor Achebe C. H. from the Department of Mechanical Engineering, Nnamdi Azikwe University, Awka. His contributions were of significant impact on the success of this research output.

References

1. Choudhari, C. S., Sapali, S.N. (2016). Performance investigation of natural refrigerant R290 as a substitute to R22 in refrigeration systems. *Energy Procedia*, Vol. 109, pp. 346-352.
2. Rajput, R. K. (2013). *Thermal Engineering*. New Delhi, Laxmi Publications Ltd., pp. 795-827.
3. James, M. C. (2002). Emissions and environmental impacts from air conditioning and refrigeration systems. *International Journal of Refrigeration*, Vol. 25, pp. 293-305.
4. James, M. C., (2008). The next generation of refrigerants – Historical review, considerations, and outlook. *International Journal of Refrigeration*, Vol. 31, pp. 1123-1133.
5. James, M. C., Glenn, C. H., (2001). Refrigerant data summary. *Engineered Systems*, Vol. 18(11), pp. 74-888.

6. Sarthak, M. T., Prajapati, R. P., Solanki, D. C. (2017). Performance analysis of a domestic refrigerator using various alternative refrigerant. *International Journal of Engineering Development and Research*, Vol. 5(2), pp. 642-659.
7. Devotta, S. (2005). Performance assessment of HC-290 as a drop-in substitute to HCFC-22 in a window air conditioner. *International Journal of Refrigeration*, Vol. 28, pp. 594-604.
8. Purkayastha, B., Bansal, P.K. (1998). Experimental study on HC290 and a commercial liquified petroleum gas (LPG) mix as suitable replacement for HCFC22. *International Journal of Refrigeration*, Vol. 21, pp. 213-217.
9. Chang, Y. S., (2000)., Performance and heat transfer characteristics of hydrocarbon refrigerants in a heat pump system. *International Journal of Refrigeration*, Vol. 23, pp. 232-242.
10. Panneerselvam, S. (2016). Performance characteristics of various refrigerant blends in a refrigeration kit. *Journal of Chemical and Pharmaceutical Sciences*, Vol. 9(4), pp. 3070-3076.
11. ASHRAE (2001). *ASHRAE Handbook – Fundamentals*. ASHRAE, Atlanta.
12. Ali, R. (2011). Calculating the global warming potential of refrigerant gas mixes, *Ecometrica*, Vol. 2, pp. 17-20.
13. Uwadiae, M. E., Akintunde, M. A., Ogedengbe, T. I., (2017). Experimental investigation of R-134a and R-600a refrigerant blend in domestic vapor compression refrigeration system. *Nigerian Journal of Technology*, Vol. 36(4), pp. 1138-1144.
14. Neeraj, A., Shriganesh, P., Prasant, N., (2016). Experimental studies of a domestic refrigerator using R290/R600a Zeotropic blends. *Energy Procedia*, Vol. 109, pp. 425-430.

JOURNAL OF ENGINEERING SCIENCES

Volume 9, Issue 1 (2022)

Ablieieva I. Yu., Geletukha G. G., Kucheruk P. P., Enrich-Prast A., Carraro G., Berezhna I. O., Berezhnyi D. M. (2022). Digestate potential to substitute mineral fertilizers: Engineering approaches. Journal of Engineering Sciences, Vol. 9(1), pp. H1–H10, doi: 10.21272/jes.2022.9(1).h1

Digestate Potential to Substitute Mineral Fertilizers: Engineering Approaches

Ablieieva I. Yu.[1*[0000-0002-2333-0024]], Geletukha G. G.[2[0000-0002-5249-3092]], Kucheruk P. P.[2[0000-0003-1888-0774]], Enrich-Prast A.[3[0000-0003-3561-0936]], Carraro G.[3[0000-0003-0091-3646]], Berezhna I. O.[1[0000-0001-9606-4241]], Berezhnyi D. M.[1[0000-0002-0751-4835]]

[1] Sumy State University, 2, Rymskogo-Korsakova St., 40007, Sumy, Ukraine;
[2] Institute of Engineering Thermophysics of the National Academy of Sciences of Ukraine, 2a, Marii Kapnist Street, 03057, Kyiv, Ukraine;
[3] Linköping University, SE-581 83 Linköping, Sweden

Article info:
Submitted: February 18, 2022
Accepted for publication: May 27, 2022
Available online: June 2, 2022

***Corresponding email:**
i.ableyeva@ecolog.sumdu.edu.ua

Abstract. The study aims to define the potential and technological aspects of the digestate treatment for its application as a biofertilizer. Life cycle assessment methodology was used in terms of digestate quality management. The potential of nutrients, organic carbon, and useful microelements in the digestate allows for its consideration as a mineral fertilizer substitute and soil improver. The valorization of digestate as fertilizer requires quality management and quality control. Based on the research focus, the successful soil application of digestate post-treatment technologies was analyzed. Among the different commercial options for digestate treatment and nutrient recovery, the most relevant are drying, struvite precipitation, stripping, evaporation, and membranes technology. Comparing the physical and chemical properties of the whole digestate, separated liquid, and solid liquor fractions showed that in the case of soil application of granular fertilizer, nutrients from the digestate are released more slowly than digestate application without granulation. However, realizing this potential in an economically feasible way requires improving the quality of digestate products through appropriate technologies and quality control of digestate products. To support the manufacture of quality digestate across Europe, the European Compost Network developed a concept for a pan-European quality assurance scheme.

Keywords: anaerobic digestion, climate change, life cycle assessment, soil degradation, sustainable land management, waste utilization, industrial diversification.

1 Introduction

Biogas reactors (BRs) are designed to produce methane from organic waste by anaerobic digestion (AD). BR produce leftovers, also known as digestate that has been successfully used as biofertilizer due to their high contents of mineralized Nitrogen (N), Phosphorus (P), Potassium (K), and organic materials [1]. Recycling organic materials to land is considered the best practicable environmental option in most circumstances, completing both natural nutrient and carbon cycles. Organic materials are valuable sources of major plant nutrients, essential for plant growth and sustainable crop production. Organic materials also provide a valuable source of organic matter, improving soil water holding capacity, workability, structural stability, etc. [2]. Digestate reduces the potential for soil erosion and improves productivity by increasing the soil organic matter and soil fertility and supplying additional nutrients [3].

Digestate is normally used as a biofertilizer without any further processing, substituting industrially produced mineral fertilizers. However, the need for efficient nutrient management, required by regulations on manure application in high livestock density areas, along with depletion of the finite reserves of phosphorous and potassium, make a recovery and recycling of nutrients [4].

Effective use of digestate is exceptionally relevant in Ukraine. The developed agro-industrial sector of Ukraine's economy, with a large share of agricultural land, requires considerable fertilizers. Actual management practice and land ownership during the years of Ukraine's independence have had a negative impact on soil fertility, which is resulted into the loss of large humus proportion, imbalance of nutrients content, soils acidification and

alkalinity, deficits of mobile forms of phosphorus, potassium, and microelements, chemical and radiation pollution, and erosion. These conditions are found in intensive production with the dominant use of mineral fertilizers and the critical fall in the volume of organic fertilizers application [5].

Digestate is highly suitable as an organic fertilizer or soil improver. In Ukraine, digestate is currently produced at least on 26 biogas plants in the agro-industrial complex. The primary raw materials used are cattle and swine manure, poultry litter, maize silage, and sugar beet pulp. One example of small biogas plants is the Integro company biogas plant, which digests poultry manure.

The specific use of raw materials for biogas production amounts to approximately 1.9 tons for each produced MWh of gross biogas energy [6]. Thus, according to reasonably approximate estimates, the total formation of raw digestate in Ukraine is 1.5–1.6 mln tons per year as of 2020.

Practically any products, by-products, and wastes of agro-industrial production of organic origin can be raw materials for biogas production and, therefore, the source of digestate. Typical feedstock for biogas plants can be of plant and animal origin (animal excrements, agricultural residues, and by-products, organic wastes from food and agro-industries, industrial organic wastes, organic fraction of municipal solid waste, food waste, sewage sludge, energy crops). Different types of substrates can influence the nitrogen concentration, share of ammoniacal nitrogen, total organic carbon (TOC), total solids (TS) content, volatile solids (VS) content, and VS/TS ratio.

2 Literature Review

The addition of digestate increases the soil nutrient levels (N, P, K) and microbial diversity [7, 8]. Digestate as soil improver must be suitable for organic matter content according to the EU standards on fertilizer properties. Among the most significant and necessary organic material carbon and nitrogen have a key role in microbiological processes in the soil as well as carbon is the most widely used energy source. The efficiency of agronomic use depends on their relative ratios. Amount of N as well as N form, organic or mineral, effects on digestate potential as fertilizer [7].

The application of digestate increased soil nutrient supply with improvements in topsoil total N, extractable P and extractable Mg ($P<0.05$ at 4 of the 7 sites for each of these nutrients), extractable K ($P<0.05$ at 6 of the 7 sites), and extractable S ($P<0.05$ at 3 of the 7 sites) [9].

Digestate varies in its nutrient content, depending on the substrates, nature of the anaerobic digestion process and post-digestion treatment. Digestate is an excellent source of readily available N (i.e., ammonium) which is potentially available for immediate crop uptake. Food-based digestate typically contains around 80 % of its total N content as rumen ammonia nitrogen (RAN), compared with around 70 % for pig slurry and 45 % for cattle slurry. Digestion of livestock slurry will typically increase RAN by around 10 % of the total N content [10]. However, an increase of RAN while digesting such materials like straw, food wastes is much higher due to less RAN content in raw matter. RAN increase can reach 70–80 % for these kinds of materials.

Digestate addition in the soil is more effective than mineral fertilizers used to increase available P for plants. Since P deficiency is a significant nutrient problem in calcareous soils, where high pH and carbonate content in the soil makes P less accessible to plants, adding biofertilizers is an adequate strategy to alleviate the deficit of P [11].

Additionally, digestate contains small quantities of trace elements, with the amounts present depending on concentrations in the feedstocks used. However, digestate could also contain unwanted materials and contaminants of biological, chemical, or physical nature.

Feedstocks from agriculture and human food waste are, in most cases, low in chemical impurities [12]. Nevertheless, stringent quality requirements for digestate also imply strict control of these materials. Two categories of chemicals are particularly concerned for the quality of digestate used as fertilizer, heavy metals (HM), and organic pollutants.

The effect of repeated digestate and compost applications on soil and crop quality was carefully studied by Bhogal et al. in the work package [9]. Obtained results showed stability in the concentration e of heavy metals in the topsoil after digestate addition except for topsoil total and extractable Cu. Soil treatment with repeated digestate addition had little effect on soil organic contaminant compound (OCC) concentrations, but the concentration of polycyclic aromatic hydrocarbons (PAHs), dioxins and furans, and phthalates and concentrations were low or at the limits of analytical detection. Besides this, digestate can decrease the concentration of Cr in the soil due to the potential redox reduction based on microbial activity improving after digestate application. Digestate addition provides Pseudomonas, Microbacterium, and Bacillus development that could reduce Cr(VI) to Cr(III) resulting in the bioavailability decrease and immobilization of Cr(VI) for plants [13].

The content of HM in digestates from AD plants processing feedstock from agriculture, food waste, and residues from food processing is normally within the suitability of agricultural fertilizers [14]. Nevertheless, technical and monitoring strategies that could reduce polluting hazards of the digestate before soil application would avoid soil contamination and prevent emissions.

The main aim of this study is to define the potential and technological aspects of the digestate treatment before its application as a biofertilizer. More specifically the focus is on the specific research tasks:

1) to propose a life cycle assessment methodology for digestate quality management;

2) to research all factors, particularly engineering approaches, that must be important to improve the quality and ecological safety of digestate as biofertilizer;

3) to develop the recommendation for soil application of main types of digestate-derived products and provide a quality assurance scheme for them.

Given the ever-increasing demand for energy in recent years, there is an urgent need to invest in clean and sustainable forms of energy. In this way, it will be possible to ensure that the energy needed by humanity around the world is sufficient. In particular, biomass energy can provide significant economic benefits, and guarantees are formed to monitor the mitigating impact on the environment [15].

3 Research Methodology

3.1 Digestate quality indicators

The quality of digestate as organic fertilizer could be described by the four main indicators, namely nutrients content, phase state, stability, and impurities content (Figure 1).

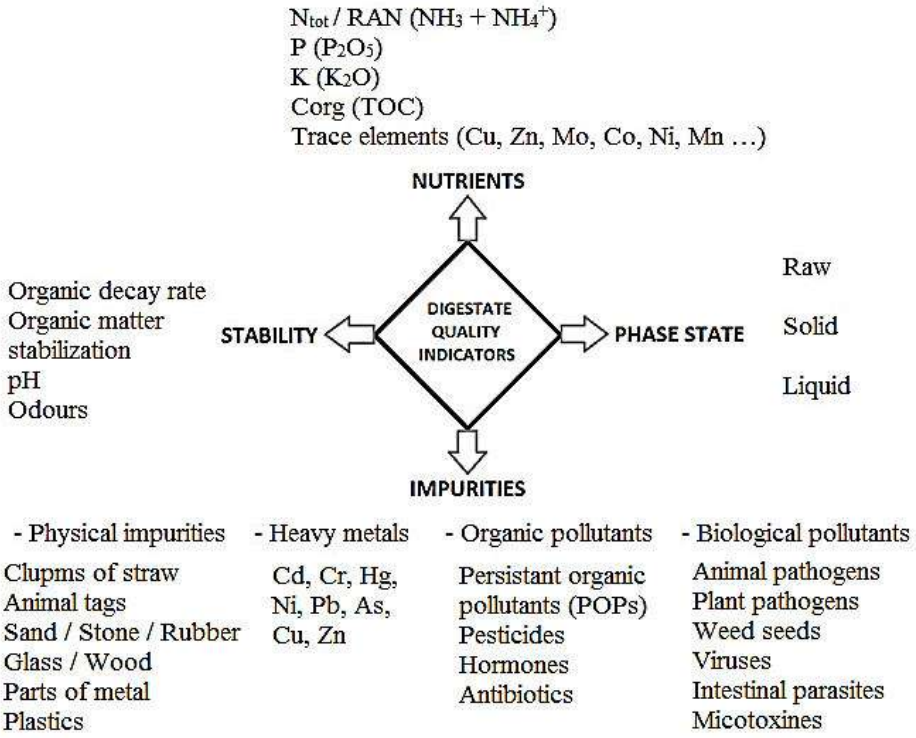

Figure 1 – Digestate quality indicators

The content of nutrients, humic substances, and trace elements in the digestate determines its fertilizing value. Simultaneously, the over-content of certain types of pollution impairs its commercial value, limits the list of applications, or makes it impossible to use it further without additional processing. To define how to improve the quality of digestate quality control system can be used.

3.2 Digestate quality management

Life cycle assessment methodology was used in terms of digestate quality management. The production and recycling of digestate as fertilizer requires quality management and quality control throughout the whole life cycle of AD, from the production of the AD feedstock until the final utilization of digestate as fertilizer. Quality management implies the use of high-quality feedstock, pre-processing of specific feedstock types, close control of the AD process, and process parameters affecting digestate quality, digestate processing, declaration, and optimal storage and application as fertilizer. The overall matrix for digestate quality management can be presented in Figure 2.

There are two main ways how to manage digestate quality, namely prevention and processing. The rule of thumb is that if efficient pollutant removal cannot be guaranteed either by pre-treatment or through the AD process, the material must not be used as feedstock in biogas plants whose digestate is used as fertilizer or for other agricultural purposes.

Prevention methods combine raw materials quality control at the stages of their formation in technological processes, collection, transportation, and storage. Getting into raw materials unwanted components such as sand, stones, plastic, other synthetic materials can be avoided by quality control of technological processes and logistic operations. It is also important to ensure the quality of seasonal raw materials (maize silage, pulp, crop residues) when stored for a long time. For example, it is necessary to avoid the fungal formations in raw material by maintaining the required acidity and water content.

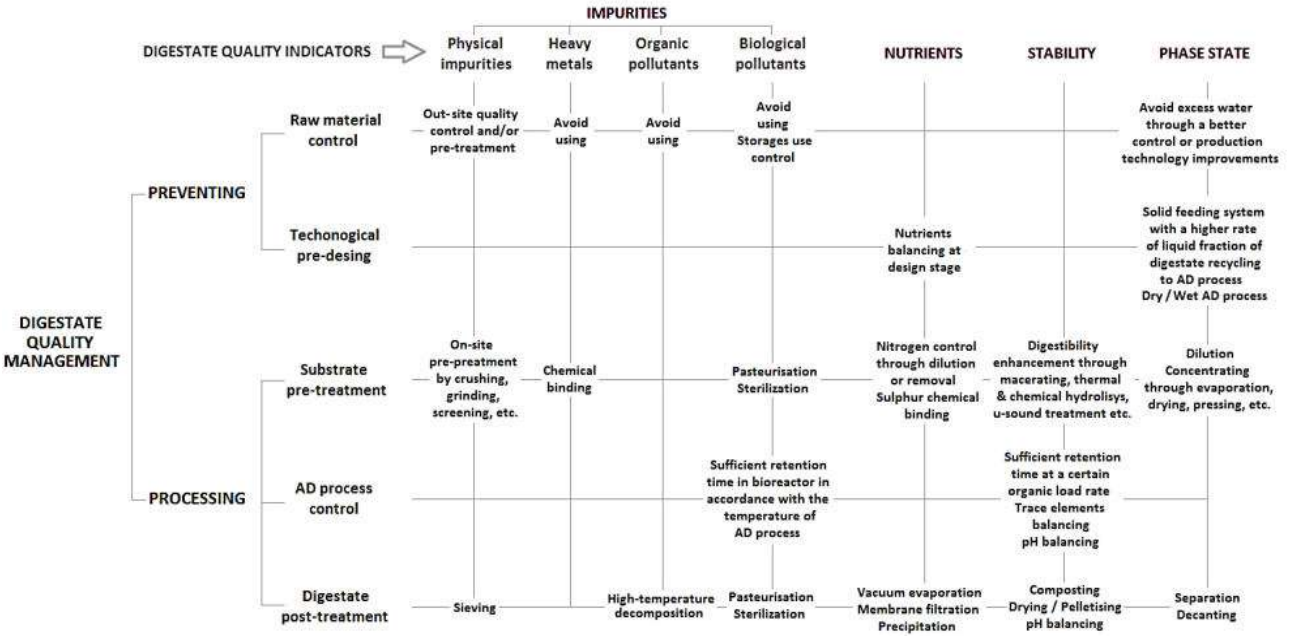

Figure 2 – Digestate quality management matrix

The digestate processing methods include substrate pre-treatment, AD process control, and digestate post-treatment technologies.

Feedstock pre-treatment involves three main methods: pre-sanitation, digestibility enhancement, and solid-liquid separation. In European biogas plants, pre-sanitation usually involves pre-heating specific feedstocks by batch pasteurization at 70°C for 1 hour or pressure sterilization at 133 °C and 2.4 bar (absolute) 20 minutes [3].

In some cases, pre-treatment is also needed where raw feedstock contains physical impurities. It could be processed by simple screening.

AD process control is mostly based on the residence time of the feedstock inside the digester at constant process temperature. Retention times are quoted as hydraulic retention time (HRT), minimum guaranteed retention time (MGRT), and sludge retention time (SRT) to avoid washing out bacteria and colonies. The AD process has a sanitation effect whereby it can inactivate most pathogens in the feedstock mixture inside the digester. Pathogen inactivation/destruction is mainly the result of the combined effect of process temperatures (thermophile or mesophile) and the retention times of feedstock inside the digester. In general, the higher the temperature and the longer the retention time, the higher the pathogen inactivation/destruction effect.

Digestate treatment includes some possible processing steps: solid-liquid separation (SLS), and specific treatments to recover of N, P, K components since N and K mostly follow the liquid fraction (LF) and P follows the solid fraction (SF).

The goal of separation is to separate the digestate into a liquid and solid fraction mechanically. There is no substantial reduction in volume; only the need for storage tanks for liquid digestate is reduced by around 10–20 % by separating the solid fraction, depending on the composition of the starting materials and separation technology. Separation is usually the first step before further processing to obtain concentrated LF and SF suitable for direct and ecologically safe utilization. At least partial process water recycling is recommended, reducing the treatment effort for LF. Specific processing of SF allows to improve its stability and additionally concentrate.

4 Results

Our previous research study showed that centrifugation is one of the most effective solid-liquid separation technologies for digestate to obtain a solid fraction with a high level of dry matter and improve nutrient fractionation between the two fractions [16]. Thus, given the uneven distribution of nutrients in solid and liquid fractions (Figure 3), solid-liquid separation gives the two products with specific functionality [4]. As the leading share of nitrogen is in liquid fraction, there should be attention paid to how to optimally handle it, guarantying preservation of nitrogen, and further the most effective assimilation by plants.

The centrifuge has a very high water-solid separation, especially for digestate with low DM content. However, precipitating/flocculating agents need to be added to improve separation efficiency. The further solid fraction can be dried with or without granulation.

Among the different commercial options for digestate treatment and nutrient recovery, the most relevant for LF are evaporation, struvite precipitation, ammonia stripping, membranes technology, and drying for SF. Digestate pellets production followed by nutrient supplementation/correction may also be considered a commercially viable option.

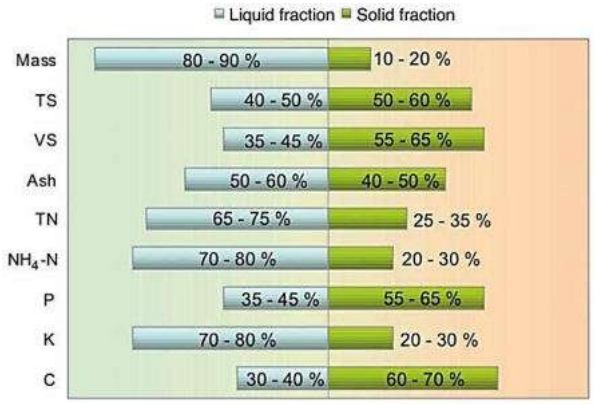

TS – Total Solids, VS – Volatile Solids, TN – Total Nitrogen

Figure 3 – Distribution of the principal constituents after solid-liquid separation [4]

Drying and evaporation are the suitable methods to reduce digestate volume for SF and LF, respectively. Moreover, drying is an efficient way to use large amounts of waste heat from biogas Combined Heat and Power (CHP). For dried digestate, the desired DM content (up to over 90 %) can be set via drying time and temperature. Since heat is demanded in great quantities for such technologies, heat availability is the crucial factor to consider whether it would be feasible or not. As most biogas plants, especially in Ukraine, produce heat in excess, which is currently not utilized, it could be an option to valorize it through digestate volume reduction. Most frequently, belt dryers are used (Figure 4) in which the digestate is placed on a conveyor belt and dried at temperatures of 60–150 °C for about 2 hours. A similar principle applies to push turn, fluid bed, and drum dryers, in which the digestate is transported through the hot air by the movement of vanes, air injection, or a rotating drum. Hot air is blown through a motionless pile with trailer or container dryers.

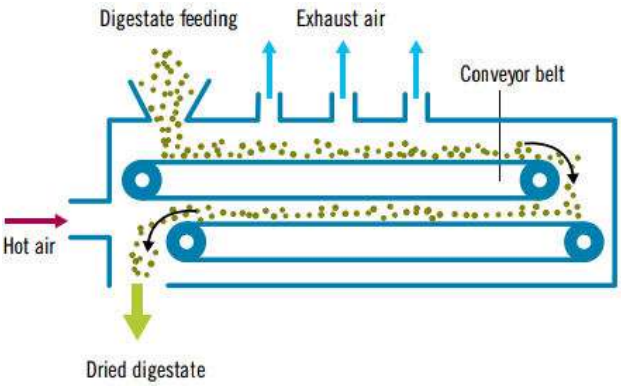

Figure 4 – Belt drier principal scheme [3]

In solar-assisted drying, the digestate is distributed on the floor of a large greenhouse and rearranged by a self-propelled turning trolley. Warm air at around 40 °C is blown onto the digestate layers by fans. Drying is supported by solar radiation into the greenhouse.

Depending on the technology used, the heat requirement is 0.75–1.20 MWt·h of thermally evaporated water per cubic meter (kWh_{th}/m^3 H_2O).

Our previous research [17] indicates the ecological and economic efficiency of energy-saving multi-stage shelf dryers with convective fluidized bed drying, particularly for granular biofertilizer production from the digestate. The developed complex technological process allowed simultaneously achieving several Sustainable Development Goals, including Goals 6, 7, 9, 12, 13, and 15.

Ammonium and phosphate can be removed from the digestate by struvite precipitation (Figure 5), also known as MAP (magnesium ammonia phosphate) precipitation. In order to achieve the best nutrient recovery performance magnesium is added in excess, so that nutrient concentrations are approximately 1.3:1:0.9 for Mg:N:P.

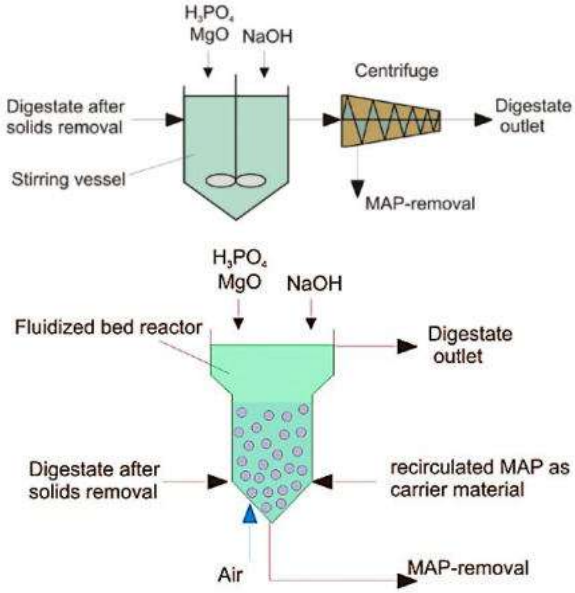

Figure 5 – Possible process options for struvite precipitation [4]

As ammonia is almost always in excess in digestate, magnesium oxide and phosphoric acid are added to the digestate. In addition, pH is slightly decreased to the most favorable for struvite precipitation value at the level of 8.5–9.0 which is in line according to data considered by Silicano et al. in a review [18]. The resulting struvite is a good fertilizer as N, P, and Mg are valuable plant nutrients.

Recovery of nitrogen and phosphorus by precipitation of struvite ($MgNH_4PO_4 \cdot 6H_2O$) can improve N and P management because they may be exported from farms over large distances at relatively low cost. Magnesium-ammonium-phosphate products can contain 12.65 % P in pure compound, while struvite precipitated from organic waste contains from 6 to 12 % [19].

The main disadvantage of struvite precipitation is that a large amount of chemicals is needed, translating into high operational costs. An alternative process can be to recover the chemicals, as struvite releases ammonium and water after heating to well above 100 °C. The resulting magnesium hydrogen phosphate can then be reused for

precipitating ammonium and as phosphorus and magnesium source to treat raw wastewater. Researchers studied different decomposition techniques, including struvite pyrogenation, distillation, acidolysis, chlorination, and electrolysis were studied over the last 10 years [18].

Gas stripping is a process whereby volatile substances are removed from a liquid by gas flow through the liquid. In digestate processing, the aim is to recover nitrogen from the liquid in the form of ammonia. The volatility of ammonia in an aqueous solution can be enhanced by increasing the temperature and the pH. So, in digestate processing, excess heat can be used for heating up the digestate, and the pH can be increased by degassing to remove CO_2 or by the addition of alkali. For ammonia stripping in digestate, three main processes are applied: air stripping, vapor stripping, and biogas stripping.

The significant advantage of ammonia stripping is that a standardized, pure nitrogen fertilizer product can be absorbed onto an acidic solution to be recovered and used. In addition, such a fertilizer liquid can enrich other digestate fractions in digestate processing to a standardized nitrogen concentration, which can increase their marketability. This direction must be very topical for further study, moreover, the evidence base for ammonia stripping for recovery of phosphorus and nitrogen from anaerobic digestate was considered too small referred to the outcomes of the recent systematic review [20]. Vacuum evaporation (Figure 6) occurs in a closed system, which means no exhaust air is produced. The liquid digestate is distributed on the inner surface of the evaporator, the internal heat plates, or the heat exchangers. The reduced pressure reduces the boiling temperature to 40–75°C, which means H_2O, CO_2, NH_3 vaporizes. This steam mixture enters a scrubber and is flushed with a countercurrent acidic solution. The condensed product can be recovered.

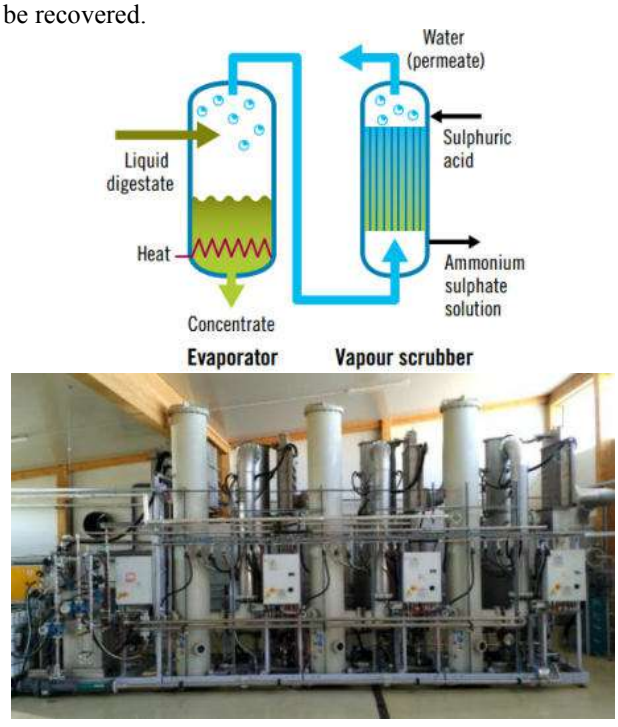

Figure 6 – Vacuum evaporator [3]

Figure 7 – Membrane filtration process with reverse osmosis modules [3]

The performance of the membrane depends on the characteristics of the filtered liquid; therefore, a drawback of such membrane purification processes is that only a limited amount of the digestate will be purified water, and about 50 % of the digestate is accumulated as by-products. The following fractions accumulate in the process: solid fraction, ultrafiltration retentate, reverse osmosis concentrate. The ultrafiltration retentate is often recycled into the biogas plant and/or the solid-liquid separation step to reduce the amounts. Membrane purification is quite expensive and requires a considerable amount of energy with 10–30 kWh_{el}/m^3 input. To improve the process of the digestate membrane filtration optimization could be applied. Basically, it is based on the optimal economic criteria, including the minimal energy consumption for the process performance [21].

The following cases show that evaporation and stripping technologies for digestate processing are used at a commercial scale. From the technological point of view, all the technologies are also applicable in Ukraine. However, it should be proven to be economically feasible and their preconditions exist.

5 Discussion

It is difficult to screen a broad spectrum of chemical pollutants at reasonable costs in practice. For the biogas plant operator, the cheapest and safest way to avoid chemical impurities in digestate is therefore the rigorous selection and quality control of the AD feedstock. Positive lists and feedstock declaration/description are therefore helpful tools, but may only be used only as a guide, and could never substitute the quality control of feedstock materials. Quality control has the determinant role in achieving the required standards of quality for digestate applied as fertilizer and in ensuring the long-term sustainability and safety of this practice.

The main disadvantages of digestate from biogas stations are the variability of its physical and chemical composition and the risks associated with insufficient control of biological safety during its processing, storage, transportation, and application. Thus, without adjustment of the biogas plant operation aimed at creating and

controlling the quality of the target product – standard-quality organic fertilizer from digestate for market – the digestate can only be considered as a potential source of valuable elements of organic origin, suitable for compensation of appropriate nutrients from mineral fertilizers. The market quality product must have standardized characteristics, with appropriate techniques for monitoring compliance with such standards.

Accordingly, most countries have strict limits on concentrations of chemical, physical and biological pollutants in any material that is to be applied to land, whilst others place limits on the soil content of such pollutants. National guidelines for impurities in organic residues include maximal values in % DM for total impurities and different fractions such as plastics, metal, glass, iron metals, non-iron metals, stone. Appropriate fertilizer regulations or similar standards was developed and implemented in Austria, Belgium, Finland, France, Germany, Italy, Netherlands, Norway, Spain, Sweden more than 20 years referring to the review by Teglia et al. [22]. Consequently, according to local conditions, Ukrainian legislation can be adopted with European regulations.

Another feature of digestate is the issue of quality and biosecurity control during long-term storage before application. The presence of a certain proportion of unstabilized organic matter and moisture determines the risks associated with the development of undesirable biological processes in the digestate (both solid and liquid fraction), and accordingly changes in the physical and chemical properties, formation of bacterial or fungal nature contamination, etc. Thus, the creation of a market product from digestate is possible only after stabilization, which involves the removal of excess moisture.

The solid fraction of the digestate after the separator has greater potential for market application than the liquid one, consistent with the results of other studies [23, 24]. Thus, in addition to direct use as fertilizer and soil improver, composting with various organic materials for compost production is also possible. Composting is a way to further stabilize and disinfect organic matter, and therefore, in terms of marketing strategies, digestate composting has obvious advantages in terms of long-term quality preservation. The scope of compost covers both the direct use as both organic fertilizer and soil improver and the use of compost as soil substitution in horticulture, greenhouse farming, mushroom cultivation, and domestic and industrial flower growing. In addition, compost is used in general landscaping, technical planning of territories, and landscaping of urban areas. One more potential application could be a digestate or compost for landfills covering or restoring contaminated and/or unproductive land fertility.

The digestate pellets can be optimally marketed in smaller packages in garden centers. The digestate pellets dissolve when exposed to moisture, which means that the nutrients contained are provided to the plant. At present, only a few biogas plants pelletize dried digestate in Europe and subsequently market it outside the agricultural sector, although the potential is estimated to be very high. Digestate pellets can additionally be refined to special fertilizers with mineral or organic additives.

As mentioned above drying of the SF is the main method to concentrate DM and decrease water content to simplify storage and transporting of biofertilizer. Another tip for discussion is the efficiency of applied fertilizer in terms of nutrient content, bioavailability, and nutrient release time. From this point of view, granular fertilizer must be considered a product with high agro-ecological effect and success market demand [25]. One of the advantages of the granular fertilizer from liquid digestate technology is that nutrients from the AD liquor adsorbed onto the solid core material are released more slowly. In addition, granules are easier to handle with crops than small particles. For example, powders tend to be blown away from target sites and are easily washed away. Moreover, the risks associated with handling fine materials, for example, inhalation, are reduced. Granules also have enhanced flow properties when compared to small particles. For instance, small particles have a greater tendency to cake and stick than granular materials. This makes the granular fertilizer easier to apply to a field using mechanical spreaders than powdered fertilizers. A comparison of the physical and chemical properties of whole digestate, separated liquor and fibre and various commercially available fertilizers has indicated that:

− solid fraction of digestate may be suitable for composting with other organic residuals and use on fields;

− liquid fraction of digestate may be suitable for spreading on large surfaces of agricultural fields.

Resuming all the methods of digestate processing, the following digestate-derived products can be obtained as shown in Table 1.

The potential of the organic fertilizer market in Ukraine, including digestate and fertilizers products from digestate is significant with high demand.

The potential of organic fertilizers has traditionally been associated with the introduction of animal and poultry manure. The form of Ukrainian statistical data submission makes it difficult to estimate the actual amount of nutrients coming from manure into the fields and the proportion of such fertilizers from the total volume of their generation. Indirectly, the estimated total potential of nutrients contained in the manure can be estimated by annual generation volume and the specific nutrient content per unit of dry matter.

The volume of the digestate market is related to the development of biogas market in Ukraine. Today, digestate volumes can be estimated at 1.5–2.0 million tons/year. With each additional MW of installed electricity capacity launch based on biogas, an additional 40–50 thousand tons/year of digestate will be generated.

Table 1 – The main types of digestate derived products (DDP)

Digestate derived product	Nutrients	Methods of processing	Energy consumption, kWh_{el}/m^3	Application and market niches
Solid fraction of digestate (SFD)	N – 25–35 % of RD P – 55–65 % of RD K – 20–30 % of RD C – 60–70 % of RD	Solid-liquid separation of RD	0.2–0.6 – SP 2–5 – DC 1.2–5 – BP	Complex organic fertilizer. Soil improver. Co-composting. Soil reclamation. Component for DSFD and DP production.
Liquid fraction of digestate (LFD)	N – 65–75 % of RD P – 35–45 % of RD K – 70–80 % of RD C – 60–70 % of RD	Solid-liquid separation of RD	0.2–0.6 – SP 2–5 – DC 1.2–5 – BP	Fast-released complex organic fertilizer at nearby agriculture lands. Component for DDP production.
Dried solid fraction of digestate (DSFD)	as in SFD (NH_3 reduced via heating)	Drying of SFD	750–1200 kWh_{therm}/m^3 H_2O	Slow-released organic fertilizer. Soil improver. Component for DP production.
Digestate pellets (DP)	as in DSFD	Pelletizing of DSFD	30–50 kWh_{el}/t	Slow-released concentrated organic fertilizer. Energy production.
Ammonium sulphate (AS)	$(NH_4)_2SO_4$	Air/Steam stripping of LFD with H_2SO_4 regeneration	5–10 kWh_{el} + 45–100 kWh_{th} /m^3	Substitution of artificial ammonium sulphate. Chemical industry.
Ammonia water (AW)	$NH_3 \cdot H_2O$ 25–35 % of NH_3	Steam stripping of LFD	5–10 kWh_{el} + 45–100 kWh_{th} per 1 m^3	Substitution of artificial ammonia water. Chemical industry.
Magnesium ammonia phosphate (struvite) (MAP)	$MgNH_4PO_4 \cdot 6H_2O$	Precipitation of permeate after filtration of LFD	10–15 kWh_{el}/m^3	Substitution of N, P fertilizers. Chemical industry.
N-reached MAP (N+MAP)	MAP + AS	Enrichment with AS		Substitution of N, P fertilizers.
Reverse osmosis-concentrate (RO-C)	Complex	Micro–, ultra–, nano–filtration, RO	10–30 kWh_{el}/m^3	Fast-released concentrated organic fertilizer.
Granular fertilizer (GF)	Complex	Adsorbtion in LFD		Slow-released concentrated organic fertilizer.

Notes: RD – raw digestate; RO – reverse osmosis; SP – screw press; DC – decanter centrifuge; BP – belt press

According to the forecasts of BAU [26] for the development of the biogas sector of Ukraine the installed capacity of biogas projects in agriculture can reach 551 MW_e by 2030 what means up to 20 mln tons of digestate generated per year. This is 10-times increase over 10-year period and therefore digestate application should be regulated at the national level.

Quality assurance schemes for compost and digestate products have been established in several EU countries over the past 25 years. Regulation and specifications on digestate management in selected countries (Canada, Sweden France, Germany, and United Kingdom) are clearly described in appropriate Guidelines as considered by Logan and Visvanathan [27]. They form the backbone of sustainable recycling of bioresources, ensuring that quality products are manufactured consistently and placed on the market with high quality. To support the manufacture of quality compost and digestate across Europe, The European Compost Network e.V. (ECN) developed a concept for a pan-European quality assurance scheme (ECN-QAS) within its working group "Quality Assurance and Standardisation". Nevertheless, based on our critical analysis of national standards for compost and digestate concentration thresholds for some pollutants (i.e., HM) are difference for USA (US EPA United States Environmental Protection Agency), UK and Germany (British PAS British Public Available Specification; RAL GZ251 German standards for compost).

In Ukraine, certification of organic fertilizers can be carried out as part of organic production activities. The first Ukrainian certification body to carry out inspection and certification of organic production is LLC "Organic Standard". As a general approach to producing organically means respecting the rules on organic farming. These rules are designed to promote environmental protection, maintain biodiversity, and build consumer trust in organic products. This means that organic producers need to adopt different approaches to maintaining soil fertility including:

− encourage to switch from mineral nitrogen fertilizers to more sustainable alternatives with incentives;

− cultivation of nitrogen fixing plants and other green manure crops to restore the fertility of the soil;

− crop rotation etc.

Ukraine should also regulate reliable professional practice in the application of fertilizers on agricultural land by the requirements for upper application limits,

determination of nutrient demand of the plant, nutrient surpluses, blocking periods, and storage capacity for storing organic fertilizers to follow the requirements of the European Nitrates Directive. So, organic production is a complex approach supported among others the use of biofertilizers. Regulations are necessary to consider the requirements and environmentally compatible use of biofertilizers. These can be set at a regional, national, or continental level.

Thus, further research can assess the presence and level in digestate of such contaminants as heavy metals, pesticides and hormones that potentially may enter biogas plants via feedstocks. Also, to evaluate whether other factors influence the overall functioning of BR and on digestate pollutants. Methane potential will also be followed with respect of potential interest in post-digestion. The development of technologies to treat the digestate from biogas reactors is directly related with: a) Prevention of depletion of natural resource, as less minerals need to be extracted and b) Avoiding land degradation, because less natural areas will suffer the impacts of element extraction.

Obtaining biogas from organic waste makes it possible, at a certain level, to talk about achieving the goals of sustainable development: energy – obtaining high-calorie fuel; agrochemical – obtaining environmentally friendly biofertilizers; ecological – utilization of organic waste; financial – reduction of costs for the disposal of organic waste and the purchase of energy; social – the ability to meet social needs on a local scale [28].

Processing biomass by anaerobic fermentation yields two key products: which can be used on agricultural land.

Therefore, the use of digestate as biofertilizers will be a growing factor in achieving high levels of energy independence, environmental security, and financial growth, contributing to sustainable development goals.

6 Conclusions

Anaerobic digestion technology is an essential link in organic recycling in agriculture. Digestate is highly suitable for use as an organic fertilizer or soil improver. The production and recycling of digestate as fertilizer requires quality management and quality control throughout the whole AD cycle from feedstock production until the final utilization of digestate. Quality management based on the life cycle assessment methodology implies using high-quality feedstock, pre-processing of specific feedstock types, close control of the AD process, and process parameters affecting digestate quality, digestate processing, declaration, and optimal storage and application as biofertilizer.

There are two main ways how to manage digestate quality, namely prevention and processing. The rule of thumb is that if efficient pollutant removal cannot be guaranteed either by pre-treatment or through the AD process, the respective material must not be used as feedstock in biogas plants where digestate is used as fertilizer or for other agricultural purposes. Among the different commercial options for digestate treatment and nutrient recovery after solid-liquid separation, evaporation, struvite precipitation, ammonia stripping, and membranes technology are the most relevant for LF, and drying is better for SF.

The potential of nutrient, organic carbon and useful microelements in the digestate of agricultural biogas plants allows its consideration as mineral fertilizer substitution and soil improvement. However, the realization of this potential in an economically feasible way requires the development of both methods of preparation and quality control of digestate products and the market of organic fertilizers and soil improvers in Ukraine.

Application and market niches of the main types of digestate derived products were offered as well as methods of their processing. Like other European countries, Ukraine should develop and implement its own rules to specify requirements for organic fertilizer constitution, e.g., what substances can be used, limit values on heavy metals and other pollutants, relevant nutrient contents, and requirements on labeling and marketing.

Acknowledgments

We are thankful to the Civic union “Bioenergy Association of Ukraine” for supporting research work under the project “Stand-alone assignment market study on possibilities for utilization of organic fertilizers and supporting of partnership, knowledge sharing and marketing activities”, funded by the EBRD FINTECCC TC Programme (2019, Contract No.C43289/1018/5362).

The authors acknowledge the Swedish Foundation for International Cooperation in Research and Higher Education which allowed this scientific cooperation to start within Swedish Initiative Grant STINT project "Advancing towards circular bio-based economy through biogas solutions in Sumy, Ukraine" (2022-2023, Contract IB2020-8692, 2020-10-26).

The Research Project was also carried out as planned research projects of the Department of Ecology and Environmental Protection Technologies, Sumy State University, connected with subject “Reduction of the technogenic load on the environment from oil production facilities: prospects for the application of biotechnology” according to the scientific and technical program of the Ministry of Education and Science of Ukraine (state registration 0121U114460).

References

1. Slepetiene, A., Kochiieru, M., Jurgutis, L., Minkeviciene, A., Skersiene, A., Belova, O. (2022). The Effect of Anaerobic Digestate on the Soil Organic Carbon and Humified Carbon Fractions in Different Land-Use Systems in Lithuania. *Land*, Vol. 11(1), pp. 1-17, doi:10.3390/land11010133.
2. Barlog, P., Hlisnikovsky, L., Kunzova, E. (2020). Effect of Digestate on Soil Organic Carbon and Plant-Available Nutrient Content Compared to Cattle Slurry and Mineral Fertilization. *Agronomy,* Vol. 10(3), pp. 1-16, doi: 10.3390/agronomy10030379.
3. Wilken, D., Rauh, S., Fruhner-Weiß, R., Strippel, F., Bontempo, G., Kramer, A., Fürst, M., Wiesheu, M., Kedia, G., Chanto, C. H., Mukherjee, A., Siebert, S., Herbes, C., Kurz, P., Halbherr, V., Dahlin J., Nelles, M. (2018). *Digestate as a fertilizer*. Fachverband Biogas e.V. Dr. Claudius da Costa Gomez (V.i.S.d.P.), Freising, Germany.
4. Drosg, B., Fuchs, W., Al Seadi, T., Madsen, M., Linke, B. (2015). *Nutrient Recovery by Biogas Digestate Processing*. IEA Bioenergy, UK.
5. Lal, R. (2015). Restoring soil quality to mitigate soil degradation. *Sustainability*, Vol. 7(5), pp. 5875–5895, doi: 10.3390/su7055875.
6. Dekker, H., Decorte, M. (2021). *Statistical Report of the European Biogas Association*. EBA, Brussels, Belgium.
7. Nkoa, R. (2014). Agricultural benefits and environmental risks of soil fertilization with anaerobic digestates: a review. *Agronomy for Sustainable Development*, Vol. 34, pp. 473-492, doi: 10.1007/s13593-013-0196-z.
8. Coelho, J. J. J., Hennessy, A., Casey, I., Bragança, C. R. S., Woodcock, T., Kennedy, N. (2020). Biofertilisation with anaerobic digestates: A field study of effects on soil microbial abundance and diversity. *Applied Soil Ecology*, Vol. 147, pp. 103403, doi: 10.1016/j.apsoil.2019.103403.
9. Bhogal, A., Taylor, M., Nicholson, F., Rollett, A., Williams, J., Newell Price, P., Chambers, B., Litterick, A., Whittingham, M. (2015). *DC-Agri; field experiments for quality digestate and compost in agriculture – WP1 report*. WRAP, UK.
10. Taylor, M., Chambers, B., Litterick, A., Longhurst, P., Tyrrel, S., Gale, P., Tompkins, D. (2012). Risk-Based Guidance for BSI PAS110 Digestates in GB Agriculture. *7th European Biosolids and Organic Resources Conference*. The Royal Armouries, Leeds, UK, doi: 10.13140/RG.2.1.5137.1604.
11. Bustamante, M. A., Said-Pullicino, D., Agullo, E., Andreu, J., Paredes, C., Moral, R. (2011). Application of winery and distillery waste composts to a Jumilla (SE Spain) vineyard: Effects on the characteristics of a calcareous sandy-loam soil. *Agriculture, Ecosystems & Environment,* Vol. 140(1-2), pp. 80-87, doi: 10.1016/j.agee.2010.11.014.
12. Govasmark, E., Stab, J., Holen, B., Hoornstra, D., Nesbakk, T. (2011). Chemical and microbiological hazards associated with the recycling of anaerobic digested residue intended for use in agriculture. *Waste Management,* Vol. 31(12), pp. 2577–2583, doi: 10.1016/j.wasman.2011.07.025.
13. Song, Z., Fang, L., Wang, J., Zhang, C. (2019). Use of biogas solid residue from anaerobic digestion as an effective amendment to remediate Cr(VI)-contaminated soils. *Environmental Science and Pollution Research,* Vol. 26(3), doi: 10.1007/s11356-019-04786-y.
14. Al Seadi, T., Lukehurst, C. (2012). *Quality management of digestate from biogas plants used as fertiliser*. IEA Bioenergy, UK.
15. Dada, O., Mbohwa, C. (2018). Energy from waste: A possible way of meeting goal 7 of the sustainable development goals. *1st Africa Energy Conference*. South Africa, Vol. 5, pp. 10577–10584.
16. Ablieieva, I., Berezhna, I., Berezhnyi, D., Prast, A. E., Geletukha, G., Lutsenko, S., Yanchenko, I., Carraro, G. (2022). Technologies for Environmental Safety Application of Digestate as Biofertilizer. *Ecological Engineering & Environmental Technology,* Vol. 23(3), pp. 106–119, doi: 10.12912/27197050/147154.
17. Ablieieva, I., Artyukhova, N., Krmela, J., Malovanyy, M., Berezhnyi, D. (2022). Parameters and Operating Modes of Dryers in terms of Minimizing Environmental Impact and Achieving the Sustainable Development Goals. *Drying technology*, Vol. 40(6), pp. 12, doi: 10.1080/07373937.2022.2081174.
18. Siciliano, A., Limonti, C., Curcio, G. M., Molinari, R. (2020). Advances in Struvite Precipitation Technologies for Nutrients Removal and Recovery from Aqueous Waste and Wastewater. *Sustainability*, Vol. 12(18), doi: 10.3390/su12187538.
19. Szymanska, M., Szara, E., Wąs, A., Sosulski, T., van Pruissen, G. W., Cornelissen, R. L. (2019). Struvite—An Innovative Fertilizer from Anaerobic Digestate Produced in a Bio-Refinery. *Energies*, Vol. 12(2), pp. 296, doi: 10.3390/en12020296.
20. Lorick, D., Macura, B., Ahlström, M., Grimvall, A., Harder, R. (2020). Efectiveness of struvite precipitation and ammonia stripping for recovery of phosphorus and nitrogen from anaerobic digestate: a systematic review. *Environmental Evidence*, Vol. 9, pp. 27, doi: 10.1186/s13750-020-00211-x.
21. Huliienko S. V. Korniienko Y. M., Gatilov K. O. (2020). Modern trends in the mathematical simulation of pressure-driven membrane processes. *Journal of Engineering Sciences*, Vol. 7(1), pp. F1-F21, doi: 10.21272/jes.2020.7(1).f1.
22. Teglia, C., Tremier, A., Martel, J.-L. (2011). Characterization of Solid Digestates: Part 1, Review of Existing Indicators to Assess Solid Digestates Agricultural Use. *Waste Biomass Valorization*, Vol. 2(1), pp. 43-58, doi: 10.1007/s12649-010-9051-5.
23. Maucieri, C., Nicoletto, C., Caruso, C., Sambo, P., Borin, M. (2017). Effects of digestate solid fraction fertilisation on yield and soil carbon dioxide emission in a horticulture succession. *Italian Journal of Agronomy*, Vol. 12, pp. 116-123, doi: 10.4081/ija.2017.800.
24. Horta, C., Carneiro, J. P. (2022). Use of Digestate as Organic Amendment and Source of Nitrogen to Vegetable Crops. *Applied Sciences*, Vol. 12(1), doi: 10.3390/app12010248.
25. Rigby, H., R Smith, S. (2011). *New Markets for Digestate from Anaerobic Digestion*. Department of Civil Environmental Engineering, London, UK.
26. Geletukha, G., Zheliezna, T. (2021). Prospects for Bioenergy Development in Ukraine: Roadmap until 2050. *Ecological Engineering & Environmental Technology*, Vol. 5, pp. 73–81. doi: 10.12912/27197050/139346.
27. Logan, M., Visvanathan, C. (2019). Management strategies for anaerobic digestate of organic fraction of municipal solid waste: Current status and future prospects. *Waste Management & Research,* Vol. 37(1), pp. 27–39, doi: 10.1177/0734242X1881.
28. Pawlita-Posmyk, M., Wzorek, M. (2018). Biogas production from the perspective of sustainable development. *Economic and Environmental Studies*, Vol. 18(3), pp. 1043-1057, doi: 10.25167/ees.2018.47.1.

JOURNAL OF ENGINEERING SCIENCES

Volume 9, Issue 1 (2022)

Chubur, V., Chernysh, Y., Ferchau, E., Zaffar N. (2022). Effect of phosphogypsum addition on methane yield in biogas and digestate properties during anaerobic digestion. Journal of Engineering Sciences, Vol. 9(1), pp. H11-H18, doi: 10.21272/jes.2022.9(1).h2

Effect of Phosphogypsum Addition on Methane Yield in Biogas and Digestate Properties During Anaerobic Digestion

Chubur V.[1], Chernysh Y.[1], Ferchau E.[2], Zaffar N.[2]

[1] Sumy State University, 2, Rymskogo-Korsakova st., 40007, Sumy, Ukraine;
[2] TU Bergakademie Freiberg, 7, Gustav-Zeuner St., 09599, Freiberg, Germany

Article info:
Submitted: February 11, 2022
Accepted for publication: May 30, 2022
Available online: June 3, 2022

***Corresponding email:**
v.chubur@ecolog.sumdu.edu.ua

Abstract. The study discussed the use of phosphogypsum by-product waste in anaerobic digestion processes. Besides the production of biogas from plant substrate with the addition of phosphogypsum, the focus was placed on the enrichment of digestate with phosphogypsum as a mineral additive to increase the concentration of valuable macro-and microelements. The component composition of the obtained digestates was analyzed, and opportunities for additional research were determined. Research on the use of mineral additives in anaerobic digestion is considered promising. Phosphogypsum favors the quality of digestate as an organic mineral fertilizer with a higher content of mineral components. Furthermore, the contribution of phosphogypsum to plant substrate to achieve higher biogas production is not apparent, but with an impact on the component composition of biogas; however, there is an opportunity to consider the potential benefits of using the additive with another type of substrate waste for the anaerobic digestion process.

Keywords: biogas, anaerobic digestion, phosphogypsum, digestate, methane.

1. Introduction

Perennial grasses are considered promising energy crops due to a number of characteristics that make them particularly interesting for intensive biomass production compared to annual crops: high yield potential, high lignin and cellulose content in their biomass, high calorific value, low water content, and low complexity of field treatment. In addition, energy herbaceous crops can improve biodiversity conditions, provide opportunities for simultaneous phytoremediation and erosion control, increase soil organic carbon, and mediate water flow and nutrient content [1].

Among such perennial grasses, canary reed grass shows great energy potential in Europe for direct combustion as a feedstock for pellets and other solid biofuels [2] and biotechnology with biogas production [3].

A promising way to improve the application of beneficial elements to the soil is using digestates as a bio-fertilizer. Canary reed grass can provide an opportunity to enrich the soil with beneficial elements. This perennial herbaceous and fast-growing plant demonstrates a high biomass yield of 5-10 t dry weight/ha/year combined with a moderately high potential for accumulation of target elements [4].

It is worth noting that the application of complex compost based on mixing phosphogypsum, superphosphate, and plant residues into the recultivated soil allows reducing the content of mobile forms of heavy metals (Co, Mn, Cu, Ni, Pb) by 60-70% and more per year due to the translation of heavy metals into forms of organic complexes and metal salts that are difficult for plants to access [5]. Phosphogypsum can be considered an acid-resistant mineral carrier, which is also a source of macro-and microelements for the growth process of the necessary ecological and trophic groups of bacteria. Immobilizing carrier from phosphogypsum with an altered surface is characterized by low porosity whereby a stable biofilm can be formed on the surface of the granules. Consequently, phosphogypsum is also promising for use as an immobilizing carrier for bacteria in bioreactors.

The study aimed to evaluate the biogas production process from Phalaris arundinacea, focusing on the recovery and enrichment of digestate with phosphogypsum as a mineral additive to increase the

useful macro-and microelements. Accordingly, the following tasks were set:

- to study the effect of adding phosphogypsum on the biogas yield compared with the control;
- to study the component composition of the obtained digestates and determine the prospects for further research.

2. Literature Review

The quality of digestate as a fertilizer can be changed by variations of organic waste raw material and additives in anaerobic digestion. Several studies have studied the effect of mineral additives on the biogas yield, its quality, and the component composition of the liquid and solid phase of digestates. Inorganic additives that can improve anaerobic digestion processes are considered in [6]. Inorganic mineral additives can be zeolite, magnetite, metal nanoparticles, industrial wastes, and pH-regulating additives.

Porous additives such as zeolites are well suited for ammonium removal. It has been studied [7] that the removal efficiency of ammonia nitrogen N-NH_4 increased linearly with zeolite, and in digestate effluent levels increased from 10% to 49%. The higher sorption capacity was observed in the variant of anaerobic digestion of plant waste with a smaller zeolite dose. Studies [8] have also revealed a connection between the influence of the ionic exchange of zeolites on the ability to contain the amount of nitrogen by growing strawberries. It was considered that the best efficiency of ammonium removal using zeolites is better at a pH close to 8, which matches the normal pH of the liquid digestate fraction. Nitrogen from digestate is slowly released over time and gradually converted to nitrate. There is no linear proportional effect in terms of increasing plant productivity with the addition of higher amounts of nitrogen has been observed. Therefore, the gradual release of nitrate is a good indicator.

Phosphogypsum can also become a base in complex fertilizers. It has positive results as a meliorant on saline soils to improve the physical and chemical properties and soil fertility [9].

There is known research [10] on using phosphogypsum additive in slow-release fertilizer mixtures. Such fertilizer mixtures are promising for use on acidified soils.

Moreover, using phosphogypsum in the composting process to produce organic-mineral compost with conserved nitrogen has already been investigated. The study [11] demonstrated a positive effect of mixing phosphogypsum with pig manure and cornstalk, which can effectively conserve nitrogen during composting. By adding phosphogypsum, phosphorus additives increased the NH^{4+}-N content of the compost. The higher NH^{4+}-N content might be caused by the low pH of the matrix with the addition of phosphogypsum, thus preventing the conversion of NH^{4+}-N to NH_3. Therefore, the ammonia emission is decreased.

The studies [12, 13] confirm the effects in decreasing NH_3 but increasing N_2O emissions during composting, in combination with sewage sludge or kitchen waste composting.

This means that making a mixture of slow-release fertilizers with phosphogypsum can be an excellent solution to decrease the acidity and salinity of soils. Besides blending, there is interest in exploring joint anaerobic digestion of organic waste with phosphogypsum to produce an environmentally safe organomineral fertilizer with a higher mineral element content due to the rich mineral composition of phosphogypsum (Ca, K, P, Si). Usually, the availability of phosphorus in the soil solution is relatively low, is already researched [14] the degradation of the substance in the processes of anaerobic digestion with the result of improving the availability of phosphorus for plants.

All these factors are considered promising for using organic-mineral complexes of biofertilizers. Mineral component improves both the elemental composition of the biofertilizer and acts as an additional element of nutrition in the processes of bacterial processing of organic raw materials, with an impact on the quality of the product [15].

Phosphogypsum can also become an immobilization acid-resistant carrier, providing the environment with the content of macro-and microelements for biofilm [16], which opens up the possibility of its use in technologies of anaerobic digestion.

Regarding the production of complex organomineral fertilizers, the organic part of the fertilizer is provided by the degradation of organic waste by anaerobic digestion, which has obtained two options of target products, fertilizer and biogas. Consequently, the complex production process provides obtaining green energy through biogas production during processing organic matter into fertilizer.

Furthermore, it should be mentioned that the use of phosphate waste as an additive [17] stimulated the degradation of organic waste and demonstrated the potential to reduce the risk of heavy metal pollution when applying composted organic waste to the soil by enhancing the decomposition of organic matter with transformation into humus with chelated complexes Cu and Zn. Based on composting studies, the target for continuing research on organic fertilizer (digestsate) with phosphogypsum additive for binding heavy metals in the soil was also determined.

3. Research Methodology

3.1 Characteristics of Phalaris arundinacea

Canary grass reed is characterized by a high natural concentration and variety of alkaloids and contains some anthocyanins, with lignin, cellulose, and ash content of 23%, 37%, 2% for the dry matter. Essential advantages of that plant are high yield, low cost of cultivation, and ability to grow in different conditions. Besides using bioenergy, it can be used for phytoremediation and removal of nitrogen compounds [5].

3.2 Characteristics of phosphogypsum

The phosphogypsum content (Fig. 1) includes a significant mass fraction of calcium (from 391 mg/g fresh phosphogypsum from the upper site to 236 mg/g phosphogypsum from terrace V), as well as sulfur (from 155 mg/g fresh phosphogypsum from the upper site to about 125 mg/g phosphogypsum from terraces I, II, III, and V), silicon impurities (from 8, 3 mg/g fresh phosphogypsum from the upper site to about 5 mg/g phosphogypsum from Terraces IV and V), sodium (from 6.4 mg/g phosphogypsum from Terrace II to about 3.5 mg/g phosphogypsum from Terraces III and IV) phosphorus (from about 2 mg/g fresh phosphogypsum from the upper platform and V terrace to 1.5 mg/g phosphogypsum from II terrace) and other impurities (trace elements and heavy metals) content of which is less than 1 mg/g. The content of particular elements, such as aluminum and iron, highly fluctuates in the composition of impurities.

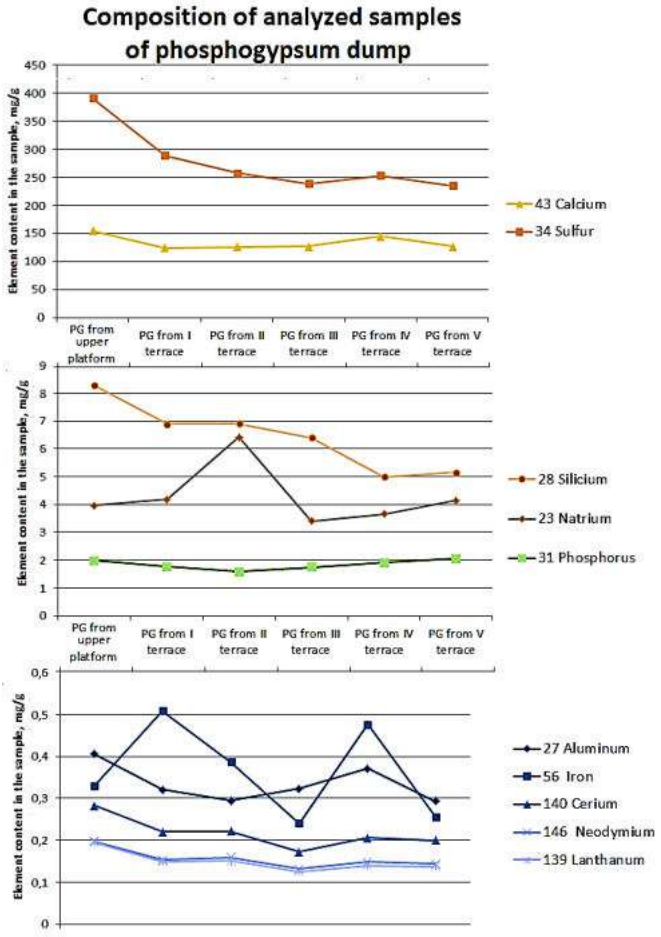

Figure 1 – Composition of elements in the analyzed samples from phosphogypsum dumps

Semihydrate gypsum transforms into dihydrate form during landfilling. In the main crystalline phase, landfill phosphogypsum includes compounds $CaSO_4$-$2H_2O$ (gypsum) and $CaPO_4(OH)$-$2H_2O$ [18].

The specificity of the physical condition of fine-milled particles of phosphogypsum, distributed in a homogeneous medium, determines phosphogypsum's relatively high mineral dispersity. Consequently, its colloids are a low rate of diffusion and unbalanced solubility, and not possible to get through the fine-pored membranes of cellular structures of organisms.

Depending on the time of phosphogypsum storage, the number of phosphorus compounds in the composition decreases, which is explained by the process of gradual transition into water-soluble forms, leaching deep into the dump or the soil of the surrounding areas. Fluorine compounds in fresh waste phosphogypsum are present for a short period in the dump. Therefore, fluorine compounds do not have time to experience the long-term effects of air-dust emission and leaching.

The increase in iron compounds, especially on terrace IV, can be explained by its washout from the upper terraces of the dump or by washout from the layers of recultivated soil located above the phosphogypsum layer.

The interaction of mineral particles of phosphogypsum with the soil substrate is based on the processes of dissolution by mineral acids, root excretions, transformation by microorganisms and effects of organic acids, and interactions of phosphogypsum particles with extracellular compounds.

Consequently, phosphogypsum waste does not contain highly toxic substances that can inhibit the functioning of microbial groups in bioprocesses.

3.3 Characteristics of the inoculum

The biogas batch experiments was conducted at the lab of TU Bergkakademie Freiberg. The inoculum for the anaerobic digestion was taken from previous tests using digestate from agricultural plant waste with 80% cow manure and 20% grass silage and residues from the farm. The component composition of the inoculum used is shown in Table 1.

Table 1 – Composition of elements in the inoculum, mg/g

K	Ca	Mg	Si	Fe	Na	P
64.1	55.6	21.1	14.6	12.6	9.9	8.2
Al	Zn	S	Mn	Cu	Ba	
1.3	1.2	0.8	0.6	0.3	0.1	

3.4 Biogas bench experiment

Canary grass plant substrate was used in a laboratory experiment to produce biogas by anaerobic digestion in a batch reactor at pH 7,0 and 39 °C. Adding 5% and 15% phosphogypsum (per dry weight of plant substrate) to anaerobic digestion on biogas production, methane yield, quality, and concentration of elements in digestate before and after the anaerobic digestion process was studied.

The conceptual diagram of the test is shown in Fig. 2.

Figure 2 – Experiments with additives of phosphogypsum: starting substrates

The anaerobic process was carried out for 20 days, and the calculation of substrate/inoculum proportions was carried out according to the VDI-RICHTLINIEN 4630 Fermentation of organic materials Characterisation of the substrate, sampling, collection of material data, fermentation tests [19]. Parameters that were determined at the beginning and the end of the digestion process were the pH and composition of load and digestate. During the whole digestion process, the biogas was analyzed with a laboratory gas analyzer to detect CH_4, O_2, and H_2S. MilliGascounters MGC-1 were used to control the biogas yield every day.

Fig. 3 shows the lab setup, which consisted of 2-liter bioreactors placed in a thermostat to maintain a constant temperature. Bioreactors were connected to the biogas collection bags via tubes, where gas counters were installed to calculate the volume of the produced biogas. The gas was collected in sampling bags and then analyzed with a gas analyzer for the composition of such gases as CH_4, O_2, H_2S.

Figure 3 – Lab stand for anaerobic digestion

The biodigestate obtained after anaerobic digestion was analyzed by inductively coupled plasma mass spectrometry (Fig. 4) to determine trace element concentrations.

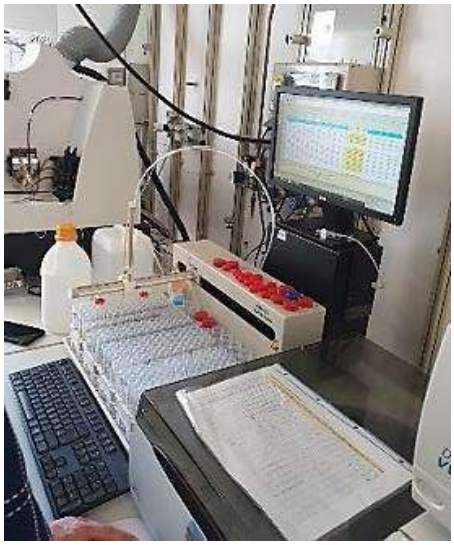

Figure 4 – ICP-MS Instrument, TU Bergakademie Freiberg

4. Results and Discussion

4.1 Analysis of anaerobic digestion performance under biogas yield

Four experiments were carried out in 2 replications: inoculum, control, 5%, and 15% phosphogypsum (PG) additive. The total amount of biogas produced from 1.5 kg substrate with inoculum fluctuates from 10 to 28 liters of biogas. Details are given in Table 2. The quality of biogas varied over time. Volumetric percentages of methane content are shown in Table 3.

Table 2 – Volume of obtained biogas, ml

Day	Inoculum	5% PG additive		15% PG additive		Control	
1	200	830	680	1215	1111	1860	1317
4	329	3166	2810	4599	4839	8479	6166
7	422	7066	6411	8755	8730	16355	11888
10	634	9291	10142	11573	11242	22133	15950
13	795	10644	13235	13564	13423	25125	18123
16	902	10814	14499	15318	15657	26653	19197
19	1042	10834	15579	16276	16225	28053	20179

Table 3 – Volumetric percentages of methane content in obtained biogas, %

Day	5% PG additive		15% PG additive		Control	
3	18	16	20	17	21	22
5	47	51	47	43	52	48
7	65	67	60	58	64	61
14	60	64	60	58	61	51
19	50	69	63	58	63	50

In the batch test operating reactor, a high rate of organic load influenced the anaerobic digestion and biogas production process, which is shown in the graphs of digestion process dynamics for 18 days (Fig. 5, Fig. 6).

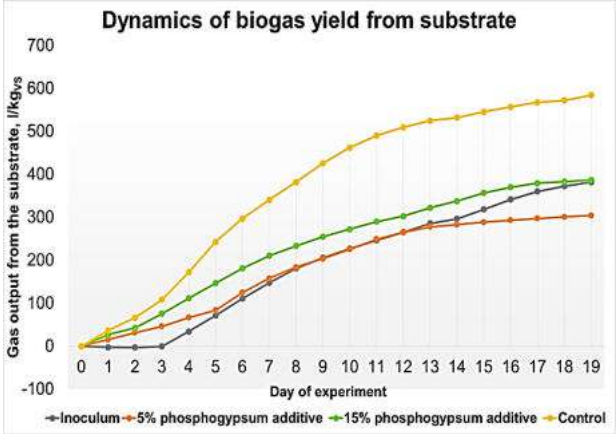

Figure 5 – Cumulative curve of biogas production from the substrate (l/kg_{VS})

Furthermore, a considerable increase in hydrogen sulfide concentration was found both in test reactors with phosphogypsum, an increase up to 3370 ppm was registered in the experiment with 5% of phosphogypsum additive from the 5th day up to the 14th day and in the experiment with 15% of phosphogypsum additive from the 5th to the 19th day, while in the control level of hydrogen sulfide during this period varied from 50 ppm to 200 ppm.

Comparing digestion processes with mineral additive 5% and 15%, the better quality, despite close in total gas volume, has been obtained in the variant with 5% addition of phosphogypsum to the dry matter mass of plant substrate. Compared with the control, an increase in mineral load factor (phosphogypsum) leads to decreased biogas production through the predominance of sulfate-reducing microorganisms in the bacterial association. Therefore, there is a demand for additional precipitation of sulfide fraction formed in the bioreactor. From that perspective, it provides an opportunity to use this type of additive for the anaerobic digestion of raw materials contaminated with heavy metals, considering the possibility of their precipitation by excessive sulfide fraction.

Accordingly, previous studies by Chernysh et al. (2018, 2019) [20, 21] substantiated the possibility of using phosphogypsum in the anaerobic digestion of sludge from municipal sewage treatment plants to stimulate the development of sulfate-reducing bacteria and increase the yield of hydrogen sulfide in biogas, which co-precipitated heavy metals from sludge in the insoluble sulfide fraction. Since the problem of sludge utilization is still highly relevant in Ukraine, it is not used in agriculture precisely because of the presence of heavy metal compounds soluble and accumulated in the plant biomass. Therefore, an important direction is to improve the environmental quality of digestate, and its detoxification for further use. Consequently, the obtained experimental data confirm the previous results and require further study of the properties of the obtained digestate. Moreover, further research needs to select combinations of co-substrates, where the process of sulfate reducer stimulation will have an ecologically significant impact on the use of digestate as a biostimulant in agriculture and urban greening.

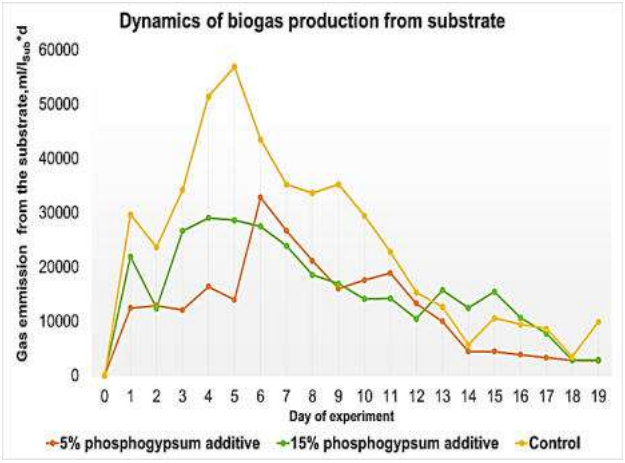

Figure 6 – Cumulative curve of daily gas production from the substrate ($ml/l_{sub} \times d$)

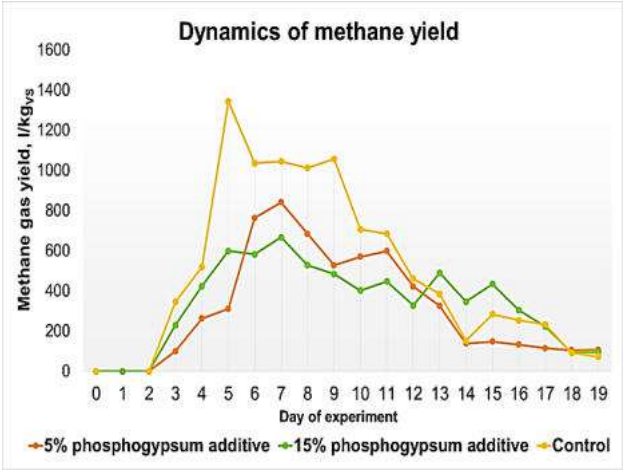

Figure 7 – Cumulative curve of methane production from the substrate (l/kg_{VS})

There are already studied [22] the properties of some mineral additives, from municipal solid waste incineration plants and construction demolition sites, as

promising sources of macro and trace elements to improve and stabilize anaerobic biogas production. The challenge in this study was to find a mineral additive that would promote anaerobic digestion without harming the microbial community of the digester. This research used additives such as incinerator slag, fly ash, boiler ash, and cement-based wastes as co-substrates for anaerobic fermentation. According to Shamurad et al. (2019), these wastes can be used as micronutrient additives to optimize the anaerobic digestion of organic materials, in particular, to prolong the efficiency of the anaerobic digestion process at a certain level of biogas productivity over a more extended time. A promising solution for dealing with substrates with high ammonia concentrations is the addition of mineral compounds (e.g., clay compounds) which can retain ionized ammonia due to their high cation-exchange capacity. In [23], the positive effect of zeolite in the anaerobic digestion process at high concentrations of ammonia was investigated. Thereby there are reasons to study the perspective of the mineral addition of phosphogypsum with livestock wastes.

4.2. Analysis of the obtained digestats

The organic part of the solid fraction of the digestate enriches the soil (improving soil conditions by reducing the humus deficit in the soil), and mineral supplement increases the soil quality [24]. The general view of the digestate of liquid and solid phases is shown in Fig. 8.

a b

Figure 8 – Image of the digestate appearance obtained after anaerobic digestion of plant substrate and phosphogypsum: a – rare phase; b – solid phase

The potassium, calcium, silicon, sulfur, and aluminum concentrations were significantly increased in the studied digestate, shown in Fig. 9. The increase in Ca, Sa, S, Al, and microdoses of the rare earth element group is related to the additional input of phosphogypsum which was rich in these components. Furthermore, the higher the level of mineral loading (percentage content of phosphogypsum), the higher the enrichment of elements in digestate, possibly due to differences in substrate availability for microorganisms and changes in chemical binding forms of elements in the composition.

Because of the high concentration of Ge (0.96 μg/g) and rare earth elements (12.26 μg/g) in the substrate used in the experiment, increasing the ratio between co-substrates leads to a decrease in the concentration of these elements (Ge 0.46 μg/g) and rare earth elements 1.6 μg/g in digestate.

Therefore, the current research aims to optimize the processes of elemental renewal, enrichment, biogas production, and identifying changes in the chemical forms of binding of target elements in digestate.

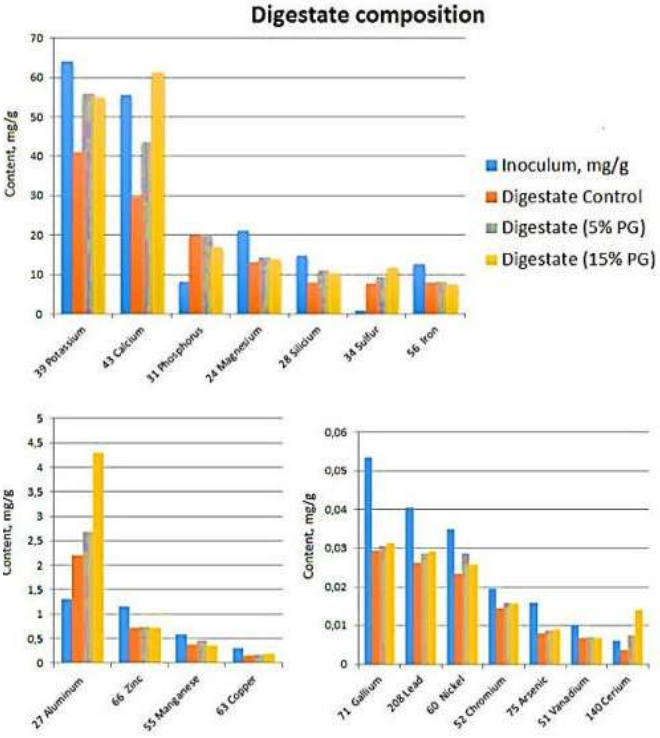

Figure 9 – Analysis of the composition of digestate obtained after anaerobic digestion of plant substrate and phosphogypsum

A decrease in phosphorus content in samples with phosphogypsum addition was noted compared to the control sample (from 19.8 μg/g to 15.1 μg/g). Hence, in the liquid fraction were isolated compounds of phosphorus, which can be used in complex with the obtained organomineral product.

Currently, an important goal is to reduce the risk of heavy metal contamination after returning biogas to the field as fertilizer. Thus, a study by Li Yi et al. (2016) [25], which was focused on reducing heavy metal pollution in pig manure, used anaerobic fermentation technology to study the effects of adding exogenous zeolite on biogas production, methane content, and changes in the proportion and chemical fractions of heavy metal zinc in digestate. The results show that zeolite does not significantly affect gas production and methane content during biogas fermentation. After fermentation within the zeolite addition, 89.88% of Zn heavy metal is contained in the biogas sludge, only 10.12% in the biogas slurry. Zeolite may be a passivator of metals in the anaerobic fermentation process.

Therefore, the relevant topic still remains the search for effective local bacterial biosorbents that can survive even under toxic environmental conditions in various metabolic states.

5. Conclusions

The use of mineral additives in anaerobic digestion is a viable factor for further research, particularly the phosphogypsum additive. However, phosphogypsum's positive influence on the improvement of digestate quality can be used as an organic mineral fertilizer with enriched mineral components. It is also definite that mixing phosphogypsum additive with plant waste does not produce a positive effect on biogas formation; nevertheless, it is possible to analyze the prospects of using the additive with animal waste with increased content of nitrogen compounds.

Subsequent studies will focus on studying organic-mineral digestion products with the addition of phosphogypsum after the digestion of various co-substrates based on organic waste under micro-field conditions.

6. Acknowledgments

The authors express gratitude to DAAD (Deutscher Academischer Austauschdienst, German Academic Exchange Service) for the opportunity to carry out the presented above research in the framework of the joint educational project "EcoMining: Development of Integrated Ph.D. Program for Sustainable Mining & Environmental Activities» between Technical University "Bergakademie Freiberg" (Germany) and Dnipro University of Technology (Ukraine).

This research project was carried out as planned research project of the Department of Ecology and Environmental Protection Technologies of Sumy State University, related to the topic "Assessment of the technogenic load of the region with changes in industrial infrastructure" according to the scientific and technical program of the Ministry of Education and Science of Ukraine (state registration no. 0121U114478); Joint Ukrainian-Czech R&D project "Bioenergy innovations in waste recycling and natural resource management", 2021-2022.

References

1. Mola-Yudego, B., Xu, X., Englund, O., Dimitriou, I. (2021). Reed canary grass for energy in Sweden: yields, land-use patterns, and climatic profile. *Forests* , Vol. 12, 897. doi: 10.3390/f12070897
2. Jasinskas, A., Streikus, D., Šarauskis, E., Palšauskas, M., Venslauskas, K. (2020). Energy evaluation and greenhouse gas emissions of reed plant pelletizing and utilization as solid biofuel. *Energies*, Vol. 13(6), 1516. doi:10.3390/en13061516
3. Roj-Rojewski S., Wysocka-Czubaszek, A., Czubaszek, R., Kamocki, A., Banaszuk, P. (2019). Anaerobic digestion of wetland biomass from conservation management for biogas production. *Biomass and Bioenergy*, Vol. 122. pp. 126–132. doi:10.1016/j.biombioe.2019.01.038.
4. Usťak S., Šinko J., Muňoz J. (2019). Reed canary grass (Phalaris arundinacea L.) as a promising energy crop. *Journal of Central European Agriculture*. 2019. Vol. 20(4), pp. 1143–1168. doi:10.5513/jcea01/20.4.2267
5. Denzanov, G., Petruk, G. (2006). Resource-saving technology of biocoversion of natural phosphates. *Environmental Bulletin*. pp. 25.
6. Liu, X., Qi, L., Chatzisymeon, E. , Yang, P., Sun W., Pang, L. (2021). Inorganic additives to increase methane generation during anaerobic digestion of livestock manure: a review. *Environmental Chemistry Letters*, Vol 19, pp. 4165-4190
7. Dębowski, M., Zieliński, M., Rusanowska, P. (2017). The utilisation of zeolites for the reduction of ammonium concentration in biogas processes. *Technical Transactions*, Vol 114(11), pp. 107-116.
8. Costamagna, G., Chiabrando, V., Fassone, E., Mania, I., Gorra, R., Ginepro, M., Giacalone, G. (2020) Characterization and use of absorbent materials as slow-release fertilizers for growing strawberry: preliminary results. *Sustainability*, Vol 12(17), 6854. doi:10.3390/su12176854
9. Makarova T. K. (2018) Economical efficiency of chemical melioration with phosphogypsum on irrigated solonetzivatnyh chornozems. Newsletter of the National University of Science and Technology. *Technical Sciences*, Vol. 4, pp. 22-30
10. Zhantasov, K., Ziyat, A., Sarypbekova, N., Kirgizbayeva, K., Iztleuov, G., Zhantasov, M., Sagitova G., Aryn A. (2022). Ecologically friendly, slow-release granular fertilizers with phosphogypsum. *Polish Journal of Environmental Studies*, Vol. 31, doi:10.15244/pjoes/144099
11. Li, Y., Luo, W., Li, G., Wang, K., Gong, X. (2018). Performance of phosphogypsum and calcium magnesium phosphate fertilizer for nitrogen conservation in pig manure composting. *Bioresource Technology*, Vol. 250, 53–59. doi:10.1016/j.biortech.2017.07.172
12. Yuan, J., Li, Y., Chen, S., Li, D., Tang, H., Chadwick, D., Li, S., Li, W., Li, G. (2018). Effects of phosphogypsum, superphosphate, and dicyandiamide on gaseous emission and compost quality during sewage sludge composting. *Bioresource Technology*, Vol. 270, 368–376. doi:10.1016/j.biortech.2018.09.023
13. Yang, F., Li, G., Shi, H., Wang, Y. (2015). Effects of phosphogypsum and superphosphate on compost maturity and gaseous emissions during kitchen waste composting. *Waste Management*, Vol. 36, 70–76. doi:10.1016/j.wasman.2014.11.012
14. Möller K., Müller, T. (2012). Effects of anaerobic digestion on digestate nutrient availability and crop growth: A review. *Engineering in Life Sciences*. Vol. 12, 242-257.

15. Ablieieva, I., Berezhna, I., Berezhnyi, D., Prast, A., Geletuha, G., Lutsenko, S., Yanchenko, I., Carraro, G. (2022) Technologies for environmental safety application of digestate as biofertilizer. *Ecological Engineering and Environmental Technology*. Vol. 23(3), pp. 106-119. doi:10.12912/27197050/147154
16. Chernysh Y. (2017). Development of an integrated model of ecologically safe phosphogypsum utilization in environmental protection technologies. *Journal of National Technical University "KhPI"*. Series: New Solutions in Modern Technologies, Vol.53(1274), pp. 152-158.
17. Wang, L., Liu, H., Prasher, S. O., Ou, Y., Yan, B., Zhong, R. (2021). Effect of inorganic additives (rock phosphate, PR and boron waste, BW) on the passivation of Cu, Zn during pig manure composting. *Journal of environmental management*, Vol. 285, 112101. doi:10.1016/j.jenvman.2021.112101
18. Chernysh, Y., Balintova, M., Plyatsuk, L., Holub, M., Demcak, S. (2018). The Influence of Phosphogypsum Addition on Phosphorus Release in Biochemical Treatment of Sewage Sludge. Inter*national Journal of Environmental Research and Public Health*, Vol. 15(6), 1269. doi:10.3390/ijerph15061269
19. VDI-4630 (2006) Fermentation of Organic Materials: Characterisation of the Substrate, Sampling, Collection of Material Data, Fermentation Tests. Verlag des Vereins Deutscher Ingenieure, Düsseldorf, 92.
20. Chernysh, Y., Balintova, M., Plyatsuk, L., Holub, M.,Demcak, S. (2018). The influence of phosphogypsum addition on phosphorus release in biochemical treatment of sewage sludge. *International Journal of Environmental Research and Public Health,* Vol. 15(6), 1269. doi:10.3390/ijerph15061269
21. Chernysh Y., Plyatsuk L. (2019). The carrier development for biofilms on the basis of technogenic wastes for pollutants treatment in the environmental protection technologies. In: Ivanov V. et al. (eds) Advances in Design, Simulation and Manufacturing. DSMIE 2018. *Lecture Notes in Mechanical Engineering*. Springer, Cham. pp. 422-432.
22. Shamurad, B., Gray, N., Petropoulos, E., Tabraiz, S., Acharya, K., Quintela-Baluja, M., Sallis, P. (2019). Co-digestion of organic and mineral wastes for enhanced biogas production: Reactor performance and evolution of microbial community and function. *Waste Management*, Vol. 87, pp. 313–325. doi:10.1016/j.wasman.2019.02.021
23. Fotidis, I. A., Kougias, P. G., Zaganas, I. D., Kotsopoulos, T. A., Martzopoulos, G. G. (2013). Inoculum and zeolite synergistic effect on anaerobic digestion of poultry manure. *Environmental Technology*, Vol. 35(10), pp. 1219–1225. doi:10.1080/09593330.2013.865083
24. Prask, H., Szlachta, J., Fugol, M., Kordas, L., Lejman, A., Tużnik, F., Tużnik, F. (2018). Sustainability biogas production from ensiled plants consisting of the transformation of the digestate into a valuable organic-mineral granular fertilizer. *Sustainability*. Vol. 10(3), 585. doi:10.3390/su10030585
25. Li, Y., Liu Y.J., Feng, Y.Y., Gong, J.L., Zhang, Z., Gu, S.Y. (2016). Effects of adding zeolite on pig manure anaerobic fermentation and the change of heavy metal Zinc in digestate. *Renewable Energy Resources*, Vol. 34(6), pp.943-948.

JOURNAL OF ENGINEERING SCIENCES

Volume 9, Issue 1 (2022)

Javanbakht T. (2022). Automated decision-making with TOPSIS for water analysis. Journal of Engineering Sciences, Vol. 9(1), pp. H19-H24, doi: 10.21272/jes.2022.9(1).h3

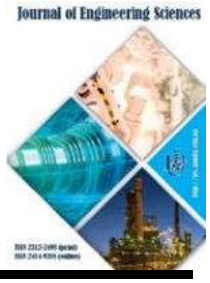

Automated Decision-Making with TOPSIS for Water Analysis

Javanbakht T.

Department of Computer Science, University of Quebec in Montreal,
201, President Kennedy St., Montreal, Quebec H2X 3Y7, Canada

Article info:
Submitted: April 4, 2022
Accepted for publication: June 3, 2022
Available online: June 6, 2022

***Corresponding email:**
javanbakht.taraneh@courrier.uqam.ca

Abstract. This paper aims to present a new application of TOPSIS with an automated decision-making process for the analysis of drinking water. For this purpose, the algorithm was modified with a fuzzy disjunction, and the maximal output values were set to one. The properties of drinking water, such as total dissolved solids, hardness, electrical conductivity, and cost, were the criteria analyzed in this study. These criteria were analyzed with unmodified and modified algorithms. Therefore, the modified TOPSIS was also used to optimize the parameters of the candidates. The appearance of the value of 1.0 in the algorithm's output was due to the confusion of an individual's categories of drinking water and undrinkable water. The advantage of this investigation was that, for the first time, it allowed automated decision-making to detect the drinking water in different samples and analyze them according to their characteristics. This would be important in developing new technologies for detecting and analyzing drinking water in the environment. The results of this paper can be applied in materials sciences and engineering.

Keywords: TOPSIS, water, automated decision-making, computational engineering, process innovation.

1 Introduction

Drinking water is essential for human life and is in high demand in many countries [1-3]. Many people worldwide do not have access to safe drinking water [4]. The chemistry and toxicology of the chemicals in underground water can determine their characteristics for performing essential drinking water production processes [5].

The Technique for Order of Preference by Similarity to Ideal Solution (TOPSIS) is an appropriate decision-making method with diverse applications in science and engineering [6-10]. The candidates' ranking in this method is performed according to their distances from ideal solutions and their closeness coefficients [11-15].

The characteristics of drinking water, such as its total dissolved solids, hardness, electrical conductivity, and cost, must be analyzed [16-19]. The modified version of the TOPSIS method can help determine which water sample would be more appropriate according to its rank.

Moreover, the automated decision-making process must be performed with the modified algorithm. This would make the distinction between drinking water and non-consumable water. This analysis would help the next generation of robots distinguish and analyze different drinking water samples without human intervention. As the amount of drinking water can decrease during the next decades on the planet, researching this material on other planets would be essential for human survival.

Demarcator theory is a theory according to which three characteristics, called the demarcators, are found in the category members for their distinction from the members of other categories. The strong and weak demarcators have an impact on this distinction.

However, the marginal demarcators do not positively affect this distinction, but their consideration leads to category confusion and inconsistency in epistemic beliefs [8, 20, 21].

According to the demarcator theory, the total dissolved solids in samples is their strong demarcator that impacts the distinction of drinking water from undrinkable water. In contrast, hardness and electrical conductivity are the weak demarcators that have less effect for this distinction. The transparency and amount of water and its cost cannot affect the importance of drinking water and undrinkable water. These marginal demarcators do not help humans distinguish the members of these categories.

This work aimed to optimize the drinking and undrinkable water samples with unmodified and modified TOPSIS methods.

For this purpose, the following tasks were performed:

1) optimization of water samples with unmodified TOPSIS;

2) modification of TOPSIS with the Łukasiewicz fuzzy disjunction;

3) optimization of water samples with modified TOPSIS.

The prediction, detection, and analysis of drinking water samples with modified TOPSIS with an automated decision-making process have not been performed previously. The results of this paper can find their applications in science and engineering.

2 Research Methodology

2.1 TOPSIS method

The TOPSIS code in Python is available on the GitHub website https://github.com/Glitchfix/TOPSIS-Python/blob/master/topsis.py. It was used for the optimization of parameters in this paper.

The main steps of this code were described previously [12].

2.2 Modified TOPSIS

The modified TOPSIS, including the Łukasiewicz fuzzy disjunction developed in new software, was used in this paper as described previously [8]. In the data analysis with the modified algorithm, the members of two categories of drinking water (candidates C1 and C2) and undrinkable water (C3, C4, and C5) were considered.

The category confusion due to humans' inappropriate consideration of the criteria that led to the inconsistency of their epistemic beliefs was analyzed as explained previously [8]. In the second series of analyses with the modified algorithm, turbidity as a marginal demarcator of water, which was a cost criterion, was added to the evaluation matrix. The categories confusion due to the consideration of this criterion as a profit criterion was evaluated with the fuzzy disjunction. This was because individuals mistakenly considered it a characteristic that positively distinguished the two water categories. The maximal value of 1.0, according to the Łukasiewicz fuzzy disjunction was observed in the evaluation matrix in the output.

3 Results and discussion

The first series of results were obtained with the unmodified TOPSIS algorithm.

Table 1 shows the evaluation matrix of water samples as candidates and their criteria.

Table 1 – Evaluation matrix of water samples as candidates and their criteria

Candidates/ Criteria	Total dissolved solids	Hardness	Electrical conductivity	Cost
C_1	very low	very low	low	high
C_2	very low	very low	low	medium
C_3	medium	medium	medium	low
C_4	medium	medium	medium	medium
C_5	high	high	high	medium

Tables 2 and 3 show the matrices of triangular fuzzy data and their mean values, respectively.

Tables 4 and 5 show the matrix of the weights applied for each criterion of the water samples and the criteria matrix, respectively.

Table 6 shows the distances between the best and worst alternatives, the similarity coefficients, and rankings for water samples.

Table 2 – Matrix of triangular fuzzy data

Candidates/ Criteria	Total dissolved solids	Hardness	Electrical conductivity	Cost
C_1	0.1, 0.2, 0.3	0.1, 0.2, 0.3	0.2, 0.3, 0.4	0.7, 0.8, 0.9
C_2	0.1, 0.2, 0.3	0.1, 0.2, 0.3	0.2, 0.3, 0.4	0.4, 0.5, 0.6
C_3	0.4, 0.5, 0.6	0.4, 0.5, 0.6	0.4, 0.5, 0.6	0.2, 0.3, 0.4
C_4	0.4, 0.5, 0.6	0.4, 0.5, 0.6	0.4, 0.5, 0.6	0.4, 0.5, 0.6
C_5	0.7, 0.8, 0.9	0.7, 0.8, 0.9	0.7, 0.8, 0.9	0.4, 0.5, 0.6

Table 3 – Matrix of the mean values of triangular fuzzy data

Candidates/ Criteria	Total dissolved solids	Hardness	Electrical conductivity	Cost
C_1	0.2	0.2	0.3	0.8
C_2	0.2	0.2	0.3	0.5
C_3	0.5	0.5	0.5	0.3
C_4	0.5	0.5	0.5	0.5
C_5	0.8	0.8	0.8	0.5

Table 4 – Weights applied for each criterion of water samples

Alternatives/ Values	Total dissolved solids	Hardness	Electrical conductivity	Cost
$C_1 – C_5$	0.5	0.5	0.5	0.5

Table 5 – Criteria matrix for water samples

Alternatives/ Values	Total dissolved solids	Hardness	Electrical conductivity	Cost
$C_1 – C_5$	false	false	false	false

Table 6 – The distances from the best and worst alternatives (d_i^* and d_i^-), the similarity coefficients (CC_i)and rankings for water samples

Candidates	d_i^*	d_i^-	CC_i	Ranking
C_1	0.1027	0.2207	0.6824	2
C_2	0.0411	0.2292	0.8479	1
C_3	0.1054	0.1550	0.5952	3
C_4	0.1132	0.1315	0.5374	4
C_5	0.2245	0.0617	0.2154	5

The second series of results were obtained with the modified TOPSIS algorithm. The Łukasiewicz fuzzy disjunction was applied to allow only the values equal to or below 1.0 to appear in the output.

Table 7 shows the evaluation matrix of water samples as candidates and their criteria.

Tables 8 and 9 show the matrices of triangular fuzzy data and their mean values, respectively.

Table 7 – Evaluation matrix of water samples as candidates and their criteria

Candidates/ Criteria	Total dissolved solids	Hardness	Electrical conductivity	Cost	Turbidity
C_1	very low	very low	low	high	very low
C_2	very low	very low	low	medium	very low
C_3	medium	medium	medium	low	medium
C_4	medium	medium	medium	medium	medium
C_5	high	high	high	medium	medium

Table 8 – Matrix of triangular fuzzy data

Candidates/ Criteria	Total dissolved solids	Hardness	Electrical conductivity	Cost	Turbidity
C_1	0.1,0.2,0.3	0.1,0.2,0.3	0.2,0.3,0.4	0.7,0.8,0.9	0.1,0.2,0.3
C_2	0.1,0.2,0.3	0.1,0.2,0.3	0.2,0.3,0.4	0.4,0.5,0.6	0.1,0.2,0.3
C_3	0.4,0.5,0.6	0.4,0.5,0.6	0.4,0.5,0.6	0.2,0.3,0.4	0.4,0.5,0.6
C_4	0.4,0.5,0.6	0.4,0.5,0.6	0.4,0.5,0.6	0.4,0.5,0.6	0.4,0.5,0.6
C_5	0.7,0.8,0.9	0.7,0.8,0.9	0.7,0.8,0.9	0.4,0.5,0.6	0.4,0.5,0.6

Table 9 – Matrix of the mean values of triangular fuzzy data

Candidates/Criteria	Total dissolved solids	Hardness	Electrical conductivity	Cost	Turbidity
C_1	0.2	0.2	0.3	0.8	0.2
C_2	0.2	0.2	0.3	0.5	0.2
C_3	0.5	0.5	0.5	0.3	0.5
C_4	0.5	0.5	0.5	0.5	0.5
C_5	0.8	0.8	0.8	0.5	1.0

In Table 9, in comparison with table 3, the maximal value of 1.0 was observed for the last alternative due to the Łukasiewicz fuzzy disjunction, which showed the confusion of both drinking categories and undrinkable water samples by an individual.

Tables 10 and 11 show the matrix of the weights applied for each criterion of the water samples and the criteria matrix, respectively.

Table 12 shows the distances between the best and worst alternatives, the similarity coefficients, and rankings for water samples.

Table 10 – Weights applied for each criterion of water samples

Alternatives/ Values	Total dissolved solids	Hardness	Electrical conductivity	Cost	Turbidity
$C_1 – C_5$	0.5	0.5	0.5	0.5	0.5

Table 11 – Criteria matrix for water samples

Alternatives/Values	Total dissolved solids	Hardness	Electrical conductivity	Cost	Turbidity
$C_1 – C_5$	false	false	false	false	true

Table 12 – The distances from the best and worst alternatives (d_i^* and d_i^-), the similarity coefficients (CC_i), and rankings for water samples

Candidates	d_i^*	d_i^-	CC_i	Ranking
C_1	0.1515	0.1766	0.5382	2
C_2	0.1315	0.1833	0.5824	1
C_3	0.1159	0.1329	0.5341	3
C_4	0.1205	0.1155	0.4894	4
C_5	0.1796	0.1365	0.4318	5

The comparison of the obtained results revealed several important issues. The drinking water samples, candidates 1 and 2, were ranked in the first two positions, whereas undrinkable water samples were ranked in the three last positions.

Moreover, the cost impacts the ranking of drinking water samples, and the candidate with a lower cost, the second candidate, was ranked in the first position. The candidates' distances from the best and worst alternatives and their similarity coefficients were different with the unmodified and modified algorithms.

However, the same rankings were obtained in both analyses. The appearance of the value of 1.0 in the algorithm's output was due to the confusion of an individual's categories of drinking water and undrinkable water. This could be attributed to his inconsistency in epistemic beliefs.

Previously, the characteristics of several materials were investigated [22-26]. Moreover, new materials have been explored for their diverse applications in sciences and engineering [27-30]. It has been shown that nanoparticles [31, 32], polymers [33-36], and nanocomposites [37] could be used for water treatment. TOPSIS has been used for the selection of polymers [38-41], nanomaterials [42-44], and machine process parameters [45]. It has been shown to be efficient for optimizing analytic procedures and normalization methods [46, 47], and materials [48-52].

Although TOPSIS has been used to optimize some materials, its modified version with the Łukasiewicz fuzzy disjunction has not previously been used for their optimization. In other words, none of these previous studies has been done with the automated decision-making process with modified TOPSIS. To optimize these materials, it would be required to perform the automated decision-making process with the modified TOPSIS as presented in this paper.

More investigations are needed to improve the analysis method of drinking and undrinkable water samples with the TOPSIS algorithm. In the next step, the water samples with different concentrations of ions will be investigated.

4 Conclusions

The article aims to explain the analysis results of drinking and undrinkable water samples with an automated decision-making process. The tasks of this study were performed with unmodified and modified TOPSIS algorithms. The modified TOPSIS method was obtained by adding the Łukasiewicz fuzzy disjunction to the algorithm. For this purpose, the maximal values of the membership degrees were set to one.

To perform the analysis, the modified TOPSIS algorithm with this fuzzy disjunction was used, giving comparable results to the unmodified algorithm.

Although the distances from the best and worst alternatives and similarity coefficients differed with the unmodified and modified algorithms, the same rankings were obtained in both analyses.

The appearance of the value of 1.0 in the output of the algorithm, due to the confusion of the categories of drinking water and undrinkable water by the individual, could be attributed to his inconsistency in epistemic beliefs.

Overall, the research presents a new application of TOPSIS for predicting and detecting water samples that could be applied in sciences and engineering.

References

1. Yadi, M.T. Determinants of demand for the packaged drinking water, *International Journal of Innovative Research in Engineering & Multidisciplinary Physical Sciences*, 10(4):53-60, 2022.
2. Zhu, R., Fang, Y. Application of a water supply-demand balance model to set priorities for improvements in water supply systems: A case study from the Koshi river basin, Nepal, *Int J Environ Res Public Health*, 19(3), 1606, 2022. https://doi.org/10.3390/ijerph19031606.
3. Threats to sources of drinking water and aquatic ecosystem health in Canada, National Water Research Institute, Environment Canada, NWRI Scientific Assessment Report Serie 1, 2001.
4. Clerico, E.A. The future of water reuse in America in *Research to Improve Water-use Efficiency and Cconservation : Technologies and Practices*, 30-51, 2007.
5. Emanuel, E., Simon, Y., Joseph, O. Characterization of hardness in the groundwater of Port-Au-Prince, An overview on the health significance of magnesium in the drinking water, *Aqua-LAC*, 5(2) :35-43, 2013.
6. Chen, Y., Li, K.W, Liu, S.F. An OWA-TOPSIS method for multiple criteria decision analysis, An OWA-TOPSIS method for multiple criteria decision analysis, *Expert Systems with Applications*, 38(5):5205-5211, 2011. https://doi.org/10.1016/j.eswa.2010.10.039.
7. Huang, W., Huang, Y.Y. Research on the performance evaluation of Chongqing electric power supply bureaus based on TOPSIS, *Energy Procedia*, 14:899-905, 2012. https://doi.org/10.1016/j.egypro.2011.12.1030.
8. Javanbakht, T. *Modélisation et traitement informatique de l'inconsistance des croyances épistémiques*, Thesis, University of Quebec in Montreal, 2022.
9. Ozturk, D., Batuk, F. Technique for order preference by similarity to ideal solution (TOPSIS) for spacial decision problems, *Proceedings ISPRS*, 2011.
10. Rahim, R. et al. Technique for order of preference by similarity to ideal solution (TOPSIS) method for decision support system in top management, *Information and Communication TechnologyBusiness and Management*, 7(3):290-293, 2018.
11. Indahingwati, A., Wajdi, M.B.N., Susilo, D.E., Kurniasih, N., Rahim, R. Comparison analysis of TOPSIS and fuzzy logic methods on fertilizer selection, *International Journal of Engineering and Technology*, 7(2.3):109-114, 2018. https://doi.org/10.14419/ijet.v7i2.3.12630.
12. Javanbakht, T. Analysis of nanoparticles characteristics with TOPSIS for their manufacture optimization, *Journal of Engineering Sciences*, 9(2):C1-C8, 2022. https://doi.org/10.21272/jes.2022.9(2).c1.
13. Jumarni, R.F., Zamri, N. An integration of fuzzy TOPSIS and fuzzy logic for multi-criteria decision making problems, *International Journal of Engineering and Technology*, 7(2):102-106, 2018. https://doi.org/10.14419/ijet.v7i2.15.11362.
14. Alguliyev, R., Aliguliyev, R., Yusifov, F. Modified fuzzy TOPSIS + TFNs ranking model for candidate selection using the qualifying criteria, *Soft Computing*, 24(1), 2020. https://doi.org/10.1007/s00500-019-04521-2.
15. Varnamkhasti, M.J., Sadabadi, S.A., Venicheh, A.-H. A new index for TOPSIS based on relative distance to best and worst points, *International Journal of Information Technology and Decision Making*, 16(03):695-719, 2020. https://doi.org/10.1142/S0219622020500145.
16. Thirumalini, S., Joseph, K. Correlation between electrical conductivity and total dissolved solids in natural waters, *Malaysian Journal of Science*, 28(1):55-61, 2009. https://doi.org/10.22452/mjs.vol28no1.7.
17. Büker, O. et al. Investigations on the influence of total water hardness and pH value on the measurement accuracy of domestic cold water meters, *Water*, 13, 2701, 2021. https://doi.org/ 10.3390/w13192701.
18. Clark, R.M., Goddard, H. Cost and quality of water supply, Journal of Americal Water Works Associations, 69(1):13-15, 1977. https://doi.org/10.1002/j.1551-8833.1977.tb02533.x.

19. Xianhong, Y. et al. Application analysis of conductivity in drinking water quality analysis, *International Energy, Environment and Water Resources Conference*, IOP publishing, 784, 012028, 2021. https://doi.org/10.1088/1755-1315/784/1/012028.
20. Javanbakht, T. Logique floue et arborescence comme outils de modélisation des catégories en tant que prototypes, Thesis, University of Quebec in Montreal, 2016.
21. Javanbakht, T. Être et Pensée, J. P. Beaudin & S. Robert (Eds.), BouquinBec, Montreal, 2020.
22. Javanbakht T, Laurent S, Stanicki D, David E. (2019). Related physicochemical, rheological, and dielectric properties of nanocomposites of superparamagnetic iron oxide nanoparticles with polyethyleneglycol, *Journal of Applied Polymer Science*, 136, 48280–48290. https://doi.org/10.1002/app.48280.
23. Javanbakht, T., Sokolowski, W. Thiol-ene/acrylate systems for biomedical shape-memory polymers. *Shape Memory Polymers for Biomedical Applications*, 157-166, 2015. https://doi.org/10.1016/B978-0-85709-698-2.00008-8.
24. Vollath, D., Szabó, D.V. Synthesis and properties of nanocomposites, *Advanced Engineering Materials*, 6(3):117-127, 2004. https://doi.org/10.1002/adem.200300568.
25. Djavanbakht, T., Carrier, V., André, J. M., Barchewitz, R., Troussel, P. Effets d'un chauffage thermique sur les performances de miroirs multicouches Mo/Si, Mo/C et Ni/C pour le rayonnement X mou. *Journal de Physique IV*, France, 10, 281-287, 2000. https://doi.org/10.1051/jp4:20001031.
26. Javanbakht, T., Laurent, S., Stanicki, D., Frenette, M. Correlation between physicochemical properties of superparamagnetic iron oxide nanoparticles and their reactivity with hydrogen peroxide. *Canadian Journal of Chemistry*, 98, 601-608, 2020. https://doi.org/10.1139/cjc-2020-0087.
27. Kaur, M., Tripathi, P.K. The basic properties of graphene and its applications, *International Journal of Research and Analytical Reviews*, 937-944, 2018.
28. Javanbakht, T., Ghane-Motlagh, B., Sawan, M. Comparative study of antibiofilm activity and physicochemical properties of microelectrode arrays. *Microelectronic Engineering*, 229, 111305, 2020. https://doi.org/10.1016/j.mee.2020.111305.
29. Javanbakht, T., Hadian, H., Wilkinson, K. J. Comparative study of physicochemical properties and antibiofilm activity of graphene oxide nanoribbons. *Journal of Engineering Sciences*, 7(1), C1-C8, 2020. https://doi.org/10.21272/jes.2020.7(1).c1.
30. Javanbakht, T., David, E. Rheological and physical properties of a nanocomposite of graphene oxide nanoribbons with polyvinyl alcohol. *Journal of Thermoplastic Composite Materials*, 0892705720912767, 2020. https://doi.org/10.1177/0892705720912767.
31. Silver nanoparticles for water pollution monitoring and treatments: Ecosafety challenge and cellulose-based hybrids solution, *Polymers*, 12(8): 1635, 2020. https://doi.org/10.3390/polym12081635.
32. Nagar, A., Pradeep, T. Clean water through nanotechnology: Needs, gaps, and fulfillment, *ACS Nano*, 14(6):6420–6435, 2020. https://doi.org/10.1021/acsnano.9b01730.
33. Giwa, A. et al. *Polymeric materials for clean water*, Ed. R. Das, Springer, 167-190, 2019.
34. Khodakarami, M., Bagheri, M. Recent advances in synthesis and application of polymer nanocomposites for water and wastewater treatment, *Journal of Cleaner Production*, 296, 126404, 2021. https://doi.org/10.1016/j.jclepro.2021.126404.
35. Serajuddin, Chowdhury, A.I. et al. Application of a polymer in drinking water treatment: A case study, *5th International Conference on Civil Engineering for Sustainable Development*, 2020.
36. Adeola, A.O., Nomngongo, P.N. Advanced polymeric nanocomposites for water treatment applications: A holistic perspective, *Polymers*, 14(12):2462, 2022. https://doi.org/10.3390/polym14122462.
37. Beyene, H.D., Ambaye, T.G. Application of sustainable nanocomposites for water purification process, in *Sustainable Polymer Composites and Nanocomposites*, pp.387-412, 2019. https://doi.org/10.1007/978-3-030-05399-4_14.
38. Ardhiyanto, N.K., Pujiyanto, E., Rosyidi, C.N. Multi responses optimization of plastic injection molding for biodegradable polymers using Taguchi method and TOPSIS, *AIP Conference Proceedings*, 2097(1):030064, 2019. https://doi.org/10.1063/1.5098239.
39. Alaaeddin, M.H. et al. Polymer matrix materials selection for short sugar palm composites using integrated multi criteria evaluation method, *Composites B: Engineering*, 176, 107342, 2019. https://doi.org/10.1016/j.compositesb.2019.107342.
40. Narayanan, N.S. et al. Evaluation and optimization of surface roughness and metal removal rate through RSM, GRA, and TOPSIS techniques in turning PTFE polymers, Advances in Manufacturing Technology, 595-605, 2019. https://doi.org/10.1007/978-981-13-6374-0_65.
41. Chohan, J.S. et al. Taguchi S/N and TOPSIS based optimization of fused deposition modelling and vapor finishing process for manufacturing of ABS plastic parts, Materials, 13(22): 5176, 2020. https://doi.org/10.3390/ma13225176.
42. Yadav, R., Lee, H.-H. Fabrication, characterization, and selection using FAHP-TOPSIS technique of zirconia, titanium oxide, and marble dust powder filled dental restorative composite materials, *Polymers Advanced Technologies*, 33(1):3286-3295, 2022. https://doi.org/10.1002/pat.5780.
43. Zhang, K., Zhan, J., Yao, Y. TOPSIS method based on a fuzzy covering approximation space: An application to biological nano-materials selection, *Information Sciences*, 502, 297-309. https://doi.org/10.1016/j.ins.2019.06.043.
44. Loganathan, T.M. et al. Effect pf *Cyrtostachys renda* fiber loading on the mechanical, morphology, and flammability properties of multi-walled carbon nanotubes/phenolic bio-composites, *Nanomaterials*, 11(11):3049, 2021. https://doi.org/10.3390/nano11113049.

45. Shunmugesh, K., Panneerselvam, K. Optimization of machine process parameters in drilling of CFRP using multi-objective Taguchi technique, TOPSIS and RSA techniques, *Polymers and Polymer Composites*, 25(3):185-192, 2017.
46. Al-Hazmi, H. et al. Application of TOPSIS for selection and assessment of analytical procedures for ibuprofen determination in wastewater, *Current Analytical Chemistry*, 12(4): 261-267, 2016. https://doi.org/10.2174/1573411012666151009194541.
47. Yang, W.-C., et al. Materials selection method using TOPSIS with some popular normalization methods, *Engineering Research Express*, 3, 015020, 2021. https://doi.org/10.1088/2631-8695/abd5a7.
48. Marzouk, M., El-Razek, M.A. Selecting demolition waste materials disposal alternatives using fuzzy TOPSIS technique, *International Journal of Nature Computing Research*, 6(2):38-57, 2020. https://doi.org/10.4018/IJNCR.2017070103.
49. Chen, C.-H. A hybrid multi-criteria decision-making approach based on ANP-entropy TOPSIS for building materials supplier selection, *Entropy*, 23(12):1597. https://doi.org/10.3390/e23121597.
50. Banwet, D.K., Majumdar, A. Comparative analysis of AHP-TOPSIS and GA-TOPSIS methods for selection of raw materials in textile industries, *Proceedings of the 2014 International Conference on Industrial Engineering and Operations Management*, 2071-2080, 2014.
51. Rao, A.Y. Koona, R. Selection of optimum hybrid composite material for structural applications through TOPSIS technique, *International Journal of Surface Engineering and Interdisciplinary Materials Science*, 10(1):1-15, 2022.
52. Tiwari, S.K., Pande, S. Selection of gear materials using MCDM-TOPSIS approach, *International Journal of Manufacturing and Materials Processing*, 3(2), 2017. https://doi.org/10.37628/ijmmp.v3i2.411.

JOURNAL OF ENGINEERING SCIENCES

Volume 9, Issue 1 (2022)

Copyright Agreement

We, the Authors of the Article publishing in the Journal of Engineering Sciences, in the case of acceptance for publication, transfer to Founders and Editorial Board the underlined rights:

– publishing this article in English and distribution of the printed version;

– English translation of the article and distribution of the hard copy of the translation;

– distribution of the electronic version of the article through any electronic means (by hosted on the official website of the Journal, in electronic databases, repositories, etc.).

We reserve the rights without the consent of the Editorial Board or Founders:

– to use the article materials partially or in whole for educational purposes;

– to use the article materials partially or in whole to write own dissertations;

– to use the article materials for thesis preparing, conference materials, as well as for presentations;

– to post electronic copies (including the final electronic version downloaded from the official website of the Journal):

– on the personal web-sources of all the co-authors (websites, webpages, blogs, etc.);

– on the web-sources of authors working organizations (including electronic institutional repository);

– on the International scientometric databases;

– on non-commercial open-access sources.

In all cases, the presence of citations to the article or hyper-link to the electronic copy of the journal's official website is obligatory.

By this agreement, we also certify that the submitted article:

– does not violate the copyrights of other persons or organizations;

– has not been published previously in other publishing houses and submitted for publication in other Journals.

JOURNAL OF ENGINEERING SCIENCES

Volume 9, Issue 1 (2022)

Dear Authors of the Journal of Engineering Sciences!

The Editorial Board of the Journal of Engineering Sciences pays special attention to the structure of the articles according to the **List of Scientific Professional Editions of Ukraine** (Category "B", Minutes No. 1208 of 07.11.2018, Appendix No. 8). Only original articles by the authorship of up to 5 authors are accepted for publication according to the **Template** with the following elements:

– general statement of the problem and its relationship with the essential scientific or practical problems;
– analysis of the recent investigations and publications in the same research field;
– statement of the significance of the general problem that was not solved before;
– statement of the purpose of the research article;
– description of the initial data of the research with the justification of the achieved scientific results;
– conclusions and ways for further development of the research.

All the articles are reviewed by the independent double-blind procedure.

All the authors should send via e-mail **jes@teset.sumdu.edu.ua** the electronic version of the following materials:
– article **in English** according to the **Template**;
– information about authors and their affiliation with the related address.

ATTENTION!
If one of the mentioned components is not sent or there are many stylistic, orthographic, and grammatical errors, the article will not be considered by the Editorial Board and will not be reviewed.

The minimum size of the materials:
1. Scientific – theoretical articles (up to 25,000 symbols; about 14 pages) that deal with the theoretical research and descriptions of physical laws concerning the investigated phenomena; theoretical generalizations and fundamental principles proved by the experimental research data.
2. Scientific-practical articles (up to 10,000 symbols; about 6 pages) that deal with scientific experiments and recent experience. They include the proposed methods for the experimental research or means to observe the studied phenomena. An essential part of these articles is the description of the achieved results and their explanation acquired in immediate interaction with the object of investigations, its significance, and practical implementations.
3. Scientific-methodological articles (up to 15,000 symbols; about 8 pages) that deal with the review of processes, methods, instruments for solving scientific and applied problems; the statement of the new methodology, results of which allow creating more precise methodology based on an up-to-date methodology for the implementation of discovered laws.

Ministry of Education and Science of Ukraine
Sumy State University

JOURNAL OF ENGINEERING SCIENCES

Scientific Journal

Volume 9, Issue 1 (2022)

Відповідальний за випуск
І. В. Павленко

Комп'ютерне складання та верстання:
Х. В. Берладір

Обкладинка:
В. О. Іванов

Коректор:
С. М. Симоненко

Responsible for release:
Ivan Pavlenko

Computer design and typesetting:
Kristina Berladir

Cover page:
Vitalii Ivanov

Corrector:
Svitlana Symonenko

Підписано до друку 30.06.2021. Формат 60x84/8.
Папір офс. Друк офс.
Ум. друк. арк. 17,91. Обл.-вид. арк. 24,36.
Наклад 100 прим. Замовлення №
Сумський державний університет, вул. Римського-Корсакова, 2, 40007, м. Суми, Україна
Свідоцтво про внесення суб'єкта видавничої справи до Державного реєстру
ДК № 3062 від 17.12.2007.

Надруковано у друкарні Сумського державного університету,
вул. Римського-Корсакова, 2, 40007, м. Суми, Україна

Editorial Board: 2, Rymskogo-Korsakova St., 40007, Sumy, Ukraine; Apt. M-211
Contact Phones: +380-993-845-740
E-mail: jes@teset.sumdu.edu.ua
Website: https://jes.sumdu.edu.ua

State registration certificate of the print mass-media No. 20499-10299 PR.